Solution reactivity studies of group 15 Zintl ions

A thesis submitted in partial fulfilment of the requirements for the degree of

Doctor of Philosophy at the University of Oxford

Caroline Mary Knapp

Corpus Christi College

Oxford

August 2013

Abstract

Solution reactivity studies of group 15 Zintl ions

Caroline Knapp — Doctor of Philosophy
Corpus Christi College — Trinity 2013

The reactivity of group 15 Zintl ions, E_7^{3-} (E = P, As), towards a number of transition and post-transition metal reagents has been studied. The synthesis and characterisation of the resulting novel cluster anions are described herein.

The reactions of E_7^{3-} with $[Cu_5(mes)_5]$, MPh_2 (M = Zn, Cd) and $InPh_3$ yielded the Cu–Cu bridged species $[Cu_2(E_7)_2]^{4-}$ (E = P, As), the group 12 bridged cluster anions $[M(E_7)_2]^{4-}$ (M = Zn: E = P, As; M = Cd: E = P), and the In-functionalised Zintl ions $[E_7InPh_2]^{2-}$, respectively.

P_7^{3-} and As_7^{3-} have been found to react with a number of metal salts, namely $[M(nbe)_3][SbF_6]$ and MCl (M = Ag, Au), $InCl_3$, TlCl and MI_2 (M = Sn, Pb). These reactions formed the Ag–Ag and Au–Au bridged complexes $[M_2(HP_7)_2]^{2-}$ (M = Ag, Au), the In-bridged species $[In(E_7)_2]^{3-}$ (E = P, As), the Tl-derivatised Zintl ions $[TlE_7]^{2-}$ (E = P, As), and the sixteen vertex cluster anions $[ME_{15}]^{3-}$ (M = Sn, Pb; E = P, As).

The reactivity of P_7^{3-} towards a series of group 8 compounds has also been studied. The reactions of P_7^{3-} with $FeCl_2$ and $[Ru(PPh_3)_3Cl_2]$ produced $[M(HP_7)_2]^{2-}$ (M = Fe, Ru). NMR studies showed that these species can be deprotonated to form $[M(P_7)_2]^{4-}$ (M = Fe, Ru). These Fe and Ru complexes are isoelectronic with ferrocene. In addition, P_7^{3-} reacts with $[Ru(COD)(\eta^3\text{-}CH_2C(CH_3)CH_2)_2]$ to form $[(C_4H_7)P_7Ru(COD)]^{2-}$.

Both P_7^{3-} and As_7^{3-} undergo transition metal mediated activation reactions in the presence of $[Co(PEt_2Ph_2)(mes)_2]$, yielding $[Co(\eta^5\text{-}P_5)\{\eta^2\text{-}HP_2(mes)\}]^{2-}$ and $[Co(\eta^3\text{-}As_3)\{\eta^4\text{-}As_4(mes)_2\}]^{2-}$, respectively.

Acknowledgements

First and foremost, I would like to thank my supervisor, Dr Jose Goicoechea, for giving me the opportunity to be involved in this exciting and challenging project. I am extremely grateful for his support, dedication and, above all, his unwavering enthusiasm, without which the last four years would have been nowhere near as enjoyable.

I would like to acknowledege the contributions of the following people to the project: Jose for solving many of my crystal structures and performing many of the DFT calculations; Melissa Raybould and Professor John McGrady for carrying out further DFT calculations; Dr Nick Rees for helping with some of the NMR experiments and simulations; Dr Amber Thompson for helping with some of the crystallography; and my Part II students Joe Large, Charlotte Jackson and Amy Pritchard, and our Summer student Bethan Westcott for their contributions to the synthetic work described herein.

I would like to thank everyone from the Goicoechea group, past and present, particularly Dr Mark Denning, our former Postdoc, for much help and advice, and for training me in the fine art of making Zintl phases, and my fellow DPhil students Dr Binbin Zhou, Dr Mark Irwin, Rob Turbervill, Gaby Espinoza Quintero and Andy Jupp for all their help and words of wisdom, the crystallography, the proofreading and, most importantly, the musical education. I would also like to thank all the other lovely and talented people who I've had the good fortune to share lab S11 with: David Hansen, Ed Gore-Randall, Rhiannon Jenkins, Belinda Hitchins, Charlotte Jackson, Joe Large, Amy Pritchard, Charlie Webb, Laurence Doyle, Pete Hill, Becca Musgrave, Melissa Raybould, Phil McCullough, Ben Clough, Bethan Westcott and Jordan Waters.

Last but by no means least, I would like to thank my wonderful family and friends for all their support and for making me laugh. A special mention goes to Dr Jonathan Ayling for putting up with far more than his fair share of tears, tantrums and terrible saxophone playing.

Abbreviations

@	centred
°	degree
°C	degrees Celsius
18-crown-6	1,4,7,10,13,16-hexaoxacyclooctadecane
2-Ad	2-adamantyl
2,2,2-crypt	4,7,13,16,21,24-hexaoxa-1,10-diazabicyclo[8.8.8]hexacosane
δ	chemical shift
ε	dielectric constant
η	hapticity
λ	wavelength
μ	bridge
μL	microlitre
μM	micromolar
$\rho(\mathbf{r})$	charge density
A	alkali metal
Å	Ångström
AIM	Atoms in Molecules
anal.	analysis
Ar	aryl group

Ar^{Dipp_2}	C_6H_3-2,6-(C_6H_3-2,6-$^{i}Pr_2$)$_2$
av	average
BCP	bond critical point
BDE	bond dissociation energy
bipy	2,2-bipyridine
Bu	butyl
calcd.	calculated
CCD	charge coupled device
cm^{-1}	wavenumber
COD	1,5-cyclooctadiene
COSY	correlation spectroscopy
Cp	cyclopentadienyl
Cp*	pentamethylcyclopentadienyl
Cp″	1,3-di-*tert*-butylcyclopentadienyl
CSD	Cambridge Structural Database
Cy	cyclohexyl
d	doublet
dcpm	bis(dicyclohexylphosphino)methane
dd	doublet of doublets
DFT	density functional theory
Dipp	2,6-diisopropylphenyl
DME	dimethoxyethane
DMF	dimethylformamide
DMSO	dimethylsulfoxide
dppe	1,2-bis(diphenylphosphino)ethane

dppm	bis(diphenylphosphino)methane
E, E′	*p*-block element
en	ethylenediamine
EPR	electron paramagnetic resonance
ESI	electrospray ionisation
Et	ethyl
g	gram, g-factor
G	Gauss
Hex	hexyl
HMQC	heteronuclear multiple quantum coherence
HOMO	highest occupied molecular orbital
HPLC	high performance liquid chromatography
Hz	Hertz
i	*ipso*
^{i}Bu	*iso*-butyl
^{i}Pr	*iso*-propyl
IR	infra-red
J	coupling constant
K	Kelvin
kJ	kilojoule
kV	kilovolt
L	ligand
LCT	liquid chromatography time of flight
LUMO	lowest unoccupied molecular orbital
m	multiplet

m	mass, *meta*
M	metal, molar
Me	Methyl
mes	mesityl (2,4,6-trimethylphenyl)
mg	milligram
MHz	megahertz
mL	millilitre
mm	millimetre
mmol	millimole
mol	mole
MS	mass spectrometry
n	integer
nbe	norbornene (bicyclo[2.2.1]hept-2-ene)
NBO	natural bond order
nixantphos	4,6-bis(diphenylphosphino)phenoxazine
NMR	nuclear magnetic resonance
Np	neopentyl (Me_3CCH_2–)
np_3	tris(2-diphenylphosphinoethyl)amine
o	*ortho*
p	*para*
Ph	phenyl
ppm	parts per million
Pr	propyl
py	pyridine

R, R′	alkyl group
RCP	ring critical point
s	singlet
t	triplet
^{t}Bu	*tert*-butyl
td	triplet of doublets
Tf	triflyl (CF_3SO_2–)
THF	tetrahydrofuran
tol	toluene
triphos	1,1,1-tris((diphenylphosphino)methyl)ethane
V	Volt
w/w	by weight
x	integer
X	anion
y	integer
z	charge

Contents

Chapter 1 Introduction

1.1 Group 15 elements

The focus of this thesis is the reactivity of group 15 Zintl ions, E_7^{3-} (E = P, As, Sb). Phosphorus, arsenic and antimony are all subject to the "double bond rule", which states that elements with a principal quantum number greater than two should not be able to form (p–p)π bonds with themselves or with other elements.[1] Later research has shown that all three elements are, in fact, capable of forming multiple bonds, however compounds featuring E–E multiple bonds are rare compared with those containing E–E single bonds.[2] Phosphorus, arsenic and antimony all have a tendency to catenate and exist in several allotropic forms, reflecting the variety of ways in which catenation can be achieved. One allotrope of phosphorus, known as white phosphorus, consists of discrete tetrahedral P_4 molecules, in which each P atom is bonded to the other three *via* a single bond (Figure 1.1).[2,3] This form is also the most reactive and thermodynamically the least stable in the solid state. An analogous form of arsenic, known as yellow arsenic, consists of discrete As_4 tetrahedra, however this form rapidly decomposes into the more stable grey allotrope, which will be discussed below.[2]

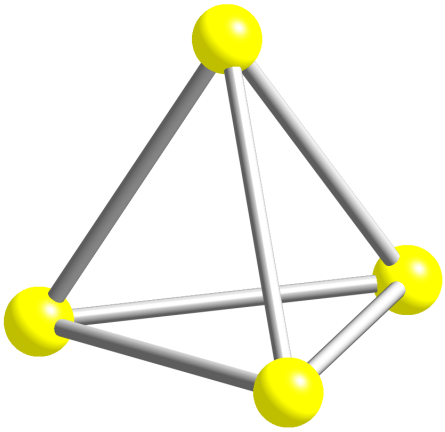

Figure 1.1: Ball and stick diagram of the P_4 molecule.[3]

If white phosphorus is heated to temperatures above 250 °C, amorphous red phosphorus is obtained, which is much less reactive than the white allotrope.[2] Amorphous red phosphorus can be transformed into various crystalline forms by further heating. All of the forms of red phosphorus are believed to have highly polymeric structures, in which three-dimensional networks are formed by breaking one P–P bond in each P_4 tetrahedron and forming new bonds to the two neighbouring P_4 units (Figure 1.2). The structures of black arsenic and black antimony are also thought to be polymeric.

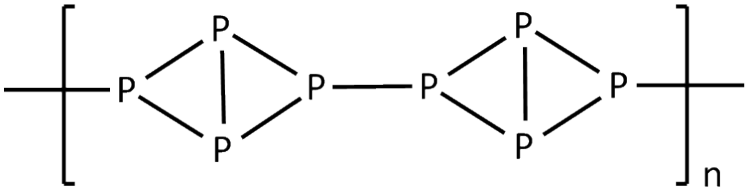

Figure 1.2: Diagram showing part of the polymeric structure of red phosphorus.

A third allotrope of phosphorus, known as Hittorf's phosphorus, consists of P_8 and P_9 groups linked alternately by pairs of P atoms to form polymeric chains with a P_{21} repeat unit (Figure 1.3).[2,4] The chains form infinite layers, which are stacked in pairs.

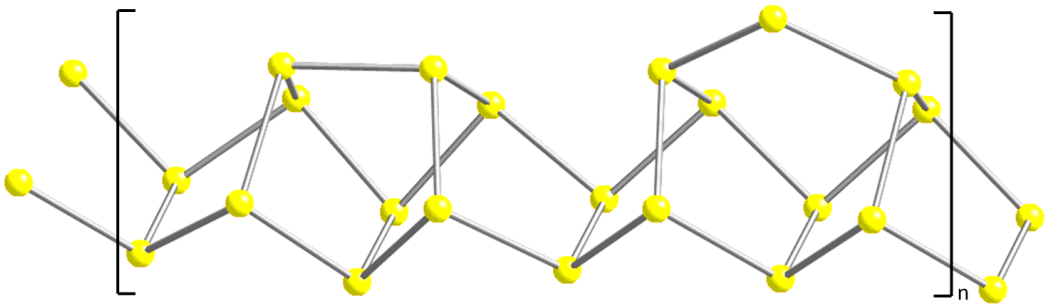

Figure 1.3: Ball and stick diagram showing the P_{21} repeating unit in Hittorf's phosphorus.[4]

The thermodynamically most stable allotropes of phosphorus, arsenic and antimony, known respectively as black phosphorus, grey arsenic and metallic antimony, all have layered structures that consist of interlocked six-membered rings (Figure 1.4).[2] Grey arsenic and metallic antimony are the most common allotropes of these two elements.

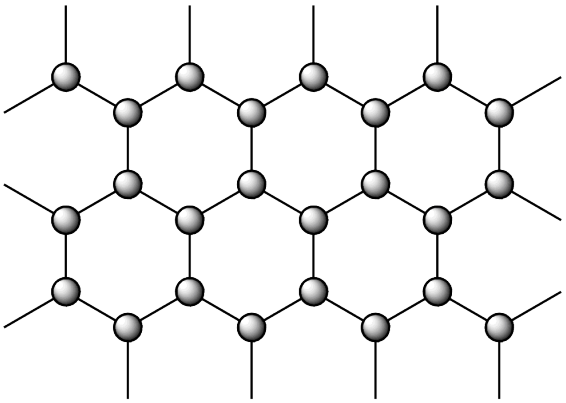

Figure 1.4: Diagram showing a section of a single layer of the structure of black phosphorus, grey arsenic or metallic antimony (viewed from above).

A number of compounds of the group 15 elements have structures that can be derived from the tetrahedral P_4 molecule. For example, the sulfides, E_4S_3 (E = P, As), can be obtained by inserting a sulfur atom into three of the E–E bonds of the E_4 tetrahedron.[5,6] The group 15 Zintl ions, E_7^{3-} (E = P, As, Sb), are isostructural to E_4S_3 and can be obtained in a similar fashion (Figure 1.5).[7]

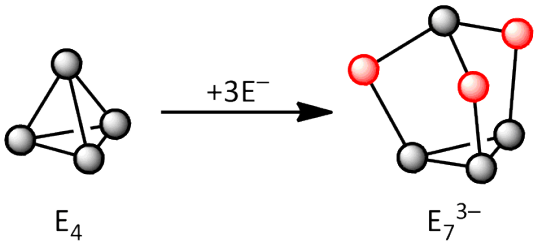

Figure 1.5: Diagram showing the relationship between E_4 and E_7^{3-}. Atoms possessing a formal negative charge are shown in red.

1.2 History of Zintl ions

Zintl clusters were discovered in 1891 by Joannis, who observed that metallic sodium reacted with excess lead in liquid ammonia to form intensely coloured green solutions.[8–10] Joannis also discovered that sodium reacted with excess antimony under the same conditions to produce yellow solutions. Later research carried out by Kraus showed that elemental tin could be dissolved in ammonia solutions of sodium, yielding deep red solutions.[11] Studies by Smyth gave a maximum solubility in liquid ammonia of 2.24 lead atoms per sodium atom, while Peck showed that a maximum of 2.33 antimony atoms per sodium atom could be dissolved.[12,13] The anionic species responsible for these intensely coloured liquid ammonia solutions were

identified by Eduard Zintl in the 1930s, using potentiometric titrations; Pb_9^{4-}, Sn_9^{4-}, Sb_7^{3-} and As_7^{3-} were all identified by this method.[14–17]

It was later found that solutions of Zintl clusters could be obtained by dissolving pre-formed precursor alloys of the post-transition elements and alkali or alkaline earth metals in liquid ammonia or ethylenediamine. These alloys, known as Zintl phases, have the general formula M_xE_y (M = alkali or alkaline earth metal; E = *p*-block element) and are produced by heating a stoichiometric mixture of the elements for several days under an inert atmosphere. It is assumed that there is a complete electron transfer from M to E, resulting in the formation of E_y^{x-} in solution. The first example of a Zintl ion abstracted from a solid state precursor was reported by Kummer and Diehl, who observed that an alloy of composition $NaSn_{2.4–2.5}$ dissolved in ethylenediamine to produce the compound Na_4Sn_9·6–8en upon crystallisation.[18] Since then, a number of solid state phases containing Zintl cluster anions have been synthesised. These include the group 15 Zintl phases M_3E_7 (M = Li, Na, K, Rb, Cs; E = P, As, Sb) and M_3E_{11} (M = Na, K, Rb, Cs; E = P, As), which feature E_7^{3-} and E_{11}^{3-} cluster anions, respectively.[19–25] Alkaline earth metal-containing Zintl phases, $M_3(E_7)_2$ (M = Sr, Ba; E = P, As) have also been reported.[7,26,27] Examples of group 14 Zintl phases include $M_4E'_4$ (M = Na, K, Rb, Cs; E′ = Si, Ge, Sn, Pb), $M_4E'_9$ (M = K, Rb, Cs; E′ = Ge, Sn, Pb) and $M_{12}E'_{17}$ (M = Na, K, Rb; E′ = Si, Ge, Sn), which feature $E'_4{}^{4-}$, $E'_9{}^{4-}$, and a 2:1 stoichiometric mixture of $E'_4{}^{4-}$ and $E'_9{}^{4-}$ cluster anions, respectively.[28–42] $E'_4{}^{4-}$ cluster anions are also present in the alkaline earth metal-containing Zintl phases $M_2E'_4$ (M = Sr, Ba; E′ = Si, Ge).[43]

The next major breakthrough in the field was the discovery in 1975 by Corbett and co-workers that the solubility of Zintl phases could be improved by adding the cation sequestering agent 2,2,2-crypt (4,7,13,16,21,24-hexaoxa-1,10-diazabicyclo[8.8.8]hexacosane), which forms complexes with alkali metal cations and prevents the transfer of electrons from the Zintl ions back to the cations, hence stabilising Zintl ions in solution.[44] Complexation also forms cations of a comparable size to that of the cluster anions, which facilitates crystallisation. Much later, research by Fässler and Hoffmann showed that 18-crown-6 (1,4,7,10,13,16-hexaoxacyclooctadecane) could also be used as a sequestering agent.[45]

Since the 1970s, a huge variety of Zintl cluster anions have been discovered. These include the group 15 Zintl ions E_7^{3-} (E = P, As, Sb), E_{11}^{3-} (E = P, As, Sb) and E_4^{2-} (E = P, As, Sb, Bi), and

the group 14 Zintl ions $E'_4{}^{4-}$ (E′ = Si, Ge, Sn, Pb), $E'_5{}^{2-}$ (E′ = Si, Ge, Sn, Pb) and $E'_9{}^{n-}$ (E′ = Si, Ge, Sn, Pb; n = 2, 3, 4) (Figure 1.6).[7,24,27,29,30,32,43,44,46–62]

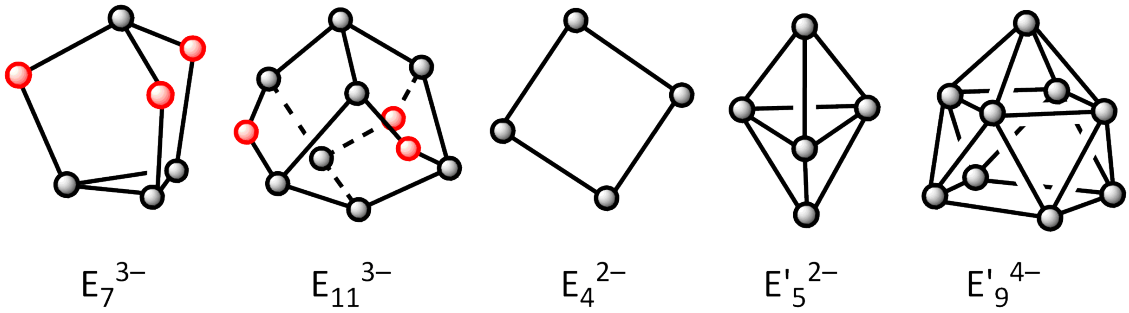

Figure 1.6: Examples of some of the structures adopted by Zintl ions. Atoms possessing a formal negative charge are shown in red.

1.3 Structure and bonding in $E_7{}^{3-}$ cluster anions

Unlike the electron-deficient $E'_9{}^{n-}$ (n = 2, 3 or 4) Zintl ions of the group 14 elements, the group 15 Zintl ions, $E_7{}^{3-}$, are electron-precise, and their bonding can be described using the conventional two-centre two-electron bond model. $E_7{}^{3-}$ has a nortricyclane-like structure with C_{3v} point symmetry, consisting of a three-membered ring of basal E atoms (E5, E6 and E7 in Figure 1.7), three two-connect bridging E atoms (E2, E3 and E4 in Figure 1.7) and a single three-connect E atom at the apex (E1 in Figure 1.7). A negative charge can be assigned to each two-connect bridging E atom.

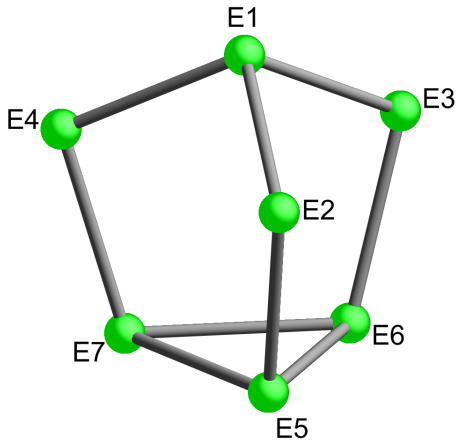

Figure 1.7: Ball and stick diagram of $E_7{}^{3-}$.

The first compound of a group 15 Zintl ion to be characterised by single crystal X-ray diffraction was $Sr_3(P_7)_2$, which was synthesised by Von Schnering in 1972.[7] This was followed by the crystal structures of $[Na(2,2,2\text{-crypt})]_3[Sb_7]$ and $Ba_3(As_7)_2$ in 1975 and 1977,

respectively.[27,44] It was observed that the bond lengths within the cluster anions vary depending on their position in the E_7^{3-} cage. The three basal E–E bonds (E5–E6, E5–E7 and E6–E7) are longer than the bonds to the apical E atom (E1–E2, E1–E3 and E1–E4), which are in turn longer than the bonds linking the bridging E atoms to the base (E2–E5, E3–E6 and E4–E7).[7,27,44] The relatively long bond lengths for the basal atoms are indicative of significant ring strain and, in the case of the P_7^{3-} cluster, are similar to those in white phosphorus (2.21 Å).[3] The mean bond lengths for E_7^{3-} (E = P, As, Sb) are provided in Table 1.1.

Table 1.1: Mean bond lengths for E_7^{3-}.[7,27,44]

Bond	Mean bond length in P_7^{3-} (Å)	Mean bond length in As_7^{3-} (Å)	Mean bond length in Sb_7^{3-} (Å)
E1–E2 E1–E3 E1–E4	2.21	2.432	2.78
E2–E5 E3–E6 E4–E7	2.17	2.399	2.70
E5–E6 E5–E7 E6–E7	2.25	2.498	2.86

^{31}P NMR spectroscopy studies have shown that the P_7^{3-} anion is fluxional both in solution and in the solid state.[63,64] At room temperature, the only observable feature in the solution ^{31}P NMR spectrum of P_7^{3-} is a non-specific broad signal. If the temperature is raised to 50 °C, a singlet at δ = –119 ppm is observed. At this temperature, all seven P atoms are equivalent on the NMR timescale, and so the average spectrum is recorded. However, below –35 °C, the ^{31}P NMR spectrum consists of three separate signals at δ = –57.0, –103.0 and –161.7 ppm in the intensity ratio 1:3:3, corresponding to the single P atom at the apex, the three two-connect bridging P atoms, and the three basal P atoms, respectively. This temperature dependence is caused by a Cope-like rearrangement that takes place in the P_7^{3-} cluster. This process can occur because the cluster has three easily movable electron pairs centred on the three two-connect P atoms. In addition, the three-membered ring markedly reduces the activation energy for the Cope rearrangement. Each Cope rearrangement involves the breaking of one bond in the three-membered ring (–(P5–P6), –(P5–P7) or –(P6–P7)) and the formation of a new P–P bond (+(P2–P3), +(P2–P4) or +(P3–P4)) (Figure 1.8). Valence tautomerism has not been studied in the As_7^{3-} and Sb_7^{3-} clusters, though as these clusters have the same structure

as P_7^{3-}, it is likely that the Cope rearrangement can also occur in these two ions.

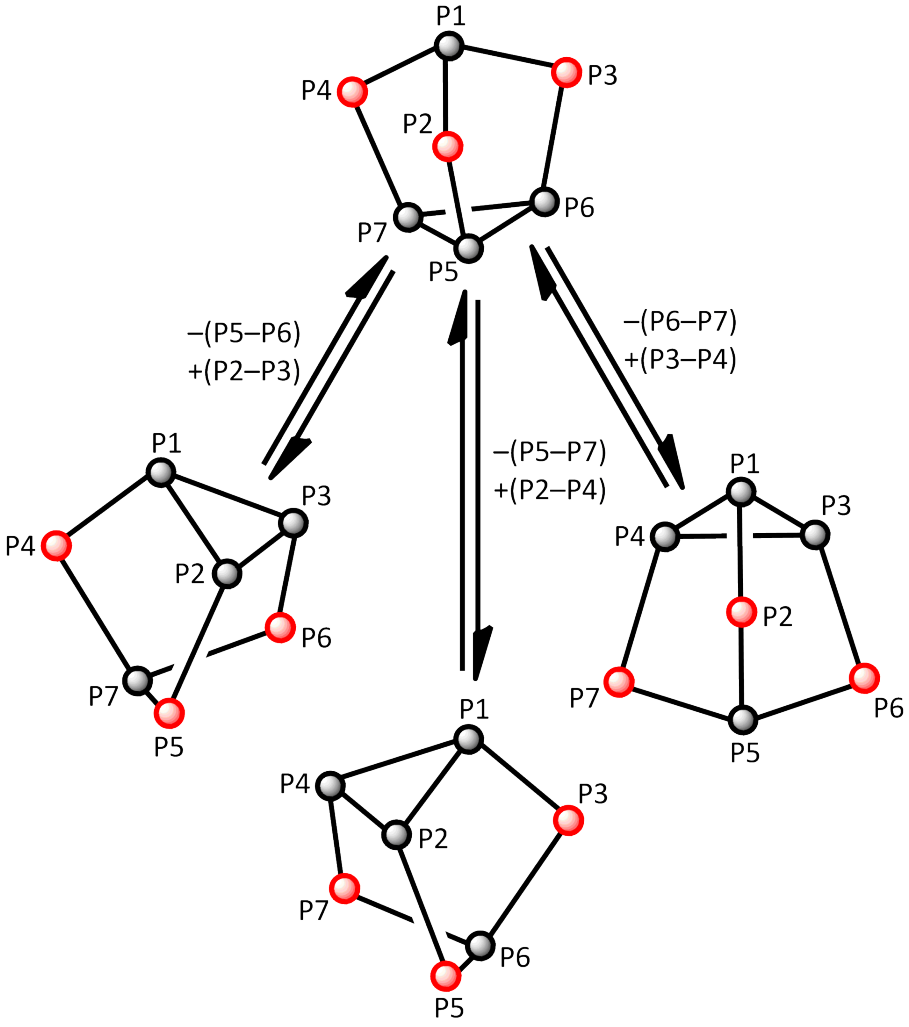

Figure 1.8: Diagram showing the Cope rearrangement taking place in P_7^{3-}. Atoms possessing a formal negative charge are shown in red.

1.4 Synthesis of protonated P_7^{3-} cages

Baudler and co-workers reported the synthesis of a number of phosphorus-containing compounds, including Li_2HP_7, LiH_2P_7 and P_7H_3.[63,65,66] Li_2HP_7 was obtained in the reaction of Li_3P_7 with P_2H_4.[67] This compound contains the monoprotonated cluster anion HP_7^{2-}. ^{31}P NMR studies showed that, much like the P_7^{3-} anion, HP_7^{2-} is fluxional in solution. At –60 °C, the ^{31}P NMR spectrum shows seven equal intensity resonances at –9.0, –67.5, –83.7, –119.4, –134.8, –145.2 and –215.9 ppm. These correspond to the protonated P atom, the apical P atom, the two two-connect P atoms, and the three basal P atoms, respectively. If the temperature is increased, six of these resonances broaden and coalesce. The resonance corresponding to the protonated P atom remains unchanged, since this atom is not involved

in the fluxional process. As for the P_7^{3-} cluster, these observations are consistent with a Cope-like rearrangement (Figure 1.9).

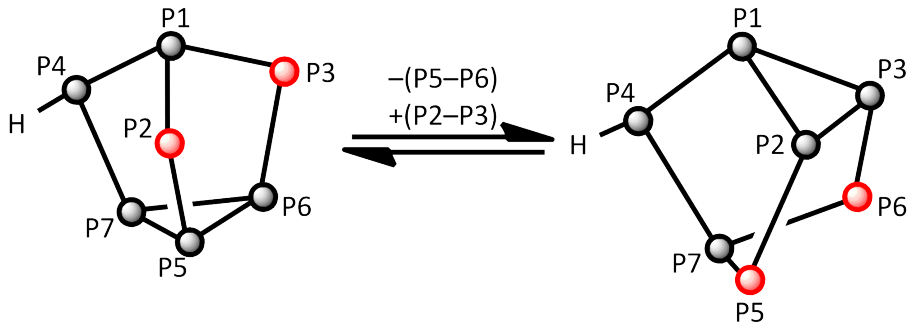

Figure 1.9: Diagram showing the Cope rearrangement taking place in HP_7^{2-}. Atoms possessing a formal negative charge are shown in red.

An alternative synthesis of HP_7^{2-} was reported by Korber in 2004.[68] K_3P_7 was found to react with a proton-charged ion exchange resin in liquid ammonia in the presence of $[PPh_4]Br$ to form HP_7^{2-}, which was isolated as the $[PPh_4]^+$ salt. Later research by Dai and Xu showed that HP_7^{2-} could be obtained by stirring K_3P_7 and a cation sequestering agent in ethylenediamine.[69] The proton was thought to originate from adventitious moisture present in either the ethylenediamine solvent or the cation sequestering agent. Most recently, research published by the Goicoechea group has shown that HP_7^{2-} can be produced in good yields by reacting K_3P_7 with an equimolar amount of degassed and deionised water in pyridine.[70]

Baudler and co-workers were also the first to report the synthesis of $H_2P_7^-$.[65] LiH_2P_7 was formed in the reaction between Li_3P_7 and P_7H_3. The ^{31}P NMR spectrum of this compound shows five resonances at 0.0, –45.4, –79.2, –113.1 and –199.8 ppm with relative intensities 2:1:1:1:2, corresponding to the two protonated P atoms, the single two-connect P atom, the apical P atom, and the three basal P atoms, respectively. This is consistent with $H_2P_7^-$ having a symmetrical structure, as shown in Figure 1.10. It was later discovered that dialkylated E_7^{3-} cages, $R_2E_7^-$, also have symmetrical structures, as discussed in Section 1.6.1.1.

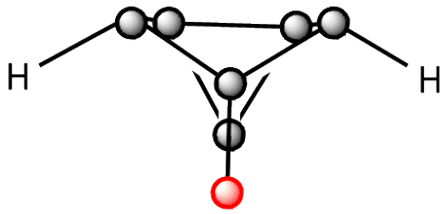

Figure 1.10: Diagram showing the proposed structure of $H_2P_7^-$ (viewed from above). Atoms possessing a formal negative charge are shown in red.

Research by Korber and Von Schnering showed that $H_2P_7^-$ can also be synthesised from K_3P_{11} and $[PPh_4]Cl$ in liquid ammonia.[71] A crystal structure of the $[PPh_4]^+$ salt was obtained, however the positions of the hydrogen atoms could not be determined.

The neutral triprotonated cluster, P_7H_3, was synthesised in the reaction of $P_7(SiMe_3)_3$ with three equivalents of MeOH (the synthesis of $P_7(SiMe_3)_3$ will be discussed in Section 1.6.1.1).[65] ^{31}P NMR studies showed that two isomers of P_7H_3 are present in solution: an asymmetric isomer and a symmetric isomer, which give rise to seven and three ^{31}P NMR resonances, respectively (Figure 1.11).

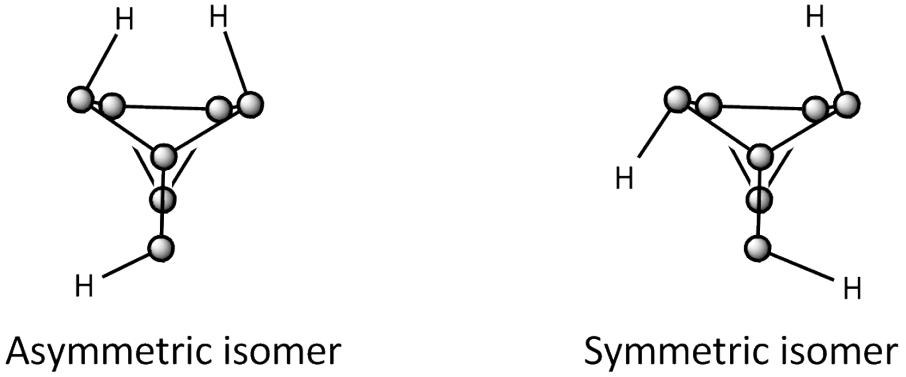

Figure 1.11: Diagram showing the two isomers of P_7H_3 (viewed from above).

1.5 Synthesis of higher nuclearity polypnictide cages

A number of higher nuclearity polypnictide cages that are based on the E_7^{3-} Zintl anions have been reported. All of these polypnictides are electron-precise clusters, where the two-connect atoms carry a formal negative charge. Reduction of white phosphorus with lithium in liquid ammonia formed the P_{14}^{4-} cluster anion, which was isolated as the $[Li(NH_3)_4]^+$ salt.[72] As_{14}^{4-} was synthesised in the reaction of Rb_4As_6 with $SbPh_3$ in liquid ammonia in the presence of 18-crown-6.[72] A crystal structure of the [Rb(18-crown-6)]$^+$ salt was obtained. These E_{14}^{4-}

species are dimers of E_7^{3-} cages linked *via* a single E–E bond (Figure 1.12). The apical E atoms point in opposite directions ("up-down" isomers).

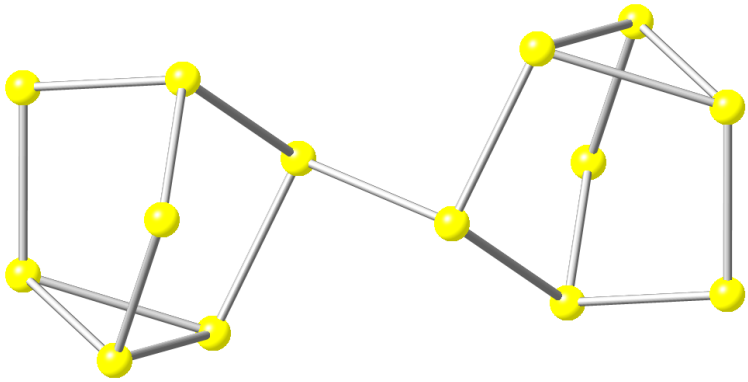

Figure 1.12: Ball and stick diagram of P_{14}^{4-}.[72]

Miluykov and co-workers showed that P_{14}^{4-} could also be obtained by refluxing PCl_3 and sodium in THF or by reacting red phosphorus with sodium in ethylenediamine.[73] The ^{31}P NMR spectrum of P_{14}^{4-} obtained by Miluykov shows several poorly resolved multiplets, which could not be assigned.

The synthesis of P_{16}^{2-} was first reported by Von Schnering and co-workers, who reacted Na_3P_7 with $[PPh_4]Cl$ in THF to form $[PPh_4]_2[P_{16}]$.[74] The P_{16}^{2-} cluster anion consists of two P_7 cages bridged by two further P atoms (Figure 1.13). In this case, the two apical P atoms point in the same direction (an "up-up" isomer).

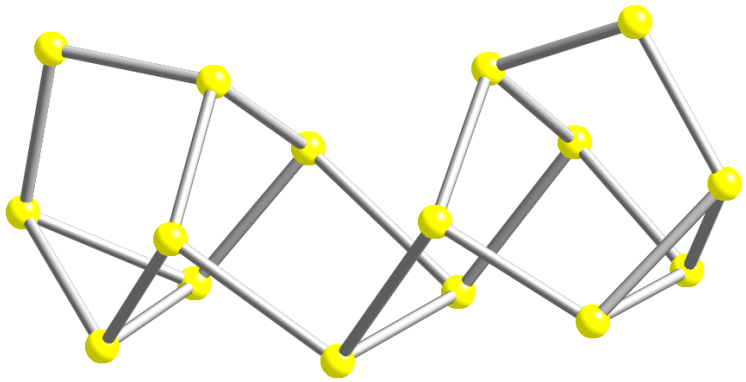

Figure 1.13: Ball and stick diagram of P_{16}^{2-}.[74]

Further studies on P_{16}^{2-} were carried out by Baudler, who observed that Li_2P_{16} could be synthesised by reacting white phosphorus with $LiPH_2$, as well as *via* the disproportionation of Li_2HP_7 in THF.[75,76] The ^{31}P NMR spectrum of P_{16}^{2-} shows six resonances at 60, 38, 6, –34, –134 and –172 ppm, which have relative intensities 2:1:1:1:1:2 and are consistent with the

solid state structure.

The reaction of white phosphorus with substoichiometric amounts of sodium in DME or THF formed Na_3P_{21}, which features the P_{21}^{3-} anion.[77] This species consists of two nortricyclane-like P_7 clusters linked *via* a norbornadiene-like P_7 cage (Figure 1.14). The structure of P_{21}^{3-} is closely related to that of Hittorf's phosphorus, which features P_8 and P_9 groups linked by pairs of P atoms.[4]

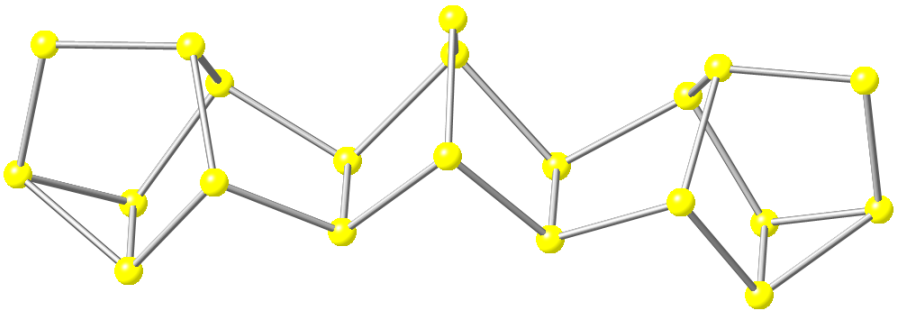

Figure 1.14: Ball and stick diagram of P_{21}^{3-}.[77]

The ^{31}P NMR spectrum of P_{21}^{3-} shows seven resonances at 72, 61, –15, –108, –118, –146 and –169 ppm with relative intensities 2:8:2:1:2:2:4. Eight resonances would be expected based on the solid state structure, however the intensity of the resonance at 61 ppm suggests that this resonance arises from two sets of four equivalent P atoms.

1.6 Reactivity studies on E_7^{3-}

The reactions of group 15 Zintl ions can be divided into two types: those in which the E_7^{3-} cage is retained in the product, and those in which fragmentation of the E_7^{3-} cage has occurred, resulting in the formation of larger heteroatomic cluster alloys. If the E_7^{3-} cage is retained, it can exhibit three possible bonding modes: η^1, η^2 and η^4, which act as two-, four- and six-electron donors, respectively (Figure 1.16). The bonding mode exhibited by the cluster is therefore strongly dependent on the electron configuration of the element to which it is bonded. For η^4-coordination to occur, one of the E–E bonds within the three-membered ring has to break, which results in the cluster adopting a norbornadiene-like structure (Figure 1.15).

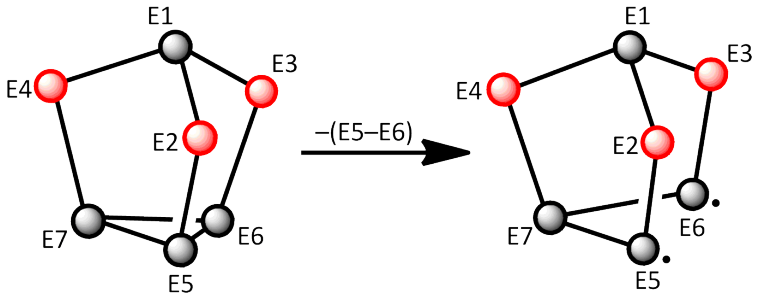

Figure 1.15: Diagram showing the nortricyclane–norbornadiene transition in E_7^{3-}. Atoms possessing a formal negative charge are shown in red.

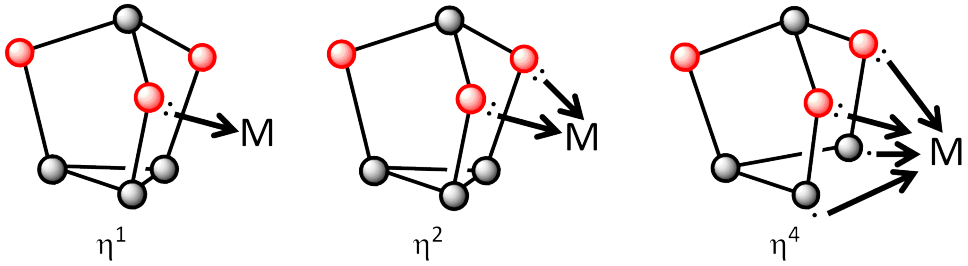

Figure 1.16: Diagram showing the three possible bonding modes of E_7^{3-}. Atoms possessing a formal negative charge are shown in red.

1.6.1 Reactions in which the E_7^{3-} cage is retained

1.6.1.1 Alkylation reactions of E_7^{3-}

Both P_7^{3-} and As_7^{3-} react with tetraalkylammonium salts, $[RR'_3N]X$ (R = R′ = Me, Et, Bu; R = $PhCH_2$, $EtOCOCH_2$, EtOCOCHMe: R′ = Me; X = Cl, Br, I) to form $R_2E_7^-$ ions (E = P: R = Me, Et, Bu, $PhCH_2$, $EtOCOCH_2$, EtOCOCHMe; E = As: R = $PhCH_2$).[78,79] The reactions are stereospecific, and only one of three possible isomers is formed in each case. Two isomers (I and II) have C_s point symmetry, with mirror planes running between the alkyl groups, resulting in two pairs of equivalent E atoms with the remaining three being unique. For the third isomer (III), all seven E atoms are inequivalent (Figure 1.17). The ^{31}P NMR spectra of $R_2P_7^-$ show five second order resonances with relative intensities 2:1:1:1:2. In the case of $(PhCH_2)_2P_7^-$, these resonances appear at 40.5, –35.5, –116.0, –128.0 and –165.0 ppm, although all $R_2P_7^-$ species have very similar spectra. These observations are consistent with either Isomer I or Isomer II. Using steric arguments, it was concluded that Isomer I is the structure adopted by these compounds.[78] Single crystal X-ray diffraction studies have shown that Isomer I is also present in the solid state (Figure 1.18).

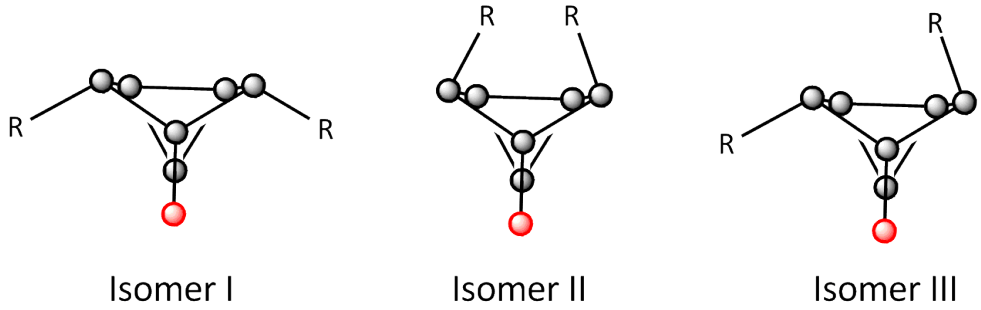

Figure 1.17: Diagram showing the three possible isomers of $R_2E_7^-$ (viewed from above). Atoms possessing a formal negative charge are shown in red.

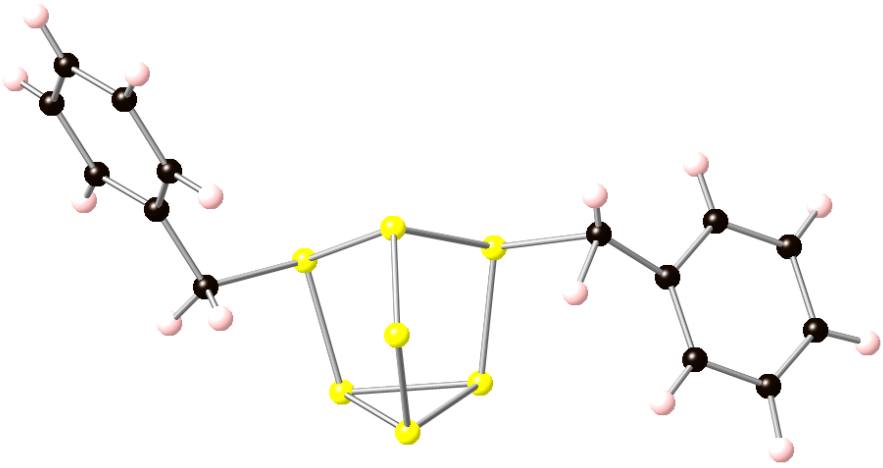

Figure 1.18: Ball and stick diagram of $(PhCH_2)_2P_7^-$.[79] P atoms are shown in yellow, C atoms are shown in black and H atoms are shown in pink.

Eichhorn proposed that these alkylation reactions proceed *via* nucleophilic attack by the E_7^{3-} cluster anion on one of the α-carbon atoms of the $[RR'_3N]^+$ group.[78,79] This is consistent with the observation that the more electrophilic $PhCH_2$, $EtOCOCH_2$ and EtOCOCHMe groups are transferred to the cluster in the reactions with $[(PhCH_2)Me_3N]^+$, $[(EtOCOCH_2)Me_3N]^+$ and $[(EtOCOCHMe)Me_3N]^+$, respectively.

Miluykov and co-workers observed that P_7^{3-} reacts with two equivalents of alkyl tosylate to form $R_2P_7^-$ (R = ^{i}Pr, ^{i}Bu).[80] As for the reactions with tetraalkylammonium salts, only one symmetric isomer was formed, which was again assumed to be Isomer I.

Research by Baudler, Von Schnering and Fritz has shown that P_7^{3-} reacts with three equivalents of alkyl bromide to form the neutral species P_7R_3 (R = Me, Et, ^{i}Pr, Bu, ^{i}Bu).[81–83] In this case, the product can be one of two possible isomers: an asymmetric isomer or a symmetric isomer (Figure 1.19). The ^{31}P NMR spectra of P_7R_3 show ten resonances, seven of which can be assigned to the asymmetric isomer and three of which correspond to the symmetric

isomer. The ratio of asymmetric isomer to symmetric isomer depends on the size of the alkyl substituents, with bulkier substituents favouring the formation of the less sterically hindered symmetric isomer. Reaction of P_7^{3-} with three equivalents of alkyl tosylate also forms P_7R_3 (R = ^{i}Pr, Bu, ^{i}Bu, 3-C_5H_{11}, C_6H_{13}).[80]

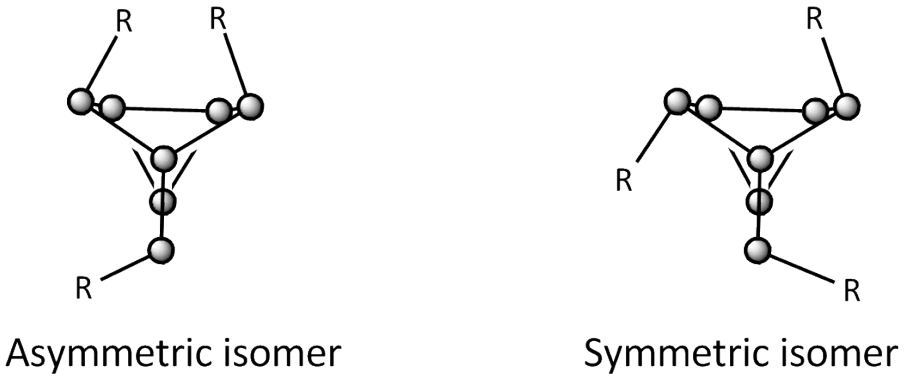

Figure 1.19: Diagram showing the two possible isomers of P_7R_3.

In addition, P_7^{3-} and As_7^{3-} react with the group 14 compounds $R_3E'X$ to form $E_7(E'R_3)_3$ (E = P: $E'R_3$ = SiH_3, SiH_2Me, $SiMe_3$, $SiMe_2PEt_2$, $SiPh_3$, $GeMe_3$, $SnMe_3$; E = As: $E'R_3$ = $SiMe_3$; X = Cl, Br, I).[82–84] These reactions are analogous to the alkylation reactions described above, and as for the alkylation reactions, two possible isomers can be formed. However, in this case, the ^{31}P NMR spectra of $P_7(E'R_3)_3$ show only three resonances, indicating that only the symmetric isomer is produced. As an example, the ^{31}P NMR spectrum of $P_7(SiH_3)_3$ shows resonances at –18, –76 and –139 ppm with relative intensities 3:1:3. These correspond to the three functionalised P atoms, the single P atom at the apex, and the three basal P atoms, respectively.

P_7^{3-} has also been found to react with the group 15 compounds ^{t}Bu$_2$PF and ^{t}Bu$_2$SbCl to form $P_7(E^tBu_2)_3$ (E = P, Sb).[85] ^{31}P NMR studies showed exclusive formation of the symmetric isomer in solution, while single crystal X-ray diffraction studies showed that this isomer is also present in the solid state (Figure 1.20).

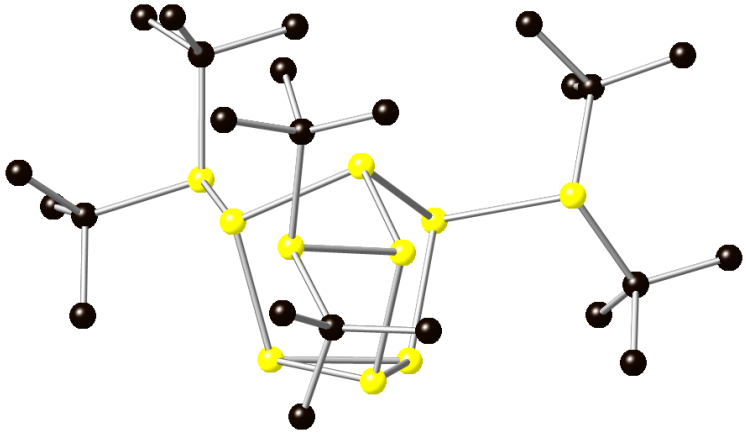

Figure 1.20: Ball and stick diagram of $P_7(P^tBu_2)_3$.[85] P atoms are shown in yellow and C atoms are shown in black. H atoms are omitted for clarity.

Miluykov argued that these alkylation reactions can be considered to be an example of kinetic versus thermodynamic control.[80] The alkylation of E_7^{3-} likely involves sequential addition of organic substituents to all of the equatorial atoms, therefore it is reasonable to assume that $R_2E_7^-$ is an intermediate in the formation of E_7R_3. Inversion at one of the alkylated E atoms in Isomer I is not required for the asymmetric isomer of E_7R_3 to form, and this isomer is the kinetic product. The symmetric isomer of E_7R_3 can only be formed from Isomer I if inversion occurs at an alkylated E atom. This process has a high activation energy and, therefore, the symmetric isomer forms more slowly than the asymmetric isomer. However, the symmetric isomer has a lower energy than the asymmetric isomer, as it is less sterically hindered. The symmetric isomer can therefore be regarded as the thermodynamic product, and its formation is favoured by the bulky $E'R_3$ and ER_2 groups (E' = Si, Ge, Sn; E = P, Sb).

1.6.1.2 $P_7(FeCp(CO)_2)_3$

P_7^{3-} reacts with three equivalents of $[FeCp(CO)_2Br]$ to form $P_7(FeCp(CO)_2)_3$.[86] This compound is analogous to the alkylated and group 14- and 15-substituted compounds described above and, as for the group 14- and 15-substituted compounds, the ^{31}P NMR spectrum shows three resonances, indicating that only the symmetric isomer is formed. These resonances appear at 47.7, –48.7 and –159.3 ppm, have relative intensities 3:1:3, and can be assigned to the three Fe-bound P atoms, the single apical P atom, and the three basal P atoms, respectively. The exclusive formation of the symmetric isomer can be explained by the fact that the $FeCp(CO)_2$

groups are extremely bulky and favour the formation of the less sterically hindered symmetric isomer. Single crystal X-ray diffraction studies showed that the symmetric isomer is also present in the solid state (Figure 1.21).

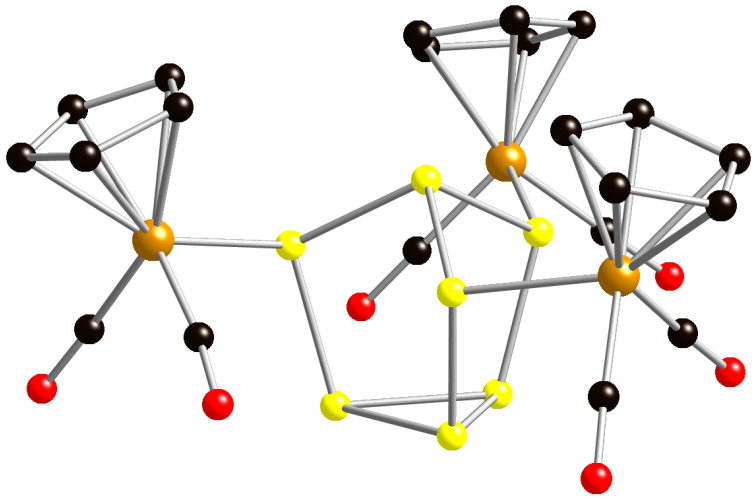

Figure 1.21: Ball and stick diagram of $P_7(FeCp(CO)_2)_3$.[86] P atoms are shown in yellow, Fe atoms are shown in brown, C atoms are shown in black and O atoms are shown in red. H atoms are omitted for clarity.

1.6.1.3 $[E_7M(CO)_3]^{3-}$ (E = P, As, Sb; M = Cr, Mo, W)

Ethylenediamine solutions of E_7^{3-} react with toluene solutions of $[M(CO)_3L]$ in the presence of 2,2,2-crypt to form $[E_7M(CO)_3]^{3-}$ ions (E = P, As, Sb; M = Cr, W: L = mesitylene; M = Mo: L = cycloheptatriene).[87,88] Research by Bolle and Tremel showed that $[Sb_7Mo(CO)_3]^{3-}$ can also be formed by reacting Sb_7^{3-} with $[Mo(CO)_4(bipy)]$.[89] These complexes consist of norbornadiene-like E_7^{3-} groups bonded to $M(CO)_3$ centres in an η^4-fashion (Figure 1.22). The $[E_7M(CO)_3]^{3-}$ cluster anions are eighteen-electron species, in which the transition metal is in the zero oxidation state and the η^4-E_7^{3-} group is acting as a six-electron donor. Single crystal X-ray diffraction studies on $[E_7Cr(CO)_3]^{3-}$ showed that the E_7^{3-} cages are not symmetrical and that there are asymmetries in the non-bonding E4–E5 and E6–E7 distances of between 0.20 and 0.35 Å.

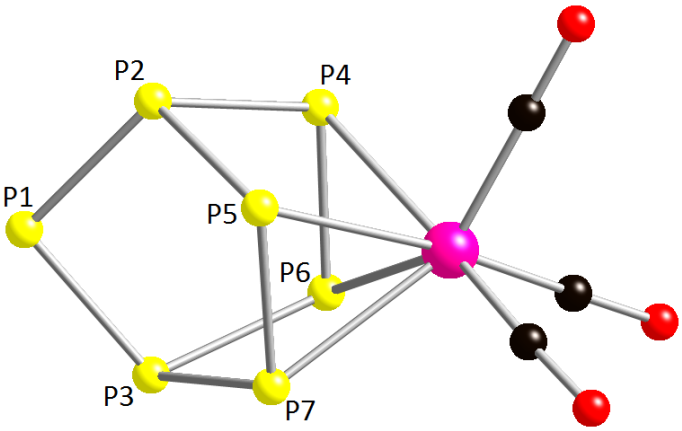

Figure 1.22: Ball and stick diagram of $[P_7Cr(CO)_3]^{3-}$.[88] P atoms are shown in yellow, the Cr atom is shown in pink, C atoms are shown in black and O atoms are shown in red.

Fenske-Hall molecular orbital calculations were used to investigate the electronic structure of $[E_7M(CO)_3]^{3-}$. The η^4-E_7^{3-} groups can be considered to be isoelectronic with a rectangularly distorted cyclobutadienediide dianion and possess four frontier orbitals of π-type symmetry (π_1, π_2, π_3 and π_4 in Figure 1.23). In the case of P_7^{3-}, the two π bonding orbitals, π_1 and π_2, are lower in energy than the π anti-bonding orbitals, π_3 and π_4, as expected. This represents the limiting case of rectangularly distorted cyclobutadienediide. The strength of the π bonding decreases on descending group 15, causing the stabilisation of π_2 and the destabilisation of π_3 to decrease. For Sb_7^{3-}, these two orbitals are almost degenerate, and this represents the undistorted limit for cyclobutadienediide.

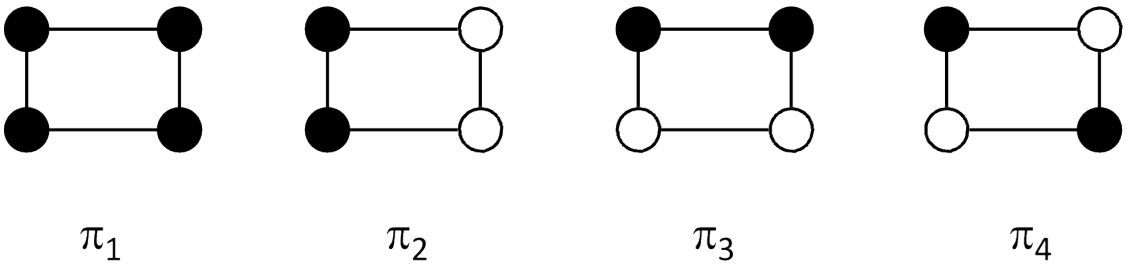

Figure 1.23: Diagram showing the frontier molecular orbitals of rectangularly distorted cyclobutadienediide (viewed from above).

Further calculations were carried out for the $[E_7Cr(CO)_3]^{3-}$ cluster anions in order to investigate the orbital interactions within the complexes. The π_2 and π_3 orbitals are stabilised on complexation due to interactions with orbitals of the $Cr(CO)_3$ fragment. The π_4 orbital is the LUMO. For $[As_7Cr(CO)_3]^{3-}$, the HOMO is the lone pair centred on the two-connect As atom, As1, while in the case of $[Sb_7Cr(CO)_3]^{3-}$, the lone pair is distributed between the

HOMO and a lower lying orbital. In contrast, the P1 lone pair in $[P_7Cr(CO)_3]^{3-}$ is stabilised relative to the As and Sb compounds and is lower in energy than the mainly Cr-based HOMO. This can be explained by the fact that P is more electronegative than As and Sb, which allows for greater stabilisation of the negative charge associated with the lone pair.

The ^{31}P NMR spectra of $[P_7M(CO)_3]^{3-}$ show three resonances with relative intensities 1:2:4. In the ^{31}P NMR spectrum of $[P_7Cr(CO)_3]^{3-}$, these resonances appear at 199, –21 and –143 ppm and can be assigned to the single two-connect P atom, the two three-connect bridging P atoms, and the four Cr-bound P atoms, respectively. However, based on the solid state structures, four resonances would be expected due to the asymmetry in the P4–P5 and P6–P7 distances. This asymmetry is time-averaged in solution *via* an intramolecular "wagging" process, which renders the four metal-bound P atoms equivalent to each other (Figure 1.24).

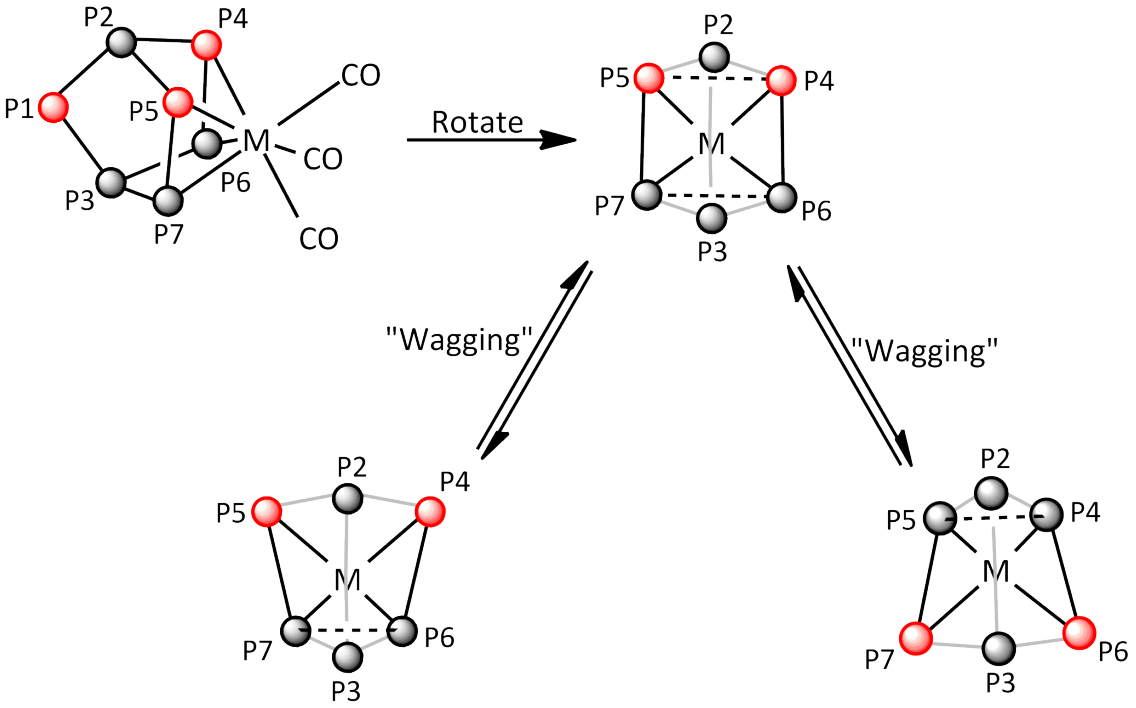

Figure 1.24: Diagram showing the intramolecular "wagging" process taking place in $[P_7M(CO)_3]^{3-}$. Atoms possessing a formal negative charge are shown in red.

The IR spectra of $[E_7M(CO)_3]^{3-}$ all show C–O stretching vibrations between 1845 and 1708 cm^{-1}. These values are low compared with those obtained for $Cr(CO)_6$ (2000 cm^{-1}) and $W(CO)_6$ (1983 cm^{-1}).[90,91] This shows that a significant amount of electron density has been transferred on to the metal atom by the E_7^{3-} cage, leading to a greater degree of back-bonding into the CO π^* orbitals. This leads to a weakening of the C–O bonds, and hence to lower frequency

C–O stretching vibrations.

Solutions of $[P_7M(CO)_3]^{3-}$ in ethylenediamine, DMF or DMSO can be protonated by weak acids with pK_a values less than eighteen, such as 9-phenylfluorene, to form $[HP_7M(CO)_3]^{2-}$ (M = Cr, W).[92] The proton bonds to the two-connect P atom furthest from the transition metal. $[HP_7M(CO)_3]^{2-}$ can in turn be deprotonated by MeO^- in ethylenediamine or DMF to reform $[P_7M(CO)_3]^{3-}$. Single crystal X-ray diffraction studies showed that, as for the non-protonated cluster anions, there is an asymmetry in the P4–P5 and P6–P7 distances. All seven P atoms should therefore be inequivalent, and seven resonances should be observed in the ^{31}P NMR spectra. However, the ^{31}P NMR spectra show only four resonances with relative intensities 1:2:2:2. This indicates that an intramolecular "wagging" process must be taking place in solution, as previously observed in the $[P_7M(CO)_3]^{3-}$ species. The IR spectra of $[HP_7M(CO)_3]^{2-}$ show three C–O stretches between 1892 and 1755 cm^{-1}. These values are higher than those recorded for $[P_7M(CO)_3]^{3-}$, and this has been attributed to the decrease in negative charge and subsequent decrease in electron density that can be donated into the CO π^* orbitals *via* back-bonding. Two H–P stretching bands are also observed between 2235 and 2210 cm^{-1}.

$[P_7W(CO)_3]^{3-}$ also reacts with tetraalkylammonium salts, $[RR'_3N]Br$ (R = R′ = Me, Et, Bu; R = $PhCH_2$: R′ = Me) to form $[RP_7W(CO)_3]^{2-}$.[78] As for the protonated cluster anions discussed previously, the ^{31}P NMR spectra of $[RP_7W(CO)_3]^{2-}$ show four resonances, indicating that an intramolecular "wagging" process is occurring. Reaction of $[P_7W(CO)_3]^{3-}$ with group 14 compounds, R_3EX (R_3E = Me_3Si, Bu_3Si, Hex_3Si, Ph_3Si, Et_3Ge, Ph_3Ge, Et_3Sn, Bu_3Sn, Cy_3Sn, Ph_3Sn, Ph_3Pb; X = Cl, Br) forms $[R_3EP_7W(CO)_3]^{2-}$.[93,94] Variable temperature ^{31}P NMR studies on $[R_3EP_7W(CO)_3]^{2-}$ showed that two different fluxional processes are taking place in solution. For example, the ^{31}P NMR spectrum of $[Cy_3SnP_7W(CO)_3]^{2-}$ recorded at –50 °C shows four resonances with relative intensities 1:2:2:2. As the temperature is increased, two of these resonances broaden and coalesce, and at 90 °C, three resonances with relative intensities 1:2:4 are observed. This is consistent with both an intramolecular "wagging" process and a pyramidal inversion process at the P1 atom, which together render the four metal-bound P atoms equivalent at high temperatures (Figures 1.24 and 1.25). The "wagging" process is fast on the NMR timescale even at –50 °C, while the inversion process is slow at low temperatures.

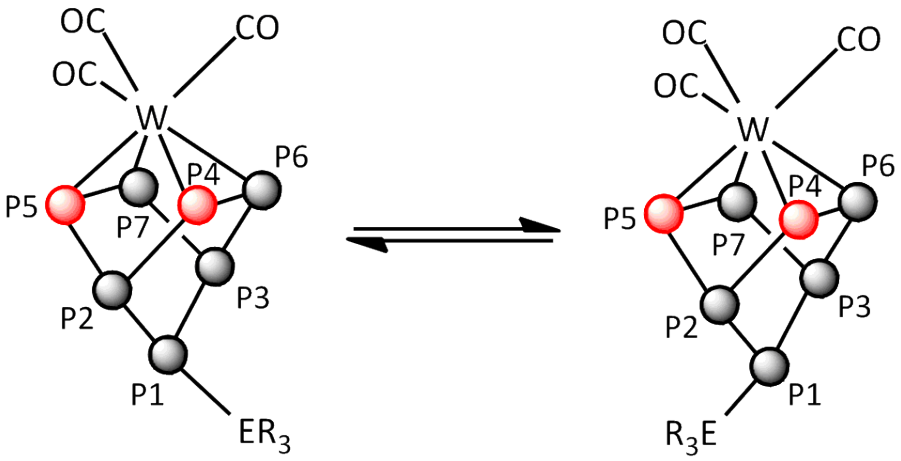

Figure 1.25: Diagram showing the pyramidal inversion process taking place in $[R_3EP_7W(CO)_3]^{2-}$. Atoms possessing a formal negative charge are shown in red.

In addition, ethylenediamine solutions of $[P_7M(CO)_3]^{3-}$ react with $[W(CO)_3(\text{mesitylene})]$ to form $[(en)(CO)_3WP_7M(CO)_3]^{3-}$ (M = Cr, W), in which the P_7^{3-} cluster is bonded to one metal centre in an η^4-fashion and to the other metal centre in an η^1-fashion (Figure 1.26).[93] As for $[R_3EP_7W(CO)_3]^{2-}$, the ^{31}P NMR spectra of these species show three resonances with relative intensities 1:2:4, indicating that both a "wagging" process and an inversion process are taking place in solution. However, in the case of $[(en)(CO)_3WP_7M(CO)_3]^{3-}$, both processes were found to be fast on the NMR timescale even at –60 °C.

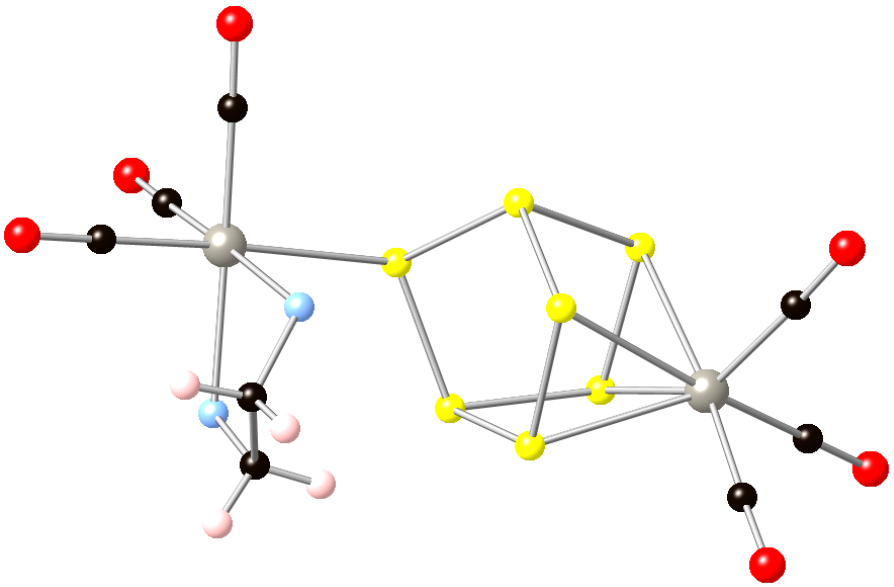

Figure 1.26: Ball and stick diagram of $[(en(CO)_3WP_7W(CO)_3]^{3-}$.[93] P atoms are shown in yellow, W atoms are shown in grey, C atoms are shown in black, O atoms are shown in red, N atoms are shown in blue and H atoms are shown in pink.

Under normal conditions, the transition metal centre in $[P_7M(CO)_3]^{3-}$ is not susceptible to

attack by Lewis bases due to its stable eighteen-electron configuration. However, under a CO atmosphere, these compounds reversibly bind a fourth CO ligand to form $[P_7M(CO)_4]^{3-}$ complexes (M = Mo, W).[95] The P_7^{3-} cage is driven from an η^4 (six-electron donating) to an η^2 (four-electron donating) coordination mode in order to accommodate the fourth CO ligand and maintain an eighteen-electron configuration at the transition metal centre. The nortricyclane-like shape of the parent P_7^{3-} cluster is recovered on changing the coordination mode (Figure 1.27). The $[P_7M(CO)_4]^{3-}$ species readily lose a CO ligand under a nitrogen atmosphere to reform $[P_7M(CO)_3]^{3-}$.

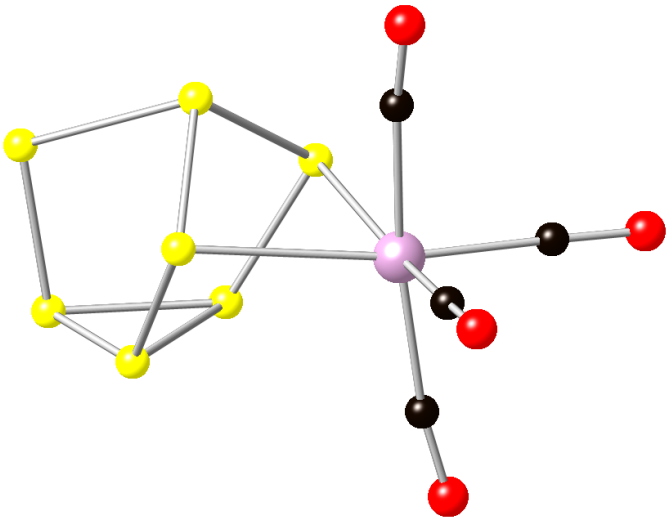

Figure 1.27: Ball and stick diagram of $[P_7Mo(CO)_4]^{3-}$.[95] P atoms are shown in yellow, the Mo atom is shown in purple, C atoms are shown in black and O atoms are shown in red.

The ^{31}P NMR spectra of $[P_7M(CO)_4]^{3-}$ show five resonances with relative intensities 1:1:1:2:2 that are consistent with the solid state structure. In the case of $[P_7Mo(CO)_4]^{3-}$, these resonances appear at 60, –11, –16, –53 and –130 ppm. The IR spectra of $[P_7M(CO)_4]^{3-}$ show four C–O stretching bands between 1940 and 1743 cm^{-1}.

Ethylenediamine solutions of $[P_7M(CO)_4]^{3-}$ can be protonated by MeOH to form $[HP_7M(CO)_4]^{2-}$.[95] These protonated cluster anions can also be synthesised by exposing $[HP_7M(CO)_3]^{2-}$ to a CO atmosphere. Similarly, $[(PhCH_2)P_7W(CO)_4]^{2-}$ can be prepared either by placing $[(PhCH_2)P_7W(CO)_3]^{2-}$ under a CO atmosphere or by reacting $[P_7W(CO)_4]^{3-}$ with $[(PhCH_2)Me_3N]Br$.[95] The basicity of the P_7^{3-} cage increases on coordination of a fourth CO ligand to the metal centre. This is shown by the fact that protonation of $[P_7M(CO)_3]^{3-}$ requires stronger acids than MeOH, while $[P_7M(CO)_4]^{3-}$ is readily protonated by MeOH. Conversely,

$[HP_7M(CO)_3]^{2-}$ is easily deprotonated by MeO^-, whereas stronger amide bases are required to deprotonate $[HP_7M(CO)_4]^{2-}$. A possible explanation for this is that the η^4-P_7^{3-} cluster in $[P_7M(CO)_3]^{3-}$ donates more electron density to the metal centre, and hence is less basic. $[HP_7M(CO)_4]^{2-}$ was observed to be more stable with respect to loss of CO than $[P_7M(CO)_4]^{3-}$. Eichhorn attributed this to the fact that P_7^{3-} is more nucleophilic than HP_7^{2-}, and so the formation of a complex featuring an η^4-cluster is more favourable for the non-protonated cage.[95] A summary of all the interconversions between $[P_7M(CO)_3]^{3-}$, $[HP_7M(CO)_3]^{2-}$, $[HP_7M(CO)_4]^{2-}$ and $[P_7M(CO)_4]^{3-}$ is provided in Figure 1.28.

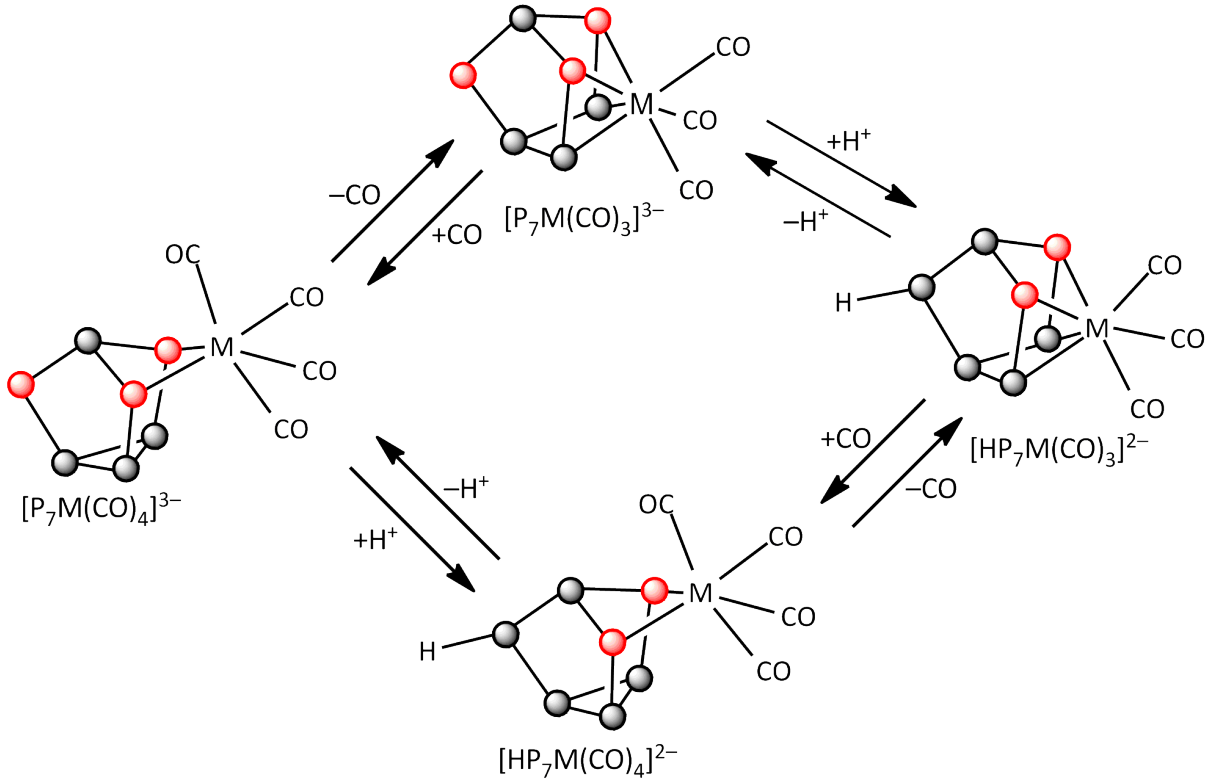

Figure 1.28: Diagram showing the interconversions between $[P_7M(CO)_3]^{3-}$, $[HP_7M(CO)_3]^{2-}$, $[HP_7M(CO)_4]^{2-}$ and $[P_7M(CO)_4]^{3-}$. Atoms possessing a formal negative charge are shown in red.

1.6.1.4 $[P_7Ni(CO)]^{3-}$

P_7^{3-} reacts with $[Ni(CO)_2(PPh_3)_2]$ in ethylenediamine in the presence of 2,2,2-crypt to form the $[P_7Ni(CO)]^{3-}$ ion.[96] This complex consists of a norbornadiene-like P_7^{3-} cluster bonded to the Ni(CO) centre in an η^4-fashion (Figure 1.29). As for the $[E_7M(CO)_3]^{3-}$ species (E = P, As, Sb; M = Cr, Mo, W) discussed previously, the η^4-P_7^{3-} cage is acting as a six-electron donor, and the Ni centre has a total of eighteen valence electrons. However, unlike $[E_7M(CO)_3]^{3-}$,

$[P_7Ni(CO)]^{3-}$ features a highly symmetrical P_7^{3-} cage, in which the P4–P5 and P6–P7 distances are approximately equal. $[P_7Ni(CO)]^{3-}$ can be protonated to form $[HP_7Ni(CO)]^{2-}$ by slow addition of MeOH at –50 °C.[96]

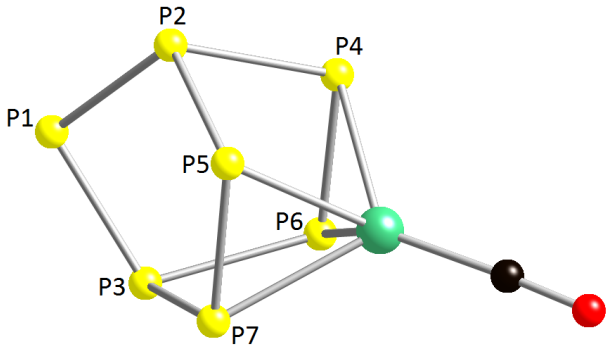

Figure 1.29: Ball and stick diagram of $[P_7Ni(CO)]^{3-}$.[96] P atoms are shown in yellow, the Ni atom is shown in green, the C atom is shown in black and the O atom is shown in red.

The ^{31}P NMR spectrum shows three second order resonances at 101, 25 and –124 ppm with relative intensities 1:2:4. These resonances are consistent with the solid state structure and correspond to the single two-connect P atom, the two three-connect bridging P atoms, and the four Ni-bound P atoms, respectively. The IR spectrum shows a C–O stretching vibration at 1785 cm^{-1}. This value is similar to those obtained for $[E_7M(CO)_3]^{3-}$ and shows that the P_7^{3-} cage is donating a significant amount of electron density to the Ni centre.

1.6.1.5 $[E_7PtH(PPh_3)]^{2-}$ (E = P, As)

Ethylenediamine solutions of E_7^{3-} react with $[Pt(PPh_3)_2(C_2H_4)]$ in the presence of 2,2,2-crypt to form $[E_7PtH(PPh_3)]^{2-}$ (E = P, As).[96,97] Deuterium labelling studies showed that the hydride ligand originates from the solvent and that acetonitrile, DMSO and DMF can also act as hydrogen donors, as well as ethylenediamine. The $[E_7PtH(PPh_3)]^{2-}$ ions can be considered as nortricyclane-like η^2-E_7^{3-} ligands bonded to twelve-electron $[PtH(PPh_3)]^+$ fragments (Figure 1.30). The hydride ligands could not be located crystallographically, however their presence coud be inferred from the ^{1}H NMR spectra, which show resonances at –10.1 and –10.8 ppm for $[P_7PtH(PPh_3)]^{2-}$ and $[As_7PtH(PPh_3)]^{2-}$, respectively. The E_7^{3-} cages act as four-electron donors to give sixteen-electron square planar Pt(II) complexes.

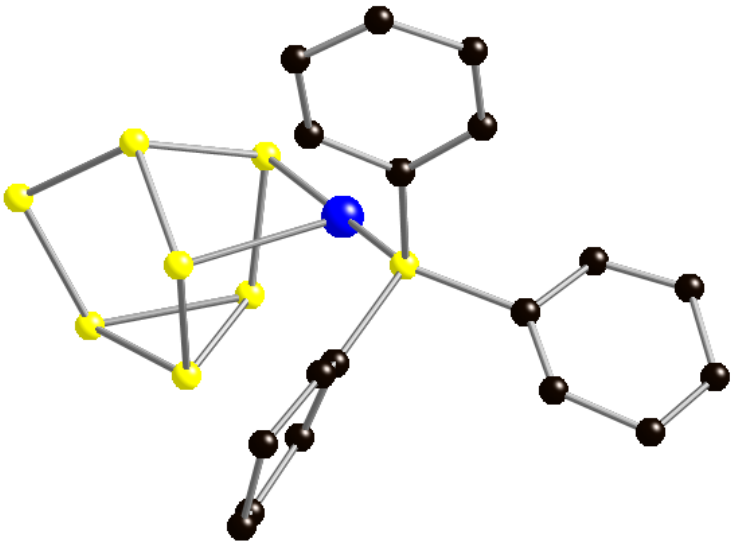

Figure 1.30: Ball and stick diagram of $[P_7PtH(PPh_3)]^{2-}$.[96] P atoms are shown in yellow, the Pt atom is shown in blue and C atoms are shown in black. H atoms are omitted for clarity.

^{31}P and ^{1}H NMR spectroscopy studies on $[P_7PtH(PPh_3)]^{2-}$ have shown that this complex is fluxional in solution.[97] The ^{31}P NMR spectrum obtained at –78 °C is consistent with the solid state structure and shows seven multiplets due to the P_7^{3-} cluster and a downfield broad doublet with ^{195}Pt satellites, corresponding to the PPh_3 ligand. On warming, the resonances for P4, P5, P6 and P7 coalesce into the baseline and re-emerge above –20 °C as a single peak of intensity four. The P2 and P3 resonances coalesce at –60 °C to give a single peak of intensity two. The resonance corresponding to P1 is not affected by the exchange process and remains sharp at all temperatures. Also, the PPh_3 resonance changes from a broad doublet at –78 °C to a quintuplet at 25 °C. In the ^{1}H NMR spectrum, the resonance due to the hydride ligand is transformed from a doublet of multiplets at approximately –10.1 ppm at –78 °C to a single multiplet at 25 °C. These data are consistent with an intramolecular two-step fluxional process, in which the P_7^{3-} cage shifts from an η^2- to an η^4-coordination mode to form an eighteen-electron intermediate. This is followed by an η^4 to η^2 shift, which leaves P4 and P5 bonded to the Pt centre and forms a bond between P6 and P7. This shifting process exchanges P4 with P6, P5 with P7, and P2 with P3. However, due to the asymmetry in the $[PtH(PPh_3)]^+$ fragment, an additional process is required to exchange all four Pt-bound P atoms. Eichhorn and co-workers proposed that this process is an additional spinning step that takes place in the η^4-intermediate (Figure 1.31).[97]

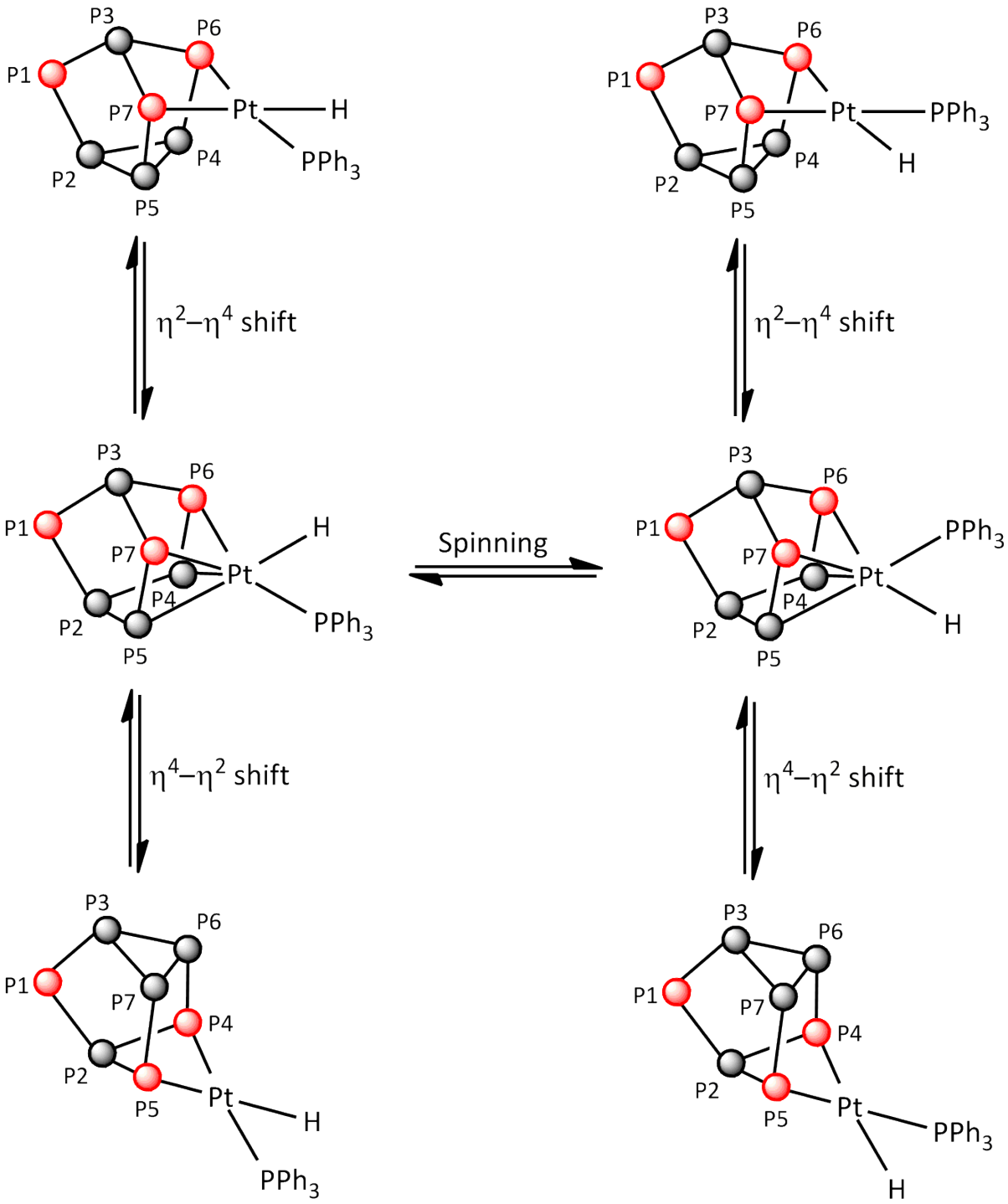

Figure 1.31: Diagram showing the exchange processes taking place in $[P_7PtH(PPh_3)]^{2-}$. Atoms possessing a formal negative charge are shown in red.

1.6.1.6 $[Pd_2(As_7)_2]^{4-}$

Ethylenediamine solutions of As_7^{3-} react with toluene solutions of $Pd(PCy_3)_2$ in the presence of 2,2,2-crypt to form $[Pd_2(As_7)_2]^{4-}$.[98] This species can be thought of as two norbornadiene-like As_7^{3-} groups bonded to a Pd_2 centre in an η^2,η^2-fashion (Figure 1.32). The Pd atoms are

in distorted square-planar environments and are linked by an axial Pd–Pd bond of 2.714(1) Å. This is longer than the sum of covalent radii for Pd–Pd single bonds (2.40 Å), but is significantly shorter than the sum of van der Waals radii for two Pd atoms (4.30 Å).[99,100] This indicates that there is a strong bonding interaction between the two Pd atoms.

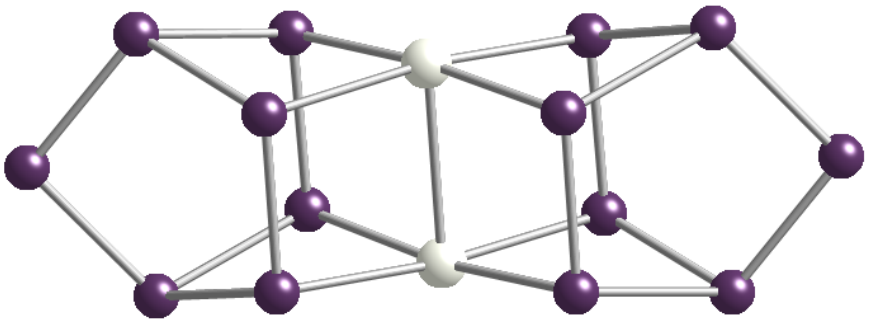

Figure 1.32: Ball and stick diagram of $[Pd_2(As_7)_2]^{4-}$.[98] Pd atoms are shown in grey and As atoms are shown in purple.

It is thought that the Pd analogue of the previously mentioned $[As_7PtH(PPh_3)]^{2-}$ ion is initially formed in this reaction, and that two of these are subsequently coupled in a redox process to form $[Pd_2(As_7)_2]^{4-}$ (Figure 1.33). This theory is consistent with the observation that H_2 gas is eliminated during the course of the reaction, however the proposed $[As_7PdH(PCy_3)]^{2-}$ intermediate has not yet been isolated.

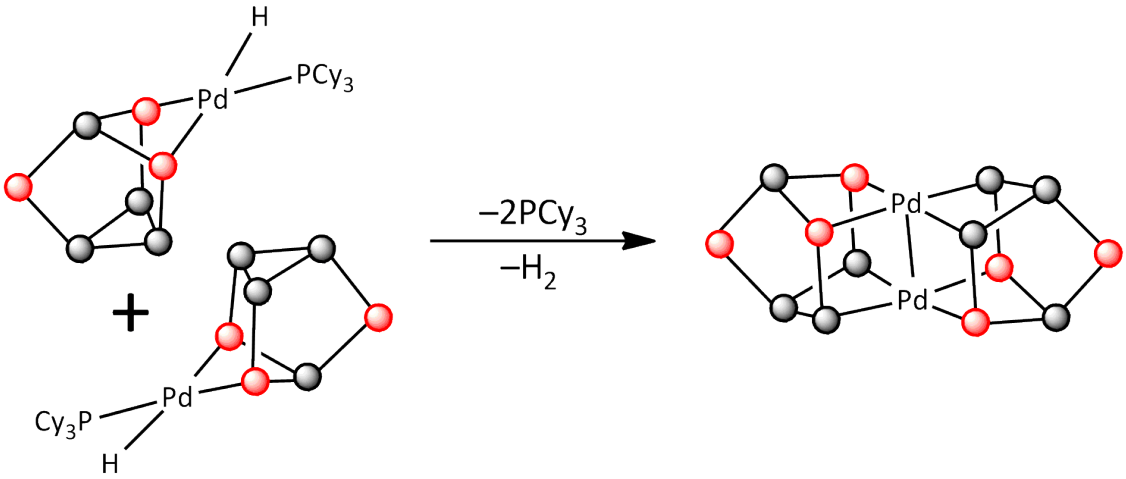

Figure 1.33: Diagram showing the formation of $[Pd_2(As_7)_2]^{4-}$ from $2[As_7PdH(PPh_3)]^{2-}$. Atoms possessing a formal negative charge are shown in red.

$[Pd_2(As_7)_2]^{4-}$ was also characterised by electrospray ionisation mass spectrometry. The negative ion mode spectrum shows an intense peak corresponding to $\{[K(2,2,2\text{-crypt})][H_2Pd_2(As_7)_2]\}^-$, as well as a weaker peak due to $[HPd_2(As_7)_2]^-$.

1.6.2 Reactions in which cluster fragmentation occurs

There are several examples of cluster fragmentation in the literature, however prior to 2008, these were limited to reactions of E_7^{3-} with arene complexes of early row transition metals and low-valent complexes of group 10 metals, such as $Ni(COD)_2$ and $Pd(PCy_3)_2$. Cluster fragmentation is more common for Sb_7^{3-} than for As_7^{3-}, and has not been observed for P_7^{3-} to date. This observation is consistent with the decrease in bond dissociation energies as group 15 is descended (BDEs: P–P: 201 kJ mol^{-1}; As–As: 146 kJ mol^{-1}; Sb–Sb: 121 kJ mol^{-1}).[101]

1.6.2.1 $[ME_8]^{n-}$ (M = Nb, Cr, Mo; E = As, Sb; n = 2, 3)

Ethylenediamine solutions of As_7^{3-} and Sb_7^{3-} react with toluene solutions of $M(arene)_2$ (M = Nb: arene = toluene; M = Cr: arene = naphthalene; M = Mo: arene = Me-naphthalene) in the presence of 2,2,2-crypt to form $[ME_8]^{n-}$ ions (M = Nb, Cr, Mo; E = As, Sb; n = 2, 3).[102–104] To date, $[NbE_8]^{3-}$ (E = As, Sb), $[MoAs_8]^{2-}$, $[MoSb_8]^{3-}$ and $[CrAs_8]^{3-}$ have been isolated and structurally characterised. The Rb^+ salt of $[NbAs_8]^{3-}$ was synthesised serendipitously by Von Schnering and co-workers in an attempt to synthesise Rb_3As_7.[105] The structures consist of crown-like *cyclo*-E_8 rings centred by transition metal ions (Figure 1.34). $[NbE_8]^{3-}$ and $[MoAs_8]^{2-}$ are formally sixteen-electron diamagnetic complexes, whereas $[MoSb_8]^{3-}$ and $[CrAs_8]^{3-}$ have seventeen valence electrons and are paramagnetic. The E_8 ring formally possesses an 8– charge and is therefore isoelectronic to S_8. This requires high oxidation state transition metals in order to account for the overall cluster charges, such as M^{5+} for $[NbE_8]^{3-}$, $[CrAs_8]^{3-}$ and $[MoSb_8]^{3-}$, and M^{6+} for $[MoAs_8]^{2-}$. The observation of a higher transition metal oxidation state in $[MoAs_8]^{2-}$ than in $[CrAs_8]^{3-}$ is consistent with the tendency of the 4*d* transition metals to adopt higher oxidation states relative to the 3*d* metals in the same ligand environment. The observation of Mo^{6+} in $[MoAs_8]^{2-}$ and Mo^{5+} in $[MoSb_8]^{3-}$ can be explained by the fact that the higher transition metal oxidation state is stabilised by the more electronegative As_8 ring relative to the less electronegative Sb_8 ring. The structural data for $[ME_8]^{n-}$ indicate that the E_8 rings are able to accommodate transition metal ions of different sizes by compression or expansion of the E–E–E bond angles. The As–As–As bond angles in $[MAs_8]^{n-}$ become progressively more acute as Nb is replaced with the smaller Mo, and Mo is replaced with the even smaller Cr.

This trend is also observed in $[NbSb_8]^{3-}$ and $[MoSb_8]^{3-}$, although the bond angles within the Sb_8 ring are smaller than those within the As_8 ring due to the larger size of Sb. This may explain why $[CrSb_8]^{n-}$ has not been isolated, as the Sb_8 ring would require even more acute Sb–Sb–Sb bond angles in order to accommodate the smaller Cr atom, which would result in a highly strained complex. The mean E–E bond lengths and E–E–E bond angles for $[ME_8]^{n-}$ are provided in Table 1.2.

Table 1.2: Mean bond lengths and bond angles for $[ME_8]^{n-}$.[102–104]

Species	Mean E–E bond length (Å)	Mean E–E–E bond angle (°)
$[NbAs_8]^{3-}$	2.446(2)	93.35(5)
$[MoAs_8]^{2-}$	2.429(2)	90.60(6)
$[CrAs_8]^{3-}$	2.426(5)	89.54(16)
$[NbSb_8]^{3-}$	2.78(1)	86.5(2)
$[MoSb_8]^{3-}$	2.786(2)	85.05(4)

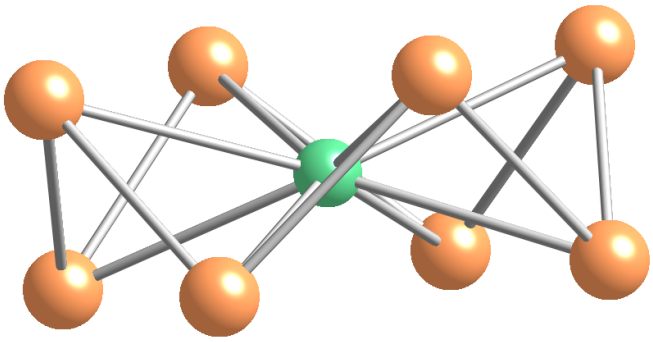

Figure 1.34: Ball and stick diagram of $[NbSb_8]^{3-}$.[102] The Nb atom is shown in green and Sb atoms are shown in gold.

The K^+ salt of $[CrAs_8]^{3-}$ crystallises in a one-dimensional chain structure of $[KCrAs_8]^{2-}$ repeating units, however the Na^+ salt and both the Na^+ and K^+ salts of $[MoAs_8]^{2-}$ and $[MoSb_8]^{3-}$ crystallise as free ion structures. The Rb^+ salt of $[NbAs_8]^{3-}$ synthesised by Von Schnering also crystallises as a one-dimensional chain structure, while the K^+ salts of $[NbAs_8]^{3-}$ and $[NbSb_8]^{3-}$ do not. The formation of one-dimensional chains in the solid state is controlled by a combination of steric effects and Coulombic repulsions. The steric factors involve the sizes of the alkali metal ion (A^+), the group 15 atom (E) and the transition metal ion (M^{n+}). The Coulombic repulsions are governed by the separation between A^+ and M^{n+}. One-dimensional chain formation occurs when A–E interactions are optimised, while the electrostatic repulsions between A^+ and M^{n+} are minimised (Figure 1.35). A small alkali metal ion must drop down into the E_8 ring in order to maximise A–E interactions, which increases

the Coulombic repulsion between A^+ and M^{n+}. For $[CrAs_8]^{3-}$, Na^+ ions appear to be too small to link the $[CrAs_8]^{3-}$ rings, while the larger K^+ ions are the right size to promote one-dimensional chain formation. The same effect is presumably operative in $[NbAs_8]^{3-}$, in which the larger Rb^+ ion favours one-dimensional chain formation, but the smaller K^+ does not. Increasing the E_8 ring diameter also requires the alkali metal ion to drop down into the ring to maximise A–E bonding, causing an increase in the electrostatic repulsion. Hence the salts of $[MoSb_8]^{3-}$ and $[NbSb_8]^{3-}$ crystallise as free ion structures. Increasing the size of the transition metal ion while keeping A^+ and E the same also increases the Coulombic repulsion and discourages chain formation. Therefore, the salts of $[MoAs_8]^{2-}$ do not form one-dimensional chains.

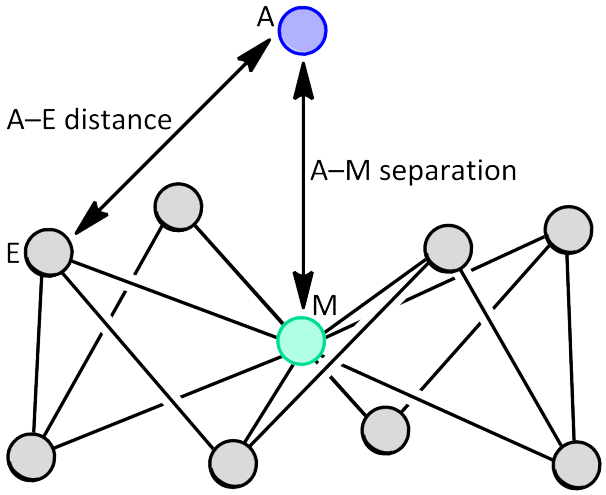

Figure 1.35: Diagram showing the distances involved in one-dimensional chain formation.

The paramagnetism of $[CrAs_8]^{3-}$ and $[MoSb_8]^{3-}$ was confirmed by EPR spectroscopy. The EPR spectrum of $[CrAs_8]^{3-}$ shows a signal at g = 2.001 with a hyperfine splitting of 3.6 G due to coupling to eight equivalent As atoms. The EPR spectrum of $[MoSb_8]^{3-}$ shows a broad signal at g ≈ 1.86, which remains broad even at 78 K. The $[ME_8]^{n-}$ species were also characterised by electrospray ionisation mass spectrometry. The negative ion mode spectra typically show peaks corresponding to $[ME_8]^-$ and $[KME_8]^-$.

1.6.2.2 $[Sb_7Ni_3(CO)_3]^{3-}$

Ethylenediamine solutions of Sb_7^{3-} react with toluene solutions of $[Ni(CO)_2(PPh_3)_2]$ in the presence of 2,2,2-crypt to give the $[Sb_7Ni_3(CO)_3]^{3-}$ ion.[106] This species can be thought of as

an electron-deficient ten-vertex cluster anion. Each Sb atom contributes three electrons to cluster bonding, and this plus the three additional electrons from the 3– charge gives a total of twenty-four cluster bonding electrons, which is equal to 2n + 4. Therefore, the cluster should have a *nido* structure according to the Wade-Mingos rules.[107–109] This is consistent with the observed structure of the ion, however the structure differs from other known ten-vertex *nido* clusters such as $B_{10}H_{14}$ and $C_2B_8H_{12}$, which feature open six-membered rings (a *nido*-10(vi) structure).[110–112] $[Sb_7Ni_3(CO)_3]^{3-}$ contains two four-membered rings fused along a common edge (a *nido*-10(iv+iv) structure) (Figure 1.36).

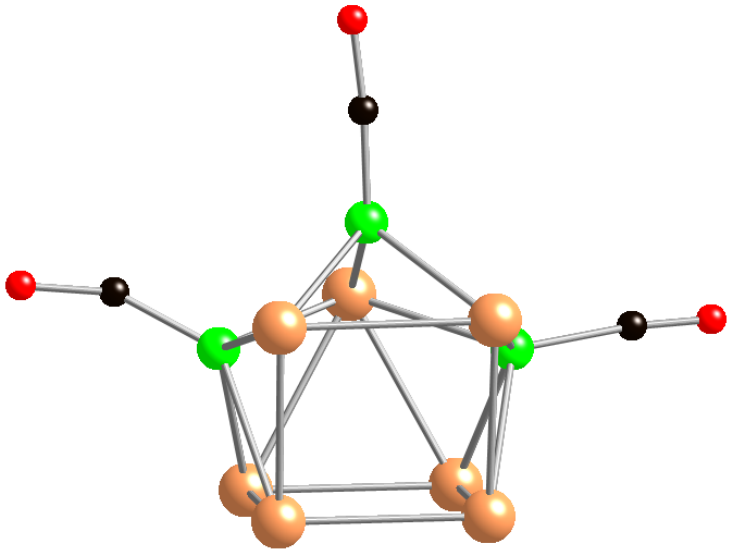

Figure 1.36: Ball and stick diagram of $[Sb_7Ni_3(CO)_3]^{3-}$.[106] Sb atoms are shown in gold, Ni atoms are shown in green, C atoms are shown in black and O atoms are shown in red.

1.6.2.3 $[As@Ni_{12}@As_{20}]^{3-}$

As_7^{3-} reacts with $Ni(COD)_2$ in ethylenediamine to form the $[As@Ni_{12}@As_{20}]^{3-}$ ion.[113] This anion consists of an icosahedral $[Ni_{12}(\mu_{12}\text{-As})]^{3-}$ fragment that resides at the centre of a dodecahedral fullerene-like As_{20} cage (Figure 1.37). The $[As@Ni_{12}@As_{20}]^{3-}$ cluster is remarkably symmetrical and has nearly perfect I_h point symmetry. Each As atom of the As_{20} cage caps a Ni_3 face and, conversely, each As_5 ring is centred by a Ni atom.

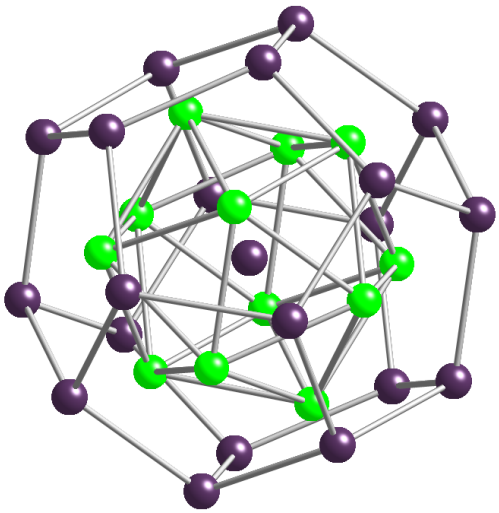

Figure 1.37: Ball and stick diagram of $[As@Ni_{12}@As_{20}]^{3-}$.[113] As atoms are shown in purple and Ni atoms are shown in green.

The As_{20} subunit has thirty As–As bonds defining the thirty dodecahedral edges, which require sixty electrons. An additional forty electrons are present as twenty lone pairs in p_z orbitals that extend radially from the centre of the cluster. This gives a total of one hundred valence electrons for the As_{20} subunit. The thirty molecular orbitals defining the As–As bonds have negligible interaction with the orbitals of the $[Ni_{12}(\mu_{12}\text{-As})]^{3-}$ fragment. The twenty p_z lone pairs, however, interact with twenty $[Ni_{12}(\mu_{12}\text{-As})]^{3-}$ orbitals of the same symmetry. These orbitals are mainly *p*-type Ni-based orbitals, with some *s* character mixed in. $[As@Ni_{12}@As_{20}]^{3-}$ possesses a total of 168 cluster valence electrons, 128 of which orginate from the $[Ni_{12}(\mu_{12}\text{-As})]^{3-}$ subunit and forty of which orginate from the As_{20} lone pairs. The complex was found to be diamagnetic, with a large HOMO–LUMO gap.[113]

Laser-desorption/ionisation-time-of-flight mass spectrometric measurements were also carried out on $[As@Ni_{12}@As_{20}]^{3-}$. The negative ion mode spectrum shows a peak due to $[As@Ni_{12}@As_{20}]^{-}$, as well as peaks correpsonding to $[Ni_{12}As_n]^{-}$, where n = 0 – 21. The successive loss of As atoms is consistent with weak As–As bonding within the As_{20} cage.

1.6.2.4 $[Ni_5Sb_{17}]^{4-}$

Ethylenediamine solutions of Sb_7^{3-} react with $Ni(COD)_2$ in the presence of 2,2,2-crypt to give the $[Ni_5Sb_{17}]^{4-}$ cluster anion.[114] The cluster contains a Ni(*cyclo*-Ni_4Sb_4) ring unit that resides inside an Sb_{13} bowl (Figure 1.38). The structure of $[Ni_5Sb_{17}]^{4-}$ is very similar to the

previously mentioned $[ME_8]^{n-}$ (M = Nb, Cr, Mo; E = As, Sb; n = 2, 3) series of compounds, in which all atoms in the E_8 ring are equidistant from the transition metal centre. The Ni atom in the centre of the Ni(*cyclo*-Ni_4Sb_4) subunit is also in the geometrical centre of the ring. This atom is bonded to the four Sb atoms in the ring and also to one Sb atom of the Sb_{13} bowl, giving overall square-pyramidal coordination geometry. Assuming that the central Ni atom is a d^8 Ni^{II} centre and that the Sb atoms are acting as two-electron donors, this results in an electronically saturated eighteen-electron configuration. Therefore, there should not be significant Ni–Ni bonding to the central Ni atom, and DFT calculations have shown this to be the case. The other four Ni atoms are in distorted trigonal prismatic environments, with five short Ni–Sb bonds and one much longer bond. $[Ni_5Sb_{17}]^{4-}$ possesses 139 valence electrons and is paramagnetic, although the EPR spectrum showed no EPR signal.[114]

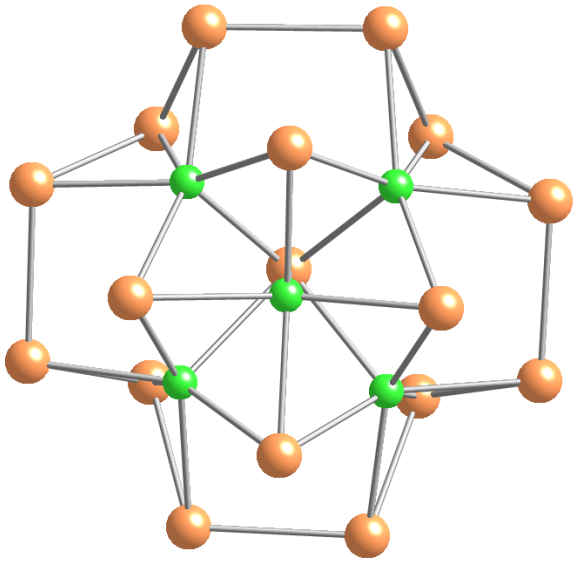

Figure 1.38: Ball and stick diagram of $[Ni_5Sb_{17}]^{4-}$ (viewed from above).[114] Ni atoms are shown in green and Sb atoms are shown in gold.

1.6.2.5 $[Pd_7As_{16}]^{4-}$

The reaction between As_7^{3-} and $Pd(PCy_3)_2$ described in Section 1.6.1.6 also gives low yields of a second cluster, $[Pd_7As_{16}]^{4-}$.[98] This species is similar to the previously mentioned $[Ni_5Sb_{17}]^{4-}$ cluster, in that $[Pd_7As_{16}]^{4-}$ also contains a M(*cyclo*-M_4E_4) cap. However, in this case, the corresponding bowl has a formula of Pd_2As_{12}, and the central Pd atom in the Pd(*cyclo*-Pd_4As_4) subunit is shifted significantly from the middle of the ring, with shorter contacts to the As

atoms than to the other Pd atoms (Figure 1.39). Assuming that the central Pd atom is a d^8 Pd^{II} centre and that each As atom is acting as a two-electron donor, a sixteen-electron configuration is achieved. Therefore, this Pd atom is electronically unsaturated and is capable of forming Pd–Pd bonds. DFT calculations also show that this Pd atom should be able to form Pd–Pd bonds.[114]

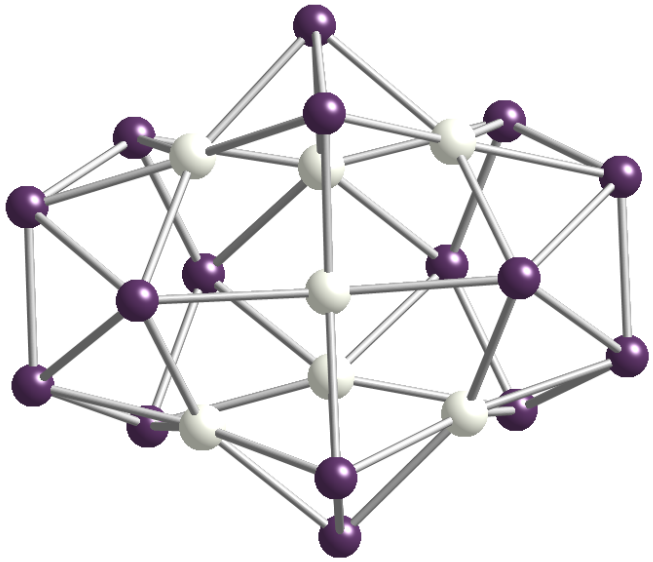

Figure 1.39: Ball and stick diagram of $[Pd_7As_{16}]^{4-}$ (viewed from above).[98] Pd atoms are shown in grey and As atoms are shown in purple.

1.7 Objectives

Prior to 2008, studies of the reactivity of group 15 Zintl ions towards homoleptic metal reagents were limited to metals formally in the zero oxidation state complexed to neutral ligands. In addition, the reactions of E_7^{3-} with compounds of group 11, group 12 and group 13 had not been studied at all. The initial aim of this project was therefore to investigate the reactivity of E_7^{3-} towards $[Cu_5(mes)_5]$, MPh_2 (M = Zn, Cd) and $InPh_3$. The results of these investigations will be discussed in Chapter 2.

Most previous research into salt metathesis reactions of E_7^{3-} was limited to alkyl salts and their heavier group 14 analogues. Only one reaction of E_7^{3-} with a metal salt had been reported, namely that of P_7^{3-} with $[FeCp(CO)_2Br]$.[86] Therefore, a further aim was to study the reactions of E_7^{3-} with a series of metal salts, and this will be described in Chapter 3.

Chapter 4 will describe the reactions of P_7^{3-} with a series of group 8 compounds. Prior to 2009,

the reactivity of group 15 Zintl ions towards group 8 compounds had not been extensively studied. This was surprising, considering that both P_4 and As_4 had been shown to react with $[(Fe(\eta^5\text{-}C_5Me_4R)(CO)_2)_2]$ and $[Ru(\eta^5\text{-}C_5Me_4R)(CO)_2Br]$ (R = Me, Et) to form group 15 analogues of ferrocene.[115–118] It seemed possible that similar species would also be formed in the reactions of E_7^{3-} with group 8 compounds.

Chapter 5 will detail the reactivity of P_7^{3-} and As_7^{3-} towards $[Co(PEt_2Ph)_2(mes)_2]$. This compound was investigated because there were no previously reported examples of E_7^{3-} reacting with Co compounds. Also, both P_4 and As_4 had been shown to undergo transition metal mediated activation reactions with similar Co compounds, and it seemed possible that E_7^{3-} would undergo similar reactions.[119–121]

1.8 References

1. Jutzi, P. *Angew. Chem., Int. Ed. Engl.* **1975**, *14,* 232–245.
2. Greenwood, N. N.; Earnshaw, A. *Chemistry of the Elements*; Elsevier: Amsterdam, 1997.
3. Simon, A.; Borrmann, H.; Craubner, H. *Phosphorus Sulfur* **1987**, *30,* 507–510.
4. Thurn, H.; Krebs, H. *Acta Crystallogr. B* **1969**, *25,* 125–135.
5. Kumar Chattopadhyay, T.; May, W.; Von Schnering, H. G.; Pawley, G. S. *Z. Kristallogr.* **1983**, *165,* 47–64.
6. Whitfield, H. J. *J. Chem. Soc. A* **1970**, 1800–1803.
7. Dahlmann, W.; Von Schnering, H. G. *Naturwissenschaften* **1972**, *59,* 420.
8. Joannis, A. *C. R. Hebd. Seances Acad. Sci.* **1891**, *113,* 795–798.
9. Joannis, A. *C. R. Hebd. Seances Acad. Sci.* **1892**, *114,* 585–587.
10. Joannis, A. *Ann. Chim. Phys.* **1906**, *7,* 5–118.
11. Kraus, C. A. *J. Am. Chem. Soc.* **1907**, *29,* 1557–1571.
12. Smyth, F. H. *J. Am. Chem. Soc.* **1917**, *39,* 1299–1312.
13. Peck, E. B. *J. Am. Chem. Soc.* **1918**, *40,* 335–347.
14. Zintl, E.; Goubeau, J.; Dullenkopf, W. *Z. Phys. Chem., Abt. A* **1931**, *154,* 1–46.
15. Zintl, E.; Harder, A. *Z. Phys. Chem., Abt. A* **1931**, *154,* 47–96.
16. Zintl, E.; Dullenkopf, W. *Z. Phys. Chem., Abt. B* **1932**, *16,* 183–212.
17. Zintl, E.; Kaiser, H. *Z. Anorg. Allg. Chem.* **1933**, *211,* 113–131.
18. Kummer, D.; Diehl, L. *Angew. Chem., Int. Ed. Engl.* **1970**, *9,* 895.

19. Manriquez, V.; Hönle, W.; Von Schnering, H. G. *Z. Anorg. Allg. Chem.* **1986**, *539,* 95–109.
20. Santandrea, R. P.; Mensing, C.; Von Schnering, H. G. *Thermochim. Acta* **1986**, *98,* 301–311.
21. Meyer, T.; Hönle, W.; Von Schnering, H. G. *Z. Anorg. Allg. Chem.* **1987**, *552,* 69–80.
22. Emmerling, F.; Röhr, C. *Z. Naturforsch. B* **2002**, *57,* 963–975.
23. Hirschle, C.; Röhr, C. *Z. Anorg. Allg. Chem.* **2000**, *626,* 1992–1998.
24. Wichelhaus, W.; Von Schnering, H. G. *Naturwissenschaften* **1973**, *60,* 104.
25. Von Schnering, H. G.; Somer, M.; Kliche, G.; Hönle, W.; Meyer, T.; Wolf, J. *Z. Anorg. Allg. Chem.* **1991**, *601,* 13–30.
26. Dahlmann, W.; Von Schnering, H. G. *Naturwissenschaften* **1973**, *60,* 429.
27. Schmettow, W.; Von Schnering, H. G. *Angew. Chem., Int. Ed. Engl.* **1977**, *16,* 857.
28. Goebel, T.; Prots, Y.; Haarmann, F. *Z. Kristallogr. NCS* **2008**, *223,* 187–188.
29. Von Schnering, H. G.; Schwarz, M.; Chang, J. H.; Peters, K.; Peters, E. M.; Nesper, R. *Z Kristallogr. NCS* **2005**, *220,* 525–527.
30. Grin, Y.; Baitinger, M.; Kniep, R.; Von Schnering, H. G. *Z. Kristallogr. NCS* **1999**, *214,* 453–454.
31. Baitinger, M.; Grin, Y.; Kniep, R.; Von Schnering. H. G. *Z. Kristallogr. NCS* **1999**, *214,* 457–458.
32. Baitinger, M.; Peters, K.; Somer, M.; Carrillo-Cabrera, W.; Grin, Y.; Kniep, R.; Von Schnering, H. G. *Z. Kristallogr. NCS* **1999**, *214,* 455–456.
33. Ponou, S.; Fässler, T. F. *Z. Anorg. Allg. Chem.* **2007**, *633,* 393–397.
34. Queneau, V.; Sevov, S. C. *Angew. Chem., Int. Ed. Engl.* **1997**, *36,* 1754–1756.
35. Hoch, C.; Wendorff, M.; Röhr, C. *Acta Crystallogr. C* **2002**, *58,* i45–i46.
36. Queneau, V.; Sevov, S. C. *Inorg. Chem.* **1998**, *37,* 1358–1360.
37. Bobev, S.; Sevov, S. C. *Polyhedron* **2002**, *21,* 641–649.
38. Todorov, E.; Sevov, S. C. *Inorg. Chem.* **1998**, *37,* 3889–3891.
39. Hoch, C.; Wendorff, M.; Röhr, C. *J. Alloys Compd.* **2003**, *361,* 206–221.
40. Queneau, V.; Todorov, E.; Sevov, S. C. *J. Am. Chem. Soc.* **1998**, *120,* 3263–3264.
41. Carrillo-Cabrera, W.; Cardoso Gil, R.; Somer, M.; Persil, Ö.; Von Schnering, H. G. *Z. Anorg. Allg. Chem.* **2003**, *629,* 601–608.
42. Von Schnering, H. G.; Baitinger, M.; Bolle, U.; Carrillo-Cabrera, W.; Curda, J.; Grin, Y.; Heinemann, F.; Llanos, J.; Peters, K.; Schmeding, A.; Somer, M. *Z. Anorg. Allg. Chem.* **1997**, *623,* 1037–1039.
43. Janzon, K. H.; Schäfer, H.; Weiss, A. *Z. Anorg. Allg. Chem.* **1970**, *372,* 87–99.
44. Corbett, J. D.; Adolphson, D. G.; Merryman, D. J.; Edwards, P. A.; Armatis, F. J. *J. Am. Chem. Soc.* **1975**, *97,* 6267–6268.
45. Fässler, T. F.; Hoffmann, R. *Angew. Chem., Int. Ed.* **1999**, *38,* 543–546.
46. Belin, C. H. E. *J. Am. Chem. Soc.* **1980**, *102,* 6036–6040.

47. Bolle, U.; Tremel, W. *J. Chem. Soc., Chem. Commun.* **1992**, 91–93.
48. Kraus, F.; Aschenbrenner, J. C.; Korber, N. *Angew. Chem., Int. Ed.* **2003**, *42,* 4030–4033.
49. Korber, N.; Reil, M. *Chem. Commun.* **2002**, 84–85.
50. Critchlow, S. C.; Corbett, J. D. *Inorg. Chem.* **1984**, *23,* 770–774.
51. Cisar, A.; Corbett, J. D. *Inorg. Chem.* **1977**, *16,* 2482–2487.
52. Goicoechea, J. M.; Sevov, S. C. *J. Am. Chem. Soc.* **2004**, *126,* 6860–6861.
53. Campbell, J.; Schrobilgen, G. J. *Inorg. Chem.* **1997**, *36,* 4078–4081.
54. Edwards, P. A.; Corbett. J. D. *Inorg. Chem.* **1977**, *16,* 903–907.
55. Corbett, J. D.; Edwards, P. A. *J. Chem. Soc., Chem. Commun.* **1975**, 984–985.
56. Joseph, S.; Suchentrunk, C.; Kraus, F.; Korber, N. *Eur. J. Inorg. Chem.* **2009**, 4641–4647.
57. Goicoechea, J. M.; Sevov, S. C. *Inorg. Chem.* **2005**, *44,* 2654–2658.
58. Belin, C. H. E.; Corbett, J. D.; Cisar, A. *J. Am. Chem. Soc.* **1977**, *99,* 7163–7169.
59. Angilella, V.; Belin, C. *J. Chem. Soc., Faraday Trans.* **1991**, *87,* 203–204.
60. Critchlow, S. C.; Corbett, J. D. *J. Am. Chem. Soc.* **1983**, *105,* 5715–5716.
61. Campbell, J.; Dixon, D. A.; Mercier, H. P. A.; Schrobilgen, G. J. *Inorg. Chem.* **1995**, *34,* 5798–5809.
62. Fässler, T. F.; Hunziker, M. *Inorg. Chem.* **1994**, *33,* 5380–5381.
63. Baudler, M. *Angew. Chem., Int. Ed. Engl.* **1982**, *21,* 492–512.
64. Sen, T.; Poupko, R.; Fleischer, U.; Zimmermann, H.; Luz, Z. *J. Am. Chem. Soc.* **2000**, *122,* 889–896.
65. Baudler, M.; Glinka, K. *Chem. Rev.* **1993**, *93,* 1623–1667.
66. Baudler, M.; Glinka, K. *Chem. Rev.* **1994**, *94,* 1273–1297.
67. Baudler, M.; Heumüller, R.; Langerbeins, K. *Z. Anorg. Allg. Chem.* **1984**, *514,* 7–17.
68. Aschenbrenner, J.C.; Korber, N. *Z. Anorg. Allg. Chem.* **2004**, *630,* 31–32.
69. Dai, F. R.; Xu, L. *Inorg. Chim. Acta* **2006**, *359,* 4265–4273.
70. Turbervill, R. S. P.; Goicoechea, J. M. *Organometallics* **2012**, *31,* 2452–2462.
71. Korber, N.; Von Schnering, H. G. *J. Chem. Soc, Chem. Commun.* **1995**, 1713–1714.
72. Hanauer, T.; Aschenbrenner, J. C.; Korber, N. *Inorg. Chem.* **2006**, *45,* 6723–6727.
73. Miluykov, V.; Kataev, A.; Sinyashin, O.; Lönnecke, P.; Hey-Hawkins, E. *Z. Anorg. Allg. Chem.* **2006**, *632,* 1728–1732.
74. Von Schnering, H. G.; Manriquez, V.; Hönle, W. *Angew. Chem., Int. Ed. Engl.* **1981**, *20,* 594–595.
75. Baudler, M.; Exner, O. *Chem. Ber.* **1983**, *116,* 1268–1270.
76. Baudler, M.; Heumüller, R.; Hahn, J. *Z. Anorg. Allg. Chem.* **1985**, *529,* 7–14.

77. Baudler, M.; Düster, D.; Langerbeins, K.; Germeshausen, J. *Angew. Chem., Int. Ed. Engl.* **1984**, *23,* 317–318.

78. Charles, S.; Fettinger, J. C.; Eichhorn, B. W. *J. Am. Chem. Soc.* **1995**, *117,* 5303–5311.

79. Mattamana, S. P.; Promprai, K.; Fettinger, J. C.; Eichhorn, B. W. *Inorg. Chem.* **1998**, *37,* 6222–6228.

80. Miluykov, V. A.; Kataev, A. V.; Hey-Hawkins, E.; Sinyashin, O. G. *Russ. Chem. Bull., Int. Ed.* **2007**, *56,* 298–303.

81. Baudler, M.; Faber, W.; Hahn, J. *Z. Anorg. Allg. Chem.* **1980**, *469,* 15–21.

82. Fritz, G.; Hoppe, K. D.; Hönle, W.; Weber, D.; Mujica, C.; Manriquez, V.; Von Schnering, H. G. *J. Organomet. Chem.* **1983**, *249,* 63–80.

83. Fritz, G.; Schneider, H. W. *Z. Anorg. Allg. Chem.* **1990**, *584,* 12–20.

84. Von Schnering, H. G.; Fenske, D.; Hönle, W.; Binnewies, M.; Peters, K. *Angew. Chem., Int. Ed. Engl.* **1979**, *18,* 679.

85. Fritz, G.; Layher, E.; Goesmann, H.; Hanke, D.; Persau, C. *Z. Anorg. Allg. Chem.* **1991**, *594,* 36–46.

86. Ahlrichs, R.; Fenske, D.; Fromm, K.; Krautscheid, H.; Krautscheid, U.; Treutler, O. *Chem. Eur. J.* **1996**, *2,* 238–244.

87. Eichhorn, B. W.; Haushalter, R. C.; Huffman, J. C. *Angew. Chem., Int. Ed. Engl.* **1989**, *28,* 1032–1033.

88. Charles, S.; Eichhorn, B. W.; Rheingold, A. L.; Bott, S. G. *J. Am. Chem. Soc.* **1994**, *116,* 8077–8086.

89. Bolle, U.; Tremel, W. *J. Chem. Soc., Chem. Commun.* **1994**, 217–219.

90. Shufler, S. L.; Sternberg, H. W.; Friedel, R. A. *J. Am. Chem. Soc.* **1956**, *78,* 2687–2688.

91. Grevels, F. W.; Jacke, J.; Klotzbücher, W. E.; Mark, F.; Skibbe, V.; Schaffner, K.; Angermund, K.; Krüger, C.; Lehmann, C. W.; Özkar, S. *Organometallics* **1999**, *18,* 3278–3293.

92. Charles, S.; Danis, J. A.; Mattamana, S. P.; Fettinger, J. C.; Eichhorn, B. W. *Z. Anorg. Allg. Chem.* **1998**, *624,* 823–829.

93. Charles, S.; Danis, J. A.; Fettinger, J. C.; Eichhorn, B. W. *Inorg. Chem.* **1997**, *36,* 3772–3778.

94. Kesanli, B.; Mattamana, S. P.; Danis, J.; Eichhorn, B. *Inorg. Chim. Acta* **2005**, *358,* 3145–3151.

95. Charles, S.; Fettinger, J. C.; Eichhorn, B. W. *Inorg. Chem.* **1996**, *35,* 1540–1548.

96. Charles, S.; Fettinger, J. C.; Bott, S. G.; Eichhorn, B. W. *J. Am. Chem. Soc.* **1996**, *118,* 4713–4714.

97. Kesanli, B.; Charles, S.; Lam, Y. F.; Bott, S. G.; Fettinger, J.; Eichhorn, B. *J. Am. Chem. Soc.* **2000**, *122,* 11101–11107.

98. Moses, M. J.; Fettinger, J.; Eichhorn, B. W. *J. Am. Chem. Soc.* **2002**, *124,* 5944–5945.

99. Pyykkö, P.; Atsumi, M. *Chem. Eur. J.* **2009**, *15,* 186–197.

100. Alvarez, S. *Dalton Trans.* **2013**, *42,* 8617–8636.

101. Huheey, J.E.; Keiter, E. A.; Keiter, R. L. *Inorganic Chemistry: Principles of Structure and Reactivity*; HarperCollins: New York, 1993.
102. Kesanli, B.; Fettinger, J.; Scott, B.; Eichhorn, B. *Inorg. Chem.* **2004**, *43,* 3840–3846.
103. Eichhorn, B. W.; Mattamana, S. P.; Gardner, D. R.; Fettinger, J. C. *J. Am. Chem. Soc.* **1998**, *120,* 9708–9709.
104. Kesanli, B.; Fettinger, J.; Eichhorn, B. *J. Am. Chem. Soc.* **2003**, *125,* 7367–7376.
105. Von Schnering, H. G.; Wolf, J.; Weber, D.; Ramirez, R.; Meyer, T. *Angew. Chem., Int. Ed. Engl.* **1986**, *25,* 353–354.
106. Charles, S.; Eichhorn, B. W.; Bott, S. G. *J. Am. Chem. Soc.* **1993**, *115,* 5837–5838.
107. Wade, K. *J. Chem. Soc. D* **1971**, 792–793.
108. Mingos, D. M. P. *Nat. Phys. Sci.* **1972**, *236,* 99–102.
109. Mingos, D. M. P. *Acc. Chem. Res.* **1984**, *17,* 311–319.
110. Brill, R.; Dietrich, H.; Dierks, H. *Acta Crystallogr. B* **1971**, *27,* 2003–2018.
111. Schaeffer, R.; Rietz, R. R. *J. Am. Chem. Soc.* **1971**, *93,* 1263–1265.
112. Hawthorne, M. F.; Garrett, P. M.; Ditta, G. S. *J. Am. Chem. Soc.* **1971**, *93,* 1265–1266.
113. Moses, M. J.; Fettinger, J. C.; Eichhorn, B. W. *Science* **2003**, *300,* 778–780.
114. Moses, M. J.; Fettinger, J. C.; Eichhorn, B. W. *Inorg. Chem.* **2007**, *46,* 1036–1038.
115. Scherer, O. J.; Brück, T. *Angew. Chem., Int. Ed. Engl.* **1987**, *26,* 59.
116. Scherer, O. J.; Brück, T.; Wolmershäuser, G. *Chem. Ber.* **1988**, *121,* 935–938.
117. Scherer, O. J.; Blath, C.; Wolmershäuser, G. *J. Organomet. Chem.* **1990**, *387,* C21–C24.
118. Scherer, O. J.; Blath, C.; Heckmann, G.; Wolmershäuser, G. *J. Organomet. Chem.* **1991**, *409,* C15–C18.
119. Scherer, O. J. *Acc. Chem. Res.* **1999**, *32,* 751–762.
120. Cossairt, B. M.; Piro, N. A.; Cummins, C. C. *Chem. Rev.* **2010**, *110,* 4164–4177.
121. Caporali, M.; Gonsalvi, L.; Rossin, A.; Peruzzini, M. *Chem. Rev.* **2010**, *110,* 4178–4235.

Chapter 2 Solution reactivity of E_7^{3-} towards homoleptic metal reagents

2.1 Introduction

Over the last twenty years, several research groups, most notably Eichhorn and co-workers, have studied the reactivity of group 15 Zintl ions towards a number of homoleptic transition metal complexes. These reactions can be divided into two types: those in which the E_7^{3-} cage is retained in the product, and those in which fragmentation of the E_7^{3-} cage occurs, resulting in the formation of larger heteroatomic cluster alloys (see Introduction for a more comprehensive overview). Cluster fragmentation is more common for Sb_7^{3-} than for As_7^{3-}, and had not been observed for P_7^{3-} at the start of this project. This observation is consistent with the decrease in bond dissociation energies as group 15 is descended (BDEs: P–P: 201 kJ mol^{-1}; As–As: 146 kJ mol^{-1}; Sb–Sb: 121 kJ mol^{-1}).[1]

2.1.1 Reactions in which the E_7^{3-} cage is retained

Prior to 2008, only one reaction of E_7^{3-} with a homoleptic metal complex was known to result in retention of the E_7^{3-} cluster cage. Ethylenediamine solutions of As_7^{3-} were found to react with toluene solutions of $Pd(PCy_3)_2$ in the presence of 2,2,2-crypt to form $[Pd_2(As_7)_2]^{4-}$, which was isolated as the $[K(2,2,2\text{-crypt})]^+$ salt.[2] Eichhorn and co-workers report that the $[Pd_2(As_7)_2]^{4-}$ product is the result of a net two-electron oxidation of the Pd and As precursors, which occurs alongside a two-electron reduction of ethylenediamine solvent molecules and subsequent hydrogen elimination.[2] The formation of hydrogen was confirmed by a hydrogen trapping experiment, in which *trans*-stilbene was hydrogenated in the presence of a Pd

catalyst. The $[Pd_2(As_7)_2]^{4-}$ cluster anion consists of two norbornadiene-like As_7^{3-} groups, each of which is bonded to two Pd atoms in an η^2-fashion (Figure 2.1). The Pd atoms are in distorted square planar coordination environments and are linked by an axial Pd–Pd bond of 2.714(1) Å. $[Pd_2(As_7)_2]^{4-}$ was also recently synthesised by Weiss, Sen and co-workers using $Pd(PPh_3)_4$.[3]

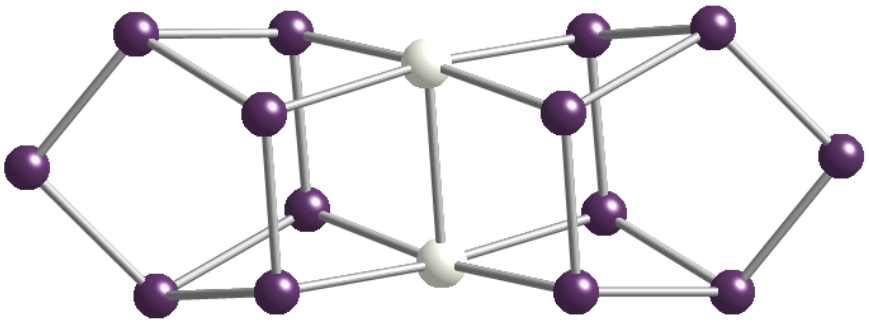

Figure 2.1: Ball and stick diagram of $[Pd_2(As_7)_2]^{4-}$. Pd atoms are shown in grey and As atoms are shown in purple.

2.1.2 Reactions in which cluster fragmentation occurs

Fragmentation of the E_7^{3-} cluster anion has been observed in several reactions of group 15 Zintl ions with homoleptic transition metal reagents. Reaction of As_7^{3-} or Sb_7^{3-} with $M(arene)_2$ (M = Nb: arene = toluene; M = Cr: arene = naphthalene; M = Mo: arene = Me-naphthalene) and $Ni(COD)_2$ yields $[ME_8]^{n-}$ (M = Nb, Cr, Mo; E = As, Sb; n = 2, 3), $[As@Ni_{12}@As_{20}]^{3-}$ and $[Ni_5Sb_{17}]^{4-}$, respectively.[4–8] In addition, the reaction of As_7^{3-} with $Pd(PCy_3)_2$ discussed in Section 2.1.1 gives low yields of a second cluster, $[Pd_7As_{16}]^{4-}$.[2] All of these reactions give rise to higher nuclearity clusters *via* reaction mechanisms that are poorly understood.

$[ME_8]^{n-}$ clusters consist of crown-like *cyclo*-E_8 rings centred by a transition metal ion (Figure 2.2). To date, $[NbE_8]^{3-}$ (E = As, Sb), $[MoAs_8]^{2-}$, $[MoSb_8]^{3-}$ and $[CrAs_8]^{3-}$ have been isolated and structurally characterised. $[NbE_8]^{3-}$ and $[MoAs_8]^{2-}$ are formally sixteen-electron diamagnetic complexes, while $[MoSb_8]^{3-}$ and $[CrAs_8]^{3-}$ have seventeen valence electrons and are paramagnetic. The E_8 ring possesses a formal 8– charge, which requires high oxidation state transition metals, such as M^{5+} for $[NbE_8]^{3-}$, $[CrAs_8]^{3-}$ and $[MoSb_8]^{3-}$, and M^{6+} for $[MoAs_8]^{2-}$. The observation of a higher transition metal oxidation state in $[MoAs_8]^{2-}$ than in $[CrAs_8]^{3-}$ is consistent with the tendency of the 4*d* transition metals to adopt higher oxidation states

relative to the 3*d* metals in the same ligand environment. The observation of Mo^{6+} in $[MoAs_8]^{2-}$ and Mo^{5+} in $[MoSb_8]^{3-}$ can be explained by the fact that the higher transition metal oxidation state is stabilised by the more electronegative As_8 ring.

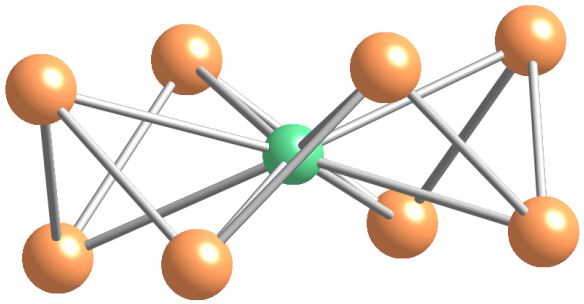

Figure 2.2: Ball and stick diagram of $[NbSb_8]^{3-}$. The Nb atom is shown in green and Sb atoms are shown in gold.

The $[As@Ni_{12}@As_{20}]^{3-}$ anion consists of an icosahedral $[Ni_{12}(\mu_{12}\text{-}As)]^{3-}$ fragment that resides at the centre of an As_{20} pentagonal dodecahedron (Figure 2.3). The cluster possesses nearly perfect I_h point symmetry, in which each As atom of the As_{20} cage caps a Ni_3 face and, conversely, each As_5 ring is centred by a Ni atom. $[As@Ni_{12}@As_{20}]^{3-}$ possesses a total of 168 cluster valence electrons, 128 of which orginate from the $[Ni_{12}(\mu_{12}\text{-}As)]^{3-}$ subunit and forty of which orginate from lone pairs on the As_{20} subunit.

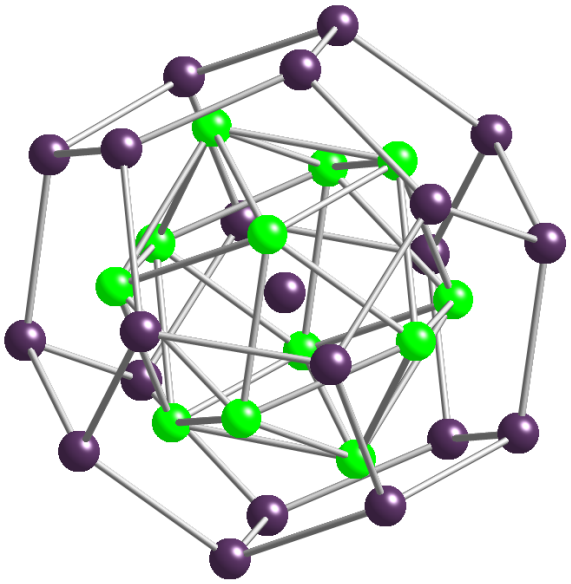

Figure 2.3: Ball and stick diagram of $[As@Ni_{12}@As_{20}]^{3-}$. As atoms are shown in purple and Ni atoms are shown in green.

The $[Ni_5Sb_{17}]^{4-}$ cluster anion contains a Ni(*cyclo*-Ni_4Sb_4) ring unit that resides inside an Sb_{13} bowl (Figure 2.4). This species has a very similar structure to the previously discussed $[ME_8]^{n-}$

(M = Nb, Cr, Mo; E = As, Sb; n = 2, 3) series of compounds. In both cases, all atoms in the E_8 or Ni_4Sb_4 ring are equidistant from the transition metal centre. The central Ni atom is bound to the four Sb atoms in the ring and also to one Sb atom of the Sb_{13} bowl, giving an overall square pyramidal coordination geometry. The other four Ni atoms are in distorted trigonal prismatic environments, with five short Ni–Sb bonds and one much longer bond.

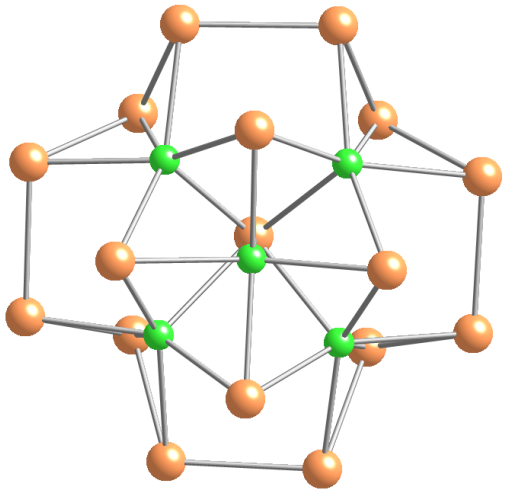

Figure 2.4: Ball and stick diagram of $[Ni_5Sb_{17}]^{4-}$ (viewed from above). Ni atoms are shown in green and Sb atoms are shown in gold.

$[Pd_7As_{16}]^{4-}$ is similar to the previously mentioned $[Ni_5Sb_{17}]^{4-}$ cluster, in that $[Pd_7As_{16}]^{4-}$ also contains a M(*cyclo*-M_4E_4) cap. However, in this case, the corresponding bowl has a formula of Pd_2As_{12}, and the central Pd atom in the Pd(*cyclo*-Pd_4As_4) subunit is shifted significantly from the middle of the ring, with shorter contacts to the As atoms than to the other Pd atoms (Figure 2.5).

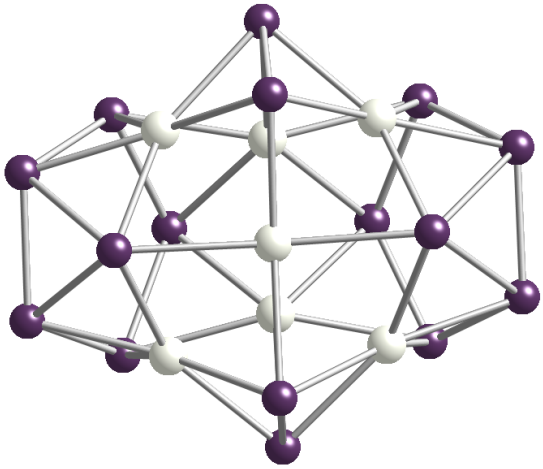

Figure 2.5: Ball and stick diagram of $[Pd_7As_{16}]^{4-}$ (viewed from above). Pd atoms are shown in grey and As atoms are shown in purple.

2.2 Objectives

Prior to 2008, studies of the reactivity of group 15 Zintl ions towards homoleptic metal reagents were limited to metals formally in the zero oxidation state complexed by neutral ligands. In addition, the reactions of E_7^{3-} with compounds of group 11, group 12 and group 13 had not been studied at all.

Group 14 Zintl clusters have been found to react with $[Cu_5(mes)_5]$ to form spherical $[Cu@E_9]^{3-}$ ions (E = Sn, Pb), and with MR_2 (M = Zn: R = Ph, mes, ^{i}Pr; M = Cd: R = Ph) to form the funtionalised Zintl clusters $[E_9MR]^{3-}$ (E = Si, Ge: M = Zn; E = Sn, Pb: M = Zn, Cd).[9–12] Research recently published by the Goicoechea group has shown that Ge_9^{4-} reacts with $InPh_3$ to form a mixture of products, including $[In(Ge_9)_2]^{5-}$, $[(Ge_9)_2InPh]^{4-}$ and $[Ge_9(InPh_3)_2]^{4-}$.[13] Ugrinov and Sevov proposed that the group 14 Zintl ions E_9^{4-}, E_9^{3-} and E_9^{2-} (E = Si, Ge, Sn, Pb) exist in equilibrium with each other and with free solvated electrons in solution.[14] The proposed mechanism of the reaction of E_9^{4-} with MR_2 (M = Zn: R = Ph, mes, ^{i}Pr; M = Cd: R = Ph) involves the reduction of one of the M–C bonds by these solvated electrons to form an MR moiety and an R^- anion, which rapidly abstracts a proton from the ethylenediamine solvent (Scheme 2.1). ^{1}H NMR spectra of the crude reaction mixtures showed that free benzene and mesitylene were formed during the course of the reactions with MPh_2 (M = Zn, Cd) and $Zn(mes)_2$, respectively.[10–12]

$$E_9^{4-} \rightleftharpoons E_9^{3-} + e^- \xrightarrow{MR_2} [E_9MR]^{3-} + R^- \xrightarrow{H_2NC_2H_4NH_2} RH + H_2NC_2H_4NH^-$$

Scheme 2.1: The formation of $[E_9MR]^{3-}$ from E_9^{4-} and MR_2.

In this chapter, the reactivity of E_7^{3-} (E = P, As) towards $[Cu_5(mes)_5]$, MPh_2 (M = Zn, Cd) and $InPh_3$ will be detailed. Reactions of E_7^{3-} with $[Cu_5(mes)_5]$ produced $[Cu_2(E_7)_2]^{4-}$ ions, in which two E_7^{3-} cages are bridged by two Cu atoms, with the formation of a Cu–Cu bond. E_7^{3-} ions react with MPh_2 to form the metal-bridged dimers $[M(E_7)_2]^{4-}$ (E = P: M = Zn, Cd; E = As: M = Zn). In these species, both E_7^{3-} groups retain the nortricyclane-like shape of the parent clusters and bond to the metal centre in an η^2-fashion. In addition, it has been found that both P_7^{3-} and As_7^{3-} react with $InPh_3$ to form the In-funtionalised Zintl ions $[E_7InPh_2]^{2-}$, which feature nortricyclane-like η^2-E_7^{3-} clusters.[15]

2.3 Solution reactivity of group 15 Zintl ions towards $[Cu_5(mes)_5]$

2.3.1 Synthesis of $[Cu_2(P_7)_2]^{4-}$ (1) and $[Cu_2(As_7)_2]^{4-}$ (2)

Ethylenediamine solutions of both K_3P_7 and K_3As_7 react with 0.2 equivalents of $[Cu_5(mes)_5]$ and approximately three equivalents of 2,2,2-crypt to form the compounds $[K(2,2,2\text{-crypt})]_4[Cu_2(E_7)_2]$ (E = P, As) (Scheme 2.2). These salts contain the Cu–Cu bridged species $[Cu_2(P_7)_2]^{4-}$ (**1**) and $[Cu_2(As_7)_2]^{4-}$ (**2**). Crystals of $[K(2,2,2\text{-crypt})]_4$[**1**] were obtained from an ethylenediamine/toluene solvent mixture, however these were both very small and excessively twinned, and proved to be unsuitable for single crystal X-ray diffraction. A number of other solvent systems were tried, however better crystals could not be obtained. The identity of the product was confirmed by $^{31}P\{^1H\}$ NMR spectroscopy and electrospray mass spectrometry. Crystals of $[K(2,2,2\text{-crypt})]_4$[**2**]·2en suitable for single crystal X-ray diffraction were obtained from an ethylenediamine solution layered with toluene.

$$2E_7^{3-} + 0.4[Cu_5(mes)_5] \longrightarrow [Cu_2(E_7)_2]^{4-} + 2mes^- \xrightarrow{2H_2NC_2H_4NH_2} 2mesH + 2H_2NC_2H_4NH^-$$

Scheme 2.2: The formation of $[Cu_2(E_7)_2]^{4-}$ from E_7^{3-} and $[Cu_5(mes)_5]$.

2.3.2 Structure of $[Cu_2(As_7)_2]^{4-}$ (2)

Cluster **2** consists of two As_7^{3-} cages bridged by a Cu_2^{2+} dimetallic centre (Figure 2.6). Each Cu atom is bound by one As_7^{3-} group in an η^4-fashion and by the other As_7^{3-} group in an η^1-fashion. The two Cu atoms are also linked by a Cu–Cu bond, giving each Cu atom a coordination number of six. Cluster 2 has C_i point symmetry, with a centre of inversion in the centre of the Cu–Cu bond. The two $CuAs_7$ fragments are therefore crystallographically equivalent.

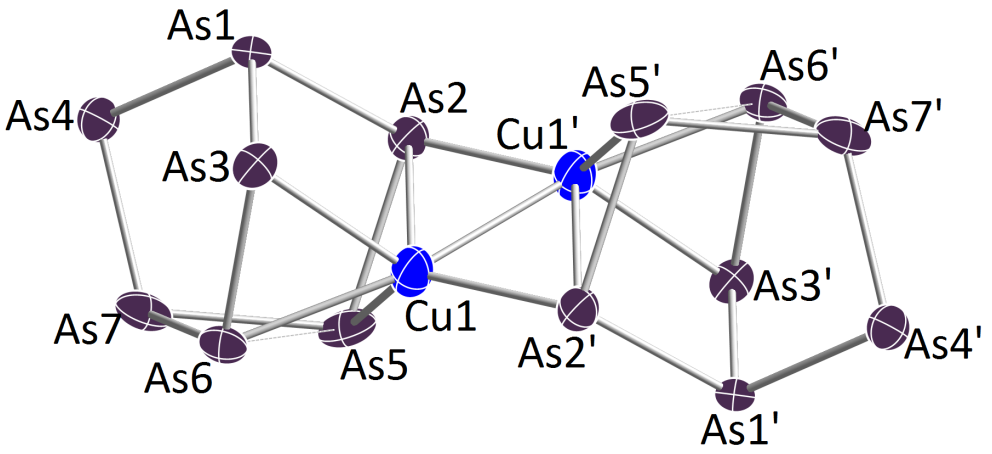

Figure 2.6: Thermal ellipsoid plot of **2** with anisotropic displacement ellipsoids pictured at 50% probability.

The As5–As6 bond is significantly lengthened to 2.772(1) Å on formation of **2**. This is approximately 0.3 Å longer than the other two basal As–As bond lengths, As5–As7 and As6–As7, which are 2.465(1) Å and 2.456(1) Å, respectively. This bond lengthening has also been observed in the previously reported $[E_7M(CO)_3]^{3-}$ complexes (E = P, As, Sb; M = Cr, Mo, W) and has been attributed to a nortricyclane–norbornadiene transition of the E_7^{3-} cluster, in which the E5–E6 bond is broken.[16,17] Interestingly, bond length data for $[As_7Cr(CO)_3]^{3-}$ show that the As5–As6 distance is significantly longer in this species, at 3.082(8) Å, than in **2**. Bolle and Tremel have reported a similar effect for $[Sb_7Mo(CO)_3]^{3-}$, in which the lengthening of the Sb5–Sb6 distance on formation of this species is much less than the lengthening of the As5–As6 distance on formation of $[As_7Cr(CO)_3]^{3-}$.[18] It has been argued that the Sb5–Sb6 bond is only partially cleaved on formation of $[Sb_7Mo(CO)_3]^{3-}$, while the As5–As6 bond is completely broken in the case of $[As_7Cr(CO)_3]^{3-}$. Eichhorn attributed this to a relative size effect, in which the larger Sb_7^{3-} cluster does not have to distort as much as the smaller As_7^{3-} in order to accommodate the $M(CO)_3$ fragment.[17] This argument may also explain the difference in As5–As6 distances in $[As_7Cr(CO)_3]^{3-}$ and **2**. The As_7^{3-} cage would have to distort less to accommodate the smaller Cu atom than to accommodate the $M(CO)_3$ fragment, and therefore the As5–As6 bond is only partially broken on formation of **2**. The As2–As3, As2–As4 and As3–As4 distances are 3.681(1) Å, 3.737(1) Å and 3.786(1) Å, respectively, which indicates that there are no bonding interactions between these three As atoms. One of the Cu–As bonds to the η^4-As_7^{3-} group, Cu1–As2, is approximately 0.2 Å longer than the others, at 2.690(1) Å. This is not the case for $[E_7M(CO)_3]^{3-}$, in which all of the M–E bonds are approximately the

same length.[17] The previously reported $[Pd_2(As_7)_2]^{4-}$ species is similar to **2**, in that it also contains two As_7^{3-} groups bridged by a dimetallic centre, however in this case, each cluster is bonded to both Pd atoms in an η^2-fashion.[2,3]

Selected bond distances are provided in Table 2.1. The short As–As bond lengths range from 2.361(1) Å to 2.465(1) Å and are in good agreement with the values for other functionalised As_7^{3-} clusters, such as $[As_7Cr(CO)_3]^{3-}$ (2.334(9) Å – 2.471(8) Å) and $[Pd_2(As_7)_2]^{4-}$ (2.362(1) Å – 2.446(1) Å).[2,17] The four short Cu–As bond lengths are in the range 2.409(1) Å – 2.490(1) Å and are comparable to the Cu–As bond lengths in $[Cu_4(As_4Ph_4)_2(PPr_3)_4]$ (2.397(1) Å – 2.519(1) Å).[19] A search of the Cambridge Structural Database (CSD) gave a mean Cu–As bond length of 2.407(av) Å, while the sum of covalent radii for Cu–As single bonds is 2.33 Å.[20,21] The Cu–Cu bond length of 2.445(2) Å is significantly shorter than the mean Cu–Cu bond length revealed by a search of the CSD (2.738(av) Å), however it is very similar to the Cu–Cu bond lengths in the $[Cu_5(mes)_5]$ precursor, which range from 2.44(1) Å to 2.50(1) Å.[20,22] The sum of covalent radii for Cu–Cu single bonds is 2.24 Å.[21]

Table 2.1: Selected bond lengths for the $[Cu_2(As_7)_2]^{4-}$ species.

Bond	Bond length in **2** (Å)
As1–As2	2.446(1)
As1–As3	2.423(1)
As1–As4	2.361(1)
As2–As5	2.400(1)
As3–As6	2.375(1)
As4–As7	2.365(1)
As5–As6	2.772(1)
As5–As7	2.465(1)
As6–As7	2.456(1)
Cu1–As2	2.690(1)
Cu1–As3	2.490(1)
Cu1–As5	2.479(1)
Cu1–As6	2.435(1)
Cu1–As2′	2.409(1)
Cu1–Cu1′	2.445(2)

2.3.3 $^{31}P\{^1H\}$ NMR spectroscopic studies on $[Cu_2(P_7)_2]^{4-}$ (1)

$^{31}P\{^1H\}$ NMR studies were carried out on a d_7-DMF solution of **1** and have indicated that the cluster anion is fluxional in solution. At –50 °C, the $^{31}P\{^1H\}$ NMR spectrum shows a broad

signal of relative intensity two at –28.8, a broad triplet of relative intensity one at –39.1 and a broad signal of relative intensity four at –81.0 ppm (Figure 2.7). These have been assigned to P1 and P7, P4, and P2, P3, P5 and P6, respectively (numbering scheme as in Figure 2.6). Assuming that **1** has the same structure as **2**, a fluxional process that renders the four Cu-bound P atoms equivalent to one another must be taking place in solution. The $^{31}P\{^1H\}$ NMR spectrum also shows resonances corresponding to HP_7^{2-}.[23] The relative intensities of the resonances suggest that an approximately 1:1 mixture of **1** and HP_7^{2-} is present.

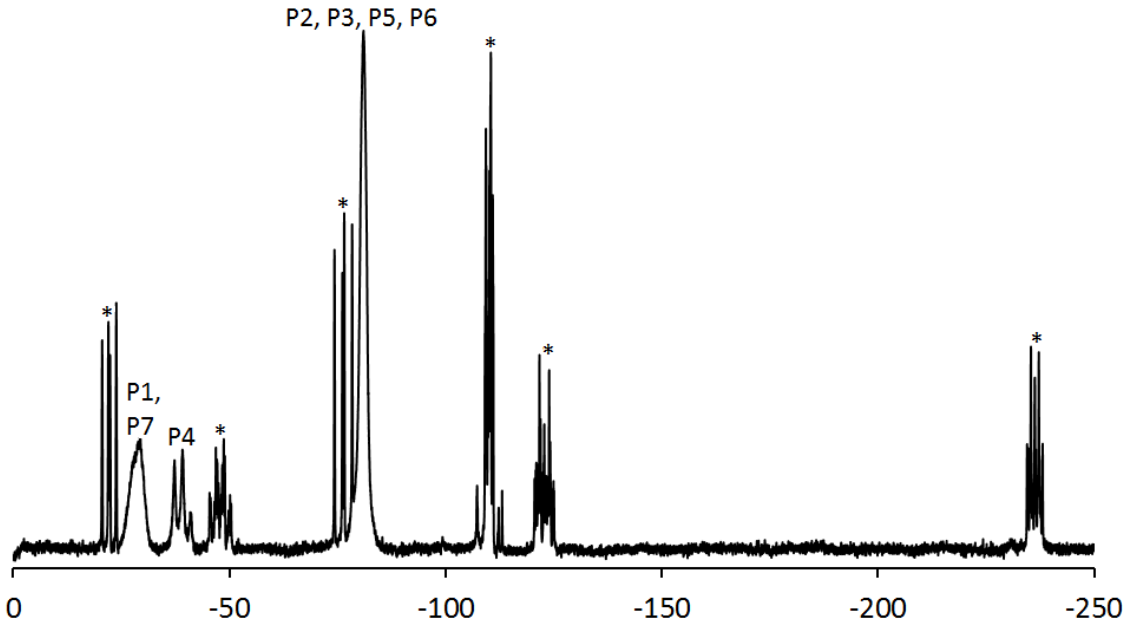

Figure 2.7: $^{31}P\{^1H\}$ NMR spectrum of **1** recorded in d_7-DMF at –50 °C. Resonances labelled * correspond to an HP_7^{2-} impurity.

2.3.4 Mass spectrometric studies

The positive and negative ion mode electrospray ionisation mass spectra of DMF solutions of **1** and **2** confirm that the products are $[Cu_2(P_7)_2]^{4-}$ and $[Cu_2(As_7)_2]^{4-}$, respectively. The clusters are observed with reduced charges as a result of oxidation during the ionisation process. There is also evidence of ion pairing between the anions and the K^+ or $[K(2,2,2\text{-crypt})]^+$ cations. The negative ion mode spectra contain peaks arising from the oxidised cluster anions, $[Cu_2(E_7)_2]^-$, as well as peaks due to the cluster anions paired with K^+ and with up to three $[K(2,2,2\text{-crypt})]^+$ ions. The major peaks in the positive ion mode spectra correspond to the cluster anions with four and five $[K(2,2,2\text{-crypt})]^+$ ions (Figures 2.8 and 2.9).

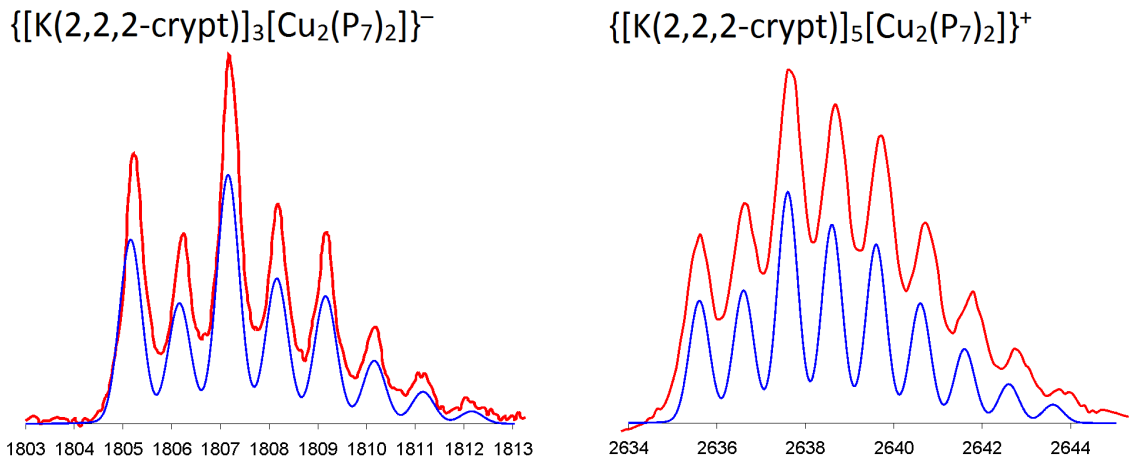

Figure 2.8: ESI-MS mass envelopes for $\{[K(2,2,2\text{-crypt})]_3[Cu_2(P_7)_2]\}^-$ and $\{[K(2,2,2\text{-crypt})]_5[Cu_2(P_7)_2]\}^+$. Predicted isotopic distributions are shown in blue and observed mass spectrometric data are shown in red.

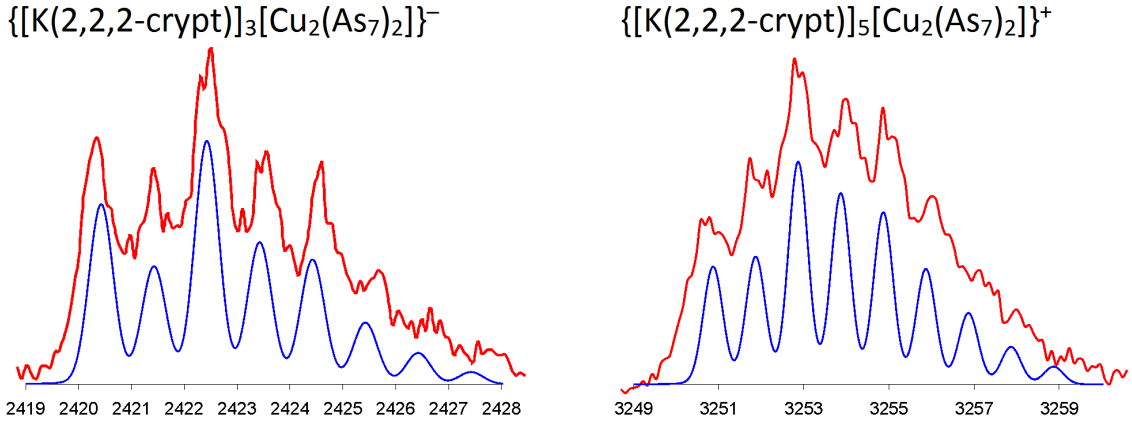

Figure 2.9: ESI-MS mass envelopes for $\{[K(2,2,2\text{-crypt})]_3[Cu_2(As_7)_2]\}^-$ and $\{[K(2,2,2\text{-crypt})]_5[Cu_2(As_7)_2]\}^+$. Predicted isotopic distributions are shown in blue and observed mass spectrometric data are shown in red.

2.4 Solution reactivity of group 15 Zintl ions towards MPh_2 (M = Zn, Cd)

2.4.1 Synthesis of $[Zn(P_7)_2]^{4-}$ (3), $[Zn(As_7)_2]^{4-}$ (4) and $[Cd(P_7)_2]^{4-}$ (5)

Ethylenediamine solutions of K_3P_7 and K_3As_7 have been found to react with 0.5 equivalents of MPh_2 (M = Zn, Cd) and approximately three equivalents of 2,2,2-crypt to form the compounds $[K(2,2,2\text{-crypt})]_4[M(E_7)_2]$ (E = P: M = Zn, Cd; E = As: M = Zn) (Scheme 2.3). These compounds contain the metal-centred cluster anions $[Zn(P_7)_2]^{4-}$ (**3**), $[Zn(As_7)_2]^{4-}$ (**4**) and $[Cd(P_7)_2]^{4-}$ (**5**).

Crystals of [K(2,2,2-crypt)]$_4$[**3**]·6py and [K(2,2,2-crypt)]$_4$[**5**]·6py suitable for single crystal X-ray diffraction were obtained from pyridine/toluene solvent mixtures, while crystals of [K(2,2,2-crypt)]$_4$[**4**] were obtained from slow diffusion of toluene into an ethylenediamine solution of the compound.

$$2E_7^{3-} + MPh_2 \longrightarrow [M(E_7)_2]^{4-} + 2Ph^- \xrightarrow{2H_2NC_2H_4NH_2} 2PhH + 2H_2NC_2H_4NH^-$$

Scheme 2.3: The formation of $[M(E_7)_2]^{4-}$ from E_7^{3-} and MPh_2.

Following our report on the formation of $[Zn(As_7)_2]^{4-}$, Weiss, Sen and co-workers independently synthesised this species, as well as its Cd analogue.[24,25] $[Zn(As_7)_2]^{4-}$ was synthesised by reacting K_3As_7 with $ZnPh_2$, while $[Cd(As_7)_2]^{4-}$ was formed in the reaction of K_3As_7 with cadmium cyclohexanebutyrate. The two cluster anions were crystallographically characterised in [K(2,2,2-crypt)]$_4$[$Zn(As_7)_2$] and [K(2,2,2-crypt)]$_4$[$Cd(As_7)_2$]. Both $[Zn(As_7)_2]^{4-}$ and $[Cd(As_7)_2]^{4-}$ comprise two nortricyclane-like As_7^{3-} cages coordinated to a central metal atom (Figure 2.10). Each As_7^{3-} is bonded to the metal in an η^2-fashion, resulting in an approximately tetrahedral coordination geometry.

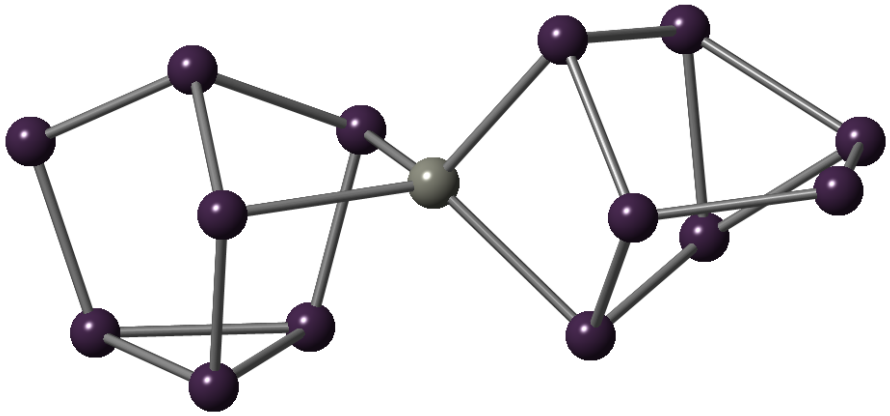

Figure 2.10: Ball and stick diagram of $[Zn(As_7)_2]^{4-}$ as reported by Weiss, Sen and co-workers. The Zn atom is shown in grey and As atoms are shown in purple.

Weiss's group have also investigated the reactivity of As_7^{3-} towards $HgPh_2$. This reaction formed a mixture of $[Hg_2(As_7)_2]^{4-}$ and $[HgAs_{15}]^{3-}$, which were isolated as the $[K(2,2,2\text{-crypt})]^+$ salts.[25,26] $[Hg_2(As_7)_2]^{4-}$ features two As_7^{3-} cages bridged by a Hg_2^{2+} group (Figure 2.11). Each As_7^{3-} cluster is bonded to one Hg atom in an η^2-fashion. The two Hg atoms are also linked by a Hg–Hg bond of 2.679(1) Å.

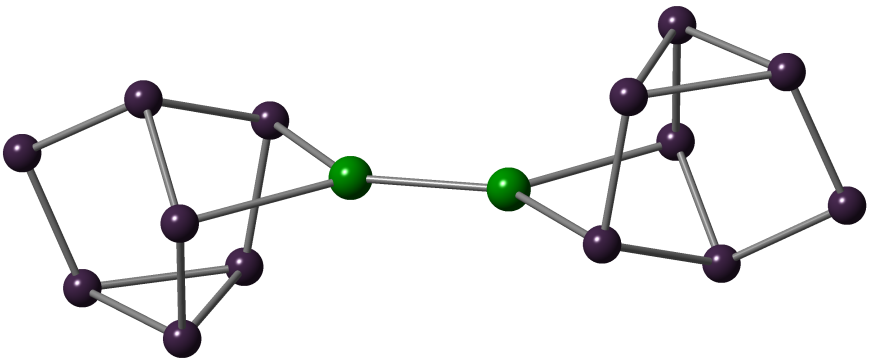

Figure 2.11: Ball and stick diagram of $[Hg_2(As_7)_2]^{4-}$ as reported by Weiss, Sen and co-workers. Hg atoms are shown in green and As atoms are shown in purple.

$[HgAs_{15}]^{3-}$ consists of two As_7^{3-} cages bridged by a Hg–As group and is structurally very similar to the previously reported P_{16}^{2-} cluster anion.[27] The Hg atom is bonded to three As atoms and adopts a trigonal planar coodination geometry (Figure 2.12).

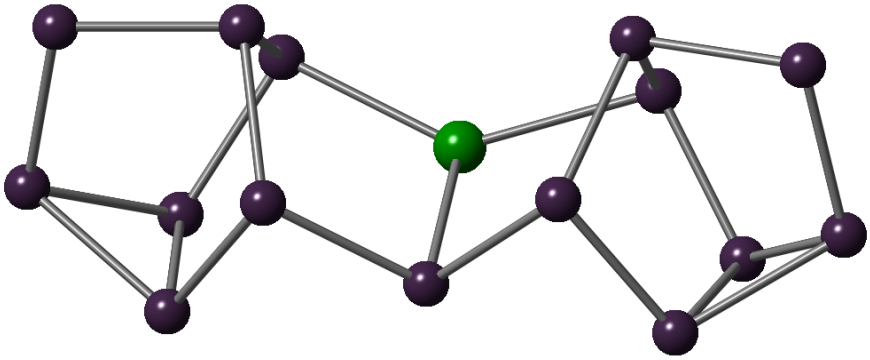

Figure 2.12: Ball and stick diagram of $[HgAs_{15}]^{3-}$ as reported by Weiss, Sen and co-workers. The Hg atom is shown in green and As atoms are shown in purple.

2.4.2 Structures of $[M(E_7)_2]^{4-}$ (3, 4 and 5)

Clusters **3**, **4** and **5** all consist of two nortricyclane-like E_7^{3-} cages coordinated to a central metal atom (Figures 2.13 and 2.14). Both E_7^{3-} groups are bonded to the metal centre in an η^2-fashion, resulting in a distorted tetrahedral coordination geometry. Each η^2-E_7^{3-} group acts as a four-electron donor, and the metal is formally in the +2 oxidation state, with a d^{10} electron configuration. The metal centre therefore possesses eighteen valence electrons and is electronically saturated. **3**, **4** and **5** are very similar to the previously reported $[P_7M(CO)_4]^{3-}$ (M = Mo, W) ions and to the $[E_7PtH(PPh_3)]^{2-}$ (E = P, As) ions, in which the E_7^{3-} cages are also bonded to the metal centre in an η^2-mode.[28–30] **3** and **5** both have C_2 point symmetry, with

a two-fold rotation axis running through the central metal atom. This renders the two P_7^{3-} cages crystallographically equivalent.

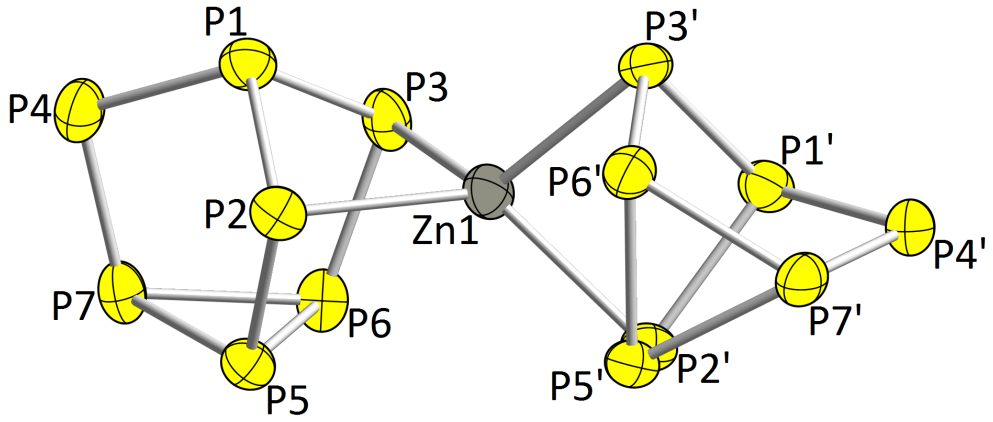

Figure 2.13: Thermal ellipsoid plot of **3** with anisotropic displacement ellipsoids pictured at 50% probability.

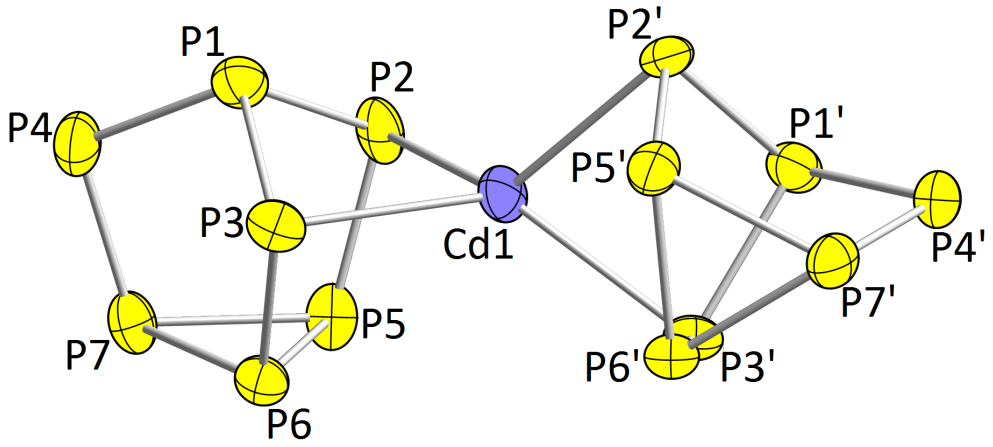

Figure 2.14: Thermal ellipsoid plot of **5** with anisotropic displacement ellipsoids pictured at 50% probability.

Selected bond lengths and angles are provided in Table 2.2. The P–P bond lengths are in the ranges 2.139(1) Å – 2.260(1) Å for **3** and 2.137(2) Å – 2.263(2) Å for **5**. These are in good agreement with the P–P bond lengths in the previously reported $[P_7PtH(PPh_3)]^{2-}$ species, which range from 2.14(2) Å to 2.26(2) Å.[30] A search of the CSD gave mean Zn–P and Cd–P bond distances of 2.407(av) Å and 2.586(av) Å, respectively, while the sums of covalent radii for Zn–P and Cd–P single bonds are 2.29 Å and 2.47 Å, respectively.[20,21] The M–P bond lengths in **3** and **5** are longer than this, however the two Zn–P bond lengths in **3** of 2.474(1) Å and 2.498(1) Å are comparable to those found in related clusters such as $[Zn_{12}Te_9(Te(mes))_6(dppm)_4]$ (2.464(5) Å – 2.521(5) Å; dppm = bis(diphenylphosphino)methane).[31] The two Cd–P bond lengths in **5** of 2.675(2) Å and 2.658(2) Å are similar to those found in closely related species such as the

Cd/P cluster $[Li(THF)_4]_2[(Ph_2P)_{10}Cd_4]$ (2.596(3) Å – 2.687(3) Å).[32]

Table 2.2: Selected bond lengths and bond angles for the $[Zn(P_7)_2]^{4-}$ and $[Cd(P_7)_2]^{4-}$ species.

Bond	Bond length in **3** (Å)	Bond length in **5** (Å)
P1–P2	2.204(1)	2.211(2)
P1–P3	2.208(1)	2.203(2)
P1–P4	2.163(1)	2.161(2)
P2–P5	2.168(1)	2.165(2)
P3–P6	2.166(1)	2.164(2)
P4–P7	2.139(1)	2.137(2)
P5–P6	2.241(1)	2.229(2)
P5–P7	2.260(1)	2.247(2)
P6–P7	2.250(1)	2.263(2)
M1–P2	2.474(1)	2.675(2)
M1–P3	2.498(1)	2.658(2)
Angle	Bond angle in **3** (°)	Bond angle in **5** (°)
P2–M1–P3	82.89(3)	77.31(4)
P2–M1–P2′	127.03(5)	124.89(7)
P2–M1–P3′	124.33(3)	126.63(5)
P3–M1–P3′	120.86(5)	131.90(7)

The crystal structure of [K(2,2,2-crypt)]$_4$[**4**] was heavily disordered, and although the X-ray diffraction data were of sufficient quality to confirm the presence of the $[Zn(As_7)_2]^{4-}$ cluster, quantitative structural data could not be determined. Better quality crystals could not be obtained, although many solvent systems were tried.

2.4.3 $^{31}P\{^1H\}$ NMR spectroscopic studies on $[Zn(P_7)_2]^{4-}$ (3) and $[Cd(P_7)_2]^{4-}$ (5)

The $^{31}P\{^1H\}$ NMR spectrum of a d_5-pyridine solution of **3** shows five resonances at –14.9, –42.9, –56.3, –104.7 and –162.3 ppm with relative intensities 2:1:1:1:2 (Figure 2.15). Based on the solid state structure, seven resonances would be expected, as the anion does not possess a plane of symmetry. The observation of only five resonances shows that **3** must be fluxional in solution. In order to obtain the ^{31}P–^{31}P coupling constants, the spectrum was simulated (Table 2.3). The intercage coupling constants were calculated to be negligibly small, and so are not considered here. The resonance at –162.3 ppm can be assigned to the two equivalent basal P atoms, P5 and P6, as basal P resonances are typically found at lower chemical shifts than other resonances.[28,33,34] The resonance at –14.9 ppm must therefore arise from the two

Zn-bound P atoms, P2 and P3. From the ^{31}P–^{31}P coupling constants, the resonances at –42.9, –56.3 and –104.7 ppm can be assigned as corresponding to P1, P4 and P7, respectively.

Table 2.3: The ^{31}P chemical shift values and coupling constants for $[Zn(P_7)_2]^{4-}$.

δ (ppm)		–42.9 P1	–14.9 P2	–14.9 P3	–56.3 P4	–162.3 P5	–162.3 P6	–104.7 P7
–42.9	P1		–253	–260	–336	23	31	41
–14.9	P2	–253		–29	–12	–411	–	–
–14.9	P3	–260	–29		–12	–	–428	–
–56.3	P4	–336	–12	–12		–	–	–418
–162.3	P5	23	–411	–	–		–179	–206
–162.3	P6	31	–	–428	–	–179		–202
–104.7	P7	41	–	–	–418	–206	–202	

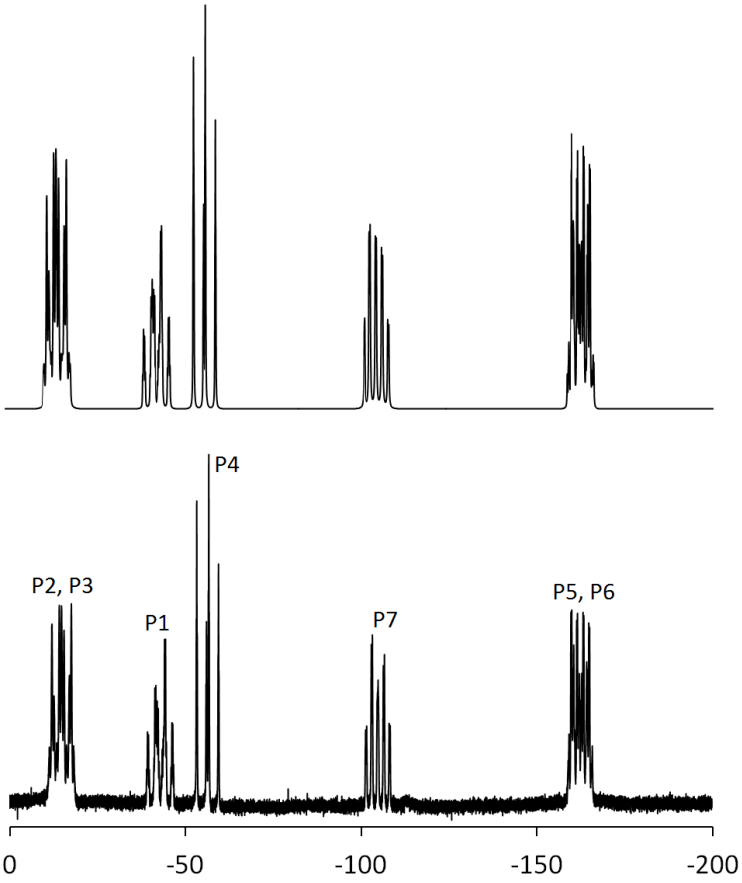

Figure 2.15: Top: The simulated ^{31}P NMR spectrum of **3**. Bottom: The ^{31}P{^{1}H} NMR spectrum of **3** recorded in d_5-pyridine.

The ^{31}P{^{1}H} NMR spectrum of a d_5-pyridine solution of **5** shows five resonances at –4.5, –36.0, –82.1, –134.7 and –161.0 ppm with relative intensities 2:1:1:1:2 (Figure 2.16). These resonances have very similar multiplet structures to those observed in the ^{31}P{^{1}H} NMR spectrum of **3** and can be assigned to P2 and P3, P1, P4, P7, and P5 and P6, in order of decreasing chemical shift.

As for **3**, the $^{31}P\{^1H\}$ NMR spectrum was simulated in order to obtain the ^{31}P–^{31}P coupling constants. The coupling constants obtained confirm that this assignment is correct (Table 2.4).

Table 2.4: The ^{31}P chemical shift values and coupling constants for $[Cd(P_7)_2]^{4-}$.

δ (ppm)		–36.0 P1	–4.5 P2	–4.5 P3	–82.1 P4	–161.0 P5	–161.0 P6	–134.7 P7
–36.0	P1		–254	–276	–350	–	–	–
–4.5	P2	–254		–	–	–403	–	–
–4.5	P3	–276	–		–	–	–416	–
–82.1	P4	–350	–	–		–	–	–426
–161.0	P5	–	–403	–	–		–210	–206
–161.0	P6	–	–	–416	–	–210		–202
–134.7	P7	–	–	–	–426	–206	–202	

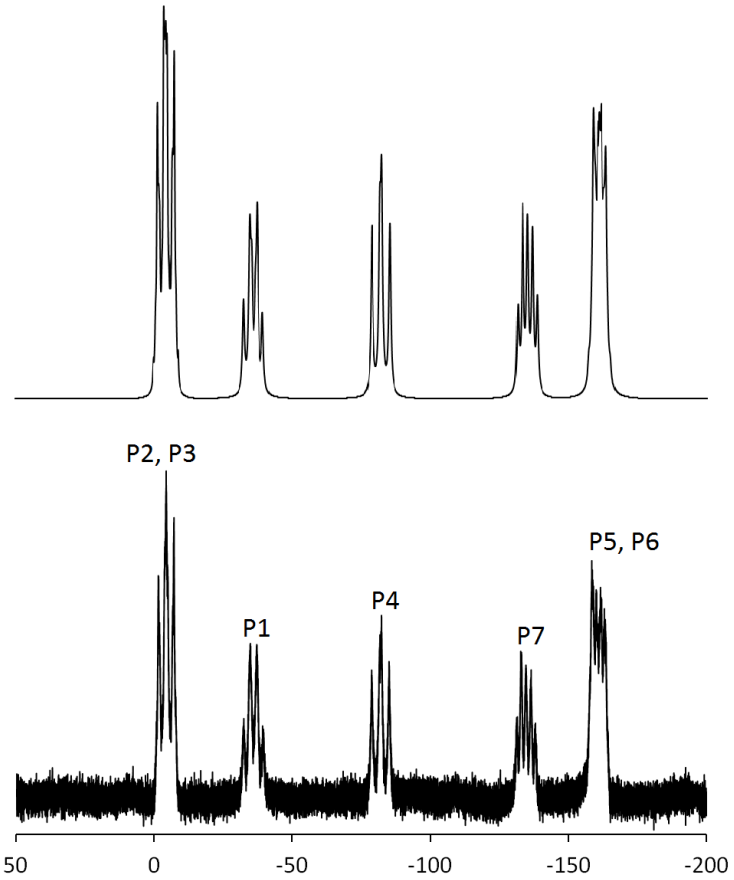

Figure 2.16: Top: The simulated ^{31}P NMR spectrum of **5**. Bottom: The $^{31}P\{^1H\}$ NMR spectrum of **5** recorded in d_5-pyridine.

2.4.4 Mass spectrometric studies

Both the positive and negative ion mode electrospray ionisation mass spectra of **3**, **4** and **5** confirm that the products are $[Zn(P_7)_2]^{4-}$, $[Zn(As_7)_2]^{4-}$ and $[Cd(P_7)_2]^{4-}$, respectively. The

negative ion mode spectra contain peaks due to the oxidised cluster anions, $[M(E_7)_2]^-$, as well as peaks due to the cluster anions coupled with K^+ and with up to three $[K(2,2,2\text{-crypt})]^+$ ions. The major peaks in the positive ion mode spectra correspond to the cluster anions with four and five $[K(2,2,2\text{-crypt})]^+$ ions (Figures 2.17, 2.18 and 2.19).

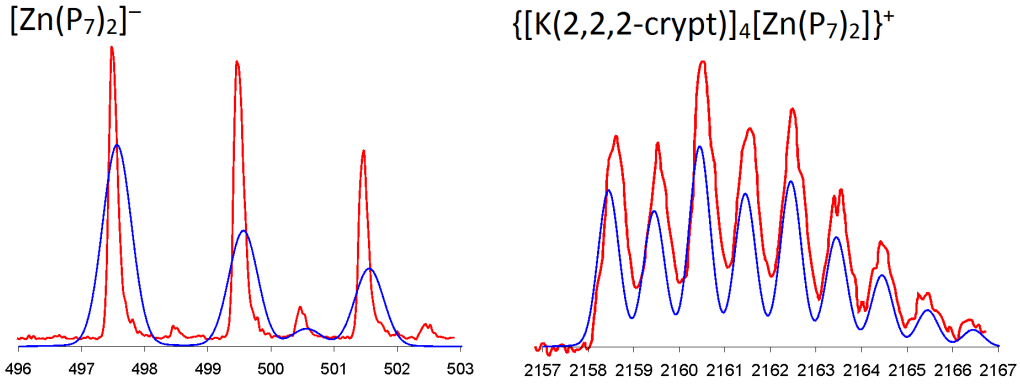

Figure 2.17: ESI-MS mass envelopes for $[Zn(P_7)_2]^-$ and $\{[K(2,2,2\text{-crypt})]_4[Zn(P_7)_2]\}^+$. Predicted isotopic distributions are shown in blue and observed mass spectrometric data are shown in red.

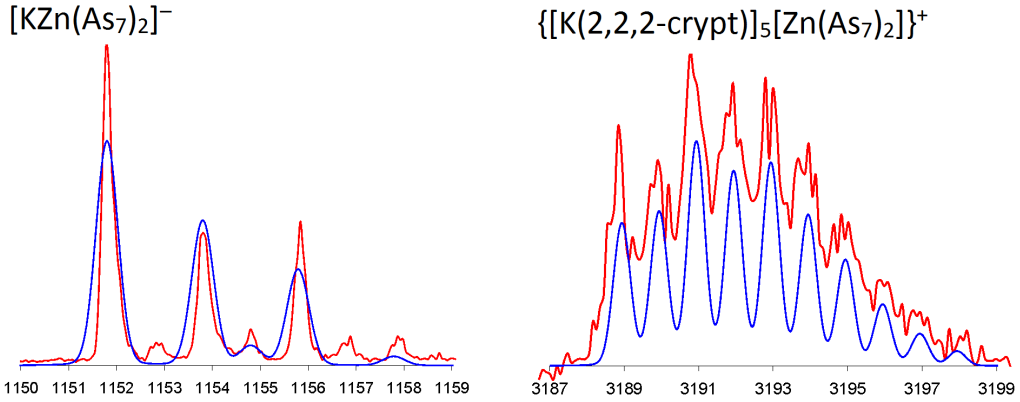

Figure 2.18: ESI-MS mass envelopes for $[KZn(As_7)_2]^-$ and $\{[K(2,2,2\text{-crypt})]_5[Zn(As_7)_2]\}^+$. Predicted isotopic distributions are shown in blue and observed mass spectrometric data are shown in red.

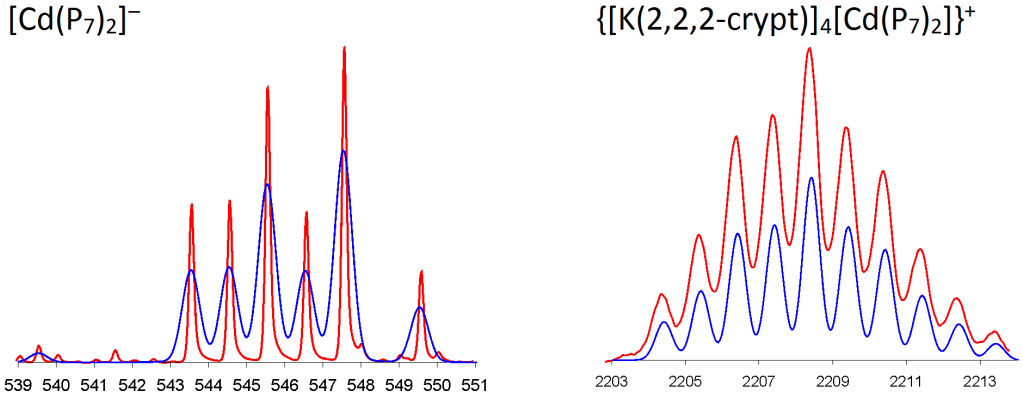

Figure 2.19: ESI-MS mass envelopes for $[Cd(P_7)_2]^-$ and $\{[K(2,2,2\text{-crypt})]_4[Cd(P_7)_2]\}^+$. Predicted isotopic distributions are shown in blue and observed mass spectrometric data are shown in red.

2.5 Solution reactivity of group 15 Zintl ions towards $InPh_3$

2.5.1 Synthesis of $[P_7InPh_2]^{2-}$ (6) and $[As_7InPh_2]^{2-}$ (7)

Ethylenediamine solutions of K_3P_7 and K_3As_7 were found to react with one equivalent of $InPh_3$ and approximately three equivalents of 2,2,2-crypt to form the compounds $[K(2,2,2\text{-crypt})]_2[E_7InPh_2]$ (E = P, As) (Scheme 2.4). These contain the $InPh_2$-derivatised Zintl clusters $[P_7InPh_2]^{2-}$ (**6**) and $[As_7InPh_2]^{2-}$ (**7**). Crystals of $[K(2,2,2\text{-crypt})]_2$[**6**] suitable for single crystal X-ray diffraction were obtained from a pyridine solution layered with toluene. Crystals of $[K(2,2,2\text{-crypt})]_2$[**7**] could not be obtained, however the identity of the product was confirmed by ^1H and $^{13}C\{^1H\}$ NMR spectroscopy, and by electrospray mass spectrometry.

$$E_7^{3-} + InPh_3 \longrightarrow [E_7InPh_2]^{2-} + Ph^- \xrightarrow{H_2NC_2H_4NH_2} PhH + H_2NC_2H_4NH^-$$

Scheme 2.4: The formation of $[E_7InPh_2]^{2-}$ from E_7^{3-} and $InPh_3$.

2.5.2 Structure of $[P_7InPh_2]^{2-}$ (6)

Cluster **6** consists of a nortricyclane-like P_7^{3-} cage bound in an η^2-fashion to a four-electron $[InPh_2]^+$ fragment, resulting in a distorted tetrahedral coordination geometry (Figure 2.20). The η^2-P_7^{3-} group acts as a four-electron donor, so that overall the In centre possesses eight valence electrons. Cluster **6** is very similar to the previously reported $[P_7M(CO)_4]^{3-}$ (M = Mo, W) and $[E_7PtH(PPh_3)]^{2-}$ (E = P, As) ions, and to the previously discussed Zn- and Cd-bridged cluster anions, in which the E_7^{3-} cages are also bonded to the metal centre in an η^2-fashion.[28–30]

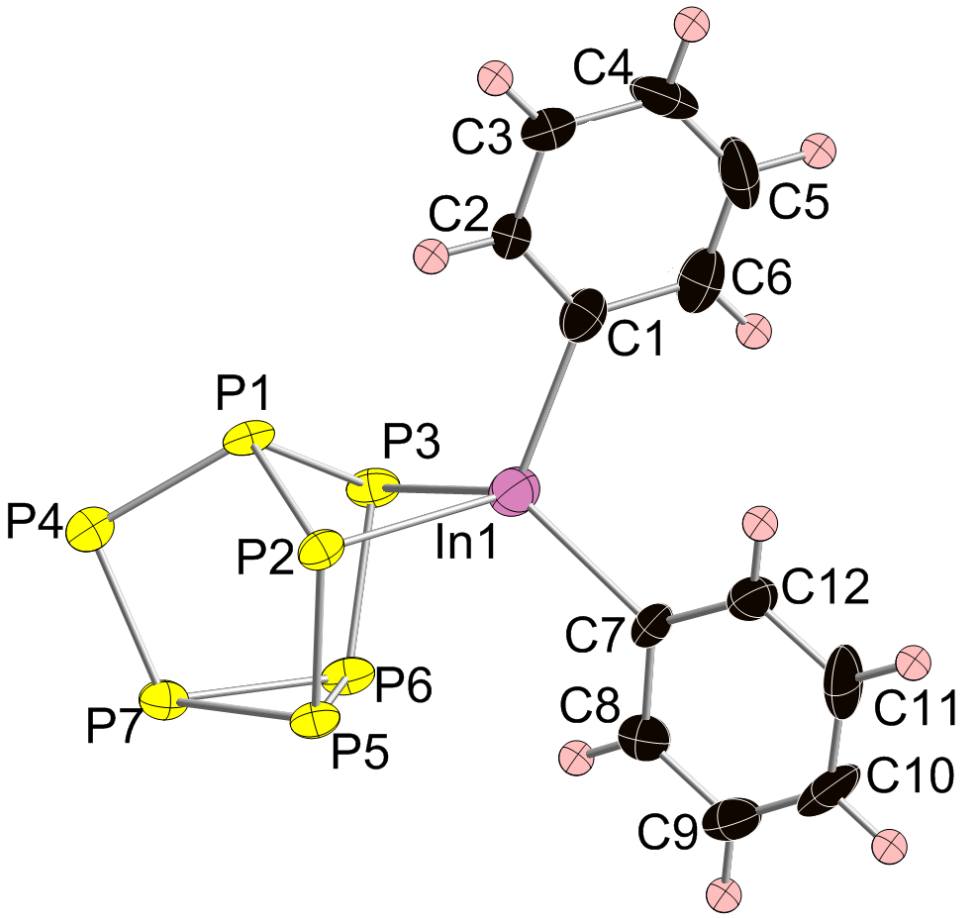

Figure 2.20: Thermal ellipsoid plot of **6** with anisotropic displacement ellipsoids pictured at 50% probability. H atom positions were geometrically fixed and are shown as small spheres of arbitrary radii.

Selected bond lengths and angles are provided in Table 2.5. The P–P bond lengths range from 2.142(2) Å to 2.261(2) Å and are in good agreement with the values reported for related species such as $[P_7PtH(PPh_3)]^{2-}$ (2.14(2) Å – 2.26(2) Å).[30] A search of the CSD gave a mean In–P bond length of 2.645(av) Å.[20] The two In–P bond lengths in **6** are slightly shorter than this, at 2.604(1) Å and 2.551(2) Å, however these bond lengths are similar to those found in $[In_3(In_2)_3(PhP)_4(Ph_2P_2)_3Cl_7(PEt_3)_3]$ (2.533(1) Å – 2.616(1) Å).[35] The sum of covalent radii for In–P single bonds is 2.53 Å.[21] The two In–C bond lengths of 2.238(6) Å and 2.195(5) Å are slightly longer than the mean In–C bond length obtained from the CSD (2.184(av) Å) and the sum of covalent radii for In–C single bonds (2.17 Å).[20,21]

Table 2.5: Selected bond lengths and bond angles for the $[P_7InPh_2]^{2-}$ species.

Bond	Bond length in **6** (Å)
P1–P2	2.203(2)
P1–P3	2.214(2)
P1–P4	2.157(2)
P2–P5	2.184(2)
P3–P6	2.166(2)
P4–P7	2.142(2)
P5–P6	2.261(2)
P5–P7	2.246(2)
P6–P7	2.248(2)
In1–P2	2.604(1)
In1–P3	2.551(2)
In1–C1	2.238(6)
In1–C7	2.195(5)
Angle	Bond angle in **6** (°)
P2–In1–P3	80.33(4)
P2–In1–C1	114.00(15)
P2–In1–C7	113.85(14)
P3–In1–C1	114.02(14)
P3–In1–C7	120.46(15)
C1–In1–C7	111.00(20)

2.5.3 ^{1}H NMR spectroscopic studies on $[P_7InPh_2]^{2-}$ (6) and $[As_7InPh_2]^{2-}$ (7)

The aromatic region of the ^{1}H NMR spectrum of **6** shows six resonances of relative intensities 2:2:2:1:2:1 (Figure 2.21). The two doublets of relative intensity two at 8.86 and 8.21 ppm correspond to two different *ortho*-environments, the two triplets, also of relative intensity two, at 7.46 and 7.18 ppm are due to two different *meta*-environments, and the two triplets of relative intensity one at 7.29 and 7.09 ppm correspond to two different *para*-environments. The *meta*-resonance at 7.18 ppm is partially obscured by a resonance at 7.22 ppm, which is due to residual amounts of protic pyridine solvent. The observation of six separate aromatic ^{1}H resonances shows that the two Ph groups must be chemically inequivalent to one another.

The aromatic region of the ^{1}H NMR spectrum of **7** shows six resonances of relative intensities 2:2:2:1:2:1 (Figure 2.22). The spectrum is very similar to the ^{1}H NMR spectrum of **6**, and this confirms that the $[As_7InPh_2]^{2-}$ species has been formed. The two doublets of relative intensity two at 8.86 and 8.24 ppm can be assigned to the two different *ortho*-environments, the two

triplets, also of relative intensity two, at 7.47 and 7.20 ppm are due to the two different *meta*-environments, and the two triplets of relative intensity one at 7.29 and 7.09 ppm correspond to the two different *para*-environments. The *meta*-resonance at 7.20 ppm is partially obscured by a resonance at 7.22 ppm, which is due to residual amounts of protic pyridine solvent.

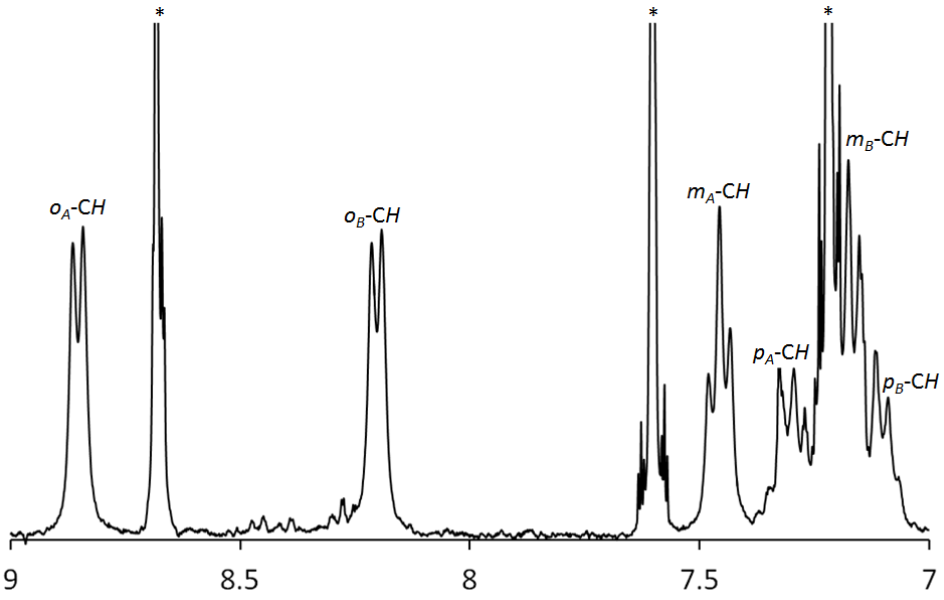

Figure 2.21: Expansion of the aromatic region of the ^{1}H NMR spectrum of **6**. Resonances labelled * correspond to trace amounts of protic pyridine present in the d_5-pyridine solvent.

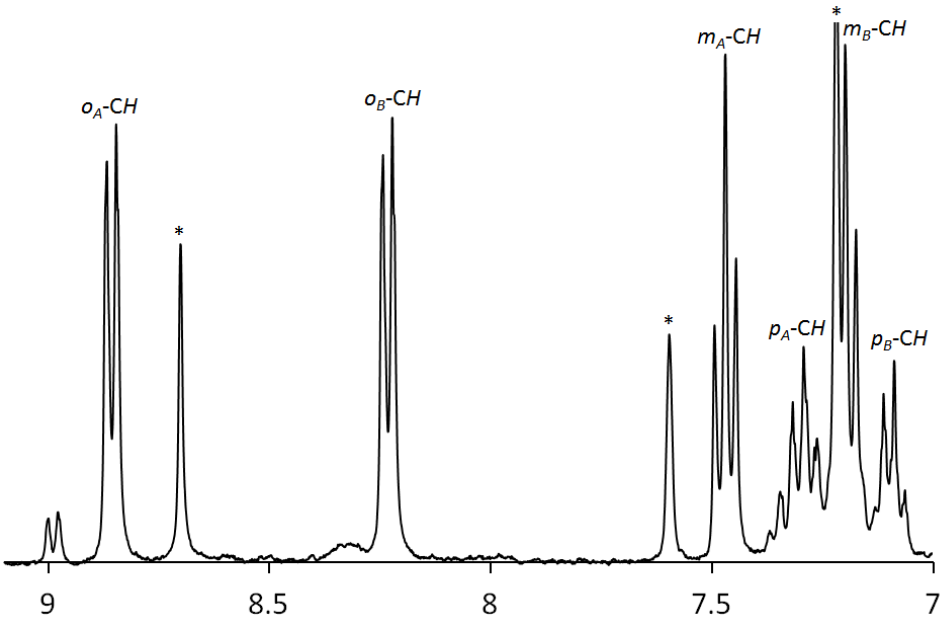

Figure 2.22: Expansion of the aromatic region of the ^{1}H NMR spectrum of **7**. Resonances labelled * correspond to trace amounts of protic pyridine present in the d_5-pyridine solvent.

^{1}H–^{1}H COSY spectra were also recorded for **6** and **7**. The COSY spectra confirm that two sets of three aromatic resonances are present, and examination of the cross peaks enables assignment of the resonances (Figures 2.23 and 2.24).

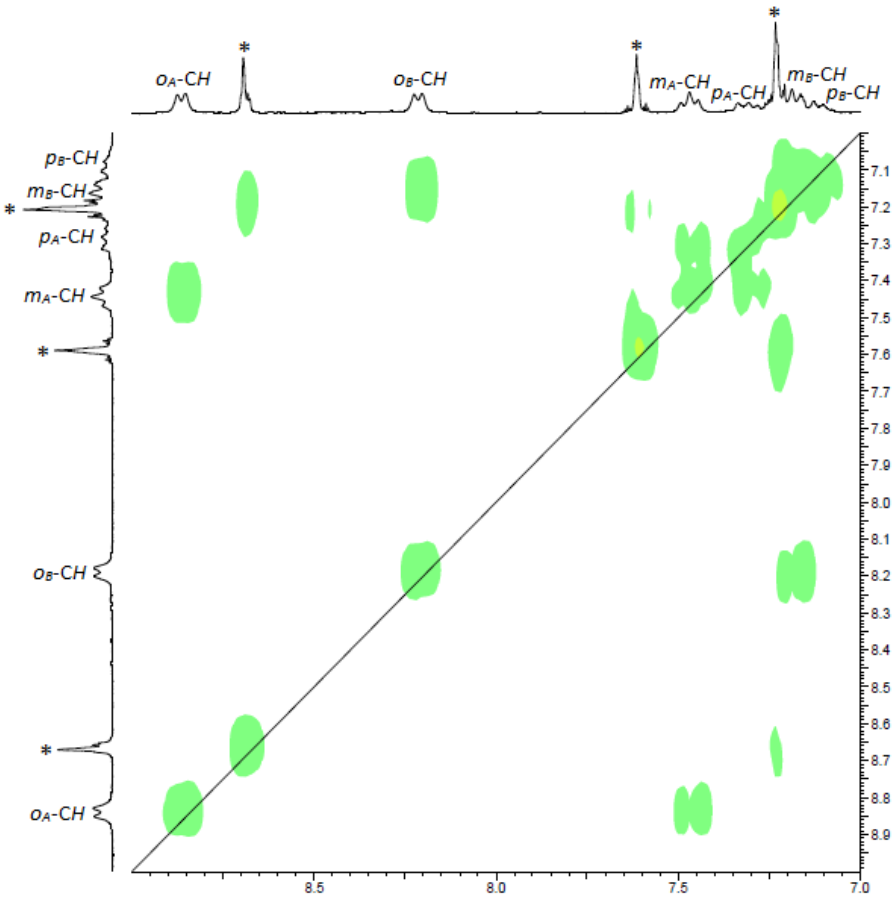

Figure 2.23: Expansion of the aromatic region of a ^{1}H–^{1}H COSY spectrum of **6**.

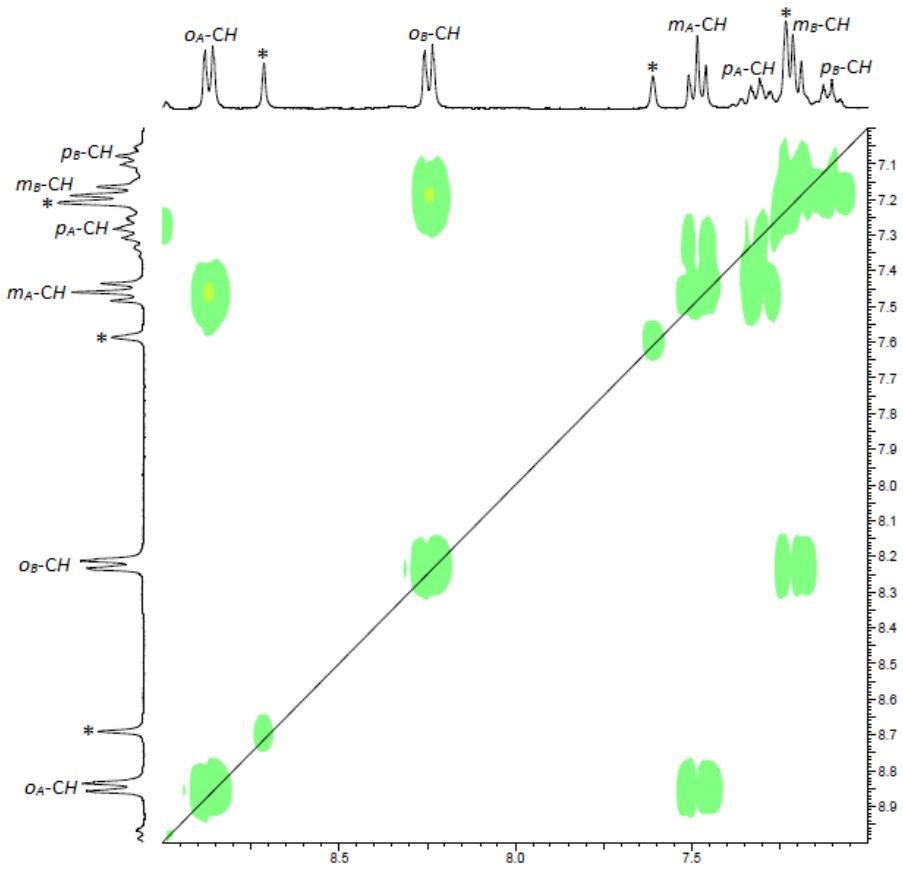

Figure 2.24: Expansion of the aromatic region of a ^{1}H–^{1}H COSY spectrum of **7**.

2.5.4 $^{31}P\{^1H\}$ NMR spectroscopic studies on $[P_7InPh_2]^{2-}$ (6)

The $^{31}P\{^1H\}$ NMR spectrum of **6** shows five resonances at 3.6, –50.7, –67.8, –76.8 and –170.0 ppm with relative intensities 2:1:1:1:2 (Figure 2.25). These resonances have very similar multiplet structures to those observed in the $^{31}P\{^1H\}$ NMR spectra of **3** and **5**, and have been assigned to P2 and P3, P1, P4, P7, and P5 and P6, respectively. The spectrum was simulated in order to obtain the ^{31}P–^{31}P coupling constants (Table 2.6). The spectrum also shows resonances that correspond to an HP_7^{2-} impurity.[23,36]

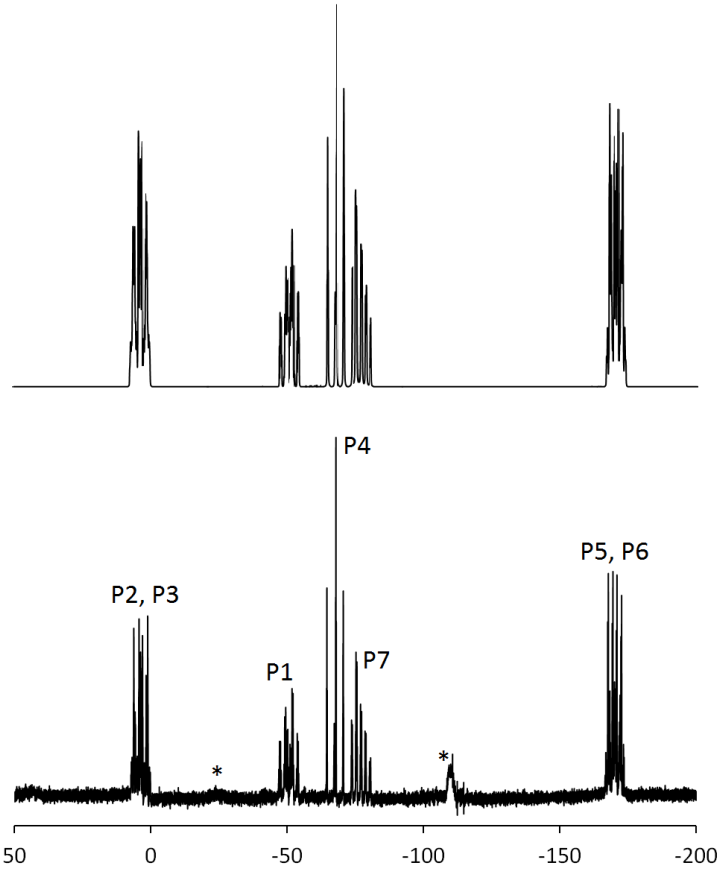

Figure 2.25: Top: The simulated ^{31}P NMR spectrum of **6**. Bottom: The $^{31}P\{^1H\}$ NMR spectrum of **6** recorded in d_5-pyridine. Resonances labelled * correspond to an HP_7^{2-} impurity.

Table 2.6: The ^{31}P chemical shift values and coupling constants for $[P_7InPh_2]^{2-}$.

δ (ppm)		–50.7 P1	3.6 P2	3.6 P3	–67.8 P4	–170.0 P5	–170.0 P6	–76.8 P7
–50.7	P1		–208	–257	–341	27	25	60
3.6	P2	–208		–30	–20	–366	–	–10
3.6	P3	–257	–30		–20	–	–410	–10
–67.8	P4	–341	–20	–20		–	–	–402
–170.0	P5	27	–366	–	–		–162	–221
–170.0	P6	25	–	–410	–	–162		–205
–76.8	P7	60	–10	–10	–402	–221	–205	

2.5.5 $^{13}C\{^1H\}$ NMR spectroscopic studies on $[P_7InPh_2]^{2-}$ (6) and $[As_7InPh_2]^{2-}$ (7)

The aromatic region of the $^{13}C\{^1H\}$ NMR spectrum of **6** shows seven separate resonances, which can be attributed to the eight different C environments (Figure 2.26). The two very weak resonances at 164.9 and 159.9 ppm can be assigned to the two different *ipso*-environments, those at 140.3 and 139.9 ppm are due to the two different *ortho*-environments, and the resonances at 127.6 and 127.1 ppm correspond to the two different *meta*-environments. The resonance at 126.0 ppm is a result of the resonances corresponding to the two different *para*-environments overlapping with each other.

The aromatic region of the $^{13}C\{^1H\}$ NMR spectrum of **7** shows eight separate resonances, which can be assigned to the eight different C environments (Figure 2.27). The spectrum is very similar to the $^{13}C\{^1H\}$ NMR spectrum of **6**, and the resonances can be assigned in a similar way. The two very weak resonances at 167.9 and 161.3 ppm correspond to the two different *ipso*-environments, the resonances at 139.9 and 139.6 ppm can be assigned to the two different *ortho*-environments, and the resonances at 127.6 and 126.9 ppm correspond to the two different *meta*-environments. The two overlapping resonances at 125.9 and 125.8 ppm are due to the two different *para*-environments.

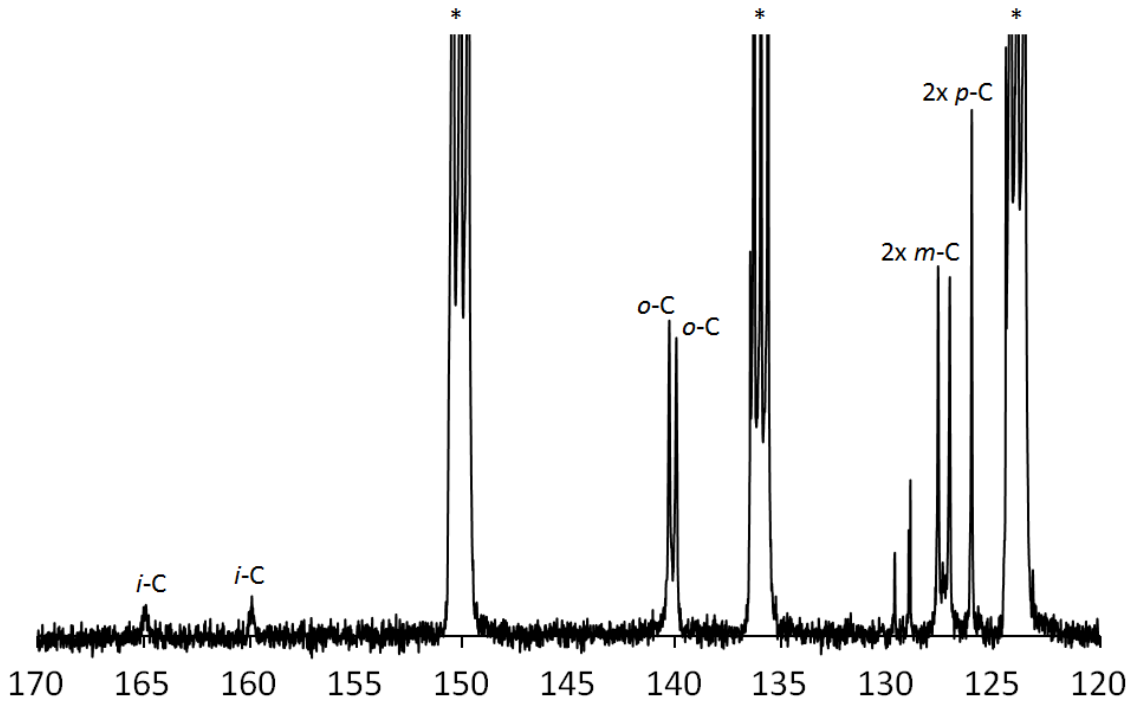

Figure 2.26: Close-up of the aromatic region of the $^{13}C\{^1H\}$ NMR spectrum of **6**. Resonances labelled * correspond to d_5-pyridine.

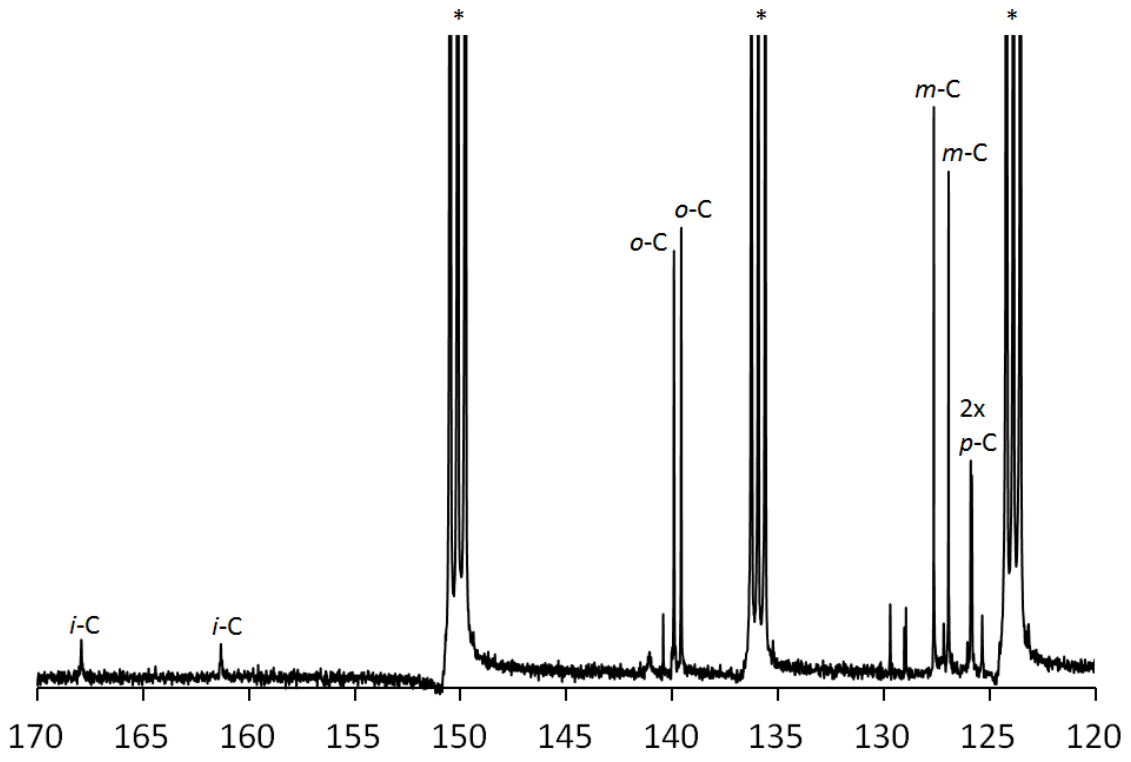

Figure 2.27: Close-up of the aromatic region of the $^{13}C\{^1H\}$ NMR spectrum of **7**. Resonances labelled * correspond to d_5-pyridine.

2.5.6 Mass spectrometric studies

Both the positive and negative ion mode electrospray ionisation mass spectra of **6** and **7** confirm that the products are $[P_7InPh_2]^{2-}$ and $[As_7InPh_2]^{2-}$, respectively. The negative ion mode mass spectra contain peaks due to the oxidised cluster anions, $[E_7InPh_2]^-$, as well as peaks due to the cluster anions accompanied by K^+ and $[K(2,2,2\text{-crypt})]^+$ charge-balancing cations. The major peaks in the positive ion mode spectra are due to the cluster anions with three $[K(2,2,2\text{-crypt})]^+$ ions (Figures 2.28 and 2.29).

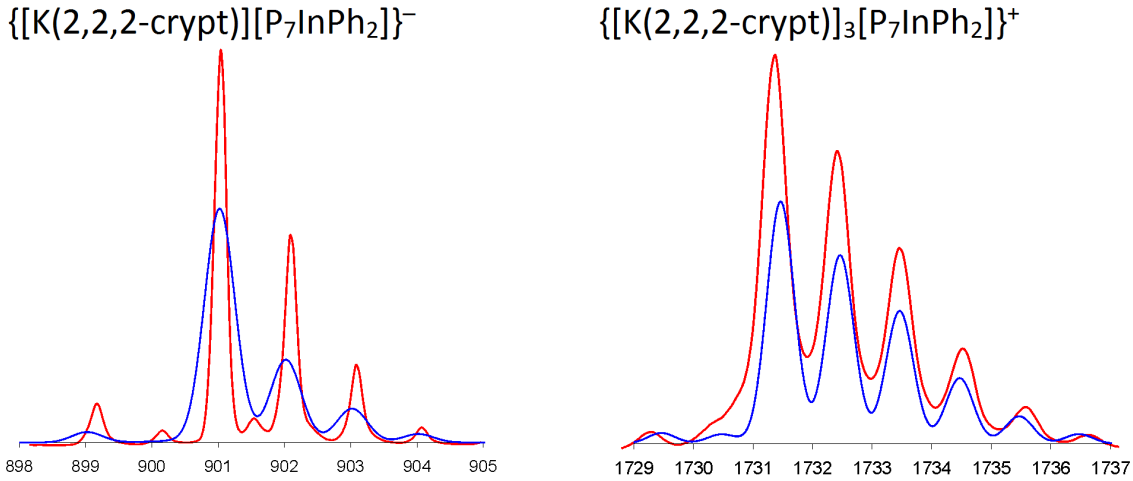

Figure 2.28: ESI-MS mass envelopes for $\{[K(2,2,2\text{-crypt})][P_7InPh_2]\}^-$ and $\{[K(2,2,2\text{-crypt})]_3[P_7InPh_2]\}^+$. Predicted isotopic distributions are shown in blue and observed mass spectrometric data are shown in red.

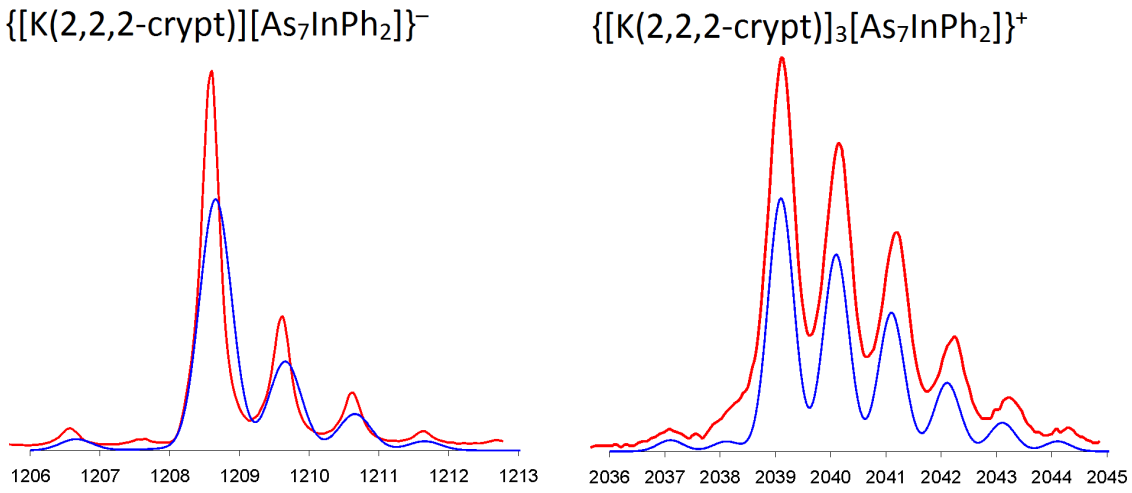

Figure 2.29: ESI-MS mass envelopes for$\{[K(2,2,2\text{-crypt})][As_7InPh_2]\}^-$ and $\{[K(2,2,2\text{-crypt})]_3[As_7InPh_2]\}^+$. Predicted isotopic distributions are shown in blue and observed mass spectrometric data are shown in red.

2.6 Conclusions

This chapter has described the synthesis and characterisation of seven previously unknown compounds of group 15 Zintl ions. The reactions of P_7^{3-} and As_7^{3-} with $[Cu_5(mes)_5]$ yielded the Cu–Cu bridged species $[Cu_2(P_7)_2]^{4-}$ (**1**) and $[Cu_2(As_7)_2]^{4-}$ (**2**). Crystals of [K(2,2,2-crypt)]$_4$[**1**] suitable for single crystal X-ray diffraction could not be produced, but the identity of this species has been confirmed by $^{31}P\{^1H\}$ NMR spectroscopy and mass spectrometry. **2** has been characterised by single crystal X-ray diffraction and mass spectrometry.

P_7^{3-} and As_7^{3-} have also been found to react with the group 12 organometallics MPh_2 (M = Zn, Cd) to form the metal-bridged dimers $[Zn(P_7)_2]^{4-}$ (**3**), $[Zn(As_7)_2]^{4-}$ (**4**) and $[Cd(P_7)_2]^{4-}$ (**5**). **3** and **5** have both been fully characterised by single crystal X-ray diffraction, $^{31}P\{^1H\}$ NMR spectroscopy and mass spectrometry. The crystal structure of [K(2,2,2-crypt)]$_4$[**4**] was found to be heavily disordered, however the identity of the product was confirmed by mass spectrometry.

In addition, the reactions of P_7^{3-} and As_7^{3-} with $InPh_3$ produced the In-functionalised Zintl ions $[P_7InPh_2]^{2-}$ (**6**) and $[As_7InPh_2]^{2-}$ (**7**). **6** has been fully characterised by single crystal X-ray diffraction, multi-element NMR spectroscopy and mass spectrometry. Crystals of [K(2,2,2-crypt)]$_2$[**7**] could not be produced, however the presence of $[As_7InPh_2]^{2-}$ was confirmed by multi-element NMR spectroscopy and mass spectrometry.

2.7 References

1. Huheey, J. E.; Keiter, E. A.; Keiter, R L. *Inorganic Chemistry: Principles of Structure and Reactivity*; HarperCollins: New York, 1993.
2. Moses, M. J.; Fettinger, J.; Eichhorn, B. *J. Am. Chem. Soc.* **2002**, *124,* 5944–5945.
3. Reber, A. C.; Mandal, S.; Qian, M.; Saavedra, H. M.; Weiss, P. S.; Khanna, S. N.; Sen, A. *J. Phys. Chem. C* **2012**, *116,* 10207–10214.
4. Kesanli, B.; Fettinger, J.; Scott, B.; Eichhorn, B. *Inorg. Chem.* **2004**, *43,* 3840–3846.
5. Eichhorn, B. W.; Mattamana, S. P.; Gardner, D. R.; Fettinger, J. C. *J. Am. Chem. Soc.* **1998**, *120,* 9708–9709.
6. Kesanli, B.; Fettinger, J.; Eichhorn, B. *J. Am. Chem. Soc.* **2003**, *125,* 7367–7376.
7. Moses, M. J.; Fettinger, J. C.; Eichhorn, B. W. *Science* **2003**, *300,* 778–780.

8. Moses, M. J.; Fettinger, J. C.; Eichhorn, B. W. *Inorg. Chem.* **2007**, *46,* 1036–1038.
9. Scharfe, S.; Fässler, T. F.; Stegmaier, S.; Hoffmann, S. D.; Ruhland, K. *Chem. Eur. J.* **2008**, *14,* 4479–4483.
10. Goicoechea, J. M.; Sevov, S. C. *Organometallics* **2006**, *25,* 4530–4536.
11. Zhou, B.; Denning, M. S.; Jones, C.; Goicoechea, J. M. *Dalton Trans.* **2009**, 1571–1578.
12. Zhou, B.; Denning, M. S.; Chapman, T. A. D.; Goicoechea, J. M. *Inorg. Chem.* **2009**, *48,* 2899–2907.
13. Hansen, D. F.; Zhou, B.; Goicoechea, J. M. *J. Organomet. Chem.* **2012**, *721–722,* 53–61.
14. Ugrinov, A.; Sevov, S. C. *J. Am. Chem. Soc.* **2003**, *125,* 14059–14064.
15. Knapp, C.; Zhou, B.; Denning, M. S.; Rees, N. H.; Goicoechea, J. M. *Dalton Trans.* **2010**, *39,* 426–436.
16. Eichhorn, B. W.; Haushalter, R. C.; Huffman, J. C. *Angew. Chem., Int. Ed. Engl.* **1989**, *28,* 1032–1033.
17. Charles, S.; Eichhorn, B. W.; Rheingold, A. L.; Bott, S. G. *J. Am. Chem. Soc.* **1994**, *116,* 8077–8086.
18. Bolle, U.; Tremel, W. *J. Chem. Soc., Chem. Commun.* **1994**, 217–219.
19. Besinger, J.; Fenske, D. *Z. Anorg. Allg. Chem.* **2001**, *627,* 1487–1494.
20. Values taken from CSD version 5.33 (2012).
21. Pyykkö, P.; Atsumi, M. *Chem. Eur. J.* **2009**, *15,* 186–197.
22. Meyer, E. M.; Gambarotta, S.; Floriani, C.; Chiesivilla, A.; Guastini, C. *Organometallics* **1989**, *8,* 1067–1079.
23. Turbervill, R. S. P.; Goicoechea, J. M. *Organometallics* **2012**, *31,* 2452–2462.
24. Qian, M.; Reber, A. C.; Ugrinov, A.; Chaki, N. K.; Mandal, S.; Saavedra, H. M.; Khanna, S. N.; Sen, A.; Weiss, P. S. *ACS Nano* **2010**, *4,* 235–240.
25. Mandal, S.; Reber, A. C.; Qian, M.; Liu, R.; Saavedra, H. M.; Sen, S.; Weiss, P. S.; Khanna, S. N.; Sen, A. *Dalton Trans.* **2012**, *41,* 12365–12377.
26. Mandal, S.; Reber, A. C.; Qian, M.; Liu, R.; Saavedra, H. M.; Sen, S.; Weiss, P. S.; Khanna, S. N.; Sen, A. *Dalton Trans.* **2012**, *41,* 5454–5457.
27. Von Schnering, H. G.; Manriquez, V.; Hönle, W. *Angew. Chem., Int. Ed. Engl.* **1981**, *20,* 594–595.
28. Charles, S.; Fettinger, J. C.; Eichhorn, B. W. *Inorg. Chem.* **1996**, *35,* 1540–1548.
29. Charles, S.; Fettinger, J. C.; Bott, S. G.; Eichhorn, B. W. *J. Am. Chem. Soc.* **1996**, *118,* 4713–4714.
30. Kesanli, B.; Charles, S.; Lam, Y. F.; Bott, S. G.; Fettinger, J.; Eichhorn, B. *J. Am. Chem. Soc* **2000**, *122,* 11101–11107.
31. Pfistner, H.; Fenske, D. *Z. Anorg. Allg. Chem.* **2001**, *627,* 575–582.
32. Beswick, M. A.; Raithby, P. R.; Russell, C. A.; Steiner, A.; Verhorevoort, K. L.; Ward, G. N.; Wright, D. S. *Angew. Chem., Int. Ed. Engl.* **1996**, *34,* 2662–2664.

33. Baudler, M. *Angew. Chem., Int. Ed. Engl.* **1982**, *21,* 492–512.

34. Charles, S.; Fettinger, J. C.; Eichhorn, B. W. *J. Am. Chem. Soc.* **1995**, *117,* 5303–5311.

35. Von Hänisch, C.; Fenske, D.; Kattannek, M.; Ahlrichs, R. *Angew. Chem., Int. Ed.* **1999**, *38,* 2736–2738.

36. Dai, F. R.; Xu, L. *Inorg. Chim. Acta* **2006**, *359,* 4265–4273.

Chapter 3 Salt metathesis reactions of E_7^{3-}

3.1 Introduction

The reactivity of P_7^{3-} towards alkyl salts and tetraalkylammonium salts has been extensively studied by a number of research groups, most notably those of Von Schnering, Fritz and Eichhorn. As_7^{3-} reacts with these compounds in the same way, however there are fewer examples in the literature. These reactions result in functionalisation of the E_7^{3-} clusters by either two or three alkyl groups, depending on the ratio of cluster to alkyl salt employed. Similar functionalisation reactions have also been found to occur with a number of group 14 and group 15 halides, and with $[FeCp(CO)_2Br]$.

A series of dialkylated $R_2E_7^-$ species (E = P: R = Me, Et, ^{i}Pr, Bu, ^{i}Bu, $PhCH_2$, $EtOCOCH_2$, EtOCOCHMe; E = As: R = $PhCH_2$) have been synthesised.[1–3] As discussed in more detail in Chapter 1, three possible isomers of $R_2P_7^-$ can be formed. Single crystal X-ray diffraction and ^{31}P NMR studies showed that the isomer obtained is symmetrical (Figure 3.1).

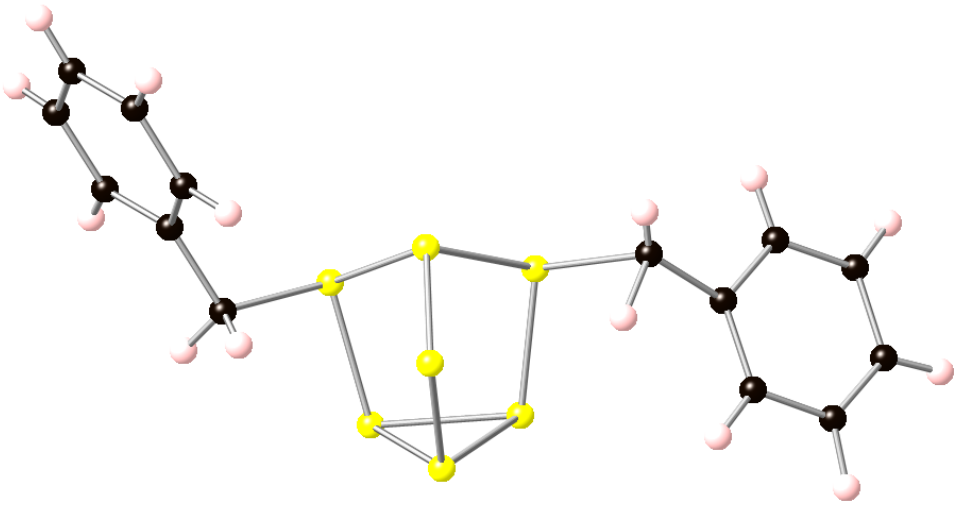

Figure 3.1: Ball and stick diagram of $(PhCH_2)_2P_7^-$. P atoms are shown in yellow, C atoms are shown in black and H atoms are shown in pink.

There are a number of previously reported examples of neutral trialkylated clusters, P_7R_3 (R = Me, Et, ^{i}Pr, Bu, ^{i}Bu, 3-C_5H_{11}, C_6H_{13}).[3–6] In this case, the product can be one of two possible isomers, an asymmetric or a symmetric isomer, and the ^{31}P NMR spectra indicate that a mixture of the two is formed (see Introduction for more details). The ratio of asymmetric isomer to symmetric isomer depends on the size of the alkyl substituents, with bulkier substituents favouring the formation of the less sterically hindered symmetric isomer. In addition, a variety of group 14- and group 15-substituted compounds, $E_7(E'R_3)_3$ (E = P: $E'R_3$ = SiH_3, SiH_2Me, $SiMe_3$, $SiMe_2PEt_2$, $SiPh_3$, $GeMe_3$, $SnMe_3$; E = As: $E'R_3$ = $SiMe_3$) and $P_7(E^tBu_2)_3$ (E = P, Sb), have been isolated.[5–8] The ^{31}P NMR spectra of $P_7(E'R_3)_3$ and $P_7(E^tBu_2)_3$ show that only the symmetric isomer is produced. An analogous metallation reaction resulted in the formation of $P_7(FeCp(CO)_2)_3$.[9] This compound is analogous to the alkylated and group 14- and 15-substituted compounds and, as for the latter species, ^{31}P NMR data indicate that only the symmetric isomer is formed. This is because the $FeCp(CO)_2$ groups are extremely bulky and favour the formation of the less sterically hindered symmetric isomer over the asymmetric isomer (Figure 3.2).

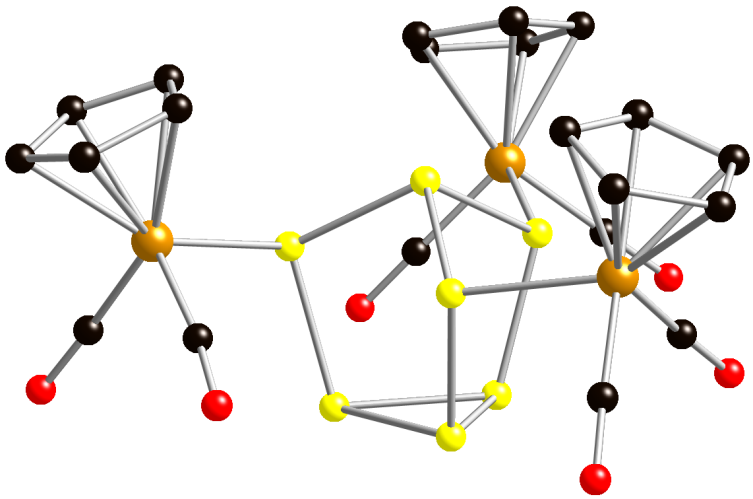

Figure 3.2: Ball and stick diagram of $P_7(FeCp(CO)_2)_3$. P atoms are shown in yellow, Fe atoms are shown in brown, C atoms are shown in black and O atoms are shown in red. H atoms are omitted for clarity.

3.2 Objectives

Prior to 2009, the vast majority of salt metathesis reactions of group 15 Zintl ions were limited to alkyl salts and their heavier group 14 analogues. Only one reaction of E_7^{3-} with a metal salt

had been reported, namely that of P_7^{3-} with $[FeCp(CO)_2Br]$.[9] In contrast, the reactivity of E_7^{3-} towards organometallic reagents had been extensively studied.[10]

In this chapter, the reactivity of E_7^{3-} (E = P, As) towards the metal salts $[M(nbe)_3][SbF_6]$ and MCl (M = Ag, Au), $InCl_3$, TlCl, and MI_2 (M = Sn, Pb) will be described. P_7^{3-} reacts with both $[M(nbe)_3][SbF_6]$ and MCl to form the M–M bridged species $[M_2(HP_7)_2]^{2-}$ (M = Ag, Au).[11] Reactions of E_7^{3-} with the group 13 salts $InCl_3$ and TlCl resulted in the formation of $[In(E_7)_2]^{3-}$ and $[TlE_7]^{2-}$, respectively. In addition, both P_7^{3-} and As_7^{3-} react with MI_2 to produce the sixteen-vertex cluster anions $[ME_{15}]^{3-}$ (M = Sn, Pb; E = P, As).[12]

3.3 Solution reactivity of P_7^{3-} towards $[M(nbe)_3][SbF_6]$ and MCl (M = Ag, Au)

3.3.1 Synthesis of $[Ag_2(HP_7)_2]^{2-}$ (8) and $[Au_2(HP_7)_2]^{2-}$ (9)

K_3P_7 was found to react with $[M(nbe)_3][SbF_6]$ (M = Ag, Au) in ethylenediamine in the presence of 2,2,2-crypt to form $[K(2,2,2\text{-crypt})]_2[M_2(HP_7)_2]$ (M = Ag, Au) (Scheme 3.1). These compounds contain the M–M bridged species $[Ag_2(HP_7)_2]^{2-}$ (**8**) and $[Au_2(HP_7)_2]^{2-}$ (**9**). The protons are thought to originate from adventitious moisture present in either the ethylenediamine solvent or the 2,2,2-crypt sequestering agent. Crystals of $[K(2,2,2\text{-crypt})]_2$[**8**] and $[K(2,2,2\text{-crypt})]_2$[**9**] suitable for single crystal X-ray diffraction were obtained from ethylenediamine solutions layered with toluene. It was later discovered that yields of **8** and **9** could be improved by replacing $[M(nbe)_3][SbF_6]$ with MCl (M = Ag, Au) and by adding the proton source $[NH_4][BPh_4]$ to the reaction mixture.

$$2P_7^{3-} + 2H^+ + 2MX \longrightarrow [M_2(HP_7)_2]^{2-} + 2X^-$$

Scheme 3.1: The formation of $[M_2(HP_7)_2]^{2-}$ from P_7^{3-} and $[M(nbe)_3][SbF_6]$ or MCl.

At the same time as we reported our findings, Weiss, Sen and co-workers described the synthesis of $[Au_2(As_7)_2]^{4-}$ by reacting K_3As_7 with $[Au(PPh_3)Cl]$.[13,14] This cluster anion was crystallographically characterised in $[K(2,2,2\text{-crypt})]_4[Au_2(As_7)_2]$ and consists of two nortricyclane-like As_7^{3-} cages bridged by a Au_2^{2+} dimetallic centre (Figure 3.3). Each As_7^{3-} is

bonded to both Au atoms in an η^1-fashion, and there is also a bonding interaction between the two Au atoms.

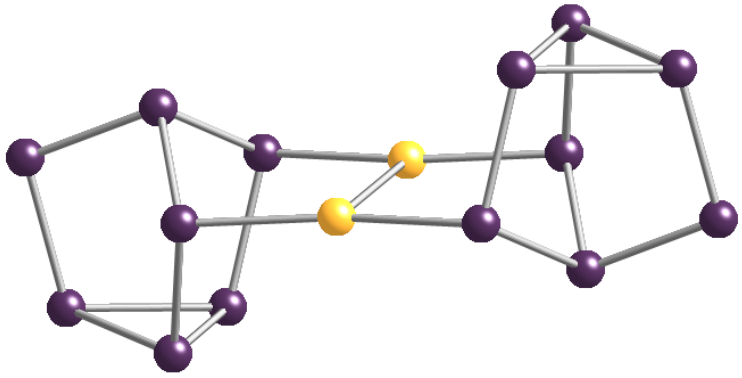

Figure 3.3: Ball and stick diagram of $[Au_2(As_7)_2]^{4-}$ as reported by Weiss, Sen and co-workers. Au atoms are shown in gold and As atoms are shown in purple.

3.3.2 Structures of $[M_2(HP_7)_2]^{2-}$ (8 and 9)

Both **8** and **9** consist of two nortricyclane-like HP_7^{2-} cages bridged by a M_2^{2+} dimetallic centre (Figures 3.4 and 3.5). Each metal atom is bound by both HP_7^{2-} clusters in an η^1-fashion. There is also a bonding interaction between the two metal atoms, giving each metal atom a "T-shaped" coordination environment. **8** and **9** are very similar to the $[Au_2(As_7)_2]^{4-}$ cluster anion reported by Weiss and Sen, differing only in their charge and the presence of two protons. [13,14] Both **8** and **9** possess a centre of inversion in the centre of the M–M bond, which renders the two HP_7^{2-} cages crystallographically equivalent.

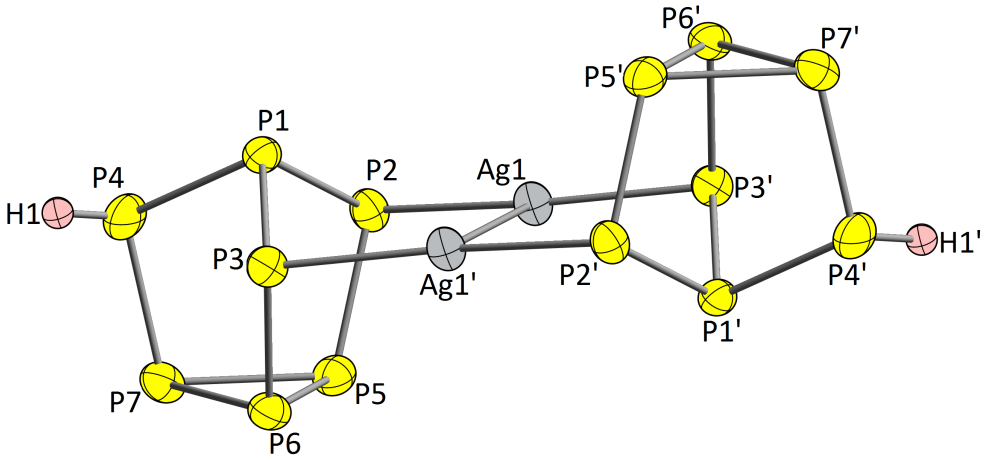

Figure 3.4: Thermal ellipsoid plot of **8** with anisotropic displacement ellipsoids pictured at 50% probability. H atoms are shown as small spheres of arbitrary radii.

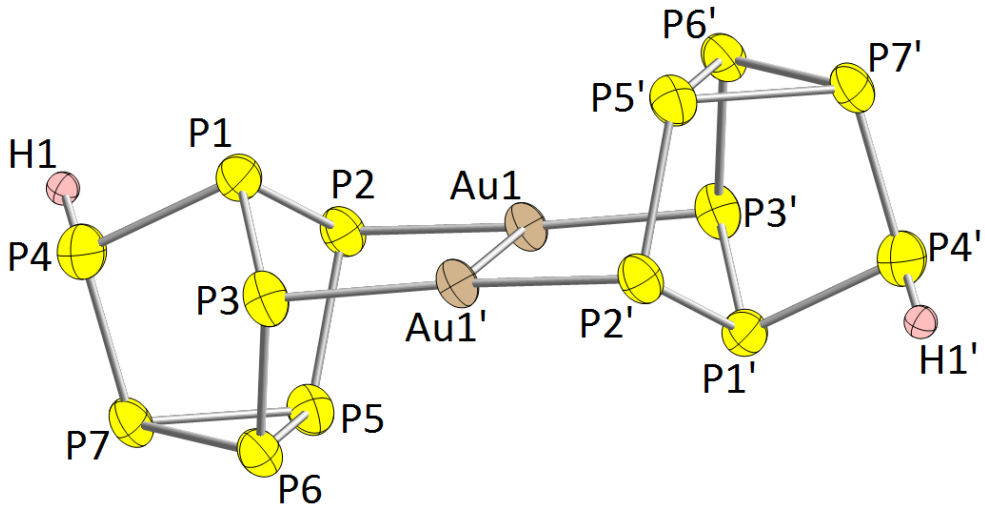

Figure 3.5: Thermal ellipsoid plot of **9** with anisotropic displacement ellipsoids pictured at 50% probability. H atoms are shown as small spheres of arbitrary radii.

8 and **9** are also closely related to the previously reported P_{16}^{2-} species, which consists of two P_7 cages bridged by two further P atoms (Figure 3.6).[15] There are, however, two major differences between this cluster anion and **8** and **9**. Firstly, the structure of P_{16}^{2-} is "bent" along the two bridging P atoms, while the bridging M atoms and the P atoms to which they are bonded are coplanar in **8** and **9**. Secondly, the apical P1 atoms of the P_7 units point in the same direction (an "up-up" isomer) in P_{16}^{2-}, while in the case of **8** and **9**, the P1 atoms point in opposite directions ("up-down" isomers). DFT calculations have shown that there is very little energy difference between the "up-down" and "up-up" isomers for **8** and **9** (0.4 kJ mol^{-1} for **8**; 2.4 kJ mol^{-1} for **9**). These findings suggest that formation of the "up-down" isomers in **8** and **9** is, in all likelihood, due to crystal packing influences.

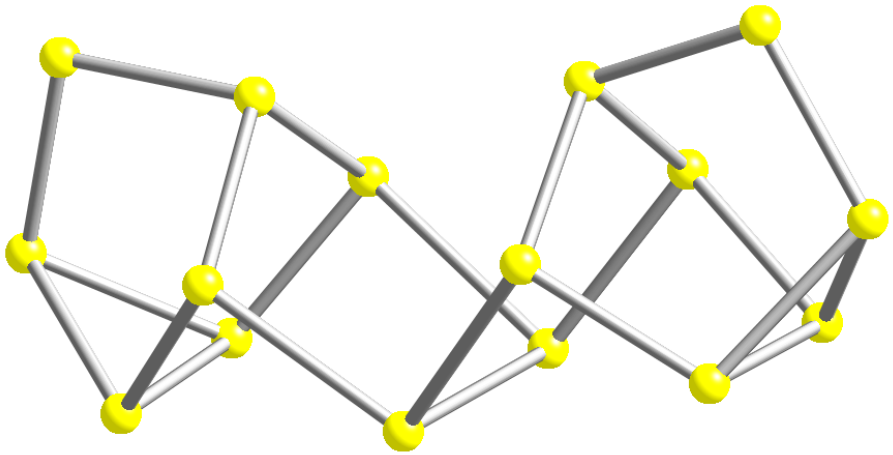

Figure 3.6: Ball and stick diagram of P_{16}^{2-}.

The positions of the protons in **8** and **9** were determined by studying the residual electron

densities in the asymmetric units of the crystal structures after all non-hydrogen atomic positions had been determined and refined anisotropically and initial hydrogen positions of the $[K(2,2,2\text{-crypt})]^+$ cations had been determined. Some of the largest residual Q peaks were observed close to the P4 atoms in chemically viable positions. The atomic coordinates and isotropic temperature factors of the hydrogen atoms in the cluster anion were freely refined, and the fit of the model to the data improved on inclusion of the protons. The final proton positions were consistent with a trigonal pyramidal coordination environment at the P4 atoms. This was found to be the case for both **8** and **9**.

Selected bond lengths for **8** and **9** are provided in Table 3.1, along with selected bond distances for the optimised structures of **8** and **9**. The P–P bond lengths are in the ranges 2.164(1) Å – 2.237(1) Å for **8** and 2.175(3) Å – 2.224(3) Å for **9**. These are similar to the P–P bond lengths in the previously reported $[P_7PtH(PPh_3)]^{2-}$ species, which also features a nortricyclane-like P_7^{3-} cluster (2.14(2) Å – 2.26(2) Å).[16] The Ag–P bonds in **8** of 2.411(1) Å and 2.415(1) Å are slightly shorter than the mean Ag–P bond distance obtained from a search of the CSD (2.449(av) Å), however they are in good agreement with the values observed for similar Ag(I)/P complexes such as $[Ag_2(dcpm)_2][OTf]_2$ (2.407(2) Å and 2.415(2) Å; dcpm = bis(dicyclohexylphosphino)methane).[17,18] The sum of covalent radii for Ag–P single bonds is 2.39 Å.[19] The Au–P bonds in **9** of 2.357(2) Å and 2.349(2) Å are longer than the mean Au–P bond distance obtained from a search of the CSD (2.285(av) Å) but are in good agreement with the Au–P bond lengths in $[Au_2(nixantphos)_2][NO_3]_2$ (2.332(3) Å and 2.347(2) Å; nixantphos = 4,6-bis(diphenylphosphino)phenoxazine).[17,20] The sum of covalent radii of Au–P single bonds is 2.35 Å.[19] The Ag–Ag and Au–Au distances in **8** and **9** of 2.947(1) Å and 3.047(1) Å, respectively, are indicative of metallophilic interactions. Theoretical considerations suggest that relativistic effects and *s*–*d* hybridisation should strengthen the Au–Au interaction in **9** relative to the Ag–Ag interaction in **8**, therefore the shorter M–M distance in **8** is unexpected.[21] This has been previously observed for a series of $[M(NH_3)_2]^+$ salts (M = Ag, Au), in which the M–M distances of the Au species are longer than those of the Ag species.[22] Computational studies by O'Grady and Kaltsoyannis showed that, in certain situations, Ag–Ag interactions may be stronger than Au–Au interactions for the same ligand environment.[23] A search of the CSD gave mean Ag–Ag and Au–Au distances of 3.048(av) Å

and 2.936(av) Å, respectively, while the sums of covalent radii for Ag–Ag and Au–Au single bonds are 2.56 Å and 2.48 Å, respectively.[17,19]

Table 3.1: Selected bond lengths for the $[Ag_2(HP_7)_2]^{2-}$ and $[Au_2(HP_7)_2]^{2-}$ species.

Bond	Experimental bond length in **8** (Å)	Calculated bond length in $\mathbf{8_{DFT}}$ (Å)	Experimental bond length in **9** (Å)	Calculated bond length in $\mathbf{9_{DFT}}$ (Å)
P1–P2	2.177(1)	2.217	2.184(3)	2.215
P1–P3	2.176(1)	2.209	2.175(3)	2.223
P1–P4	2.181(1)	2.230	2.185(3)	2.224
P2–P5	2.174(1)	2.212	2.177(3)	2.211
P3–P6	2.164(1)	2.196	2.175(3)	2.227
P4–P7	2.195(1)	2.241	2.183(3)	2.250
P5–P6	2.236(1)	2.276	2.224(3)	2.270
P5–P7	2.237(1)	2.266	2.220(3)	2.260
P6–P7	2.230(1)	2.269	2.217(3)	2.259
M1–P2	2.411(1)	2.438	2.357(2)	2.389
M1–P3	2.415(1)	2.440	2.349(2)	2.383
M1–M1′	2.947(1)	3.057	3.047(1)	3.238

3.3.3 ^{31}P NMR spectroscopic studies on $[Ag_2(HP_7)_2]^{2-}$ (8) and $[Au_2(HP_7)_2]^{2-}$ (9)

Characterisation of **8** and **9** by ^{31}P NMR spectroscopy proved extremely difficult due to the very high sensitivity of the cluster anions towards air, moisture and light. The ^{31}P NMR spectra show evidence of cluster decomposition and formation of P_{16}^{2-} and PH_3, however the spectra also consistently show seven weak resonances that do not correspond to known polyphosphide cluster anions, and which are consistent with the cluster geometries.[24,25] For **8**, these resonances appear at 17.9, 8.0, –33.7, –41.5, –86.6, –197.0 and –212.3 ppm. Two of these resonances overlap with those of the P_{16}^{2-} cluster anion. The ^{31}P NMR spectrum of **9** shows seven resonances at 83.8, 50.5, –22.4, –92.0, –154.9, –213.1 and –228.7 ppm.

3.3.4 Mass spectrometric studies

The ESI mass spectra of **8** and **9** confirm that the products are $[Ag_2(HP_7)_2]^{2-}$ and $[Au_2(HP_7)_2]^{2-}$, respectively. The negative ion mode mass spectra show peaks corresponding to the oxidised cluster anions, $[M_2(HP_7)_2]^-$, as well as peaks due to the cluster anions paired with K^+ and $[K(2,2,2\text{-crypt})]^+$ cations. The major peaks in the positive ion mode mass spectra correspond

to the cluster anions accompanied by three $[K(2,2,2\text{-crypt})]^+$ ions (Figures 3.7 and 3.8).

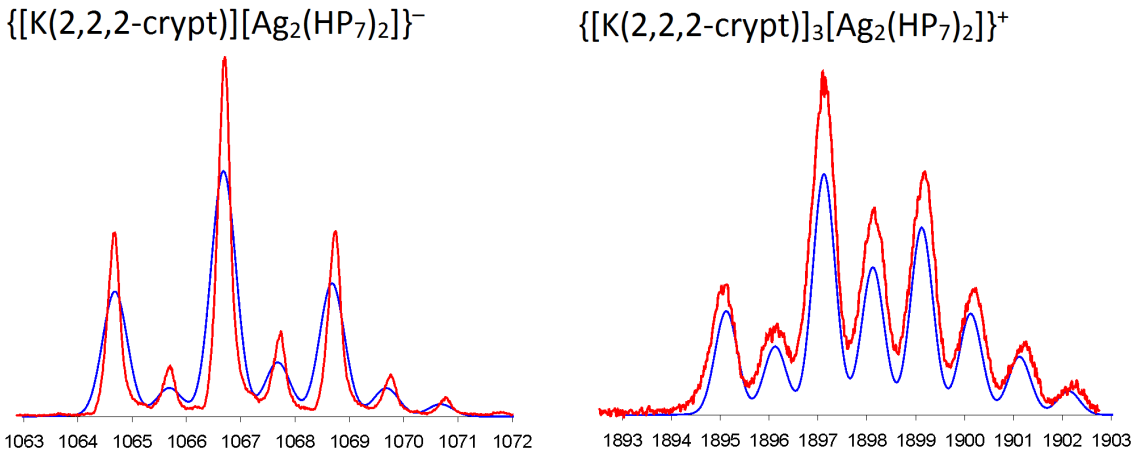

Figure 3.7: ESI-MS mass envelopes for $\{[K(2,2,2\text{-crypt})][Ag_2(HP_7)_2]\}^-$ and $\{[K(2,2,2\text{-crypt})]_3[Ag_2(HP_7)_2]\}^+$. Predicted isotopic distributions are shown in blue and observed mass spectrometric data are shown in red.

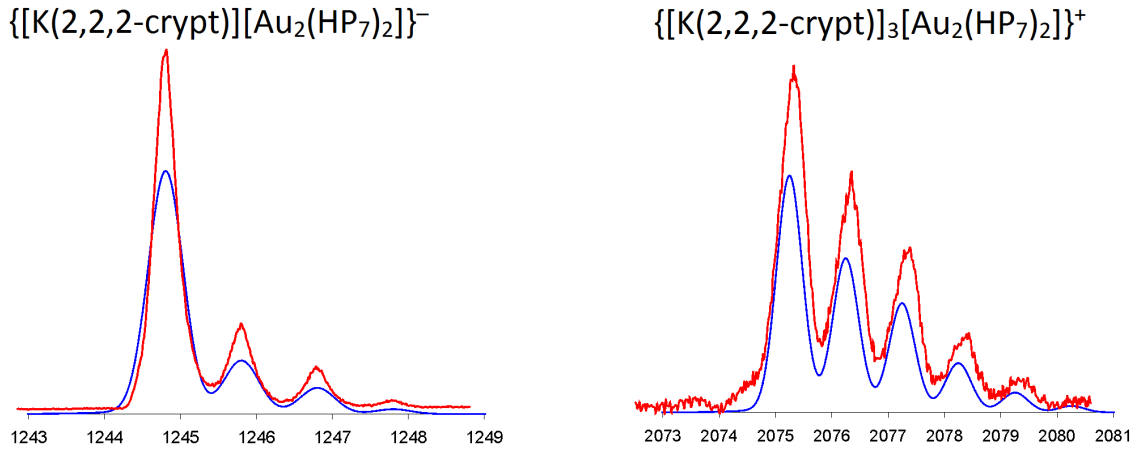

Figure 3.8: ESI-MS mass envelopes for $\{[K(2,2,2\text{-crypt})][Au_2(HP_7)_2]\}^-$ and $\{[K(2,2,2\text{-crypt})]_3[Au_2(HP_7)_2]\}^+$. Predicted isotopic distributions are shown in blue and observed mass spectrometric data are shown in red.

3.4 Solution reactivity of group 15 Zintl ions towards $InCl_3$

3.4.1 Synthesis of $[In(P_7)_2]^{3-}$ (10) and $[In(As_7)_2]^{3-}$ (11)

Ethylenediamine solutions of K_3P_7 and K_3As_7 react with 0.5 equivalents of $InCl_3$ in the presence of 2,2,2-crypt to form the compounds $[K(2,2,2\text{-crypt})]_3[In(E_7)_2]$ (E = P, As) (Scheme 3.2). These compounds contain the In-bridged cluster anions $[In(P_7)_2]^{3-}$ (**10**) and $[In(As_7)_2]^{3-}$ (**11**). Crystals of $[K(2,2,2\text{-crypt})]_3$[**10**]·3.5py suitable for single crystal X-ray diffraction were obtained from a pyridine solution layered with toluene. Crystals of $[K(2,2,2\text{-crypt})]_3$[**11**] could

not be obtained, however the identity of the product was confirmed by mass spectrometry.

$$2E_7^{3-} + InCl_3 \longrightarrow [In(E_7)_2]^{3-} + 3Cl^-$$

Scheme 3.2: The formation of $[In(E_7)_2]^{3-}$ from E_7^{3-} and $InCl_3$.

3.4.2 Structure of $[In(P_7)_2]^{3-}$ (10)

The X-ray structure of [K(2,2,2-crypt)]$_3$[**10**]·3.5py contains two crystallographically unique $[In(P_7)_2]^{3-}$ clusters in the asymmetric unit. Each cluster anion comprises two nortricyclane-like P_7^{3-} cages bridged by an In atom. Both P_7^{3-} groups are bonded to the metal centre in an η^2-fashion, resulting in a distorted tetrahedral coordination geometry (Figure 3.9). Each η^2-cluster acts as a four-electron donor, and the In is formally in the +3 oxidation state, therefore the total valence electron count of the central atom is eight electrons. **10** is isoelectronic to the $[M(P_7)_2]^{4-}$ ions (M = Zn, Cd) discussed in Chapter 2, and is also very similar to the previously reported $[P_7M(CO)_4]^{3-}$ (M = Mo, W) and $[E_7PtH(PPh_3)]^{2-}$ (E = P, As) ions, in which the E_7^{3-} cages are also bonded to the metal centre in an η^2-fashion.[16,26,27]

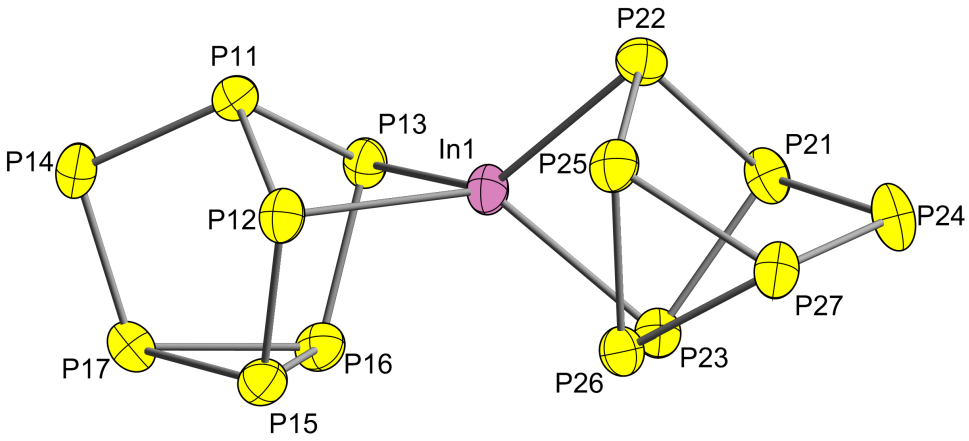

Figure 3.9: Thermal ellipsoid plot of one of the two crystallographically unique $[In(P_7)_2]^{3-}$ ions present in [K(2,2,2-crypt)]$_3$[**10**]·3.5py. Anisotropic displacement ellipoids are pictured at 50% probability.

DFT calculations were carried out in order to investigate the electronic structure of **10**. A geometry optimisation was performed, employing a continuum dielectric to model the presence of the cations in the crystal lattice. A pseudo-tetrahedral coordination geometry around the central In atom allows for a strong σ bonding interaction between the In *s* orbital and the lone pairs on P12, P13, P22 and P23 (HOMO–23). The corresponding anti-bonding

orbital is the LUMO. The In *p* orbitals can also interact with the σ orbitals on P12, P13, P22 and P23, giving rise to three bonding orbitals (HOMO–22, HOMO–14 and HOMO–13). The HOMO and HOMO–1 were found to be mainly composed of lone pair character for P14 and P24. DFT calculations showed that there is a slightly positive Mulliken spin density on the In centre (0.3857), with negative spin densities on all of the P atoms. The most negative spin density values were obtained for the formally anionic P atoms, P14 (–0.5166) and P24 (–0.5156). Both Hirschfield and Natural Population analyses revealed similar charge distributions.

Table 3.2: Selected bond lengths and bond angles for the $[In(P_7)_2]^{3-}$ species.

Bond	Experimental bond length in **10** (Å)	Calculated bond length in $\mathbf{10_{DFT}}$ (Å)
P11–P12	2.228(1)	2.258
P11–P13	2.215(1)	2.256
P11–P14	2.147(1)	2.177
P12–P15	2.173(1)	2.204
P13–P16	2.183(1)	2.203
P14–P17	2.133(1)	2.171
P15–P16	2.269(1)	2.318
P15–P17	2.240(1)	2.277
P16–P17	2.238(1)	2.277
P21–P22	2.225(1)	2.256
P21–P23	2.201(1)	2.258
P21–P24	2.145(1)	2.177
P22–P25	2.176(1)	2.204
P23–P26	2.177(1)	2.203
P24–P27	2.141(1)	2.171
P25–P26	2.269(1)	2.317
P25–P27	2.235(1)	2.277
P26–P27	2.231(1)	2.278
In1–P12	2.585(1)	2.644
In1–P13	2.592(1)	2.654
In1–P22	2.618(1)	2.653
In1–P23	2.571(1)	2.644
Angle	Experimental bond angle in **10** (°)	Calculated bond angle in $\mathbf{10_{DFT}}$ (°)
P12–In1–P13	80.12(2)	79.34
P12–In1–P22	120.55(3)	126.89
P12–In1–P23	127.25(3)	124.70
P13–In1–P22	134.07(3)	127.38
P13–In1–P23	122.53(3)	126.33
P22–In1–P23	79.53(3)	79.35

Selected bond distances and angles for one of the two crystallographically unique $[In(P_7)_2]^{3-}$ ions are provided in Table 3.2, along with selected bond distances and angles for the

optimised structure of **10**. The P–P bond lengths range from 2.133(1) Å to 2.269(1) Å and are in good agreement with the values reported for similar species such as $[P_7PtH(PPh_3)]^{2-}$ (2.14(2) Å – 2.26(2) Å).[16] The four In–P bond lengths of 2.585(1) Å, 2.592(1) Å, 2.618(1) Å and 2.571(1) Å are slightly shorter than the mean In–P bond length obtained from a search of the CSD (2.645(av) Å), however these bond lengths are similar to those found in $[In_3(In_2)_3(PhP)_4(Ph_2P_2)_3Cl_7(PEt_3)_3]$ (2.533(1) Å - 2.616(1) Å).[17,28] The In–P bond lengths in **10** are also in good agreement with those observed in the previously discussed $[P_7InPh_2]^{2-}$ species (2.604(1) Å and 2.551(2) Å). The sum of covalent radii for In–P single bonds is 2.53 Å.[19]

3.4.3 $^{31}P\{^1H\}$ NMR spectroscopic studies on $[In(P_7)_2]^{3-}$ (10)

The $^{31}P\{^1H\}$ NMR spectrum of **10** shows five resonances at 42.3, –51.3, –57.1, –104.2 and –173.0 ppm with relative intensities 2:1:1:1:2 (Figure 3.10). These resonances have very similar multiplet structures to those observed in the $^{31}P\{^1H\}$ NMR spectra of **3**, **5** and **6**, and can be assigned to P12/P22 and P13/P23, P11/P21, P14/P24, P17/P27, and P15/P25 and P16/P26, in order of decreasing chemical shift. A simulation was carried out in order to obtain the ^{31}P–^{31}P coupling constants (Table 3.3).

Table 3.3: The ^{31}P chemical shift values and coupling constants for $[In(P_7)_2]^{3-}$.

δ (ppm)		–51.3 P11/P21	42.3 P12/P22	42.3 P13/P23	–57.1 P14/P24	–173.0 P15/P25	–173.0 P16/P26	–104.2 P17/P27
–51.3	P11/P21		–225	–240	–339	26	31	65
42.3	P12/P22	–225		–46	–21	–348	–12	–23
42.3	P13/P23	–240	–46		–22	–14	–394	–21
–57.1	P14/P24	–339	–21	–22		–	–	–396
–173.0	P15/P25	26	–348	–14	–		–124	–201
–173.0	P16/P26	31	–12	–394	–	–124		–217
–104.2	P17/P27	65	–23	–21	–396	–201	–217	

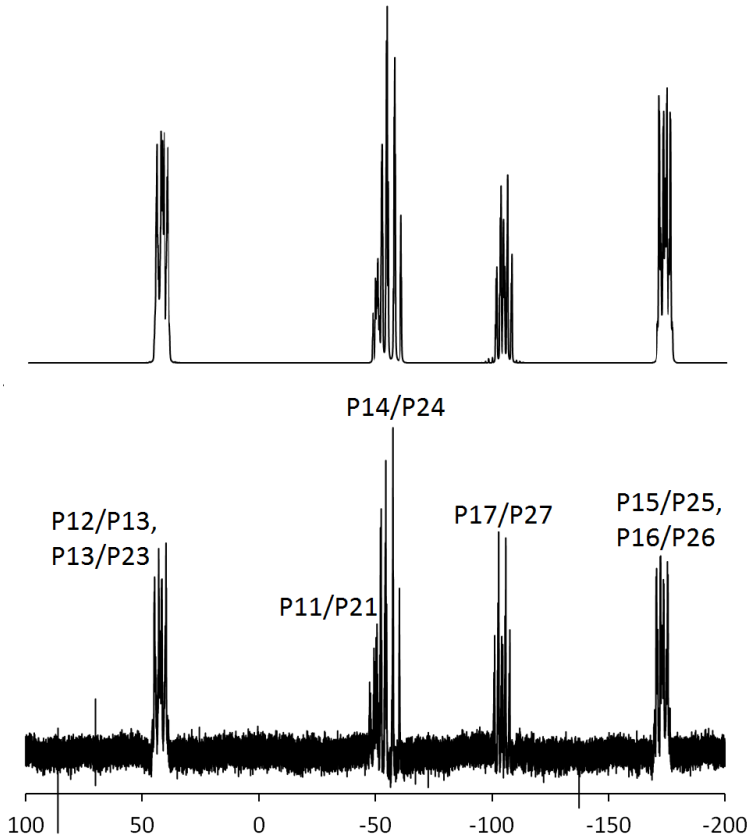

Figure 3.10: Top: The simulated ^{31}P NMR spectrum of **10**. Bottom: The ^{31}P{^{1}H} NMR spectrum of **10** recorded in d_5-pyridine.

3.4.4 Mass spectrometric studies

Both the positive and negative ion mode mass spectra of **10** and **11** confirm that the products are $[In(P_7)_2]^{3-}$ and $[In(As_7)_2]^{3-}$, respectively. The negative ion mode mass spectra contain peaks due to the oxidised cluster anions, $[In(E_7)_2]^{-}$, as well as peaks due to the cluster anions accompanied by K^+ and up to two $[K(2,2,2\text{-crypt})]^+$ cations. The major peaks in the positive ion mode spectra correspond to the cluster anions with three and four $[K(2,2,2\text{-crypt})]^+$ ions (Figures 3.11 and 3.12).

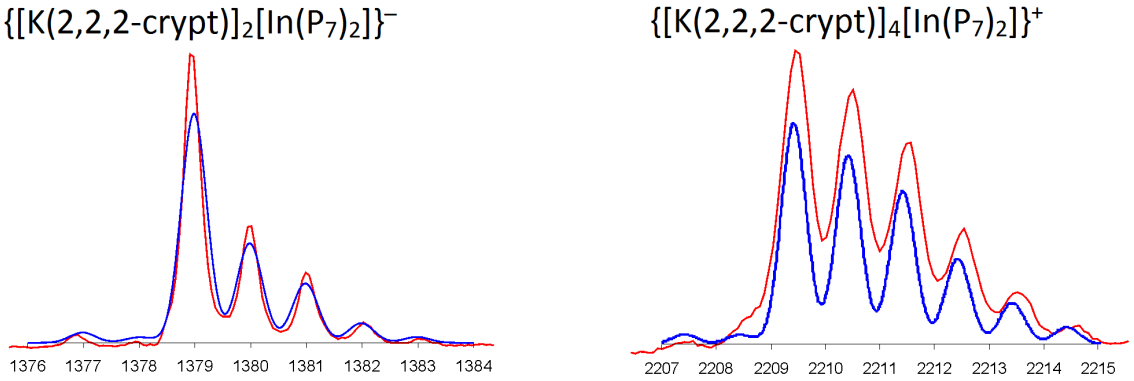

Figure 3.11: ESI-MS mass envelopes for $\{[K(2,2,2\text{-crypt})]_2[In(P_7)_2]\}^-$ and $\{[K(2,2,2\text{-crypt})]_4[In(P_7)_2]\}^+$. Predicted isotopic distributions are shown in blue and observed mass spectrometric data are shown in red.

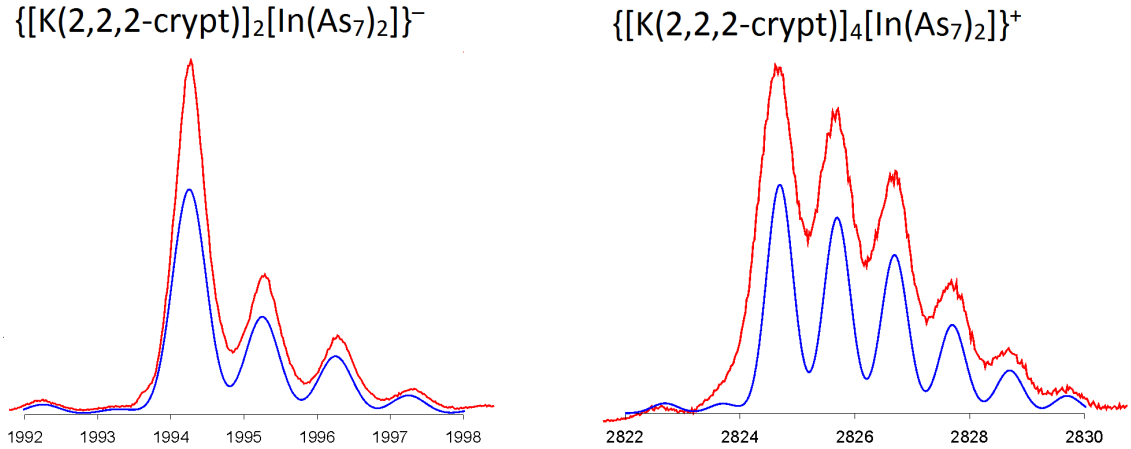

Figure 3.12: ESI-MS mass envelopes for $\{[K(2,2,2\text{-crypt})]_2[In(As_7)_2]\}^-$ and $\{[K(2,2,2\text{-crypt})]_4[In(As_7)_2]\}^+$. Predicted isotopic distributions are shown in blue and observed mass spectrometric data are shown in red.

3.5 Solution reactivity of group 15 Zintl ions towards TlCl

3.5.1 Synthesis of $[TlP_7]^{2-}$ (12) and $[TlAs_7]^{2-}$ (13)

Both K_3P_7 and K_3As_7 react with TlCl in ethylenediamine in the presence of a cation sequestering agent to form $[TlP_7]^{2-}$ (**12**) and $[TlAs_7]^{2-}$ (**13**) (Scheme 3.3). Crystals of $[K(2,2,2\text{-crypt})]_2$[**12**]·py and $[K(18\text{-crown-6})]_2$[**13**] suitable for single crystal X-ray diffraction were obtained from pyridine solutions layered with toluene.

$$E_7^{3-} + TlCl \longrightarrow [TlE_7]^{2-} + Cl^-$$

Scheme 3.3: The formation of $[TlE_7]^{2-}$ from E_7^{3-} and TlCl.

3.5.2 Structures of $[TlE_7]^{2-}$ (12 and 13)

Both **12** and **13** consist of a nortricyclane-like E_7^{3-} cage bonded to a Tl atom in an η^2-fashion (Figures 3.13 and 3.14). The X-ray structure of $[K(2,2,2\text{-crypt})]_2$[**12**]·py contains two crystallographically unique $[TlP_7]^{2-}$ cluster anions in the asymmetric unit.

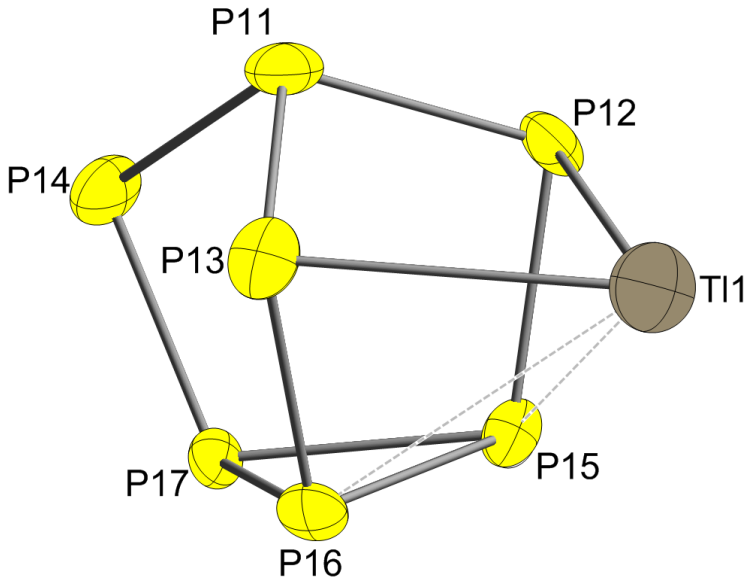

Figure 3.13: Thermal ellipsoid plot of one of the two crystallographically unique $[TlP_7]^{2-}$ ions present in $[K(2,2,2\text{-crypt})]_2$[**12**]·py. Anisotropic displacement ellipsoids are pictured at 50% probability.

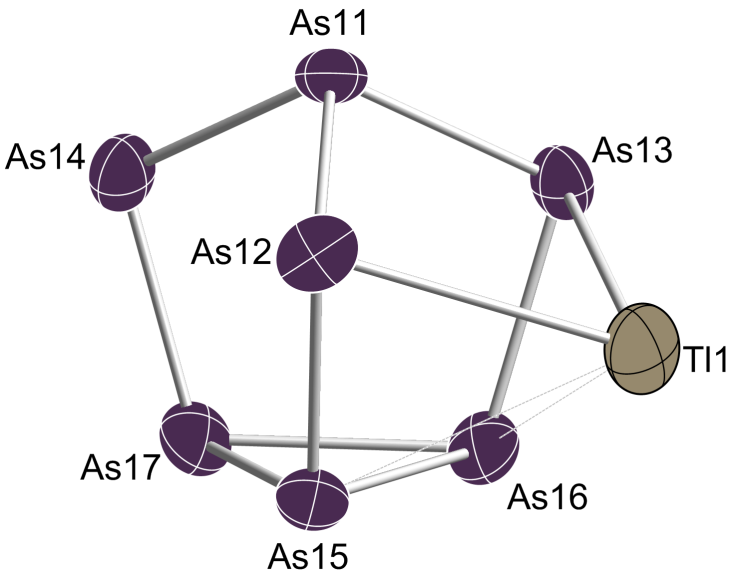

Figure 3.14: Thermal ellipsoid plot of **13** with anisotropic displacement ellipsoids pictured at 50% probability.

The Tl1–E12 and Tl1–E13 bond lengths (2.819(2) Å and 2.871(2) Å for **12**; 2.921(2) Å and 2.939(2) Å for **13**) are significantly shorter than the next nearest Tl–E contacts, Tl1–E15 and Tl1–E16

(3.114(2) Å and 3.174(2) Å for **12**; 3.147(2) Å and 3.182(2) Å for **13**). These bond distances very strongly imply that the E_7^{3-} clusters are bonded to the Tl *via* the η^2-coordination mode and not *via* the alternative η^4-coordination mode. Interestingly, the E15–E16 bonds (2.313(3) Å for **12**; 2.629(2) Å for **13**) are slightly longer than the other two basal E–E bonds, E15–E17 and E16–E17 (2.225(3) Å and 2.249(3) Å for **12**; 2.479(2) Å and 2.456(2) Å for **13**). This suggests that the E_7^{3-} clusters may possess a small amount of η^4-character. The difference in basal E–E bond lengths is greater for **13** than for **12**, while the difference in Tl–E distances is less for **13** than for **12**. This indicates that the As_7^{3-} cluster in **13** may possess slightly more η^4-character than the P_7^{3-} cage in **12**.

DFT calculations were carried out in order to investigate the electronic structures of **12** and **13**. The HOMO for both cluster anions were found to be mainly composed of Tl lone pair orbitals, with some mixing of E_7^{3-} cage orbitals, while the HOMO–1 mostly consist of lone pair contributions for P14 and As14 in **12** and **13**, respectively. The Tl atoms possess slightly positive Mulliken spin densities (0.2287 for **12** and 0.2573 for **13**), with negative spin densities on all of the P and As atoms. The most negative spin density values were obtained for the formally anionic atoms, P14 (–0.5405) and As14 (–0.5435). Both Hirschfield and Natural Population analyses revealed similar charge distributions.

Selected bond distances and angles for **12** and **13** are provided in Table 3.4, along with selected bond distances and angles for the optimised structures of **12** and **13**. The short P–P bond lengths in **12** are in the range 2.134(3) Å – 2.249(3) Å and are in good agreement with the P–P bond lengths in $[P_7PtH(PPh_3)]^{2-}$ (2.14(2) Å – 2.26(2) Å).[16] The short As–As bond lengths in **13** range from 2.354(2) Å to 2.479(2) Å and are similar to the As–As bond lengths observed in $[As_7PtH(PPh_3)]^{2-}$ (2.347(7) Å – 2.480(7) Å).[16] The Tl–P bond lengths in **12**, at 2.819(2) Å and 2.871(2) Å, are shorter than the mean Tl–P distance obtained from a search of the CSD (3.044(av) Å).[17] The sum of covalent radii for Tl–P single bonds is 2.55 Å.[19] The Tl–As bond lengths in **13** (2.921(2) Å and 2.939(2) Å) are longer than those observed in $[(Me_2TlAs(SiMe_3)_2)_2]$ (2.781(1) Å and 2.743(1) Å), the only other compound featuring Tl–As bonds to be crystallographically characterised.[29] The sum of covalent radii for Tl–As single bonds is 2.65 Å.[19]

Table 3.4: Selected bond lengths and bond angles for the $[TlP_7]^{2-}$ and $[TlAs_7]^{2-}$ species.

Bond	Experimental bond length in **12** (Å)	Calculated bond length in $\mathbf{12_{DFT}}$ (Å)	Experimental bond length in **13** (Å)	Calculated bond length in $\mathbf{13_{DFT}}$ (Å)
E11–E12	2.203(3)	2.226	2.415(2)	2.473
E11–E13	2.187(3)	2.226	2.418(2)	2.473
E11–E14	2.150(3)	2.188	2.356(2)	2.416
E12–E15	2.157(3)	2.178	2.363(2)	2.405
E13–E16	2.157(3)	2.177	2.372(2)	2.405
E14–E17	2.134(3)	2.162	2.354(2)	2.405
E15–E16	2.313(3)	2.401	2.629(2)	2.685
E15–E17	2.225(3)	2.286	2.479(2)	2.524
E16–E17	2.249(3)	2.286	2.456(2)	2.524
Tl1–E12	2.819(2)	2.972	2.921(2)	3.063
Tl1–E13	2.871(2)	2.976	2.939(2)	3.065
Tl1–E15	3.114(2)	3.261	3.147(2)	3.266
Tl1–E16	3.174(2)	3.264	3.182(2)	3.267
Angle	Experimental bond angle in **12** (°)	Calculated bond angle in $\mathbf{12_{DFT}}$ (°)	Experimental bond angle in **13** (°)	Calculated bond angle in $\mathbf{13_{DFT}}$ (°)
E12–Tl1–E13	72.87(6)	70.25	77.58(4)	75.64

3.5.3 $^{31}P\{^1H\}$ NMR spectroscopic studies on $[TlP_7]^{2-}$ (12)

$^{31}P\{^1H\}$ NMR studies on **12** have indicated that the cluster anion is fluxional in solution. At –50 °C, the $^{31}P\{^1H\}$ NMR spectrum shows two broad resonances at –99.0 and –147.2 ppm with relative intensities 1:2, as well as several resonances corresponding to HP_7^{2-} and P_{21}^{3-} impurities (Figure 3.16).[30,31] The two broad resonances have been assigned to P11 and P17, and P12, P13, P15 and P16, respectively. The resonance corresponding to P14 is believed to be coincident with one of the resonances arising from P_{21}^{3-}, which is centred at 58.2 ppm. This fluxionality is most likely to arise from an η^2–η^4–η^2 transition, which would render P12 and P13 equivalent to P15 and P16, and P11 equivalent to P17, as shown in Figure 3.15. This type of η^2–η^4–η^2 shift has been previously observed in $[P_7PtH(PPh_3)]^{2-}$.[16]

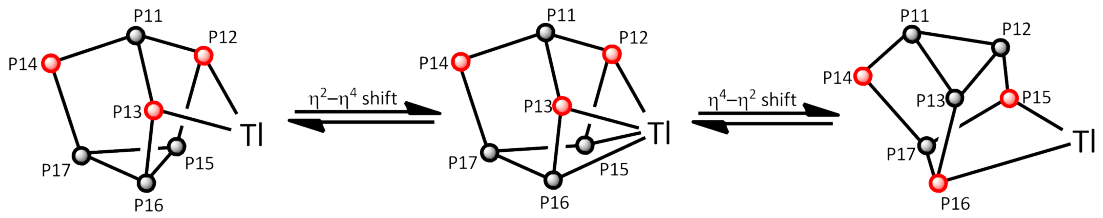

Figure 3.15: Diagram showing the proposed η^2–η^4–η^2 transition taking place in **12**. Atoms possessing a formal negative charge are shown in red.

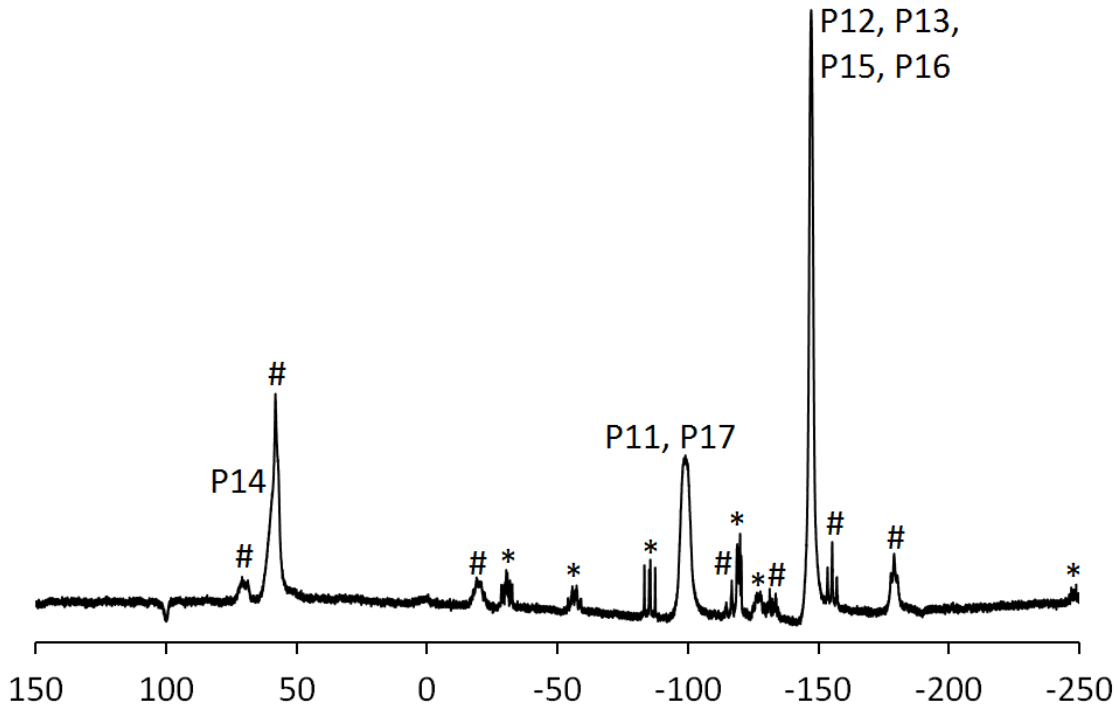

Figure 3.16: $^{31}P\{^{1}H\}$ NMR spectrum of **12** recorded in d_7-DMF at –50 °C. Resonances labelled * correspond to HP_7^{2-}, and resonances labelled # correspond to P_{21}^{3-}.

3.5.4 Mass spectrometric studies

The ESI mass spectra of **12** and **13** confirm that the products are $[TlP_7]^{2-}$ and $[TlAs_7]^{2-}$, respectively. The negative ion mode mass spectra contain peaks corresponding to the oxidised cluster anions, $[TlE_7]^-$, while the major peaks in the positive ion mode mass spectra correspond to the cluster anions paired with two and three $[K(2,2,2\text{-crypt})]^+$ or $[K(18\text{-crown-6})]^+$ ions (Figures 3.17 and 3.18).

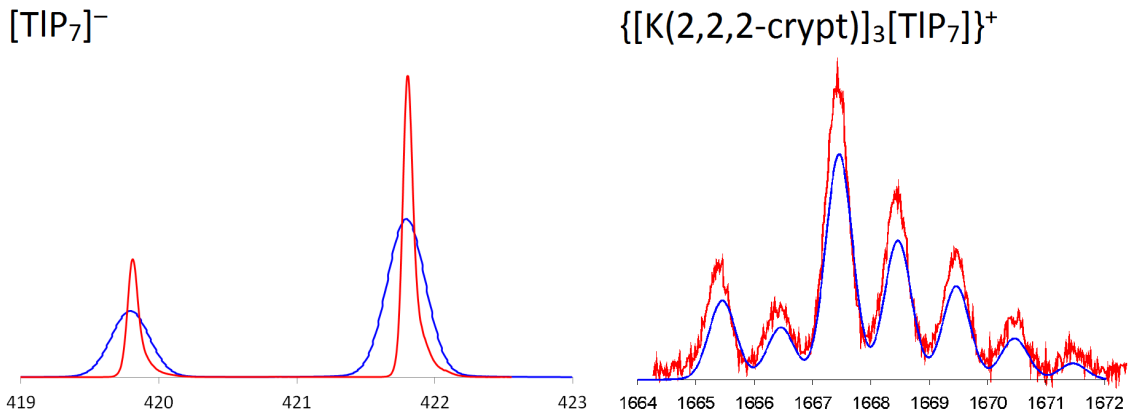

Figure 3.17: ESI-MS mass envelopes for $[TlP_7]^-$ and $\{[K(2,2,2\text{-crypt})]_3[TlP_7]\}^+$. Predicted isotopic distributions are shown in blue and observed mass spectrometric data are shown in red.

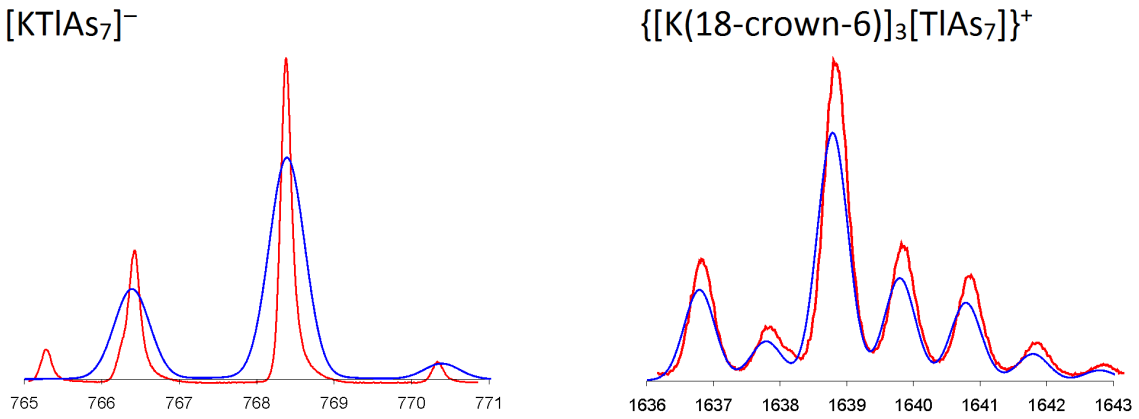

Figure 3.18: ESI-MS mass envelopes for $[KTlAs_7]^-$ and $\{K[18\text{-crown-6}]_3[TlAs_7]\}^+$. Predicted isotopic distributions are shown in blue and observed mass spectrometric data are shown in red.

3.6 Solution reactivity of group 15 Zintl ions towards MI_2 (M = Sn, Pb)

3.6.1 Synthesis of $[SnP_{15}]^{3-}$ (14), $[SnAs_{15}]^{3-}$ (15), $[PbP_{15}]^{3-}$ (16) and $[PbAs_{15}]^{3-}$ (17)

Ethylenediamine solutions of K_3P_7 and K_3As_7 react with MI_2 (M = Sn, Pb) in the presence of 2,2,2-crypt to form the compounds $[K(2,2,2\text{-crypt})]_3[ME_{15}]$ (M = Sn, Pb; E = P, As). These contain the sixteen-vertex cluster anions $[SnP_{15}]^{3-}$ (**14**), $[SnAs_{15}]^{3-}$ (**15**), $[PbP_{15}]^{3-}$ (**16**) and $[PbAs_{15}]^{3-}$ (**17**). Crystals of $[K(2,2,2\text{-crypt})]_3$[**14**]·en, $[K(2,2,2\text{-crypt})]_3$[**15**]·2en and $[K(2,2,2\text{-crypt})]_3$[**16**]·en suitable for single crystal X-ray diffraction were obtained from ethylenediamine solutions layered with diethyl ether. Crystals of $[K(2,2,2\text{-crypt})]_3$[**17**] were obtained from the same solvent mixture, however these crystals proved to be unsuitable for single crystal X-ray diffraction due to their small size. Many alternative solvent systems were tried, however better quality crystals could not be obtained. The identity of the product was confirmed by mass spectrometry.

The clusters in **14–17** are isostructural with the previously reported P_{16}^{2-} cluster anion, which consists of two P_7 units bridged by a P_2 group.[15] Two of the P atoms are two-connect, and the others are three-connect, which gives rise to a 2– charge. The replacement of a three-connect

group 15 element with a group 14 element would increase the overall negative charge of the cluster by one, as M^- (M = Sn, Pb) is isoelectronic with E (E = P, As). This is observed in **14–17**, in which one of the bridging P or As atoms has been replaced by Sn or Pb (Figure 3.19). **14–17** are also very similar to $[HgAs_{15}]^{3-}$, which was recently synthesised by Weiss, Sen and co-workers.[32]

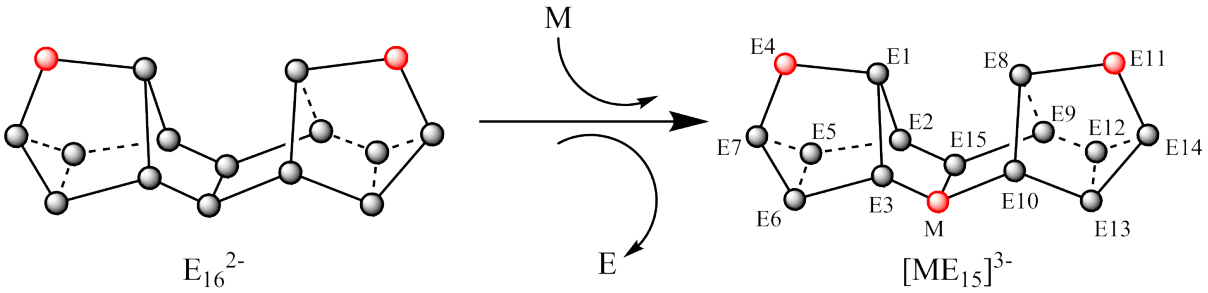

Figure 3.19: Diagram showing the relationship between E_{16}^{2-} and $[ME_{15}]^{3-}$. Atoms possessing a formal negative charge are shown in red.

3.6.2 Structures of $[ME_{15}]^{3-}$ (14, 15 and 16)

Clusters **14**, **15** and **16** all consist of two E_7 cages bridged by a M–E group (Figures 3.20, 3.21 and 3.22). The crystal structures of [K(2,2,2-crypt)]$_3$[**14**]·en and [K(2,2,2-crypt)]$_3$[**16**]·en exhibit crystallographic disorder of the cluster anion, which gives rise to a statistical mixing of the two bridging positions. This means that no meaningful discussion of bond metric parameters can be made, however it is clear that the overall cluster charge is 3^-, as there are three $[K(2,2,2\text{-crypt})]^+$ cations associated with each cluster anion. This implies that one of the atomic positions of the cluster anion must be occupied by a group 14 element. In addition, the structural refinement improves significantly if the two bridging positions are refined as having 50% P and 50% M occupancy (M = Sn, Pb), as opposed to 100% P character. The crystal structure of [K(2,2,2-crypt)]$_3$[**15**]·2en exhibits no crystallographic disorder, and the structure of the $[SnAs_{15}]^{3-}$ anion was determined unequivocally (Figure 3.22).

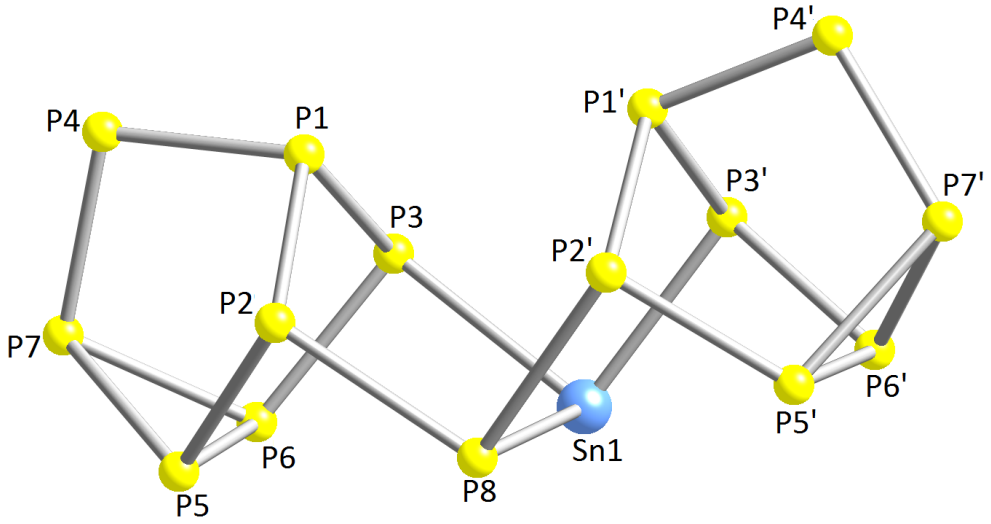

Figure 3.20: Ball and stick diagram of **14**.

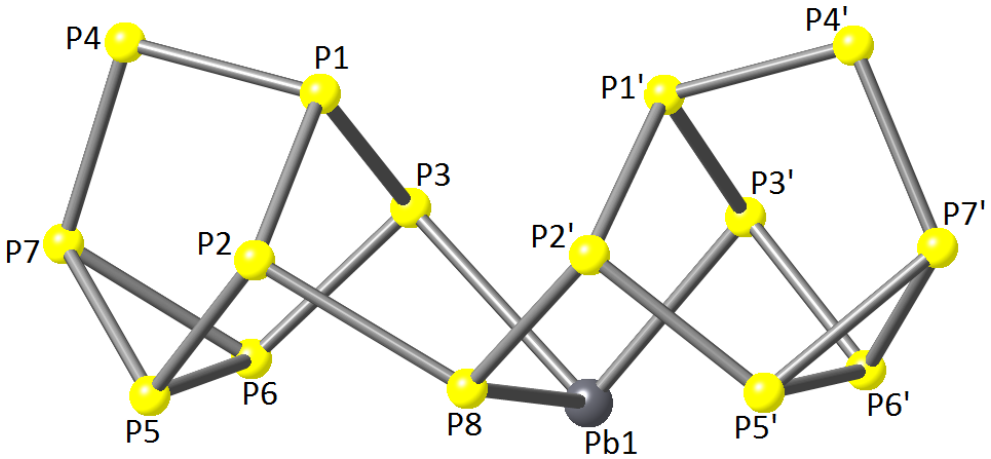

Figure 3.21: Ball and stick diagram of **16**.

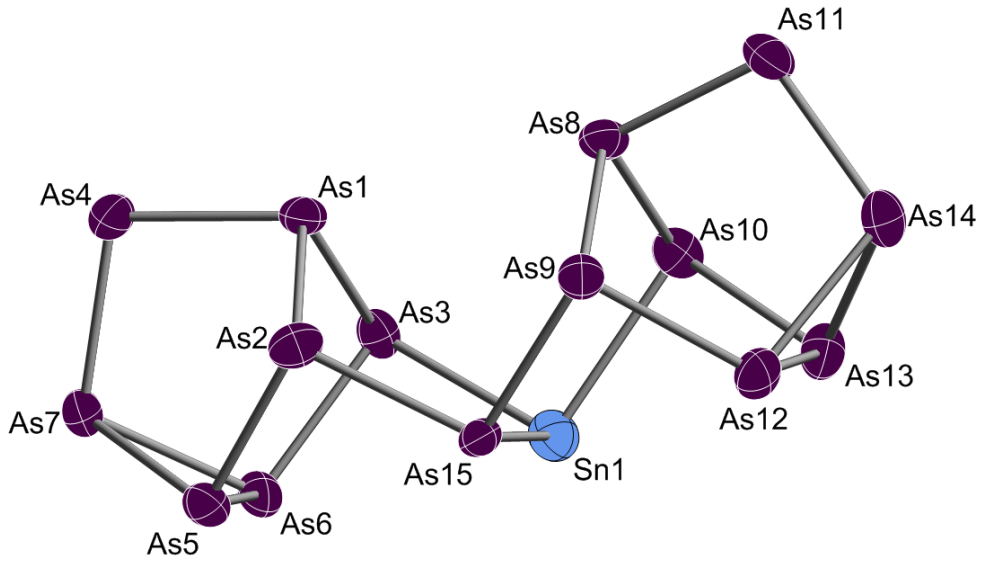

Figure 3.22: Thermal ellipsoid plot of **15** with anisotropic displacement ellipsoids pictured at 50% probability.

DFT calculations on **15** showed that the HOMO and HOMO–1 mostly consist of lone pair contributions for As4 and As11, while the HOMO–2 possesses significant Sn lone pair character. A Mulliken spin density analysis showed that all of the As atoms possess negative spin densities, with the most negative spin density values obtained for the formally anionic As atoms, As4 (–0.5815) and As11 (–0.5812). The Mulliken spin density for the Sn atom was found to be slightly positive, however a Hirschfield charge analysis gave some negative spin density on the Sn atom, as expected from the Lewis structure. An NBO analysis was consistent with each interaction in **15** being a two-centre two-electron bond.

Table 3.5: Selected bond lengths and bond angles for the $[SnAs_{15}]^{3-}$ species.

Bond	Experimental bond length in **15** (Å)	Calculated bond length in $\mathbf{15_{DFT}}$ (Å)
As1–As2	2.426(1)	2.490
As1–As3	2.409(1)	2.471
As1–As4	2.367(1)	2.414
As2–As5	2.409(1)	2.456
As2–As15	2.469(1)	2.478
As3–As6	2.397(1)	2.439
As4–As7	2.384(1)	2.435
As5–As6	2.458(1)	2.525
As5–As7	2.461(1)	2.513
As6–As7	2.454(1)	2.513
As8–As9	2.410(1)	2.489
As8–As10	2.417(1)	2.471
As8–As11	2.370(1)	2.414
As9–As12	2.412(1)	2.455
As9–As15	2.482(1)	2.477
As10–As13	2.395(1)	2.438
As11–As14	2.384(1)	2.436
As12–As13	2.466(1)	2.524
As12–As14	2.466(1)	2.512
As13–As14	2.458(1)	2.513
Sn1–As3	2.656(1)	2.753
Sn1–As10	2.647(1)	2.752
Sn1–As15	2.749(1)	2.788
Angle	Experimental bond angle in **15** (°)	Calculated bond angle in $\mathbf{15_{DFT}}$ (°)
As3–Sn1–As10	94.36(3)	94.47
As3–Sn1–As15	97.66(2)	97.24
As10–Sn1–As15	99.36(2)	97.29
As2–As15–As9	96.04(3)	95.69
As2–As15–Sn1	104.53(3)	105.14
As9–As15–Sn1	102.68(3)	105.06

Selected bond distances and angles for **15** are provided in Table 3.5, along with selected bond distances and angles for the optimised structure of **15**. The As–As bond lengths range from

2.367(1) Å to 2.482(1) Å and are in good agreement with the As–As bond lengths in similar species such as $[HgAs_{15}]^{3-}$ (2.359(1) Å – 2.472(1) Å).[32] The Sn1–As3 and Sn1–As10 bonds (2.656(1) Å and 2.647(1) Å) are significantly longer than the As2–As15 and As9–As15 bonds (2.469(1) Å and 2.482(1) Å), which is consistent with the larger atomic radius of Sn (1.40 Å compared with 1.21 Å for As).[19] The three Sn–As bond lengths of 2.656(1) Å, 2.647(1) Å and 2.749(1) Å are comparable to those found in other Sn/As clusters such as $[(^tBu_2PhSiAsSn)_4Sn(Bu)Cl]$ (2.636(3) Å – 2.760(1) Å).[33] A search of the CSD gave a mean Sn–As bond length of 2.719(av) Å, while the sum of covalent radii for Sn–As single bonds is 2.61 Å.[17,19]

3.6.3 $^{31}P\{^1H\}$ NMR spectroscopic studies on $[SnP_{15}]^{3-}$ (14) and $[PbP_{15}]^{3-}$ (16)

The $^{31}P\{^1H\}$ NMR spectrum of **14** shows eight resonances at 50.6, 22.8, –31.7, –54.0, –61.5, –115.8, –152.1 and –176.3 ppm with relative intensities 2:2:2:1:2:2:2:2 (Figure 3.23). The resonance at –54.0 ppm can be assigned to the single bridging P atom, P8, and the remaining resonances were assigned with the aid of a ^{31}P–^{31}P COSY spectrum as corresponding to P2, P1, P3, P7, P4, P6 and P5, in order of decreasing chemical shift (Figure 3.24). A simulation was carried out in order to obtain the ^{31}P–^{31}P coupling constants (Table 3.6). The spectrum also shows resonances that correspond to an HP_7^{2-} impurity.[30,34]

Table 3.6: The ^{31}P chemical shift values and coupling constants for $[SnP_{15}]^{3-}$.

δ (ppm)		22.8 P1	50.6 P2	–31.7 P3	–115.8 P4	–176.3 P5	–152.1 P6	–61.5 P7	–54.0 P8
22.8	P1		–352	–337	–355	31	–	72	–
50.6	P2	–352		–	–	–364	–	–	–312
–31.7	P3	–337	–		–	–	–376	–	–
–115.8	P4	–355	–	–		–	–	–359	–
–176.3	P5	31	–364	–	–		–175	–211	78
–152.1	P6	–	–	–376	–	–175		–226	–
–61.5	P7	72	–	–	–359	–211	–226		–
–54.0	P8	–	–312	–	–	78	–	–	

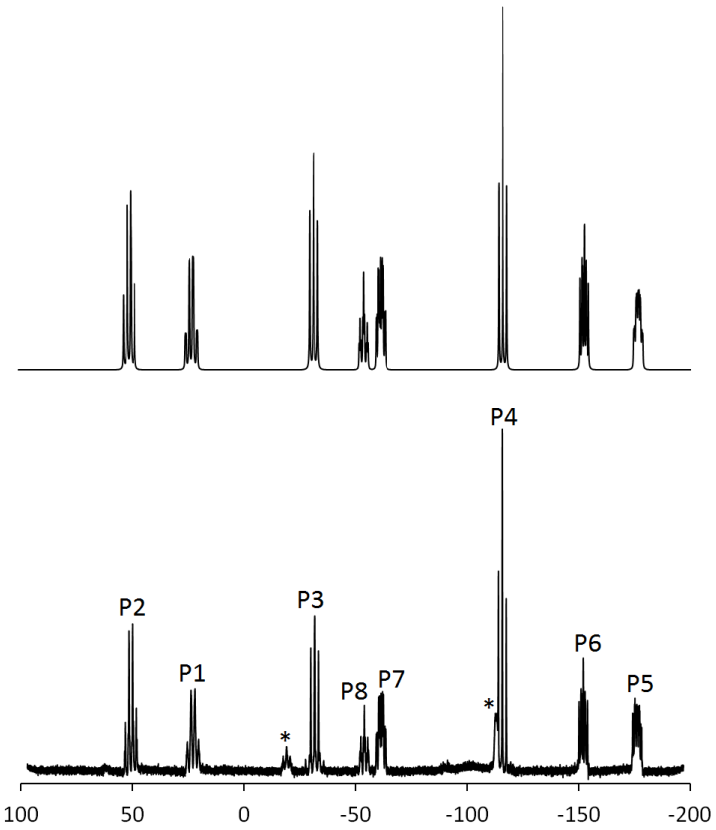

Figure 3.23: Top: The simulated ^{31}P NMR spectrum of **14**. Bottom: The ^{31}P{^{1}H} NMR spectrum of **14** recorded in d_5-pyridine. Resonances labelled * correspond to HP_7^{2-}.

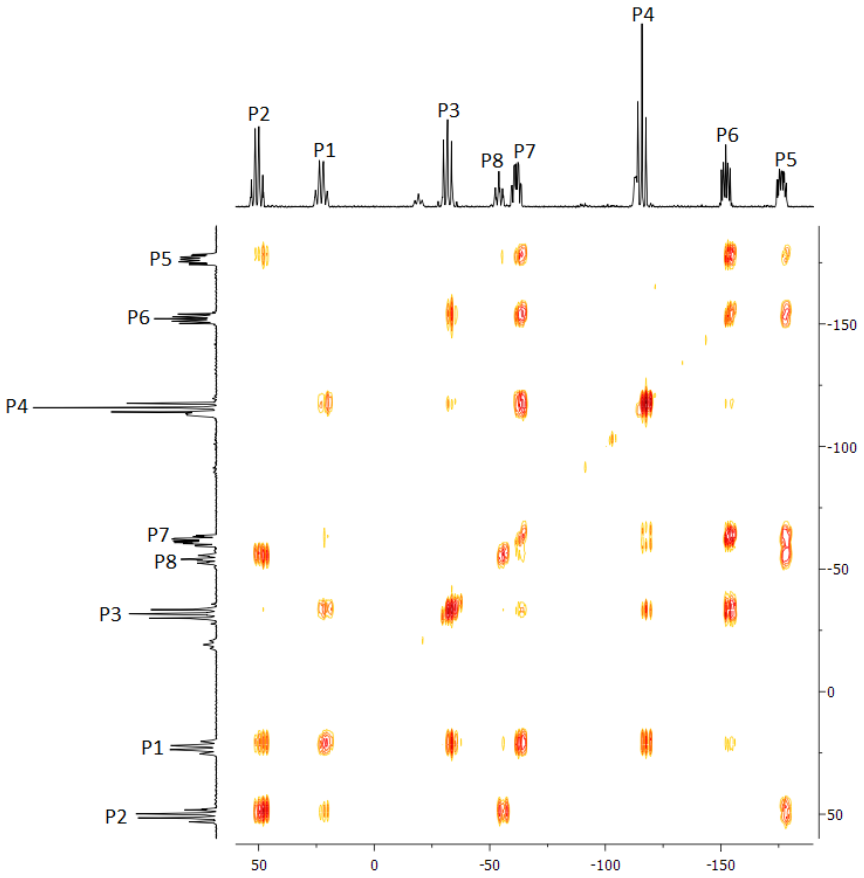

Figure 3.24: ^{31}P–^{31}P COSY spectrum of **14**.

The $^{31}P\{^1H\}$ NMR spectrum of **16** shows eight resonances at 49.5, 33.0, –40.0, –50.6, –64.8, –122.7, –153.4 and –175.4 ppm with relative intensities 2:2:2:1:2:2:2:2 (Figure 3.25). These resonances have very similar multiplet structures to those observed in the $^{31}P\{^1H\}$ NMR spectrum of **14** and can be assigned to P2, P1, P3, P8, P7, P4, P6 and P5, in order of decreasing chemical shift. A ^{31}P–^{31}P COSY spectrum confirmed that these assignments were correct (Figure 3.26). As for **14**, the $^{31}P\{^1H\}$ NMR spectrum was simulated in order to obtain the ^{31}P–^{31}P coupling constants (Table 3.7). The spectrum also shows resonances that correspond to an HP_7^{2-} impurity.[30,34]

Table 3.7: The ^{31}P chemical shift values and coupling constants for $[PbP_{15}]^{3-}$.

δ (ppm)		33.0 P1	49.5 P2	–40.0 P3	–122.7 P4	–175.4 P5	–153.4 P6	–64.8 P7	–50.6 P8
33.0	P1		–359	–322	–351	31	–	72	–
49.5	P2	–359		–	–	–367	–	–	–310
–40.0	P3	–322	–		–	–	–381	–	–
–122.7	P4	–351	–	–		–	–	–368	–
–175.4	P5	31	–367	–	–		–176	–202	87
–153.4	P6	–	–	–381	–	–176		–223	–
–64.8	P7	72	–	–	–368	–202	–223		–
–50.6	P8	–	–310	–	–	87	–	–	

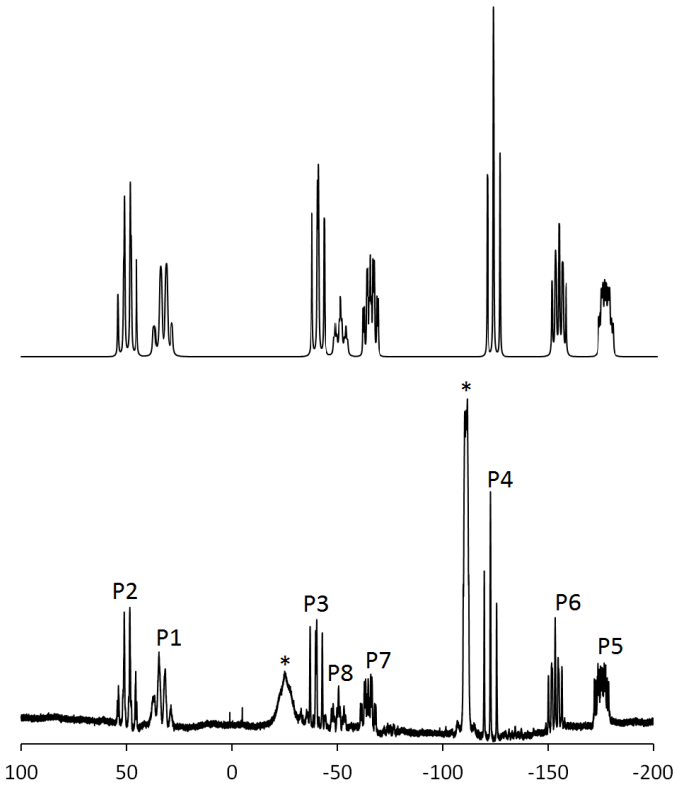

Figure 3.25: Top: The simulated ^{31}P NMR spectrum of **16**. Bottom: The $^{31}P\{^1H\}$ NMR spectrum of **16** recorded in d_5-pyridine. Resonances labelled * correspond to HP_7^{2-}.

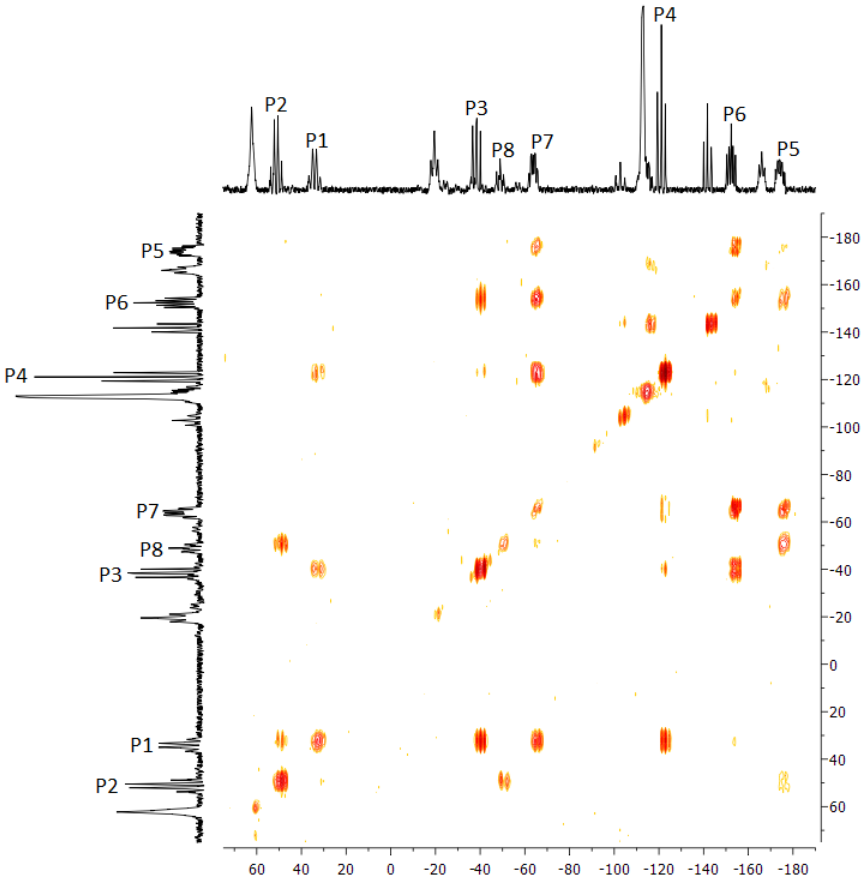

Figure 3.26: ^{31}P–^{31}P COSY spectrum of **16**.

3.6.4 Mass spectrometric studies

The ESI mass spectra of **14–17** confirm that the products are $[ME_{15}]^{3-}$ (M = Sn, Pb; E = P, As). The negative ion mode mass spectra show peaks corresponding to the oxidised cluster anions, $[ME_{15}]^{-}$, as well as peaks corresponding to the cluster anions accompanied by up to two $[K(2,2,2\text{-crypt})]^{+}$ cations. The major peaks in the positive ion mode mass spectra correspond to the cluster anions paired with three and four $[K(2,2,2\text{-crypt})]^{+}$ ions (Figures 3.27, 3.28, 3.29 and 3.30).

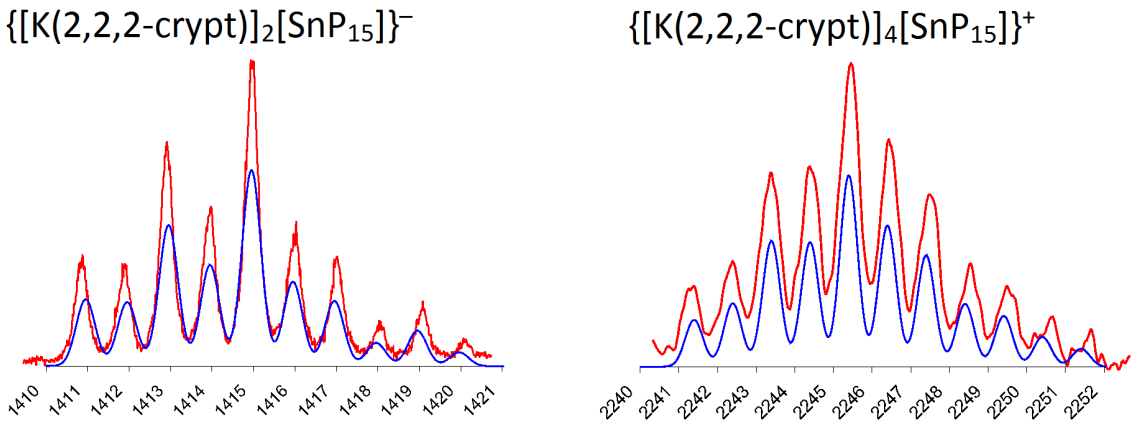

Figure 3.27: ESI-MS mass envelopes for $\{[K(2,2,2\text{-crypt})]_2[SnP_{15}]\}^-$ and $\{[K(2,2,2\text{-crypt})]_4[SnP_{15}]\}^+$. Predicted isotopic distributions are shown in blue and observed mass spectrometric data are shown in red.

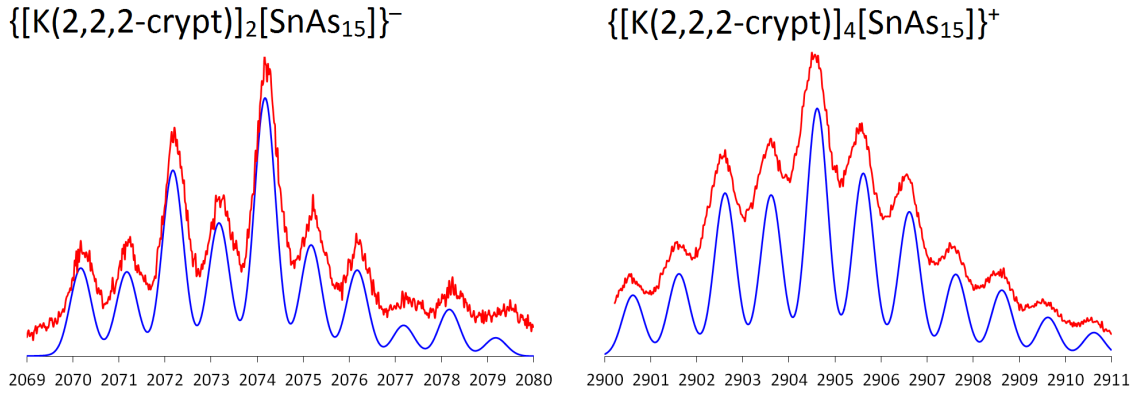

Figure 3.28: ESI-MS mass envelopes for $\{[K(2,2,2\text{-crypt})]_2[SnAs_{15}]\}^-$ and $\{[K(2,2,2\text{-crypt})]_4[SnAs_{15}]\}^+$. Predicted isotopic distributions are shown in blue and observed mass spectrometric data are shown in red.

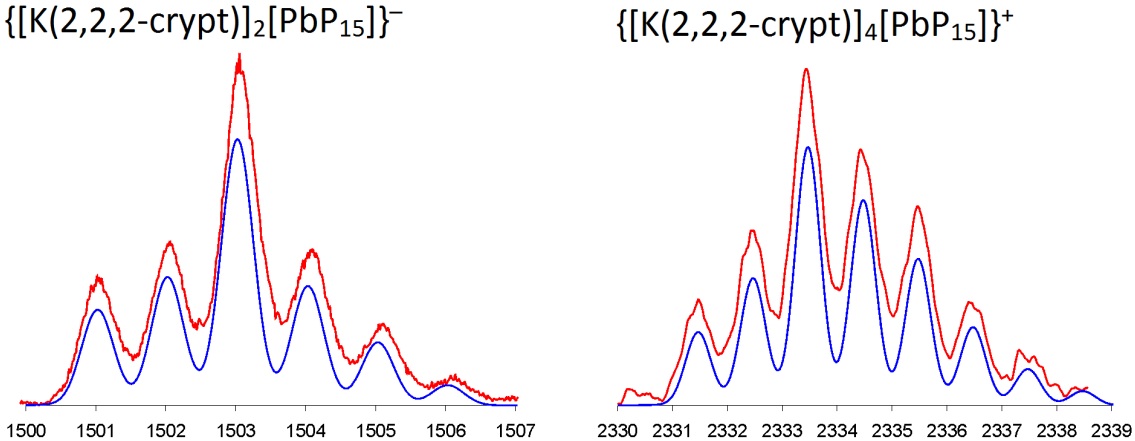

Figure 3.29: ESI-MS mass envelopes for $\{[K(2,2,2\text{-crypt})]_2[PbP_{15}]\}^-$ and $\{[K(2,2,2\text{-crypt})]_4[PbP_{15}]\}^+$. Predicted isotopic distributions are shown in blue and observed mass spectrometric data are shown in red.

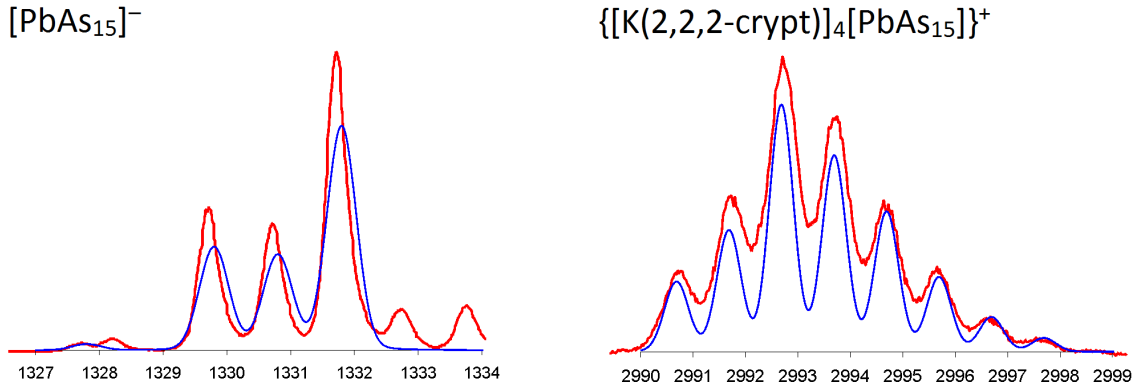

Figure 3.30: ESI-MS mass envelopes for $[PbAs_{15}]^-$ and $\{[K(2,2,2\text{-crypt})]_4[PbAs_{15}]\}^+$. Predicted isotopic distributions are shown in blue and observed mass spectrometric data are shown in red.

3.7 Conclusions

This chapter has detailed the synthesis and characterisation of ten previously unknown compounds of group 15 Zintl ions. The reaction of P_7^{3-} with $[M(nbe)_3][SbF_6]$ or MCl (M = Ag, Au) yielded the M–M bridged species $[Ag_2(HP_7)_2]^{2-}$ (**8**) and $[Au_2(HP_7)_2]^{2-}$ (**9**). Characterisation of **8** and **9** by ^{31}P NMR spectroscopy proved extremely difficult, however the identities of the products were confirmed by single crystal X-ray diffraction and mass spectrometry.

The reactions of P_7^{3-} and As_7^{3-} with $InCl_3$ produced the In-bridged dimers $[In(P_7)_2]^{3-}$ (**10**) and $[In(As_7)_2]^{3-}$ (**11**). **10** has been fully characterised by single crystal X-ray diffraction, $^{31}P\{^1H\}$ NMR spectroscopy and mass spectrometry. Crystals of $[K(2,2,2\text{-crypt})]_3$[**11**] could not be obtained, but the presence of $[In(As_7)_2]^{3-}$ was confirmed by mass spectrometry.

P_7^{3-} and As_7^{3-} have also been found to react with TlCl to form $[TlP_7]^{2-}$ (**12**) and $[TlAs_7]^{2-}$ (**13**). **12** has been characterised by single crystal X-ray diffraction, $^{31}P\{^1H\}$ NMR spectroscopy and mass spectrometry, while **13** has been characterised by single crystal X-ray diffraction and mass spectrometry.

In addition, P_7^{3-} and As_7^{3-} react with MI_2 (M = Sn, Pb) to form the sixteen-vertex cluster anions $[SnP_{15}]^{3-}$ (**14**), $[SnAs_{15}]^{3-}$ (**15**), $[PbP_{15}]^{3-}$ (**16**) and $[PbAs_{15}]^{3-}$ (**17**). **14** and **16** have been characterised by single crystal X-ray diffraction, $^{31}P\{^1H\}$ NMR spectroscopy and mass spectrometry, while **15** has been characterised by single crystal X-ray diffraction and mass spectrometry. Crystals of $[K(2,2,2\text{-crypt})]_3$[**17**] suitable for single crystal X-ray diffraction

could not be obtained, however the identity of this species has been confirmed by mass spectrometry.

3.8 References

1. Charles, S.; Fettinger, J. C.; Eichhorn, B. W. *J. Am. Chem. Soc.* **1995**, *117,* 5303–5311.
2. Mattamana, S. P.; Promprai, K.; Fettinger, J. C.; Eichhorn, B. W. *Inorg. Chem.* **1998**, *37,* 6222–6228.
3. Miluykov, V. A.; Kataev, A. V.; Hey-Hawkins, E.; Sinyashin, O. G. *Russ. Chem. Bull., Int. Ed.* **2007**, *56,* 298–303.
4. Baudler, M.; Faber, W.; Hahn, J. *Z. Anorg. Allg. Chem.* **1980**, *469,* 15–21.
5. Fritz, G.; Hoppe, K. D.; Hönle, W.; Weber, D.; Mujica, C.; Manriquez, V.; Von Schnering, H. G. *J. Organomet. Chem.* **1983**, *249,* 63–80.
6. Fritz, G.; Schneider, H. W. *Z. Anorg. Allg. Chem.* **1990**, *584,* 12–20.
7. Von Schnering, H. G.; Fenske, D.; Hönle, W.; Binnewies, M.; Peters, K. *Angew. Chem., Int. Ed. Engl.* **1979**, *18,* 679.
8. Fritz, G.; Layher, E.; Goesmann, H.; Hanke, D.; Persau, C. *Z. Anorg. Allg. Chem.* **1991**, *594,* 36–46.
9. Ahlrichs, R.; Fenske, D.; Fromm, K.; Krautscheid, H.; Krautscheid, U.; Treutler, O. *Chem. Eur. J.* **1996**, *2,* 238–244.
10. Scharfe, S.; Kraus, F.; Stegmaier, S.; Schier, A.; Fässler, T. F. *Angew. Chem., Int. Ed.* **2011**, *50,* 3630–3670.
11. Knapp, C. M.; Jackson, C. S.; Large, J. S.; Thompson, A. L.; Goicoechea, J. M. *Inorg. Chem.* **2011**, *50,* 4021–4028.
12. Knapp, C. M.; Large, J. S.; Rees, N. H.; Goicoechea, J. M. *Dalton Trans.* **2011**, *40,* 735–745.
13. Qian, M.; Reber, A. C.; Ugrinov, A.; Chaki, N. K.; Mandal, S.; Saavedra, H. M.; Khanna, S. N.; Sen, A.; Weiss, P. S. *ACS Nano* **2010**, *4,* 235–240.
14. Chaki, N. K.; Mandal, S.; Reber, A.C.; Qian, M.; Saavedra, H. M; Weiss, P. S.; Khanna, S. N.; Sen, A. *ACS Nano* **2010**, *4,* 5813–5818.
15. Von Schnering, H. G.; Manriquez, V.; Hönle, W. *Angew. Chem., Int. Ed. Engl.* **1981**, *20,* 594–595.
16. Kesanli, B.; Charles, S.; Lam, Y. F.; Bott, S. G.; Fettinger, J.; Eichhorn, B. *J. Am. Chem. Soc* **2000**, *122,* 11101–11107.
17. Values taken from CSD version 5.33 (2012).
18. Che, C. M.; Tse, M. C.; Chan, M. C. W.; Cheung, K. K.; Lee Phillips, D.; Leung, K. H. *J. Am. Chem. Soc.* **2000**, *122,* 2464–2468.
19. Pyykkö, P.; Atsumi, M. *Chem. Eur. J.* **2009**, *15,* 186–197.
20. Tunyogi, T.; Deák, A.; Tárkányi, G.; Királi, P.; Pálinkás, G. *Inorg. Chem.* **2008**, *47,* 2049–2055.

21. Pyykkö, P. *Chem. Rev.* **1997**, *97,* 597–636.

22. Mingos, D. M. P.; Yau, J.; Menzer, S.; Williams, D. J. *J. Chem. Soc., Dalton Trans.* **1995**, 319–320.

23. O'Grady, E.; Kaltsoyannis, N. *Phys. Chem. Chem. Phys.* **2004**, *6,* 680–687.

24. Baudler, M.; Heumüller, R.; Hahn, J. *Z. Anorg. Allg. Chem.* **1985**, *529,* 7–14.

25. Gorenstein, D. G. *Prog. Nucl. Mag. Res. Sp.* **1984**, *16,* 1–98.

26. Charles, S.; Fettinger, J. C.; Eichhorn, B. W. *Inorg. Chem.* **1996**, *35,* 1540–1548.

27. Charles, S.; Fettinger, J. C.; Bott, S. G.; Eichhorn, B. W. *J. Am. Chem. Soc.* **1996**, *118,* 4713–4714.

28. Von Hänisch, C.; Fenske, D.; Kattannek, M.; Ahlrichs, R. *Angew. Chem., Int. Ed.* **1999**, *38,* 2736–2738.

29. Thomas, F.; Schulz, S.; Mansikkamäki, H.; Nieger, M. *Angew. Chem., Int. Ed.* **2003**, *42,* 5641–5644.

30. Turbervill, R. S. P.; Goicoechea, J. M. *Organometallics* **2012**, *31,* 2452–2462.

31. Baudler, M.; Düster, D.; Langerbeins, K.; Germeshausen, J. *Angew. Chem., Int. Ed. Engl.* **1984**, *23,* 317–318.

32. Mandal, S.; Reber, A. C.; Qian, M.; Liu, R.; Saavedra, H. M.; Sen, S.; Weiss, P. S.; Khanna, S. N.; Sen, A. *Dalton Trans.* **2012**, *41,* 12365–12377.

33. Traut, S.; Von Hänisch, C. *Z. Anorg. Allg. Chem.* **2011**, *637,* 1777–1783.

34. Dai, F. R.; Xu, L. *Inorg. Chim. Acta* **2006**, *359,* 4265–4273.

Chapter 4 Solution reactivity of P_7^{3-} towards group 8 compounds

4.1 Introduction

The reactivity of E_7^{3-} clusters towards group 8 metal complexes has not been extensively studied. Only one example of a reaction between E_7^{3-} and a group 8 compound has been reported, namely the reaction of P_7^{3-} with [FeCp(CO)$_2$Br] to form P_7(FeCp(CO)$_2$)$_3$.[1] Related research by Scherer and co-workers has focussed on the reactivity of P_4 and As_4 towards [(Fe(η^5-C_5Me_4R)(CO)$_2$)$_2$] and [Ru(η^5-C_5Me_4R)(CO)$_2$Br] (R = Me, Et). These reactions formed the sandwich complexes [(η^5-E_5)M(η^5-C_5Me_4R)] (E = P, As; M = Fe, Ru; R = Me, Et).[2–5] These sandwich complexes can be considered to be group 15 analogues of ferrocene, in which one of the Cp^- rings has been replaced by an isolobal η^5-E_5^- ring. The E_5^- and $C_5Me_4R^-$ rings are planar and are staggered relative to each other (Figure 4.1).

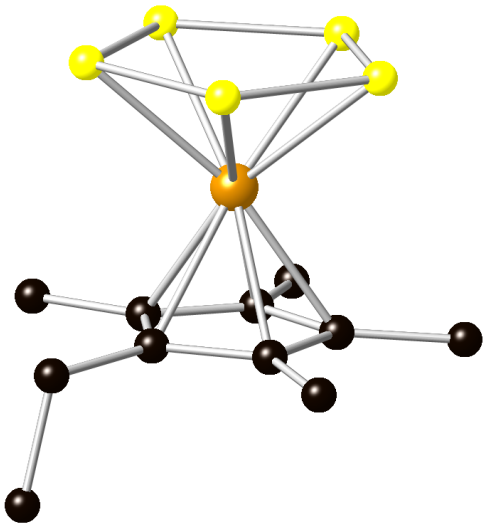

Figure 4.1: Ball and stick diagram of [(η^5-P_5)Fe(η^5-C_5Me_4Et)]. P atoms are shown in yellow, the Fe atom is shown in brown and C atoms are shown in black. H atoms are omitted for clarity.

Carbon-free metallocene analogues, in which both Cp^- ligands have been replaced by E_5^- rings, have not been isolated for group 8 metals to date, however $[Ti(\eta^5\text{-}P_5)_2]^{2-}$ was synthesised by reacting P_4 with a highly reduced Ti complex.[6] Unlike the $[(\eta^5\text{-}E_5)M(\eta^5\text{-}C_5Me_4R)]$ complexes, the solid state structure of $[Ti(\eta^5\text{-}P_5)_2]^{2-}$ features two eclipsed P_5^- rings (Figure 4.2).

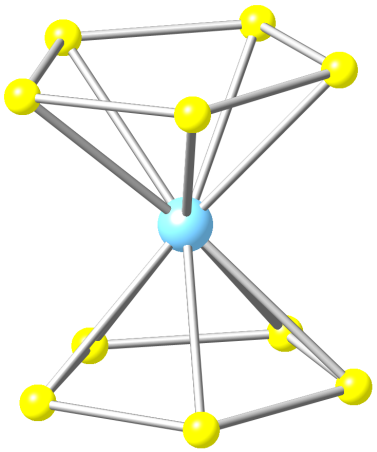

Figure 4.2: Ball and stick diagram of $[Ti(\eta^5\text{-}P_5)_2]^{2-}$. The Ti atom is shown in blue and P atoms are shown in yellow.

DFT calculations were carried out on $[Ti(\eta^5\text{-}P_5)_2]^{2-}$ and showed that the π orbitals of P_5^- are lower in energy than those of its isolobal carbon analogue, Cp^-. This means that P_5^- should be a stronger π-acceptor than Cp^-. $[Ti(\eta^5\text{-}P_5)_2]^{2-}$ was found to be inert towards CO, 2,6-dimethylphenylisocyanide and $P(OMe)_3$, while the isoelectronic MCp_2 complexes (M = Cr, Mo, W) react readily with CO to form the carbonyl complexes $[MCp_2(CO)]$ and $[MCp_2(CO)_2]$.[6,7] In additon, $[Ti(\eta^5\text{-}P_5)_2]^{2-}$ is stable towards O_2 for several weeks and only decomposes slowly in wet pyridine.[6] This is in contrast to all other known Ti(0) compounds, such as $Ti(C_6H_6)_2$, which are extremely air sensitive.[8] This indicates that the Ti centre must be much less electron-rich in $[Ti(\eta^5\text{-}P_5)_2]^{2-}$ than in previously known Ti(0) complexes and provides experimental evidence for the strong π-acceptor ability of P_5^-. Baudler and co-workers synthesised the group 6 complexes, $[(\eta^5\text{-}P_5)M(CO)_3]^-$ (M = Cr, Mo, W), and observed that the C–O stretching bands for $[(\eta^5\text{-}P_5)W(CO)_3]^-$ appear at higher frequencies than those for $[WCp(CO)_3]^-$.[9] This provides further evidence for P_5^- being a stronger π-acceptor than Cp^-.

4.2 Objectives

Prior to 2009, studies of the reactivity of group 15 Zintl ions towards group 8 compounds were extremely limited; in fact, only one reaction of E_7^{3-} with a group 8 compound had been reported.[1] This was surprising, considering that both P_4 and As_4 had been shown to react with $[(Fe(\eta^5\text{-}C_5Me_4R)(CO)_2)_2]$ and $[Ru(\eta^5\text{-}C_5Me_4R)(CO)_2Br]$ to form group 15 analogues of ferrocene. It seemed possible that similar species would also be formed in the reactions of E_7^{3-} with group 8 compounds.

This chapter will describe the reactivity of P_7^{3-} towards a series of group 8 compounds. P_7^{3-} reacts with $FeCl_2$ to form $[Fe(HP_7)_2]^{2-}$, in which two norbornadiene-like HP_7^{2-} clusters are bridged by an Fe atom.[10] NMR studies showed that this species can be deprotonated by KO^tBu or $K[N(SiMe_3)_2]$ to form $[Fe(P_7)_2]^{4-}$. The analogous Ru complexes could be obtained by reacting P_7^{3-} with $[Ru(PPh_3)_3Cl_2]$. These Fe and Ru compounds are isoelectronic with ferrocene and represent the first examples of P-containing metallocene analogues to be synthesised from P_7^{3-}. In addition, P_7^{3-} reacts with $[Ru(COD)(\eta^3\text{-}CH_2C(CH_3)CH_2)_2]$ to form $[(C_4H_7)P_7Ru(COD)]^{2-}$, in which a functionalised $(C_4H_7)P_7^{2-}$ cluster is bonded to a Ru(COD) fragment in an η^4-fashion.

4.3 Solution reactivity of P_7^{3-} towards $FeCl_2$

4.3.1 Synthesis of $[Fe(HP_7)_2]^{2-}$ (18)

K_3P_7 reacts with $FeCl_2$ in ethylenediamine in the presence of 2,2,2-crypt to form $[K(2,2,2\text{-crypt})]_2[Fe(HP_7)_2]$, which contains the Fe-bridged dianion $[Fe(HP_7)_2]^{2-}$ (**18**) (Scheme 4.1). Crystals of $[K(2,2,2\text{-crypt})]_2$[**18**] suitable for single crystal X-ray diffraction were obtained from a pyridine solution layered with toluene. It was later found that the yield could be improved by adding the proton source $[NH_4][BPh_4]$ to the reaction mixture.

$$2P_7^{3-} + 2H^+ + FeCl_2 \longrightarrow [Fe(HP_7)_2]^{2-} + 2Cl^-$$

Scheme 4.1: The formation of $[Fe(HP_7)_2]^{2-}$ from P_7^{3-} and $FeCl_2$.

Shortly after our report on the synthesis of **18**, Wolf and co-workers reported the synthesis of $[P_7FeCp^*]^{2-}$, which was obtained in the reaction of P_4 with $[K(18\text{-crown-6})][Fe(\eta^4\text{-}C_{10}H_8)Cp^*]$.[11] This cluster anion features a norbornadiene-like P_7^{3-} cage bonded to an FeCp* fragment in an η^4-fashion (Figure 4.3).

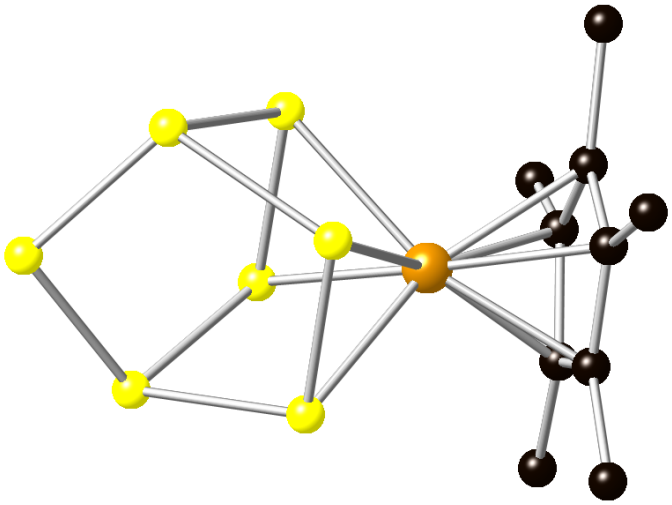

Figure 4.3: Ball and stick diagram of $[P_7FeCp^*]^{2-}$. P atoms are shown in yellow, the Fe atom is shown in brown and C atoms are shown in black. H atoms are omitted for clarity.

4.3.2 Structure of $[Fe(HP_7)_2]^{2-}$ (18)

Cluster **18** consists of two norbornadiene-like HP_7^{2-} cages bridged by an Fe atom (Figures 4.4 and 4.5). The two HP_7^{2-} cages are disordered over two positions, each with 50% occupancy, while the Fe atom sits on a centre of inversion. It is therefore not possible to determine whether the two clusters are eclipsed or staggered relative to each other in the solid state. Each HP_7^{2-} group is bonded to the Fe atom in an η^4-fashion. Each η^4-cluster acts as a six-electron donor, and the Fe is formally in the +2 oxidation state, with a d^6 electron configuration. The Fe atom therefore has eighteen valence electrons and is electronically saturated. **18** is similar to the $[P_7FeCp^*]^{2-}$ cluster anion reported by Wolf, as well as the previously reported $[E_7M(CO)_3]^{3-}$ (E = P, As, Sb; M = Cr, Mo, W) and $[P_7Ni(CO)]^{3-}$ species, which also feature η^4-E_7^{3-} clusters.[11–14]

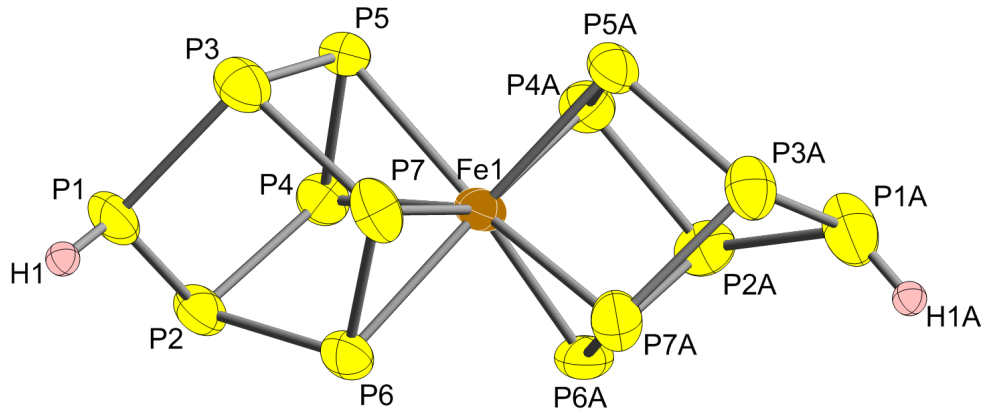

Figure 4.4: Thermal ellipsoid plot of the staggered isomer of **18** with anisotropic displacement ellipsoids pictured at 50% probability. H atoms are shown as small spheres of arbitrary radii.

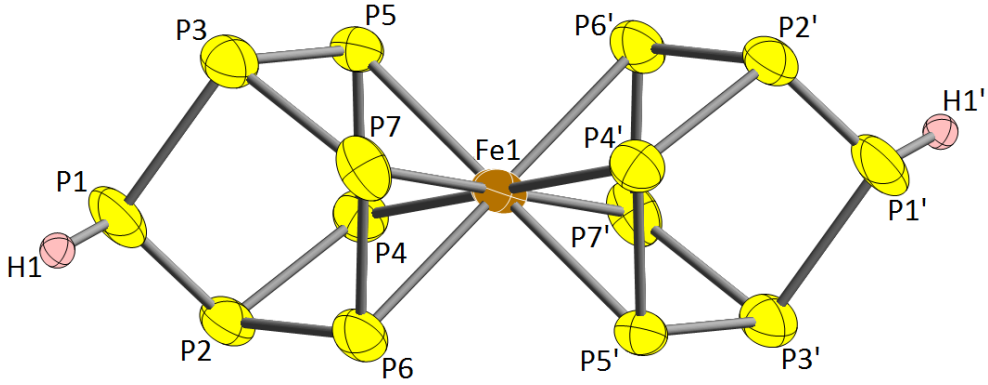

Figure 4.5: Thermal ellipsoid plot of the eclipsed isomer of **18** with anisotropic displacement ellipsoids pictured at 50% probability. H atoms are shown as small spheres of arbitrary radii.

DFT calculations were carried out in order to investigate the electronic structure of **18**. Calculations on the HP_7^{2-} cage revealed four frontier orbitals of π-type symmetry (HOMO–9, HOMO–1, HOMO and LUMO), three of which are full. These orbitals are of comparable symmetry to those of the cyclobutadienyl dianion and are able to interact with a transition metal centre. A fifth frontier orbital (HOMO–11) was found to mainly consist of P–H bonding orbital character (Figure 4.6).

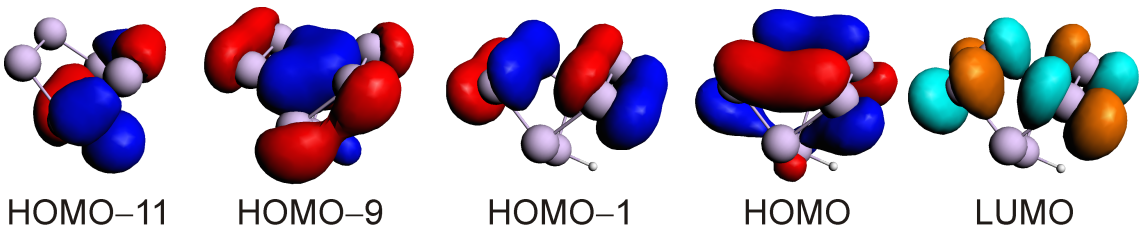

Figure 4.6: Selected frontier orbitals for the optimised structure of HP_7^{2-}.

The principal frontier orbitals for both isomers of **18** have significant metal *d* orbital

character. The HOMO for both isomers are non-bonding and are mainly composed of Fe d_{z^2} character. The HOMO–1 and HOMO–2 have significant d_{xy} and $d_{x^2-y^2}$ character, respectively. For the staggered isomer, these two orbitals are quasi-degenerate, while in the case of the eclipsed isomer, the d_{xy} orbital is non-bonding and mixes with the HOMO. The LUMO and LUMO+1 were found to have predominantly d_{xz} and d_{yz} orbital character, respectively. The corresponding π bonding orbitals are the HOMO–4 and HOMO–11 for the staggered isomer, and HOMO–4 and HOMO–9 for the eclipsed isomer (Figures 4.7 and 4.8). Figures 4.9 and 4.10 show qualitative molecular orbital diagrams for idealised D_{4d} and D_{4h} symmetries of the staggered and eclipsed isomers of an $[Fe(C_4H_4)_2]^{2-}$ type species, respectively. DFT calculations also revealed an energy difference between the staggered and eclipsed isomers of **18** of 40 kJ mol^{-1}, with the staggered isomer being lower in energy.

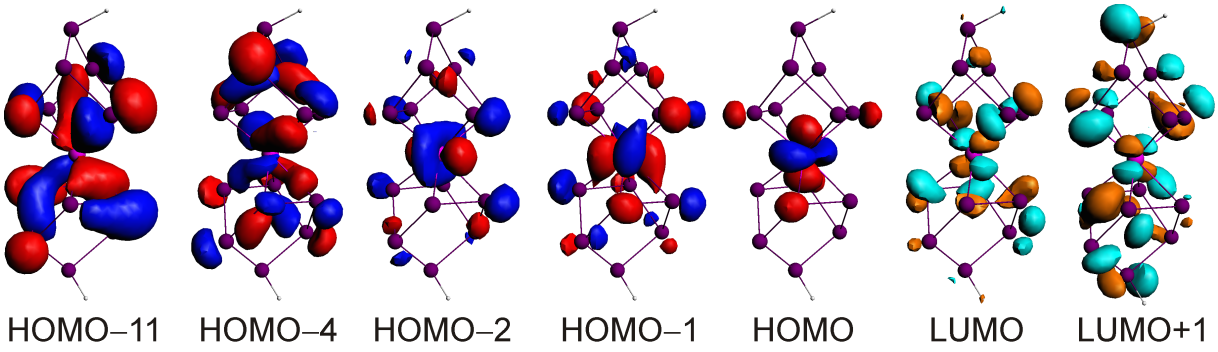

Figure 4.7: Selected frontier orbitals for the optimised structure of the staggered isomer of **18**.

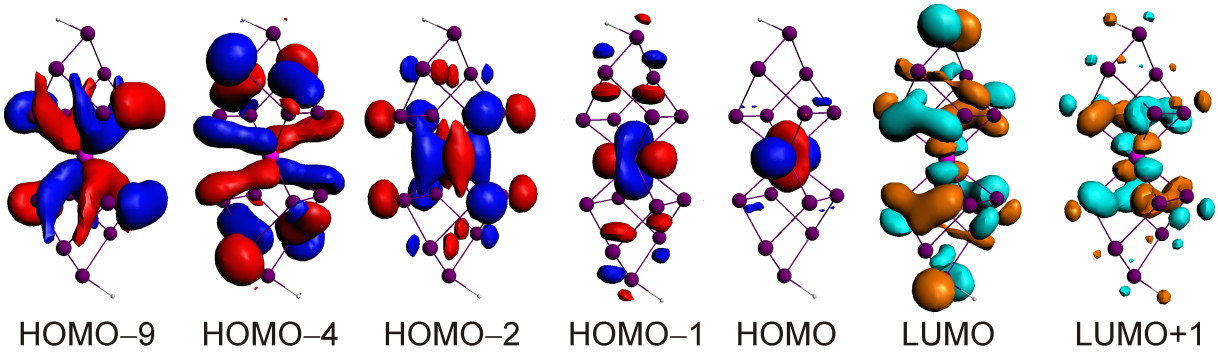

Figure 4.8: Selected frontier orbitals for the optimised structure of the eclipsed isomer of **18**.

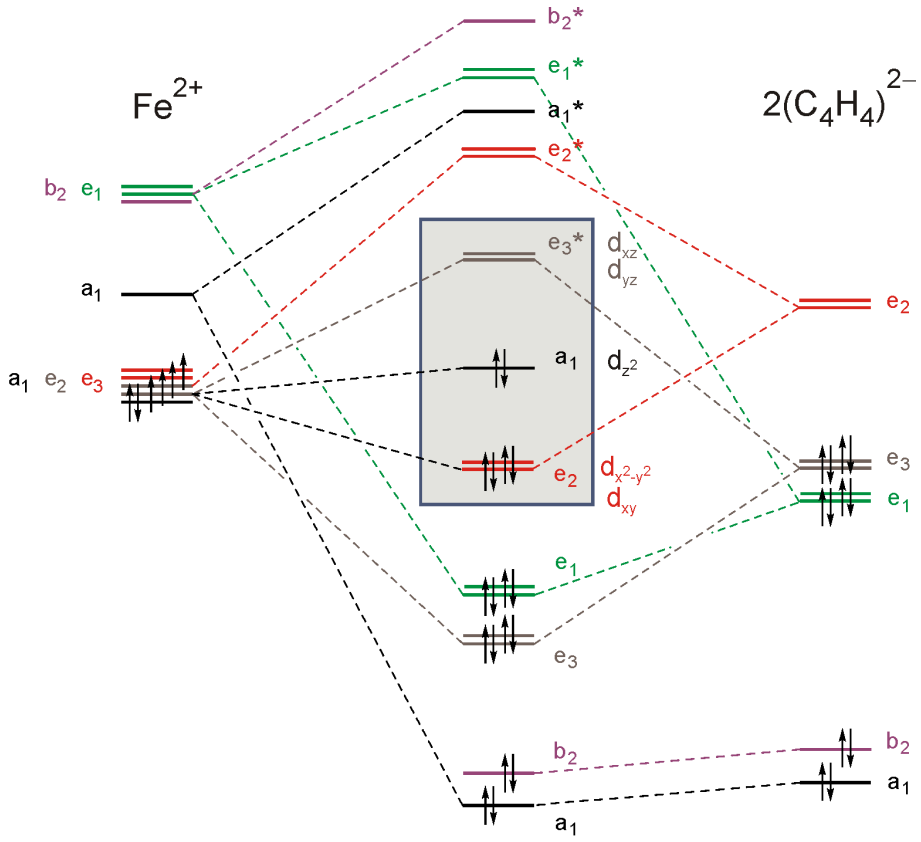

Figure 4.9: Qualitative molecular orbital diagram for the idealised D_{4d} symmetry of the staggered isomer of $[Fe(C_4H_4)_2]^{2-}$.

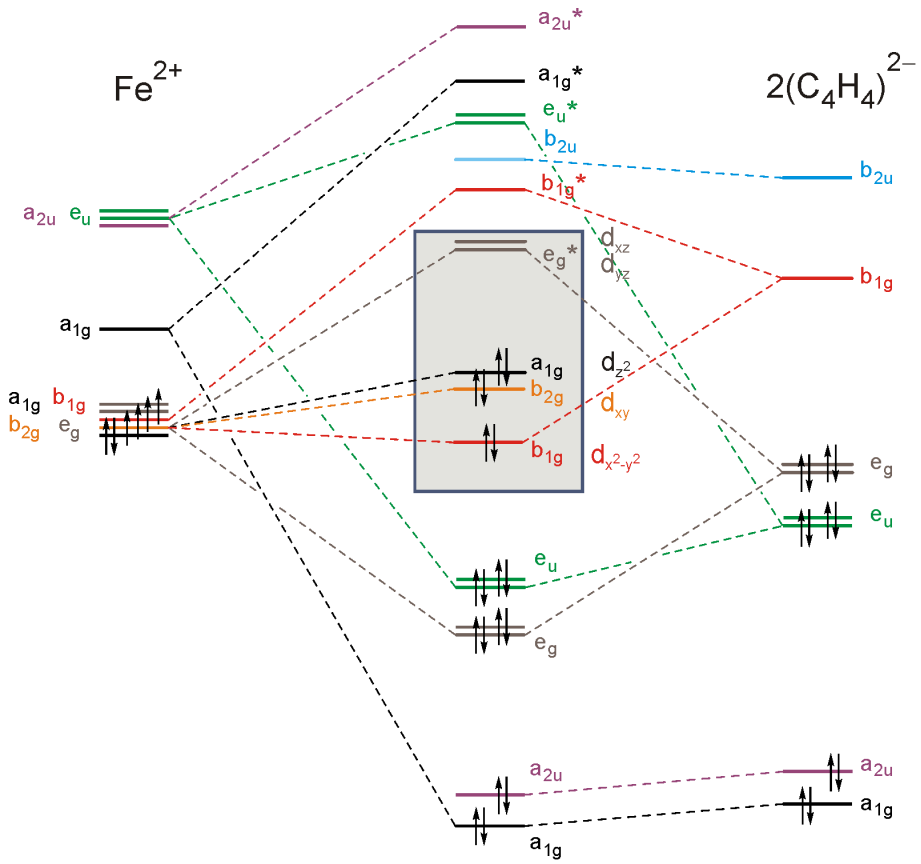

Figure 4.10: Qualitative molecular orbital diagram for the idealised D_{4h} symmetry of the eclipsed isomer of $[Fe(C_4H_4)_2]^{2-}$.

Table 4.1: Selected bond lengths for the $[Fe(HP_7)_2]^{2-}$ species.

Bond	Experimental bond length in **18** (Å)	Calculated bond length for the staggered isomer (Å)	Calculated bond length for the eclipsed isomer (Å)
P1–P2	2.051(7)	2.208	2.207
P1–P3	2.208(6)	2.204	2.203
P2–P4	2.215(3)	2.257	2.251
P2–P6	2.206(3)	2.245	2.253
P3–P5	2.206(3)	2.244	2.248
P3–P7	2.218(3)	2.261	2.251
P4–P5	2.135(3)	2.193	2.180
P4–P6	3.001(3)	3.001	2.921
P5–P7	3.023(3)	3.002	2.965
P6–P7	2.149(3)	2.164	2.155
P1A–P2A	2.177(8)	2.211	2.207
P1A–P3A	2.222(8)	2.209	2.203
P2A–P4A	2.197(3)	2.244	2.250
P2A–P6A	2.222(3)	2.256	2.253
P3A–P5A	2.206(3)	2.259	2.248
P3A–P7A	2.201(3)	2.244	2.251
P4A–P5A	2.132(3)	2.166	2.180
P4A–P6A	3.002(3)	3.004	2.921
P5A–P7A	2.985(3)	3.006	2.965
P6A–P7A	2.153(3)	2.192	2.155
Fe1–P4	2.370(2)	2.367	2.401
Fe1–P5	2.412(2)	2.388	2.399
Fe1–P6	2.464(2)	2.395	2.401
Fe1–P7	2.486(2)	2.374	2.404
Fe1–P4A	2.378(2)	2.394	2.401
Fe1–P5A	2.268(2)	2.372	2.399
Fe1–P6A	2.338(2)	2.370	2.401
Fe1–P7A	2.272(2)	2.392	2.404

Selected bond distances for **18** are provided in Table 4.1, along with selected bond distances for the optimised structures of both the eclipsed and staggered isomers. The disorder exhibited by the cluster anion precludes a meaningful discussion of bond lengths, however some general comparisons with the bond lengths in similar species can be made. The P–P bond lengths in **18** range from 2.051(7) Å to 2.222(3) Å and are, for the most part, similar to those observed in $[P_7FeCp^*]^{2-}$ (2.130(1) Å – 2.251(1) Å) and $[P_7Cr(CO)_3]^{3-}$ (2.114(8) Å – 2.237(9) Å), which also feature η^4-P_7^{3-} cages.[11,13] The P1–P2 bond appears to be anomalously short, at 2.051(7) Å, and this may be a result of the crystallographic disorder. The P4–P6, P5–P7, P4A–P6A and P5A–P7A distances are 3.001(3) Å, 3.023(3) Å, 3.002(3) Å and 2.985(3) Å, respectively. This shows that there is very little asymmetry within the HP_7^{2-} cluster cages, in contrast to $[P_7Cr(CO)_3]^{3-}$,

in which a difference in the corresponding distances of approximately 0.25 Å is observed.[13] The Fe–P bond lengths are in the range 2.268(2) Å – 2.486(2) Å. There is much more variation in these bond lengths in **18** than in $[P_7FeCp^*]^{2-}$, where the Fe–P bond lengths range from 2.314(1) Å to 2.332(1) Å.[11] This may also result from the disorder present in **18**. A search of the CSD gave a mean Fe–P bond length of 2.242(av) Å, while the sum of covalent radii for Fe–P single bonds is 2.27 Å.[15,16]

4.3.3 NMR spectroscopic studies on $[Fe(HP_7)_2]^{2-}$ (18)

The ^{1}H NMR spectrum of **18** shows a doublet at 6.56 ppm, which corresponds to the proton attached to the P_7^{3-} cage, H1/H1A. The ^{1}H–^{31}P coupling constant is equal to 169 Hz. This resonance appears as a singlet upon selective decoupling of the P1/P1A resonance (Figure 4.11). The ^{31}P NMR spectrum of **18** shows four resonances: a triplet of doublets of relative intensity one at 151.3 ppm, and three broad multiplets of relative intensity two at –0.5, –80.5 and –121.6 ppm (Figure 4.12). These resonances are consistent with the solid state structure. The resonance at 151.3 ppm appears as a triplet in the ^{31}P{^{1}H} spectrum and can be assigned to the protonated P atom, P1/P1A, while the resonance at –0.5 ppm corresponds to P2/P2A and P3/P3A (according to the numbering scheme used in Figures 4.4 and 4.5). The two remaining resonances could not be unequivocally assigned, but correspond to the P4/P4A and P5/P5A, and P6/P6A and P7/P7A sets of nuclei.

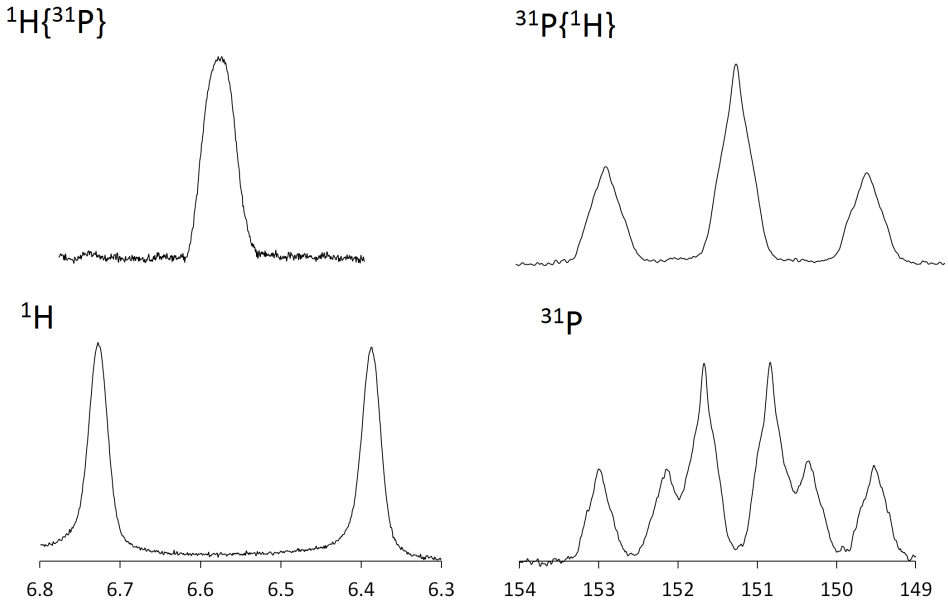

Figure 4.11: Selected regions of the ^{1}H{^{31}P}, ^{1}H, ^{31}P{^{1}H} and ^{31}P NMR spectra of **18**.

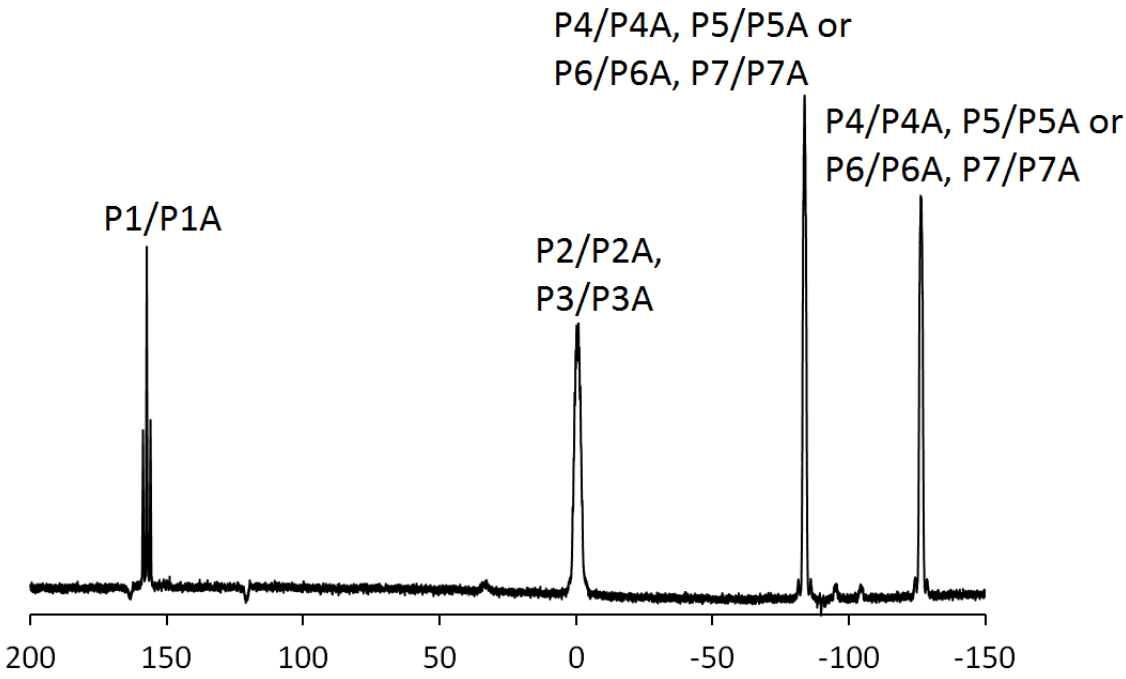

Figure 4.12: ^{31}P NMR spectrum of **18** recorded in d_5-pyridine.

4.3.4 Mass spectrometric studies

The positive and negative ion mode ESI mass spectra of **18** confirm that the product is $[Fe(HP_7)_2]^{2-}$. The negative ion mode mass spectrum shows a peak corresponding to the oxidised cluster anion, $[Fe(HP_7)_2]^-$, as well as a peak arising from the cluster anion accompanied by one $[K(2,2,2\text{-crypt})]^+$ cation. The largest peak in the postive ion mode spectrum corresponds to the cluster anion with three $[K(2,2,2\text{-crypt})]^+$ cations (Figure 4.13).

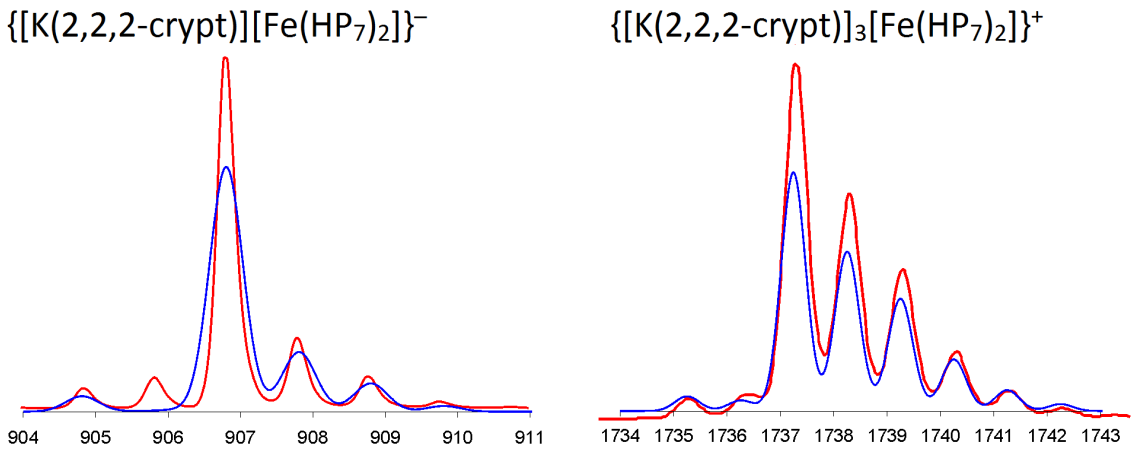

Figure 4.13: ESI-MS mass envelopes for $\{[K(2,2,2\text{-crypt})][Fe(HP_7)_2]\}^-$ and $\{[K(2,2,2\text{-crypt})]_3[Fe(HP_7)_2]\}^+$. Predicted isotopic distributions are shown in blue and observed mass spectrometric data are shown in red.

4.3.5 Reactivity studies of $[Fe(HP_7)_2]^{2-}$ (18)

NMR studies have shown that **18** can be deprotonated by two equivalents of KO^{t}Bu or K[N(SiMe$_3$)$_2$] to form $[Fe(P_7)_2]^{4-}$ (**19**) (Scheme 4.2). Crystals of neither [K(2,2,2-crypt)]$_4$[**19**] nor [K(18-crown-6)]$_4$[**19**] could be obtained, although many different solvent combinations were tried. The identity of the product was confirmed by ^{31}P NMR spectroscopy and mass spectrometry.

$$[Fe(HP_7)_2]^{2-} + 2[N(SiMe_3)_2]^- \longrightarrow [Fe(P_7)_2]^{4-} + 2(SiMe_3)_2NH$$

Scheme 4.2: The formation of $[Fe(P_7)_2]^{4-}$ from $[Fe(HP_7)_2]^{2-}$ and K[N(SiMe$_3$)$_2$].

The spectroscopic data for **19** are consistent with two norbornadiene-like P_7^{3-} clusters bonded to an Fe centre in an η^4-fashion. Each P_7^{3-} cluster acts as a six-electron donor, and the Fe is formally in the +2 oxidation state, with a d^6 electron configuration. Overall, therefore, the Fe possesses eighteen valence electrons. Geometry optimisations were performed for both the eclipsed and staggered isomers of **19**, and the optimised computed structures are shown in Figures 4.14 and 4.15.

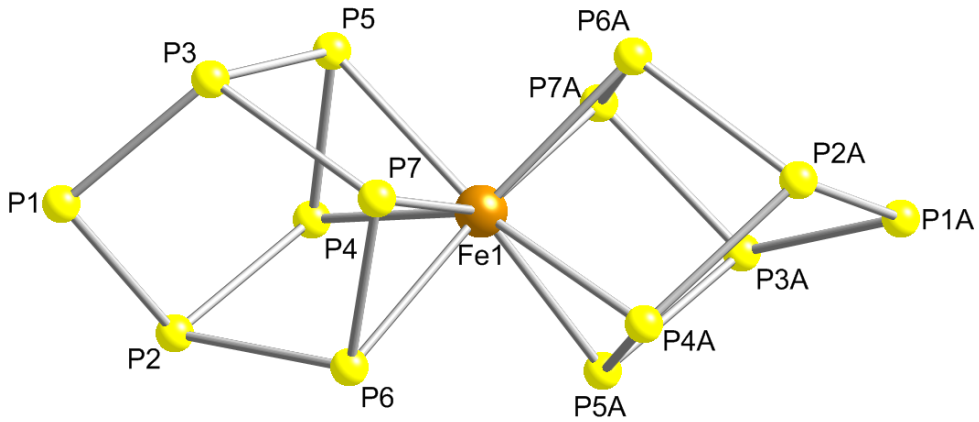

Figure 4.14: Diagram showing the optimised structure of the staggered isomer of **19**.

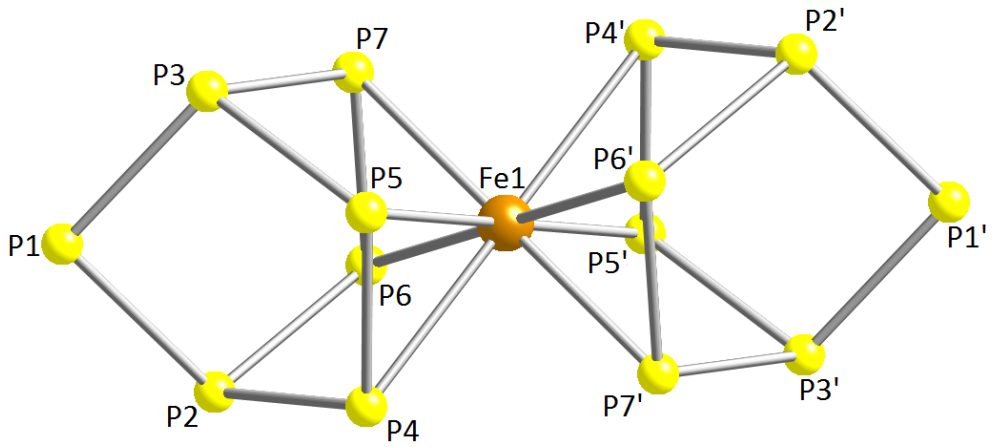

Figure 4.15: Diagram showing the optimised structure of the eclipsed isomer of **19**.

Table 4.2: Selected calculated bond lengths for the $[Fe(P_7)_2]^{4-}$ species.

Bond	Calculated bond length for the staggered isomer (Å)	Calculated bond length for the eclipsed isomer (Å)
P1–P2	2.172	2.322
P1–P3	2.170	2.152
P2–P4	2.281	2.180
P2–P6	2.266	2.216
P3–P5	2.267	2.218
P3–P7	2.283	2.189
P4–P5	2.159	2.161
P4–P6	2.954	2.982
P5–P7	2.954	2.999
P6–P7	2.159	2.149
P1A–P2A	2.171	2.322
P1A–P3A	2.170	2.152
P2A–P4A	2.267	2.180
P2A–P6A	2.281	2.216
P3A–P5A	2.282	2.218
P3A–P7A	2.266	2.189
P4A–P5A	2.158	2.161
P4A–P6A	2.952	2.982
P5A–P7A	2.947	2.999
P6A–P7A	2.159	2.149
Fe1–P4	2.371	2.385
Fe1–P5	2.384	2.220
Fe1–P6	2.386	2.384
Fe1–P7	2.370	2.301
Fe1–P4A	2.385	2.385
Fe1–P5A	2.372	2.220
Fe1–P6A	2.373	2.384
Fe1–P7A	2.383	2.301

Selected calculated bond distances for both isomers of **19** are provided in Table 4.2. The calculated P–P bond lengths for the staggered isomer range from 2.158 Å to 2.283 Å and are,

for the most part, in good agreement with the calculated P–P bond lengths for the staggered isomer of **18** (2.164 Å – 2.261 Å). The corresponding bond lengths for the eclipsed isomer of **19** are in the range 2.149 Å – 2.322 Å. Most of these bond lengths are similar to those calculated for the eclipsed isomer of **18**, which range from 2.155 Å to 2.253 Å. The P1–P2 bond appears to be anomalously long, at 2.322 Å. The calculated Fe–P bond lengths range from 2.370 Å to 2.386 Å in the staggered isomer, and from 2.220 Å to 2.385 Å in the eclipsed isomer. These are, for the most part, similar to the calculated Fe–P bond lengths in **18** (2.367 Å – 2.395 Å for the staggered isomer; 2.399 Å – 2.404 Å for the eclipsed isomer), although the Fe1–P5 bond is significantly shorter than the other calculated Fe–P bond lengths for the eclipsed isomer of **19**. However, without a crystal structure, only limited conclusions about the bonding within **19** can be drawn. Similar to **18**, the staggered isomer was calculated to be approximately 40 kJ mol^{-1} lower in energy than the eclipsed isomer.

The ^{31}P NMR spectrum of **19** shows three resonances at 234.4, –0.5 and –82.3 ppm with relative intensities 1:2:4 (Figure 4.16). These resonances are consistent with the presence of two non-protonated η^4-P_7^{3-} clusters. The four Fe-bound P atoms become chemically equivalent on deprotonation. The resonances can be assigned to P1/P1A, P2/P2A and P3/P3A, and P4/P4A, P5/P5A, P6/P6A and P7/P7A, in order of decreasing chemical shift. No differences between the ^{31}P and ^{31}P{^{1}H} spectra were observed, showing that the two P_7^{3-} clusters must be non-protonated. The spectrum was simulated in order to obtain the ^{31}P–^{31}P coupling constants (Table 4.3).

Table 4.3: The ^{31}P chemical shift values and coupling constants for $[Fe(P_7)_2]^{4-}$.

δ (ppm)		234.4 P1/P1A	–0.5 P2/P2A	–0.5 P3/P3A	–82.3 P4/P4A	–82.3 P5/P5A	–82.3 P6/P6A	–82.3 P7/P7A
234.4	P1/P1A		–375	–374	–	–	–	–
–0.5	P2/P2A	–375		–	–230	–	–233	–
–0.5	P3/P3A	–374	–		–	–233	–	–225
–82.3	P4/P4A	–	–230	–		–485	–	–
–82.3	P5/P5A	–	–	–233	–485		–	–
–82.3	P6/P6A	–	–233	–	–	–		–485
–82.3	P7/P7A	–	–	–225	–	–	–485	

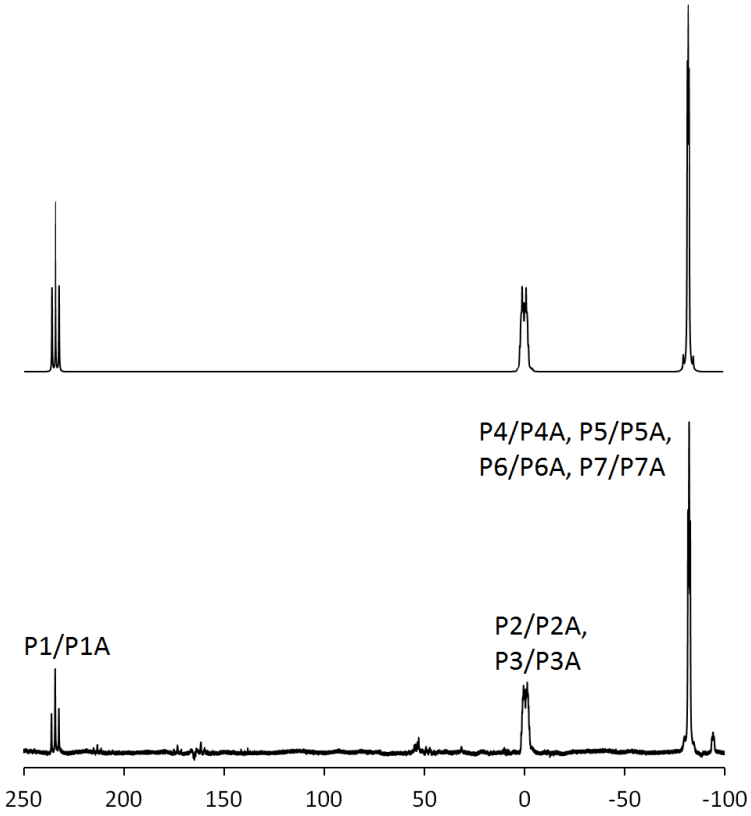

Figure 4.16: Top: The simulated ^{31}P NMR spectrum of **19**. Bottom: The ^{31}P{^{1}H} NMR spectrum of **19** recorded in d_5-pyridine.

The positive and negative ion mode mass spectra of **19** are very similar to those obtained for **18**, although more extensive ion pairing is observed due to the greater cluster charge. The dominant peak in the negative ion mode spectrum corresponds to $[Fe(P_7)_2]^-$. Peaks arising from the cluster anion accompanied by up to three $[K(2,2,2\text{-crypt})]^+$ cations are also observed. The major peaks in the positive ion mode mass spectrum correspond to the cluster anion paired with four and five $[K(2,2,2\text{-crypt})]^+$ ions.

4.4 Solution reactivity of P_7^{3-} towards $[Ru(PPh_3)_3Cl_2]$

4.4.1 Synthesis of $[Ru(HP_7)_2]^{2-}$ (20)

Ethylenediamine solutions of K_3P_7 react with $[Ru(PPh_3)_3Cl_2]$ in the presence of a cation sequestering agent to form a mixture of $[Ru(HP_7)_2]^{2-}$ (**20**) and $[Ru(P_7)_2]^{4-}$ (**21**). A pure sample of **20** could not be obtained, although the reaction was repeated many times under varying conditions. In particular, addition of the proton source $[NH_4][BPh_4]$ did not lead to the

formation of **20**, but instead resulted in significant decomposition. Other proton sources were also tried, with no success. Crystals of neither [K(2,2,2-crypt)]$_2$[**20**] nor [K(18-crown-6)]$_2$[**20**] could be obtained, although many different solvent systems were tried. The identity of the product was confirmed by ^{1}H and ^{31}P NMR spectroscopy, and by mass spectrometry.

$$2P_7^{3-} + 2H^+ + [Ru(PPh_3)_3Cl_2] \longrightarrow [Ru(HP_7)_2]^{2-} + 2Cl^- + 3PPh_3$$

Scheme 4.3: The formation of $[Ru(HP_7)_2]^{2-}$ from P_7^{3-} and $[Ru(PPh_3)_3Cl_2]$.

Cluster **20** is predicted to have the same structure as **18**, consisting of two HP_7^{2-} cages bonded to a Ru atom in an η^4-fashion (Figures 4.17 and 4.18). Each HP_7^{2-} cluster acts as a six-electron donor, while the Ru is formally in the +2 oxidation state, with a d^6 electron configuration. The Ru therefore possesses a total of eighteen valence electrons and is electronically saturated.

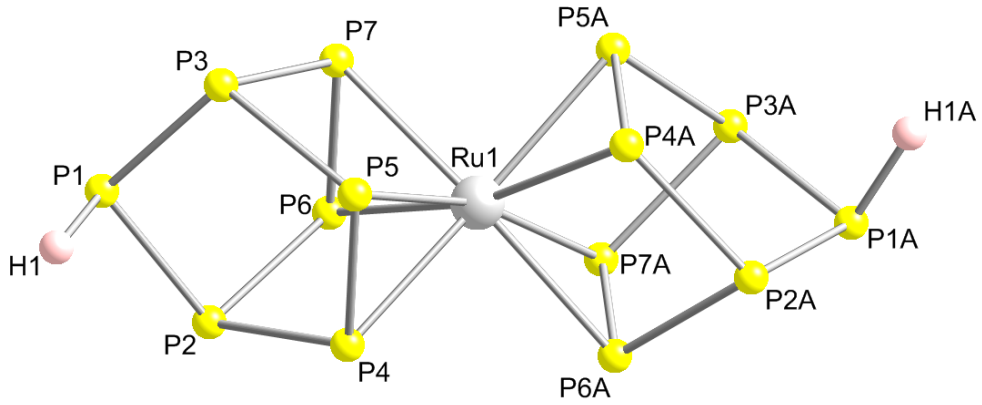

Figure 4.17: Diagram showing the optimised structure of the staggered isomer of **20**.

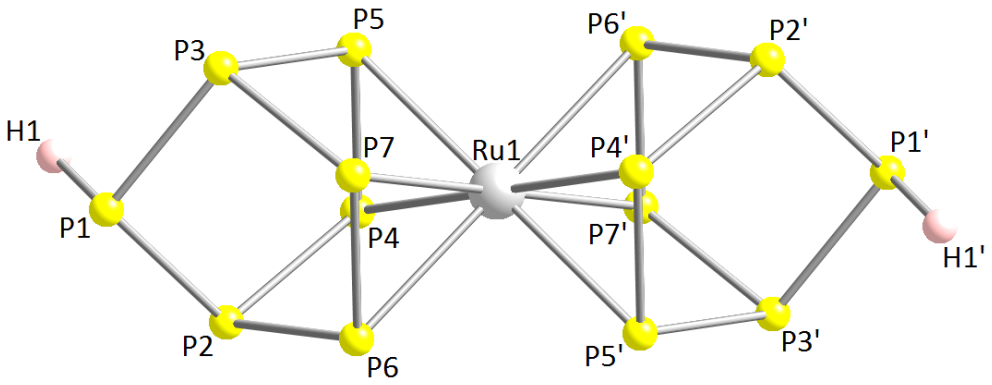

Figure 4.18: Diagram showing the optimised structure of the eclipsed isomer of **20**.

Selected calculated bond distances for both isomers of **20** are provided in Table 4.4. The calculated P–P bond lengths for the staggered isomer range from 2.162 Å to 2.258 Å and are in good agreement with the corresponding bond lengths for the staggered isomers of both **18**

(2.164 Å – 2.261 Å) and **19** (2.158 Å – 2.283 Å). In the case of the eclipsed isomer, the calculated P–P bond lengths are in the range 2.175 Å – 2.258 Å and are similar to those obtained for the eclipsed isomers of **18** (2.155 Å – 2.253 Å) and **19** (2.149 Å – 2.322 Å). The Ru–P bond lengths range from 2.496 Å to 2.504 Å for the staggered isomer, and from 2.506 Å to 2.508 Å for the eclipsed isomer. DFT calculations also gave an energy difference between the staggered and eclipsed isomers of **20** of approximately 20 kJ mol^{-1}, with the staggered isomer being slightly lower in energy.

Table 4.4: Selected calculated bond lengths for the $[Ru(HP_7)_2]^{2-}$ species.

Bond	Calculated bond length for the staggered isomer (Å)	Calculated bond length for the eclipsed isomer (Å)
P1–P2	2.203	2.216
P1–P3	2.204	2.216
P2–P4	2.254	2.256
P2–P6	2.257	2.258
P3–P5	2.255	2.256
P3–P7	2.258	2.257
P4–P5	2.163	2.175
P4–P6	3.039	3.039
P5–P7	3.033	3.049
P6–P7	2.184	2.200
P1A–P2A	2.204	2.216
P1A–P3A	2.203	2.215
P2A–P4A	2.253	2.256
P2A–P6A	2.258	2.258
P3A–P5A	2.254	2.256
P3A–P7A	2.257	2.257
P4A–P5A	2.162	2.175
P4A–P6A	3.037	3.038
P5A–P7A	3.034	3.050
P6A–P7A	2.184	2.200
Ru1–P4	2.498	2.508
Ru1–P5	2.504	2.507
Ru1–P6	2.496	2.508
Ru1–P7	2.502	2.506
Ru1–P4A	2.504	2.508
Ru1–P5A	2.503	2.507
Ru1–P6A	2.501	2.508
Ru1–P7A	2.497	2.507

4.4.2 NMR spectroscopic studies on $[Ru(HP_7)_2]^{2-}$ (20)

The ^{1}H NMR spectrum of **20** shows a doublet at 6.44 ppm (*c.f.* 6.56 ppm for **18**), which corresponds to the proton attached to the P_7^{3-} cage, H1/H1A. The ^{1}H–^{31}P coupling constant is equal to 165 Hz. This resonance appears as a singlet in the ^{1}H{^{31}P} spectrum (Figure 4.19). The ^{31}P NMR spectrum of **20** shows a triplet of doublets of relative intensity one at 125.0 ppm, and three broad multiplets of relative intensity two at 33.9, –84.0 and –126.7 ppm (Figure 4.20). These values compare well with those observed for the Fe analogue, **18** (151.3, –0.5, –80.5 and –121.6 ppm). The resonance at 125.0 ppm appears as a triplet in the ^{31}P{^{1}H} spectrum and can be assigned to the protonated P atom, P1/P1A, while the resonance at 33.9 ppm corresponds to P2/P2A and P3/P3A. The two remaining resonances could not be unequivocally assigned, but correspond to the P4/P4A and P5/P5A, and P6/P6A and P7/P7A sets of nuclei. The spectrum also shows three additional resonances at 217.3, 6.6 and –72.7 ppm with relative intensities 1:2:4, corresponding to the non-protonated cluster anion, **21**, as well as two resonances that correspond to HP_7^{2-} and a single resonance due to free PPh_3.[17–19] The integrals of the resonances suggest that an approximately 1:1 mixture of **20** and **21** is formed.

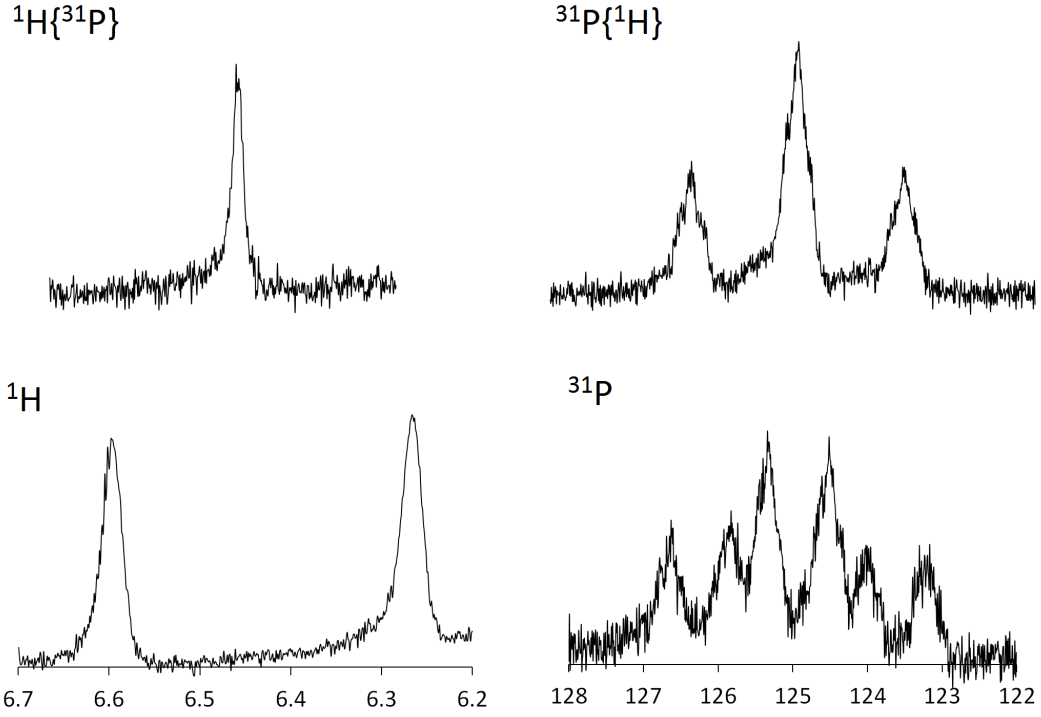

Figure 4.19: Selected regions of the ^{1}H{^{31}P}, ^{1}H, ^{31}P{^{1}H} and ^{31}P NMR spectra of **20**.

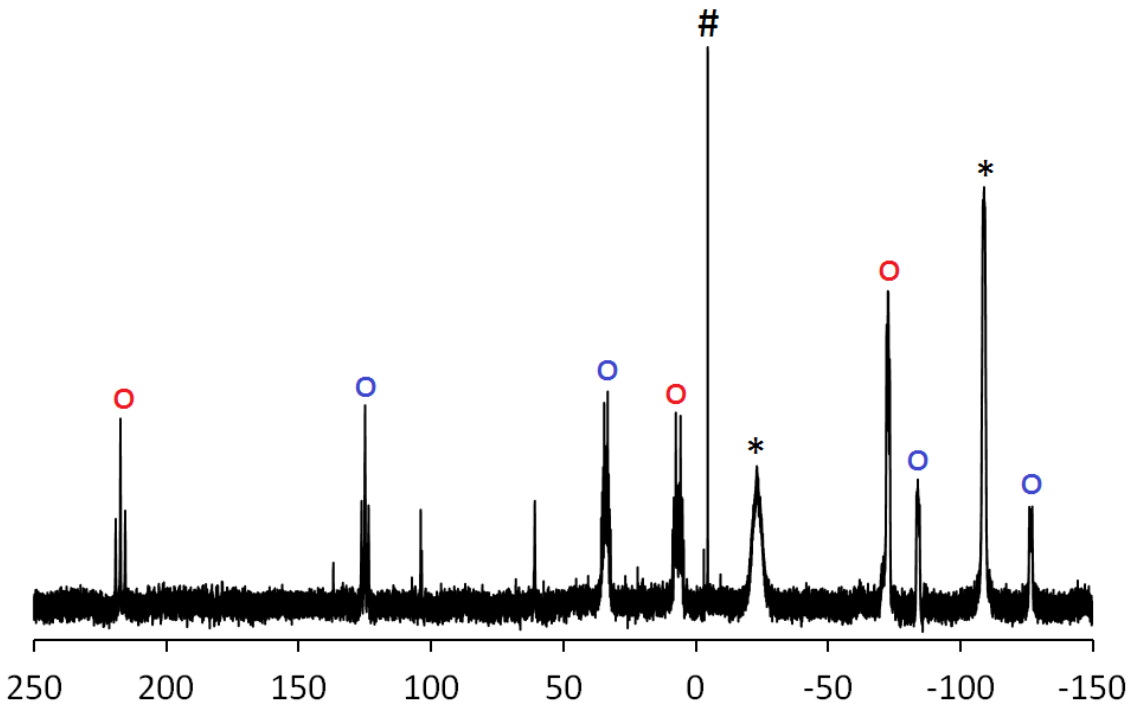

Figure 4.20: ^{31}P NMR spectrum of **20** recorded in d_5-pyridine. Resonances labelled in blue correspond to **20**, resonances labelled in red correspond to **21**, resonances labelled * correspond to HP_7^{2-}, and the resonance labelled # corresponds to PPh_3.

4.4.3 Mass spectrometric studies

The positive and negative ion mode ESI mass spectra of **20** confirm that the product is $[Ru(HP_7)_2]^{2-}$. The negative ion mode mass spectrum shows a peak due to the oxidised cluster anion, $[Ru(HP_7)_2]^-$, and a peak corresponding to the cluster anion accompanied by one $[K(2,2,2\text{-crypt})]^+$ cation. The largest peak in the positive ion mode spectrum corresponds to the cluster anion accompanied by three $[K(2,2,2\text{-crypt})]^+$ ions (Figure 4.21).

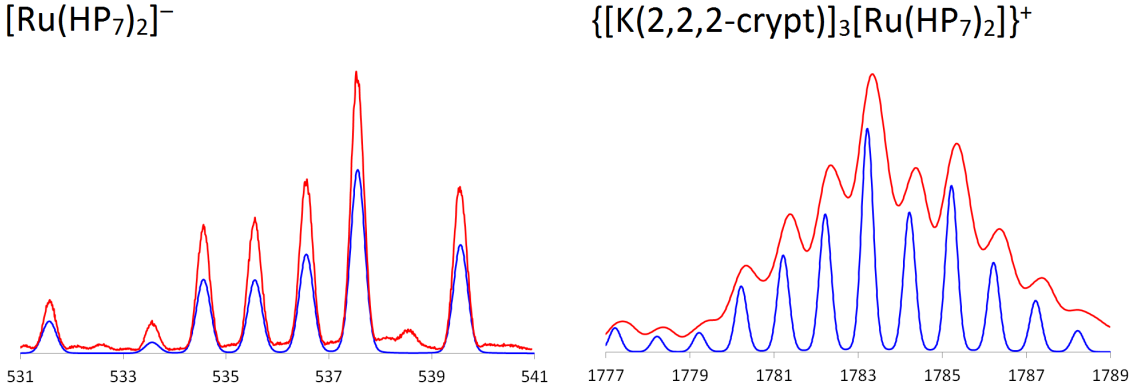

Figure 4.21: ESI-MS mass envelopes for $[Ru(HP_7)_2]^-$ and $\{[K(2,2,2\text{-crypt})]_3[Ru(HP_7)_2]\}^+$. Predicted isotopic distributions are shown in blue and observed mass spectrometric data are shown in red.

4.4.4 Reactivity studies of $[Ru(HP_7)_2]^{2-}$ (20)

As mentioned previously, a pure sample of **20** could not be obtained, however it was possible to obtain a significantly cleaner sample of the non-protonated cluster anion, **21**, by adding KO^tBu or $K[N(SiMe_3)_2]$ to a mixture of **20** and **21**. All attempts to obtain crystalline samples of $[K(2,2,2\text{-crypt})]_4$[**21**] and $[K(18\text{-crown-6})]_4$[**21**] were unsuccessful, although a variety of solvents and anti-solvents were tried. The identity of the product was confirmed by ^{31}P NMR spectroscopy and mass spectrometry.

$$[Ru(HP_7)_2]^{2-} + 2[N(SiMe_3)_2]^- \longrightarrow [Ru(P_7)_2]^{4-} + 2(SiMe_3)_2NH$$

Scheme 4.4: The formation of $[Ru(P_7)_2]^{4-}$ from $[Ru(HP_7)_2]^{2-}$ and $K[N(SiMe_3)_2]$.

Diagrams showing the optimised computed structures of the staggered and eclipsed isomers of **21** are provided in Figures 4.22 and 4.23, respectively. The spectroscopic data are consistent with two norbornadiene-like P_7^{3-} clusters bonded to a Ru centre in an η^4-fashion.

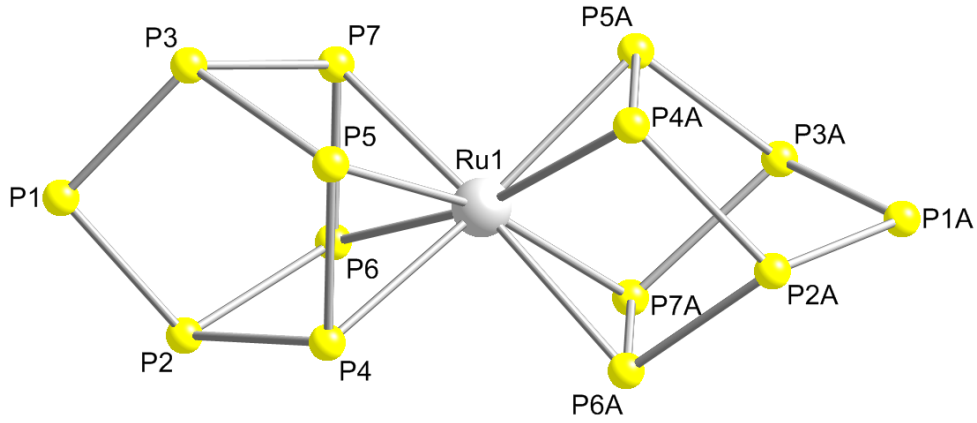

Figure 4.22: Diagram showing the optimised structure of the staggered isomer of **21**.

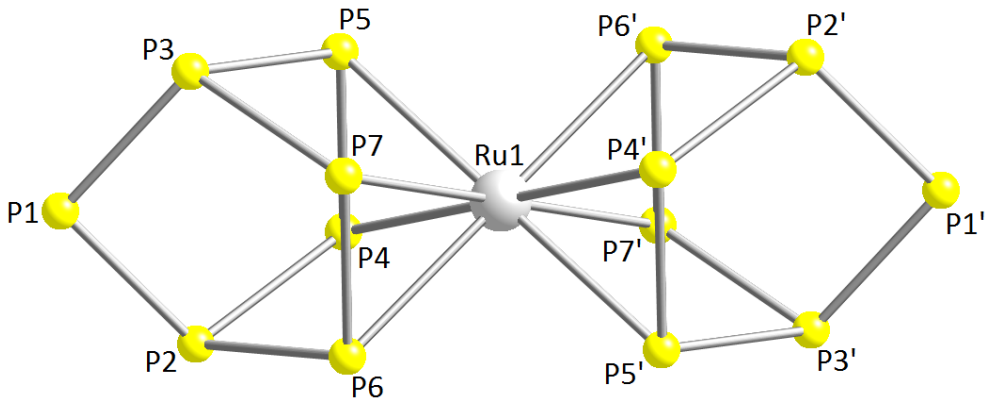

Figure 4.23: Diagram showing the optimised structure of the eclipsed isomer of **21**.

Selected calculated bond distances for both isomers of **21** are provided in Table 4.5. The calculated P–P bond lengths for the staggered isomer are in the range 2.154 Å – 2.287 Å and are in good agreement with those obtained for the staggered isomers of **18** (2.164 Å – 2.261 Å), **19** (2.158 Å – 2.283Å) and **20** (2.162 Å – 2.258 Å). The corresponding bond lengths for the eclipsed isomer range from 2.160 Å to 2.277 Å and are similar to those calculated for the eclipsed isomers of **18** (2.155 Å – 2.253 Å), **19** (2.149 Å – 2.322 Å) and **20** (2.175 Å – 2.258 Å). The Ru–P bond lengths in the staggered isomer range from 2.496 Å to 2.501 Å, while those in the eclipsed isomer range from 2.502 Å to 2.507 Å. These are similar to the Ru–P bond lengths calculated for the staggered and eclipsed isomers of **20**, which are in the ranges 2.496 Å – 2.504 Å and 2.506 Å – 2.508 Å, respectively. The staggered isomer of **21** was calculated to be approximately 5 kJ mol^{-1} lower in energy than the eclipsed isomer.

Table 4.5: Selected calculated bond lengths for the $[Ru(P_7)_2]^{4-}$ species.

Bond	Calculated bond length for the staggered isomer (Å)	Calculated bond length for the eclipsed isomer (Å)
P1–P2	2.166	2.169
P1–P3	2.167	2.169
P2–P4	2.286	2.277
P2–P6	2.285	2.276
P3–P5	2.285	2.277
P3–P7	2.286	2.277
P4–P5	2.155	2.160
P4–P6	3.002	3.000
P5–P7	2.989	2.999
P6–P7	2.154	2.161
P1A–P2A	2.167	2.169
P1A–P3A	2.166	2.169
P2A–P4A	2.285	2.277
P2A–P6A	2.287	2.276
P3A–P5A	2.285	2.277
P3A–P7A	2.286	2.277
P4A–P5A	2.155	2.160
P4A–P6A	3.000	3.000
P5A–P7A	2.994	2.999
P6A–P7A	2.154	2.161
Ru1–P4	2.499	2.506
Ru1–P5	2.496	2.507
Ru1–P6	2.500	2.507
Ru1–P7	2.500	2.502
Ru1–P4A	2.497	2.506
Ru1–P5A	2.497	2.507
Ru1–P6A	2.496	2.507
Ru1–P7A	2.501	2.502

The ^{31}P NMR spectrum of **21** shows three resonances at 212.4, 13.6 and –83.7 ppm with relative intensities 1:2:4 (Figure 4.24). These correspond to P1/P1A, P2/P2A and P3/P3A, and P4/P4A, P5/P5A, P6/P6A and P7/P7A, respectively. No differences between the ^{31}P and ^{31}P{^{1}H} spectra were observed, showing that the two P_7^{3-} clusters are not protonated. The spectrum was simulated in order to obtain the ^{31}P–^{31}P coupling constants (Table 4.6). Two resonances corresponding to an HP_7^{2-} impurity are also observed, as well as a single resonance due to free PPh_3.[17–19]

Table 4.6: The ^{31}P chemical shift values and coupling constants for $[Ru(P_7)_2]^{4-}$.

δ (ppm)		212.4 P1/P1A	13.6 P2/P2A	13.6 P3/P3A	–83.7 P4/P4A	–83.7 P5/P5A	–83.7 P6/P6A	–83.7 P7/P7A
212.4	P1/P1A		–376	–376	–	–	–	–
13.6	P2/P2A	–376		–	–251	–	–241	–
13.6	P3/P3A	–376	–		–	–243	–	–237
–83.7	P4/P4A	–	–251	–		–485	–	–
–83.7	P5/P5A	–	–	–243	–485		–	–
–83.7	P6/P6A	–	–241	–	–	–		–485
–83.7	P7/P7A	–	–	–237	–	–	–485	

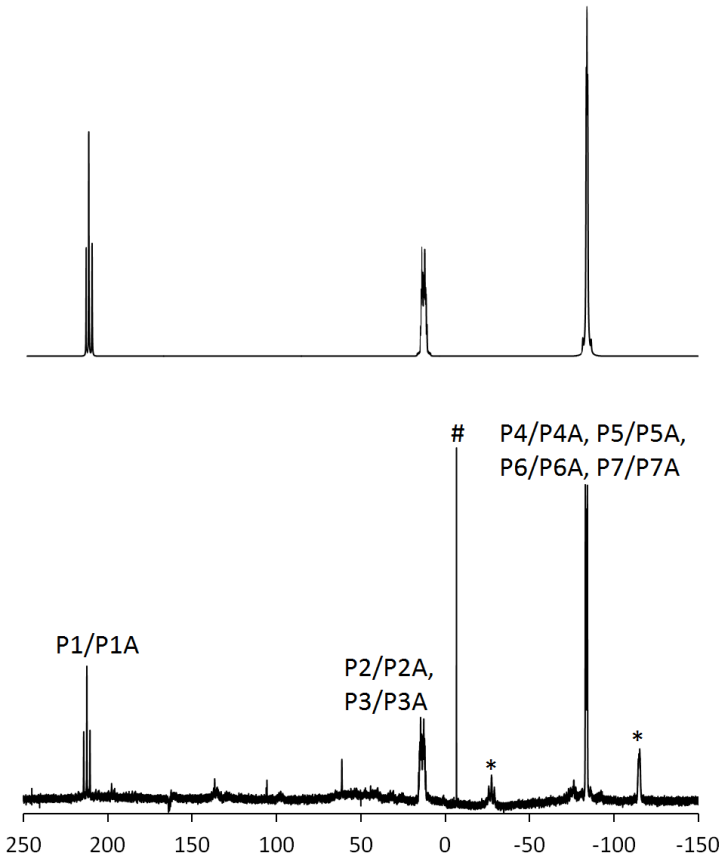

Figure 4.24: Top: The simulated ^{31}P NMR spectrum of **21**. Bottom: The ^{31}P{^{1}H} NMR spectrum of **21** recorded in d_5-pyridine. Resonances labelled * correspond to HP_7^{2-}, and the resonance labelled # corresponds to PPh_3.

The positive and negative ion mode ESI mass spectra of **21** are very similar to those of **20**, although more extensive ion pairing is observed due to the greater cluster charge. The negative ion mode spectrum shows a peak due to the oxidised cluster anion, $[Ru(P_7)_2]^-$, as well as peaks corresponding to the cluster anion accompanied by up to three $[K(2,2,2\text{-crypt})]^+$ ions. The major peaks in the positive ion mode spectrum correspond to the cluster anion paired with four and five $[K(2,2,2\text{-crypt})]^+$ ions.

4.5 Solution reactivity of P_7^{3-} towards $[Ru(COD)(\eta^3\text{-}CH_2C(CH_3)CH_2)_2]$

4.5.1 Synthesis of $[(C_4H_7)P_7Ru(COD)]^{2-}$ (22)

K_3P_7 reacts with $[Ru(COD)(\eta^3\text{-}CH_2C(CH_3)CH_2)_2]$ in ethylenediamine in the presence of 2,2,2-crypt to form $[K(2,2,2\text{-crypt})]_2[(C_4H_7)P_7Ru(COD)]$ (Scheme 4.5). This compound contains the Ru-derivatised and alkylated cluster anion $[(C_4H_7)P_7Ru(COD)]^{2-}$ (**22**). Crystals of $[K(2,2,2\text{-crypt})]_2$[**22**]·tol suitable for single crystal X-ray diffraction were obtained by slow diffusion of toluene into a solution of the compound in pyridine.

$$P_7^{3-} + [Ru(COD)(\eta^3\text{-}CH_2C(CH_3)CH_2)_2] \longrightarrow [(C_4H_7)P_7Ru(COD)]^{2-} + CH_2C(CH_3)CH_2^-$$

Scheme 4.5: The formation of $[(C_4H_7)P_7Ru(COD)]^{2-}$ from P_7^{3-} and $[Ru(COD)(\eta^3\text{-}CH_2C(CH_3)CH_2)_2]$.

4.5.2 Structure of $[(C_4H_7)P_7Ru(COD)]^{2-}$ (22)

Cluster **22** comprises a norbornadiene-like $(C_4H_7)P_7^{2-}$ cage bonded to a Ru(COD) fragment in an η^4-fashion (Figure 4.25). The Ru is formally in the zero oxidation state, with a d^8 electron configuration, and the COD ligand and the η^4-$(C_4H_7)P_7^{2-}$ cluster act as four- and six-electron donors, respectively. The Ru therefore possesses a total of eighteen valence electrons. **22** is very similar to the previously reported $[RP_7W(CO)_3]^{2-}$ (R = Me, Et, Bu, $PhCH_2$) species, which also feature alkylated η^4-E_7^{3-} clusters.[20] The C_4H_7 group is disordered over two positions, which have relative occupancies of 70% and 30%. Only the major component of the disorder is shown in Figure 4.25.

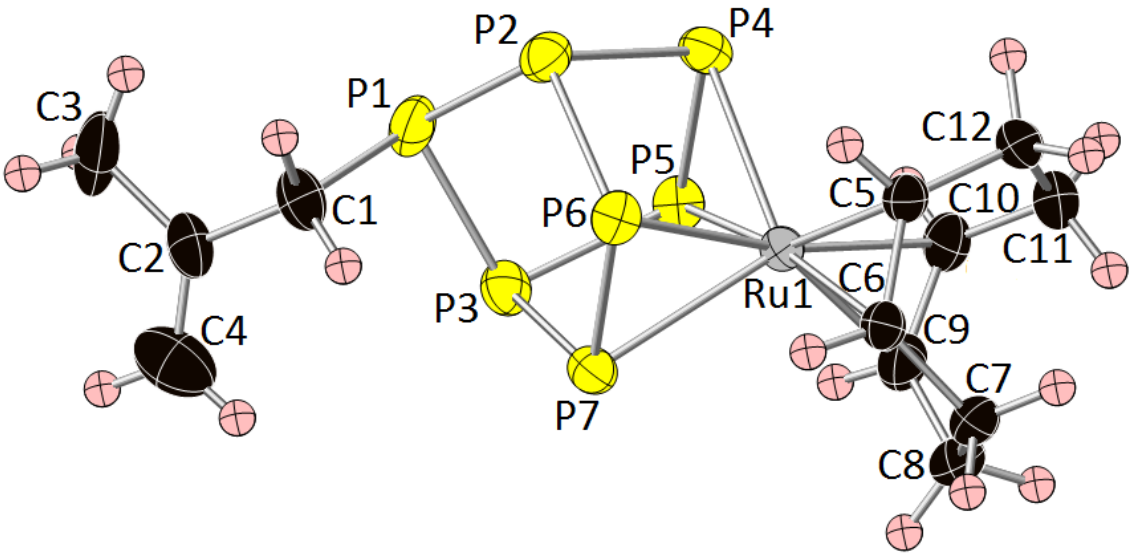

Figure 4.25: Thermal ellipsoid plot of **22** with anisotropic displacement ellipsoids pictured at 50% probability. H atoms are shown as small spheres of arbitrary radii.

Table 4.7: Selected bond lengths for the $[(C_4H_7)P_7Ru(COD)]^{2-}$ species.

Bond	Bond length in **22** (Å)
P1–P2	2.178(1)
P1–C1	1.975(5)
P1–P3	2.178(1)
P2–P4	2.201(1)
P2–P6	2.205(1)
P3–P5	2.200(1)
P3–P7	2.222(1)
P4–P5	2.170(1)
P6–P7	2.161(1)
C1–C2	1.477(6)
C2–C3	1.481(7)
C2–C4	1.330(7)
C5–C6	1.434(4)
C5–C12	1.514(4)
C6–C7	1.525(4)
C7–C8	1.540(5)
C8–C9	1.523(5)
C9–C10	1.419(5)
C10–C11	1.525(4)
C11–C12	1.523(5)
Ru1–P4	2.478(1)
Ru1–P5	2.434(1)
Ru1–P6	2.444(1)
Ru1–P7	2.508(1)
Ru1–C5	2.149(3)
Ru1–C6	2.170(3)
Ru1–C9	2.145(3)
Ru1–C10	2.159(3)

Selected bond lengths for **22** are provided in Table 4.7. The P–P bond lengths are in the range 2.161(1) – 2.222(1) Å and are in fairly good agreement with those reported for similar species, such as $[EtP_7W(CO)_3]^{2-}$ (2.137(3) – 2.215(3) Å).[20] The four Ru–P bond lengths of 2.478(1) Å, 2.434(1) Å, 2.444(1) Å and 2.508(1) Å are longer than the mean Ru–P bond length obtained from a search of the CSD (2.332(av) Å) and the sum of covalent radii for Ru–P single bonds (2.36 Å).[15,16] Within the C_4H_7 group, the C2–C4 bond (1.330(7) Å) is significantly shorter than the C1–C2 and C2–C3 bonds (1.477(6) Å and 1.481(7) Å). This is indicative of the presence of localised single and double bonds, unlike the [Ru(COD)(η^3-$CH_2C(CH_3)CH_2)_2$] precursor, in which the bonding within the η^3-$CH_2C(CH_3)CH_2$ groups is delocalised. The C–C bond lengths within the COD ligand also suggest the presence of localised single and double bonds. The C5–C12, C6–C7, C7–C8, C8–C9, C10–C11 and C11–C12 bonds (1.514(4) Å – 1.540(5) Å) are single bonds, while the C5–C6 and C9–C10 bonds (1.434(4) Å and 1.419(5) Å) are double bonds.

4.5.3 ^{1}H NMR spectroscopic studies on $[(C_4H_7)P_7Ru(COD)]^{2-}$ (22)

Obtaining a ^{1}H NMR spectrum of **22** proved extremely difficult due to the presence of impurities. Many attempts to obtain a purer sample of **22** were made, however all attempts to record a well-resolved ^{1}H NMR spectrum were unsuccessful. As discussed below, the room temperature $^{31}P\{^1H\}$ NMR spectrum of **22** indicates that rotation of the COD ligand is slow on the NMR timescale at this temperature. If this is the case, thirteen resonances should be observed in the ^{1}H NMR spectrum. The spectrum consistently shows eleven resonances at 5.11, 5.01, 4.67, 4.63, 2.20, 2.14, 1.91, 1.38, 0.64, 0.59 and 0.53 ppm, which are believed to correspond to **22**. The two remaining resonances may be coincident with resonances arising from the 2,2,2-crypt sequestering agent, which appear at 3.44, 3.37 and 2.35 ppm.

4.5.4 $^{31}P\{^1H\}$ NMR spectroscopic studies on $[(C_4H_7)P_7Ru(COD)]^{2-}$ (22)

The room temperature $^{31}P\{^1H\}$ NMR spectrum of **22** shows seven equal intensity resonances at 127.1, 83.8, 76.9, –127.7, –133.1, –139.4 and –144.5 ppm (Figure 4.26). These resonances have been assigned with the aid of a ^{31}P–^{31}P COSY spectrum as corresponding to P1, P2, P3, P4, P5, P7 and P6, respectively (Figure 4.27). The fact that seven resonances are observed shows that the seven P atoms must be chemically inequivalent to one another and suggests that rotation of the COD ligand must be slow on the NMR timescale at room temperature. The spectrum was simulated in order to obtain the ^{31}P–^{31}P coupling constants (Table 4.8). Two resonances corresponding to an HP_7^{2-} impurity are also observed.[17,18]

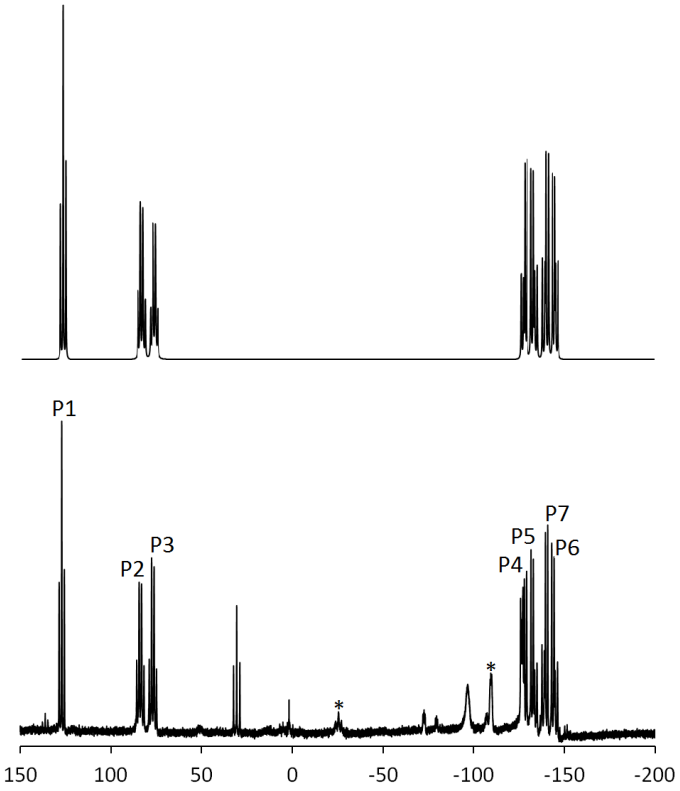

Figure 4.26: Top: The simulated ^{31}P NMR spectrum of **22**. Bottom: The $^{31}P\{^1H\}$ NMR spectrum of **22** recorded in d_5-pyridine at room temperature. Resonances labelled * correspond to HP_7^{2-}.

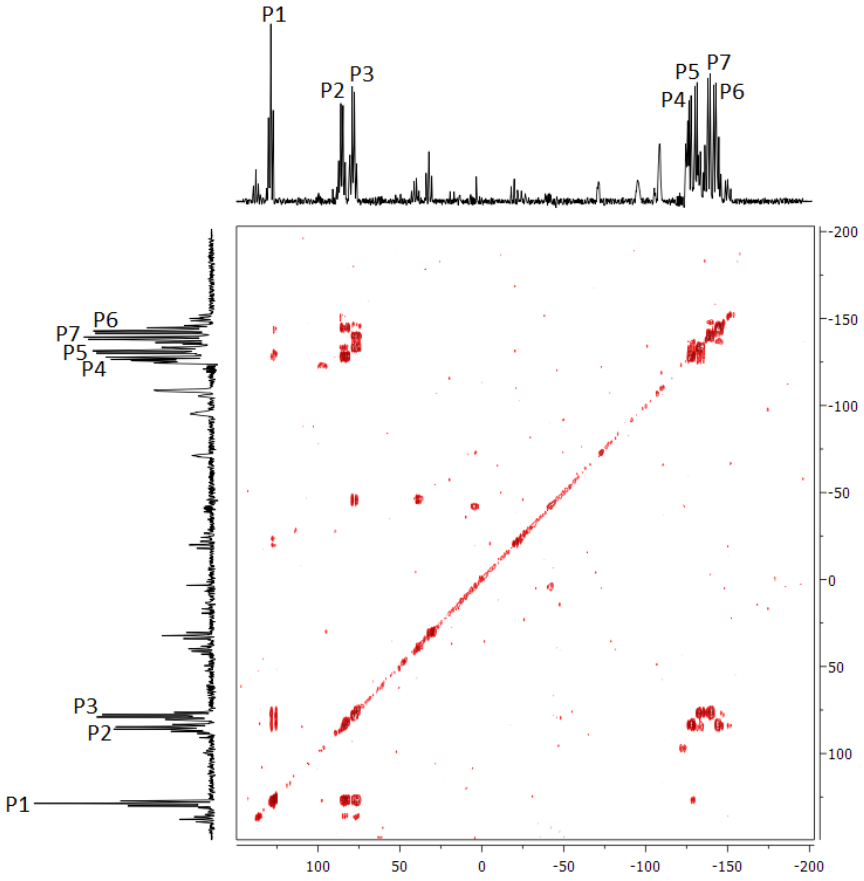

Figure 4.27: ^{31}P–^{31}P COSY spectrum of **22**.

Table 4.8: The ^{31}P chemical shift values and coupling constants for $[(C_4H_7)P_7Ru(COD)]^{2-}$.

δ (ppm)		127.1 P1	83.8 P2	76.9 P3	–127.7 P4	–133.1 P5	–144.5 P6	–139.4 P7
127.1	P1		–292	–297	–	–	–	–
83.8	P2	–292		–	–255	–	–279	–
76.9	P3	–297	–		–	–271	–	–287
–127.7	P4	–	–255	–		–413	–	–
–133.1	P5	–	–	–271	–413		–	–
–144.5	P6	–	–279	–	–	–		–384
–139.4	P7	–	–	–287	–	–	–384	

A ^{31}P{^{1}H} NMR spectrum was also recorded at 60 °C. At this temperature, the spectrum shows four resonances at 129.6, 81.4, –126.9 and –139.3 ppm, which have been assigned to P1, P2 and P3, P4 and P5, and P6 and P7, respectively (Figure 4.28). Rotation of the COD ligand is now fast on the NMR timescale, and this renders P2 equivalent to P3, P4 equivalent to P5, and P6 equivalent to P7. The resonance corresponding to P1 is unaffected, as P1 is not involved in the fluxional process.

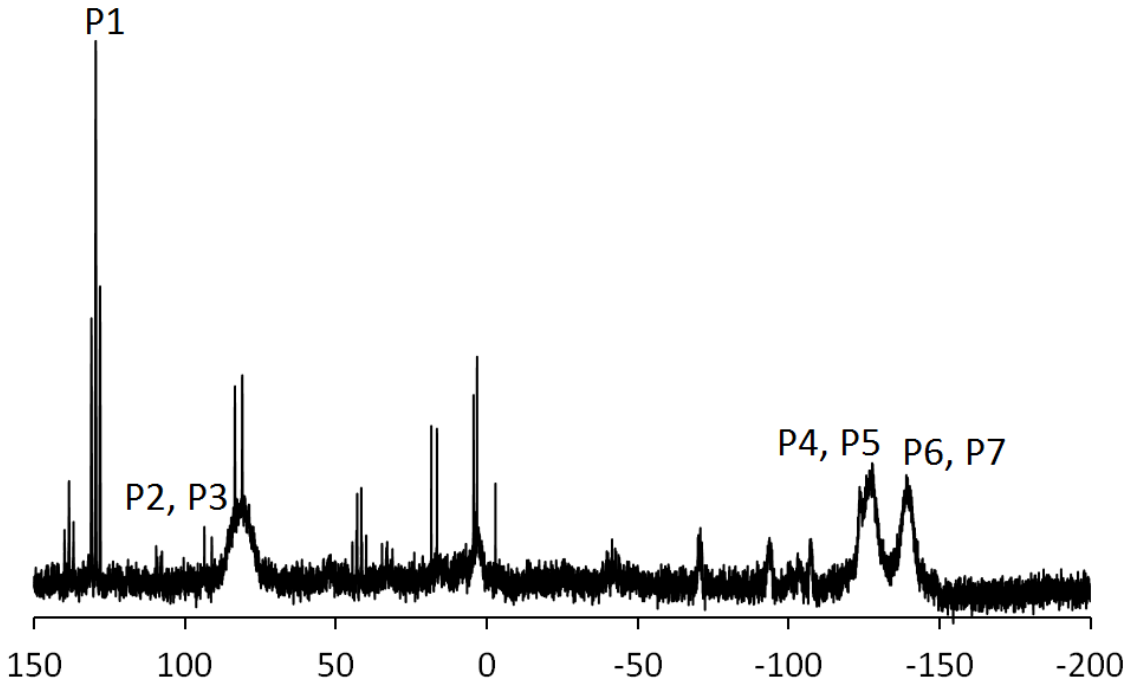

Figure 4.28: $^{31}P\{^1H\}$ NMR spectrum of **22** recorded in d_5-pyridine at 60 °C.

4.5.5 $^{13}C\{^1H\}$ NMR spectroscopic studies on $[(C_4H_7)P_7Ru(COD)]^{2-}$ (22)

A well-resolved $^{13}C\{^1H\}$ NMR spectrum of **22** could not be obtained due to the presence of impurities. If rotation of the COD ligand is slow at room temperature, twelve resonances should be observed in the $^{13}C\{^1H\}$ NMR spectrum. The spectrum consistently shows nine resonances at 130.6, 66.1, 46.3, 29.7, 28.6, 26.6, 26.0, 15.9 and 5.0 ppm, which are believed to correspond to **22**. The three remaining resonances may be coincident with resonances due to the d_5-pyridine solvent, which appear at 150.4, 135.9 and 123.9 ppm, or the 2,2,2-crypt sequestering agent, which appear at 70.9, 68.1 and 54.4 ppm.

4.5.6 Mass spectrometric studies

The positive and negative ion mode ESI mass spectra of **22** confirm that the product is $[(C_4H_7)P_7Ru(COD)]^{2-}$. The negative ion mode spectrum shows a peak corresponding to the oxidised cluster anion, $[(C_4H_7)P_7Ru(COD)]^-$, as well as peaks corresponding to the cluster anion paired with K^+ and $[K(2,2,2\text{-crypt})]^+$ cations. The major peak in the positive ion mode spectrum corresponds to the cluster anion accompanied by three $[K(2,2,2\text{-crypt})]^+$ ions (Figure

4.29).

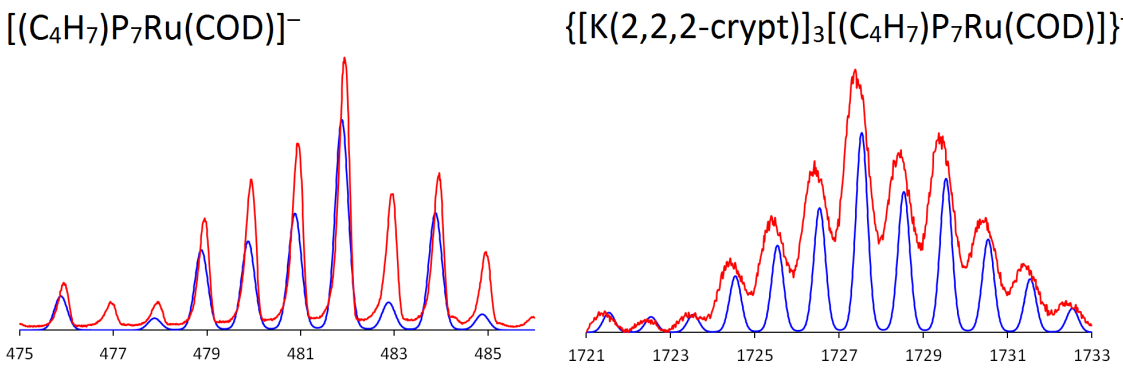

Figure 4.29: ESI-MS mass envelopes for $[(C_4H_7)P_7Ru(COD)]^-$ and $\{[K(2,2,2\text{-crypt})]_3[(C_4H_7)P_7Ru(COD)]\}^+$. Predicted isotopic distributions are shown in blue and observed mass spectrometric data are shown in red.

4.6 Conclusions

This chapter has described the synthesis and characterisation of five previously unknown compounds of group 15 Zintl ions. The reaction of P_7^{3-} with $FeCl_2$ produced $[Fe(HP_7)_2]^{2-}$ (**18**), which has been fully characterised by single crystal X-ray diffraction, ^{1}H and ^{31}P NMR spectroscopy, and mass spectrometry. NMR studies showed that **18** can be deprotonated by two equivalents of KO^{t}Bu or K[N(SiMe$_3$)$_2$] to form $[Fe(P_7)_2]^{4-}$ (**19**).

P_7^{3-} reacts with $[Ru(PPh_3)_3Cl_2]$ to form a mixture of $[Ru(HP_7)_2]^{2-}$ (**20**) and $[Ru(P_7)_2]^{4-}$ (**21**). Crystals of neither [K(2,2,2-crypt)]$_2$[**20**] nor [K(18-crown-6)]$_2$[**20**] could be obtained, but the identity of the product was confirmed by ^{1}H and ^{31}P NMR spectroscopy, and by mass spectrometry. NMR studies showed that a purer sample of the non-protonated cluster anion, **21**, could be obtained by adding KO^{t}Bu or K[N(SiMe$_3$)$_2$] to a mixture of **20** and **21**.

In addition, P_7^{3-} reacts with $[Ru(COD)(\eta^3\text{-}CH_2C(CH_3)CH_2)_2]$ to form $[(C_4H_7)P_7Ru(COD)]^{2-}$ (**22**). This cluster anion has been characterised by single crystal X-ray diffraction, $^{31}P\{^1H\}$ NMR spectroscopy and mass spectrometry.

4.7 References

1. Ahlrichs, R.; Fenske, D.; Fromm, K.; Krautscheid, H.; Krautscheid, U.; Treutler, O. *Chem. Eur. J.* **1996**, *2,* 238–244.

2. Scherer, O. J.; Brück, T. *Angew. Chem., Int. Ed. Engl.* **1987**, *26,* 59.
3. Scherer, O. J.; Brück, T.; Wolmershäuser, G. *Chem. Ber.* **1988**, *121,* 935–938.
4. Scherer, O. J.; Blath, C.; Wolmershäuser, G. *J. Organomet. Chem.* **1990**, *387,* C21–C24.
5. Scherer, O. J.; Blath, C.; Heckmann, G.; Wolmershäuser, G. *J. Organomet. Chem.* **1991**, *409,* C15–C18.
6. Urnėžius, E.; Brennessel, W. W.; Cramer, C. J.; Ellis, J. E.; Von Ragué Schleyer, P. *Science* **2002**, *295,* 832–834.
7. Tang Wong, K. L.; Brintzinger, H. H. *J. Am. Chem. Soc.* **1975**, *97,* 5143–5146.
8. Benfield, F. W. S.; Green, M. L. H.; Ogden, J. S.; Young, D. *J. Chem. Soc., Chem. Commun.* **1973**, 866–867.
9. Baudler, M.; Etzbach, T. *Angew. Chem., Int. Ed. Engl.* **1991**, *30,* 580–582.
10. Knapp, C. M.; Large, J. S.; Rees, N. H.; Goicoechea, J. M. *Chem. Commun.* **2011**, *47,* 4111–4113.
11. Schnöckelborg, E. M.; Weigand, J. J.; Wolf, R. *Angew. Chem., Int. Ed.* **2011**, *50,* 6657–6660.
12. Eichhorn, B. W.; Haushalter, R. C.; Huffman, J. C. *Angew. Chem., Int. Ed. Engl.* **1989**, *28,* 1032–1033.
13. Charles, S.; Eichhorn, B. W.; Rheingold, A. L.; Bott, S. G. *J. Am. Chem. Soc.* **1994**, *116,* 8077–8086.
14. Charles, S.; Fettinger, J. C.; Bott, S. G.; Eichhorn, B. W. *J. Am. Chem. Soc.* **1996**, *118,* 4713–4714.
15. Values taken from CSD version 5.33 (2012).
16. Pyykkö, P.; Atsumi, M. *Chem. Eur. J.* **2009**, *15,* 186–197.
17. Turbervill, R. S. P.; Goicoechea, J. M. *Organometallics* **2012**, *31,* 2452–2462.
18. Dai, F. R.; Xu, L. *Inorg. Chim. Acta* **2006**, *359,* 4265–4273.
19. Gorenstein, D. G. *Prog. Nucl. Mag. Res. Sp.* **1984**, *16,* 1–98.
20. Charles, S.; Fettinger, J. C.; Eichhorn, B. W. *J. Am. Chem. Soc.* **1995**, *117,* 5303–5311.

Chapter 5 Transition metal mediated activation of E_7^{3-} clusters

5.1 Introduction

There are several examples in the literature of activation reactions of E_7^{3-} (E = As, Sb) that result in the formation of higher nuclearity cluster alloys. Examples include $[ME_8]^{n-}$ (M = Nb, Cr, Mo; E = As, Sb; n = 2, 3) and $[Ni_5Sb_{17}]^{4-}$.[1–4] However, prior to the start of this project, there were no examples of transition metal mediated activation of E_7^{3-} to form lower nuclearity E-containing moieties. In contrast, transition metal mediated activation of E_4 (E = P, As) has been extensively investigated by a number of research groups.[5–7] Some examples of metal mediated activation of E_4 to yield E_n ligands (n = 1 – 6) will be provided in the following sections.

5.1.1 E_1 ligands

Cummins and co-workers observed that P_4 reacts with $[Mo(N(R)Ar)_3]$ to form $[Mo(P)(N(R)Ar)_3]$ (R = $C(CD_3)_2CH_3$; Ar = 3,5-$C_6H_3Me_2$).[8] The complex possesses a pseudo-tetrahedral coordination geometry, in which the three N(R)Ar ligands are arranged in a propeller-like fashion (Figure 5.1). The Mo–P bond length is 2.119(4) Å and is consistent with a Mo–P triple bond, *i.e.* a metal phosphido complex (sum of covalent radii for Mo–P triple bonds: 2.07 Å).[9] Further examples of complexes featuring a terminal E_1 ligand include $[Mo(P)(N(2\text{-}Ad)Ar)_3]$, $[M(P)(OSi^tBu_3)_3]$ (M = Mo, W) and $[Mo(As)(N(^tBu)Ar)_3]$ (2-Ad = 2-adamantyl; Ar = 3,5-$C_6H_3Me_2$).[10–12]

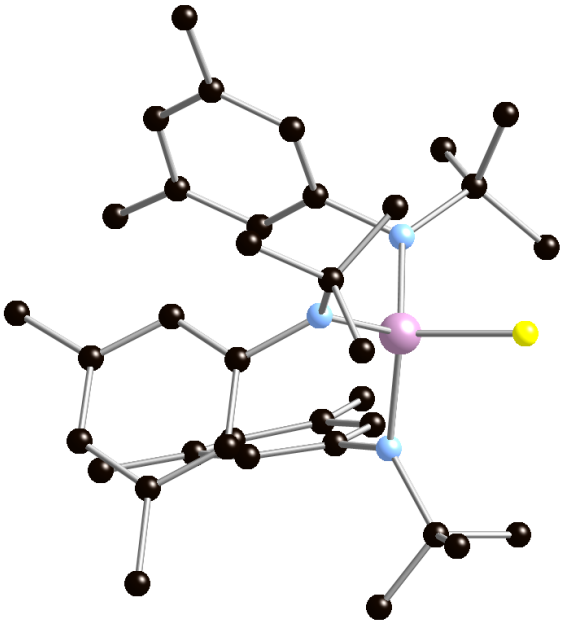

Figure 5.1: Ball and stick diagram of [Mo(P)(N(R)Ar)$_3$]. The Mo atom is shown in purple, the P atom is shown in yellow, N atoms are shown in blue and C atoms are shown in black. H and D atoms are omitted for clarity.

The reaction of P_4 with the less sterically hindered Mo complex, [Mo(N(^{i}Pr)Ar)$_3$], yielded the P-bridged species [(Mo(N(^{i}Pr)Ar)$_3$)$_2$P].[13] The geometry around the bridging P atom is approximately linear (Figure 5.2). The Mo–P bond lengths are 2.183(2) Å and 2.197(2) Å, and are consistent with Mo–P double bonds (sum of covalent radii for Mo–P double bonds: 2.23 Å).[9]

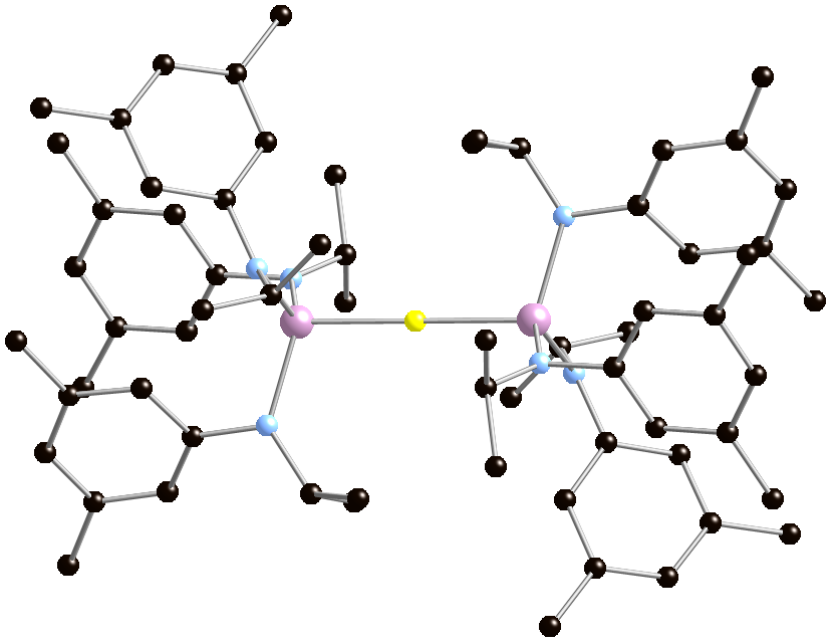

Figure 5.2: Ball and stick diagram of [(Mo(N(^{i}Pr)Ar)$_3$)$_2$P]. Mo atoms are shown in purple, the P atom is shown in yellow, N atoms are shown in blue and C atoms are shown in black. H atoms are omitted for clarity.

5.1.2 E_2 ligands

5.1.2.1 Bridging E_2 ligands

P_4 was found to react with $[(MoCp(CO)_2)_2]$ to form $[(MoCp(CO)_2)_2(\mu_2{:}\eta^2,\eta^2\text{-}P_2)]$.[14] This compound features two Mo centres bridged by a P_2 group (Figure 5.3). The P–P bond length of 2.079(2) Å is significantly shorter than the P–P bond lengths in P_4 (2.21 Å).[15] This observation can be explained by the fact that electron pair repulsions between the P atoms decrease on coordination to the Mo centre. Since the 1980s, a number of other transition metal complexes containing bridging P_2 ligands have been synthesised, including $[(Nb(N(Np)Ar)_3)_2(\mu_2{:}\eta^2,\eta^2\text{-}P_2)]$ (Np = neopentyl), $[(TaCp''(CO))_2(\mu_2{:}\eta^2,\eta^2\text{-}P_2)_2]$ (Cp'' = η^5-1,3-$C_5H_3{}^tBu_2$), $[(ReCp^*(CO)_2)_2(\mu_2{:}\eta^2,\eta^2\text{-}P_2)]$ and $[(MCp^*)_2(\mu_2{:}\eta^2,\eta^2\text{-}P_2)_2]$ (M = Fe, Co).[16–19] The As analogue has been observed in $[(Co(\eta^5\text{-}C_5Me_4R))_2(\mu_2{:}\eta^2,\eta^2\text{-}As_2)_2]$ (R = Me, Et).[20]

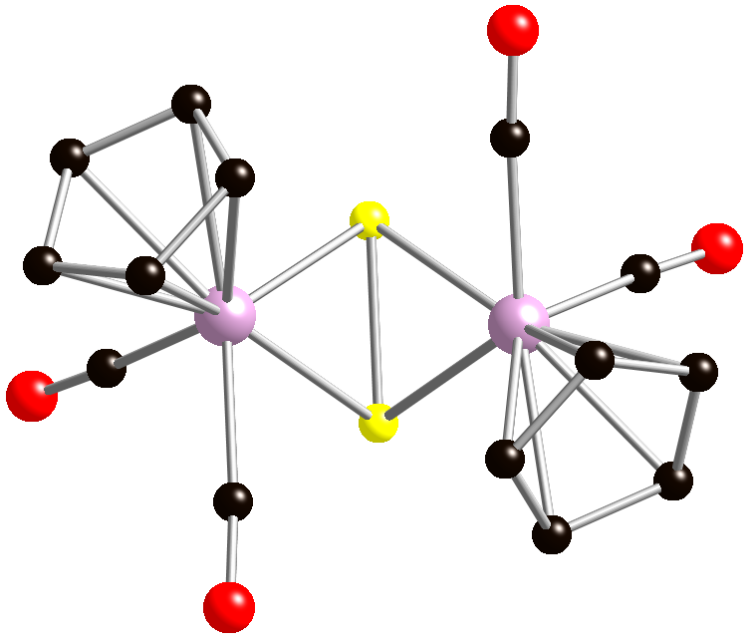

Figure 5.3: Ball and stick diagram of $[(MoCp(CO)_2)_2(\mu_2{:}\eta^2,\eta^2\text{-}P_2)]$. Mo atoms are shown in purple, P atoms are shown in yellow, C atoms are shown in black and O atoms are shown in red. H atoms are omitted for clarity.

The reactions of P_4 with $[Nb(OSi^tBu_3)_3(PMe_3)]$ and $[Ta(OSi^tBu_3)_3]$ formed $[(M(OSi^tBu_3)_3)_2(\mu_2{:}\eta^1,\eta^1\text{-}P_2)]$ (M = Nb, Ta), in which the P_2 ligand is coordinated end-on instead of side-on (Figure 5.4).[21] The Nb–P and Ta–P bond lengths of 2.325(1) Å and 2.317(4)

Å, respectively, are consistent with M–P double bonds (sum of covalent radii for Nb–P double bonds: 2.27 Å; for Ta–P double bonds: 2.28 Å).[9]

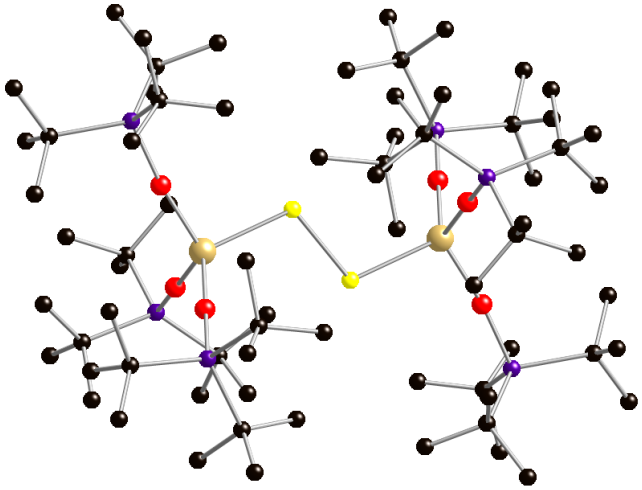

Figure 5.4: Ball and stick diagram of $[(Ta(OSi^tBu_3)_3)_2(\mu_2{:}\eta^1,\eta^1\text{-}P_2)]$. Ta atoms are shown in gold, P atoms are shown in yellow, Si atoms are shown in purple, C atoms are shown in black and O atoms are shown in red. H atoms are omitted for clarity.

5.1.2.2 P_2H_2 ligands

P_4 reacts with $[MoCp_2H_2]$ to form $[(\eta^2\text{-}P_2H_2)MoCp_2]$, which features a diphosphene-like P_2H_2 group bonded to the Mo centre in an η^2-fashion (Figure 5.5).[22] The two hydride ligands are transferred from the Mo to the P atoms during the course of the reaction. Later research by Stephan and co-workers showed that P_4 reacts with $[TaCp_2H_3]$ in a very similar way to form $[(\eta^2\text{-}P_2H_2)TaCp_2H]$.[23] In both cases, the H atoms bonded to P could not be located crystallographically, but their presence was inferred from NMR spectroscopic studies. As an example, the ^{1}H NMR spectrum of $[(\eta^2\text{-}P_2H_2)TaCp_2H]$ shows two doublets of doublets of doublets at –0.23 and –1.14 ppm, corresponding to the two P-bound H atoms.[23]

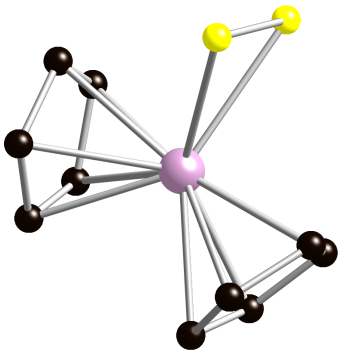

Figure 5.5: Ball and stick diagram of $[(\eta^2\text{-}P_2H_2)MoCp_2]$. P atoms are shown in yellow, the Mo atom is shown in purple and C atoms are shown in black. H atoms are omitted for clarity.

5.1.3 E_3 ligands

The reactivity of P_4 towards group 9 and group 10 metal complexes was extensively studied by Sacconi and co-workers. The first example of a complex featuring a P_3 ligand, $[(\eta^3\text{-}P_3)Co(triphos)]$ (triphos = 1,1,1-tris((diphenylphosphino)methyl)ethane), was obtained in the reaction of P_4 with $Co[BF_4]_2{\cdot}6H_2O$ in the presence of triphos.[24] This compound contains a *cyclo*-P_3 unit bonded to a Co centre in an η^3-fashion and can be obtained from the P_4 molecule by replacing one of the P atoms with an isolobal fifteen-electron Co(triphos) fragment (Figure 5.6). The η^3-P_3 ligand is able to donate three electrons to the Co centre, resulting in a total of eighteen valence electrons. This research was subsequently extended to Rh and Ir, as well as to Ni, Pd and Pt, resulting in the formation of a series of $[(\eta^3\text{-}P_3)M(triphos)]^{n+}$ complexes (M = Co, Rh, Ir: n = 0; M = Ni, Pd, Pt: n= 1).[24–27] The η^3-P_3 group has also been observed in $[(\eta^3\text{-}P_3)MCp_2(CO)_2]$ (M = Cr, Mo), and in $[(\eta^3\text{-}P_3)Nb(ODipp)_3]^-$.[28–30] Cummins and co-workers showed that AsP_3 can be synthesised by reacting $[(\eta^3\text{-}P_3)Nb(ODipp)_3]^-$ with $AsCl_3$.[30] Analogous reactions with As_4 produced complexes containing η^3-As_3 groups. Examples include $[(\eta^3\text{-}As_3)CrCp(CO)_2]$ and $[(\eta^3\text{-}As_3)MCp^*(CO)_2]$ (M = Cr, Mo, W).[31–34]

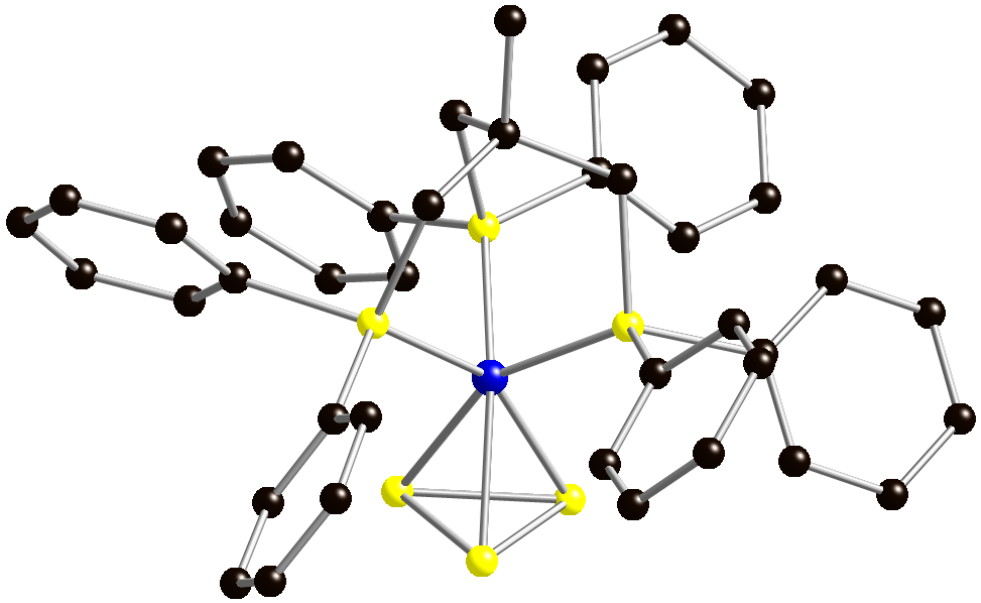

Figure 5.6: Ball and stick diagram of $[(\eta^3\text{-}P_3)Co(triphos)]$. P atoms are shown in yellow, the Co atom is shown in blue and C atoms are shown in black. H atoms are omitted for clarity.

5.1.4 E_4 ligands

5.1.4.1 Tetrahedral E_4 ligands

The first metal complex of an intact P_4 molecule to be crystallographically characterised was $[(\eta^1\text{-}P_4)Ni(np_3)]$ (np_3 = tris(2-diphenylphosphinoethyl)amine), which was synthesised in 1979 by Sacconi and co-workers by reacting P_4 with $Ni(np_3)$.[35] More recently, several other complexes of P_4 have been synthesised, including $[(\eta^1\text{-}P_4)Re(triphos)(CO)_2]^+$, $[(\eta^1\text{-}P_4)M(CO)_3(PR_3)_2]$ (M = Mo, W; R = ^{i}Pr, Cy), $[(\eta^1\text{-}P_4)MCp(dppe)]^+$ (M = Fe, Ru; dppe = 1,2-bis(diphenylphosphino)ethane) and $[(\eta^1\text{-}P_4)OsCp(PPh_3)_2]^+$.[36–39] The first example of an η^1-As_4 tetrahedron was isolated very recently in $[(\eta^1\text{-}As_4)RuCp^*(dppe)]^+$, which was synthesised by Scheer and co-workers.[40] All of these compounds contain an E_4 molecule bonded to a metal centre in an η^1-fashion (Figure 5.7).

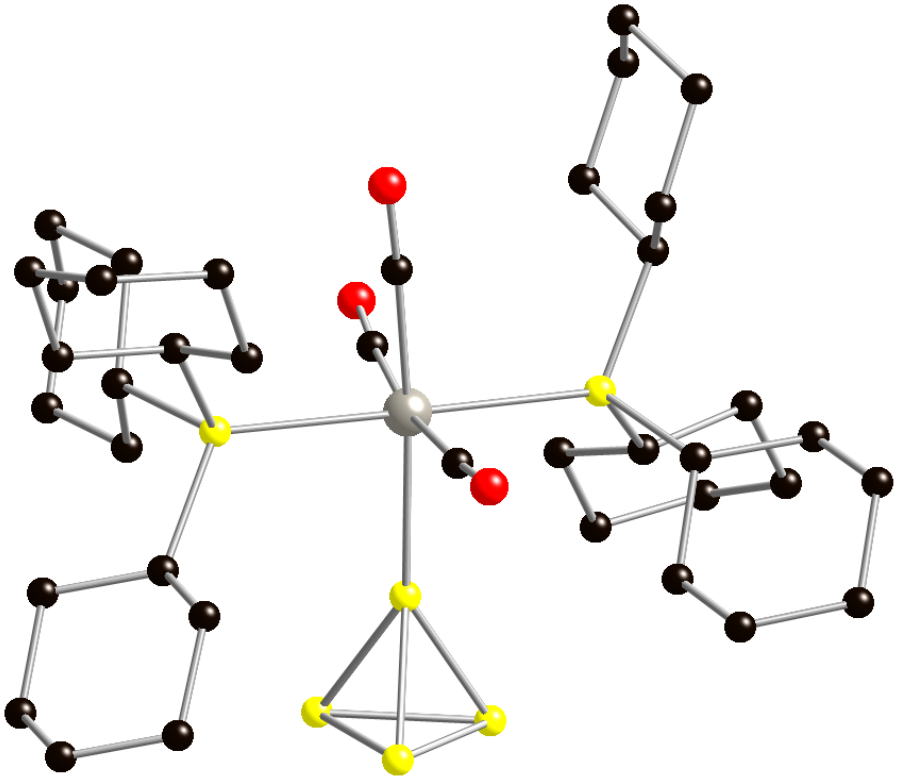

Figure 5.7: Ball and stick diagram of $[(\eta^1\text{-}P_4)W(CO)_3(PCy_3)_2]$. P atoms are shown in yellow, the W atom is shown in grey, C atoms are shown in black and O atoms are shown in red. H atoms are omitted for clarity.

Tetrahedral E_4 ligands are also able to coordinate to metal centres in an η^2-fashion. The first example of this bonding mode was the $[(\eta^2\text{-}P_4)Rh(PPh_3)_2Cl]$ complex.[41] Later research led

to the synthesis of several similar compounds, including $[(\eta^2\text{-}P_4)MCp''_2]$ (M = Zr, Hf; Cp'' = η^5-1,3-$C_5H_3{}^tBu_2$) and $[(\eta^2\text{-}E_4)CoCp^*(CO)]$ (E = P, As).[42–44] The bond between the two metal-bound E atoms is elongated significantly on coordination to the metal centre; for example, the distance between the two Co-bound P atoms in $[(\eta^2\text{-}P_4)CoCp^*(CO)]$ is 2.606(1) Å (*c.f.* 2.21 Å in uncoordinated P_4).[15,43] $[M(\eta^2\text{-}E_4)_2]^+$ complexes (M = Cu, Au: E = P; M = Ag: E = P, As) have been synthesised in the reactions between E_4 and group 11 salts in the presence of weakly coordinating anions such as $[Al(OC(CF_3)_3)_4]^-$.[45–48] These cationic species consist of two E_4 units bridged by a metal atom, with each E_4 group bonded to the metal in an η^2-fashion (Figure 5.8).

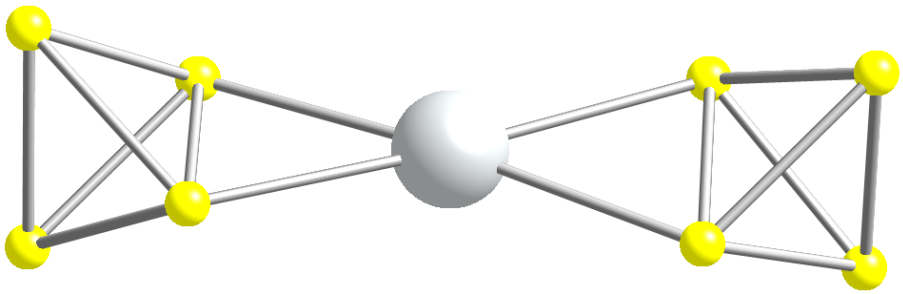

Figure 5.8: Ball and stick diagram of $[Ag(\eta^2\text{-}P_4)_2]^+$. The Ag atom is shown in grey and P atoms are shown in yellow.

5.1.4.2 Cyclic P_4 ligands

Scherer and co-workers described the synthesis of $[(\eta^4\text{-}P_4)NbCp^*(CO)_2]$ in 1989.[49] This compound was obtained by irradiation of $[NbCp^*(CO)_4]$ in the presence of P_4 and features a distorted square P_4 ligand that is bonded to the Nb centre in an η^4-fashion. Further studies showed that $[(\eta^4\text{-}P_4)VCp^*(CO)_2]$ and $[(\eta^4\text{-}P_4)TaCp''(CO)_2]$ (Cp'' = η^5-1,3-$C_5H_3{}^tBu_2$) could be prepared in a similar way.[17,50] The *cyclo*-P_4 group is also able to act as a bridging ligand, as observed in $[(Zr(PhP(CH_2SiMe_2NSiMe_2CH_2)_2PPh))_2(\mu_2{:}\eta^4,\eta^4\text{-}P_4)]$ (Figure 5.9).[51]

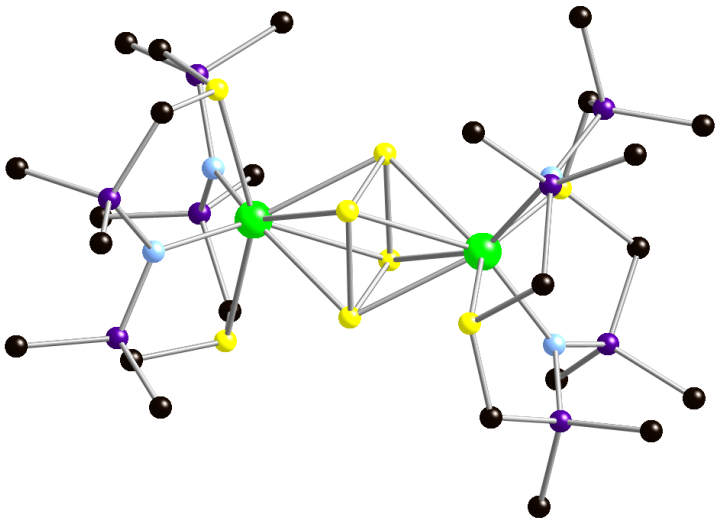

Figure 5.9: Ball and stick diagram of [(Zr(PhP($CH_2SiMe_2NSiMe_2CH_2$)$_2$PPh))$_2$(μ_2:η^4,η^4-P_4)]. Zr atoms are shown in green, P atoms are shown in yellow, C atoms are shown in black, Si atoms are shown in purple and N atoms are shown in blue. Ph groups and H atoms are omitted for clarity.

5.1.4.3 P_4R_2 ligands

P_4 reacts with [($TlAr^{Dipp_2}$)$_2$] to form [Tl_2(μ_2:η^4,η^4-P_4(Ar^{Dipp_2})$_2$)] (Ar^{Dipp_2} = C_6H_3-2,6-(C_6H_3-2,6-$^i Pr_2$)$_2$).[52] This compound consists of a butadiene-like $P_4(Ar^{Dipp_2})_2$ group coordinated to two Tl atoms in an η^4-fashion (Figure 5.10). Two Ar^{Dipp_2} groups are transferred from the Tl atoms to the two terminal P atoms during the course of the reaction. There is very little difference in the P–P bond lengths within the $P_4(Ar^{Dipp_2})_2$ unit, which suggests that the bonding is largely delocalised. Power and co-workers proposed that this compound comprises a $[P_4(Ar^{Dipp_2})_2]^{2-}$ (a tetraphosphabutadienediide) ligand coordinated to two Tl^+ ions.[52]

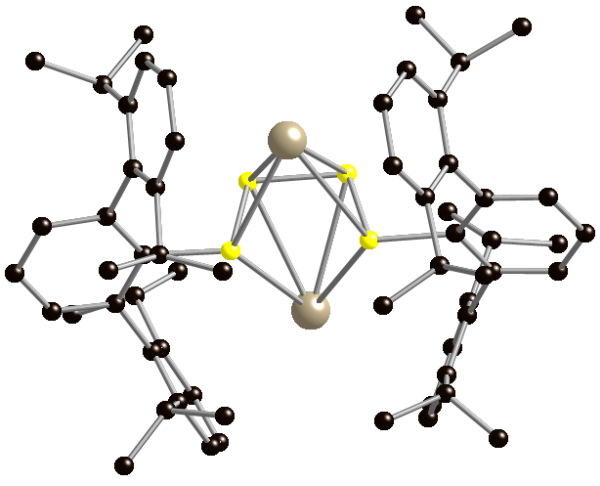

Figure 5.10: Ball and stick diagram of [Tl_2(μ_2:η^4,η^4-P_4(Ar^{Dipp_2})$_2$]. Tl atoms are shown in grey, P atoms are shown in yellow and C atoms are shown in black. H atoms are omitted for clarity.

5.1.5 E_5 ligands

Research by Scherer and co-workers showed that P_5^- and As_5^-, the isolobal P and As analogues of Cp^-, could be obtained by transition metal mediated activation of P_4 and As_4. The first compound featuring an η^5-E_5^- ligand to be synthesised was $[(CrCp^*)_2(\mu_2{:}\eta^5,\eta^5\text{-}P_5)]$.[53] This triple decker sandwich complex consists of two CrCp* fragments bridged by a P_5^- ligand (Figure 5.11). P_4 also reacts with the group 8 compounds $[(Fe(\eta^5\text{-}C_5Me_4R)(CO)_2)_2]$ and $[Ru(\eta^5\text{-}C_5Me_4R)(CO)_2Br]$ to form $[(\eta^5\text{-}P_5)M(\eta^5\text{-}C_5Me_4R)]$ (M = Fe, Ru; R = Me, Et).[54,55] These sandwich complexes can be considered to be phosphorus analogues of ferrocene, in which one of the Cp^- rings has been replaced by an η^5-P_5^- ring. There are also examples in the literature of compounds featuring η^5-As_5^- rings, including $[(Cr(\eta^5\text{-}C_5H_4R))_2(\mu_2{:}\eta^5,\eta^5\text{-}As_5)]$ (R = H, Me) and $[(\eta^5\text{-}As_5)M(\eta^5\text{-}C_5Me_4R)]$ (M = Fe, Ru; R = Me, Et).[56–58] Neutral carbon-free metallocene analogues, in which both Cp^- ligands have been replaced by E_5^- ligands, have not been isolated to date, however $[Ti(\eta^5\text{-}P_5)_2]^{2-}$ was synthesised by reacting P_4 with a highly reduced Ti complex.[59]

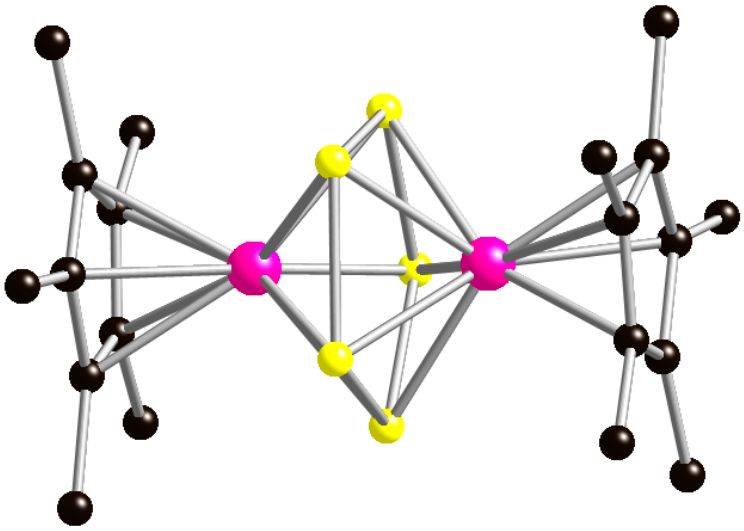

Figure 5.11: Ball and stick diagram of $[(CrCp^*)_2(\mu_2{:}\eta^5,\eta^5\text{-}P_5)]$. Cr atoms are shown in pink, P atoms are shown in yellow and C atoms are shown in black. H atoms are omitted for clarity.

5.1.6 E_6 ligands

P_4 reacts with $[(MoCp^*(CO)_2)_2]$ to form $[(MoCp^*)_2(\mu_2{:}\eta^6,\eta^6\text{-}P_6)]$.[60] η^6-E_6 ligands have also been observed in $[(Mo(\eta^5\text{-}C_5Me_4R))_2(\mu_2{:}\eta^6,\eta^6\text{-}As_6)]$ (R = Me, Et), $[(WCp^*)_2(\mu_2{:}\eta^6,\eta^6\text{-}P_6)]$ and

$[(M(\eta^5\text{-}C_5Me_4R))_2(\mu_2{:}\eta^6,\eta^6\text{-}P_6)]$ (M = V, Nb; R = Me, Et).[49,61,62] All of these complexes feature two metal centres bridged by a planar E_6 group that is isolobal with benzene (Figure 5.12).

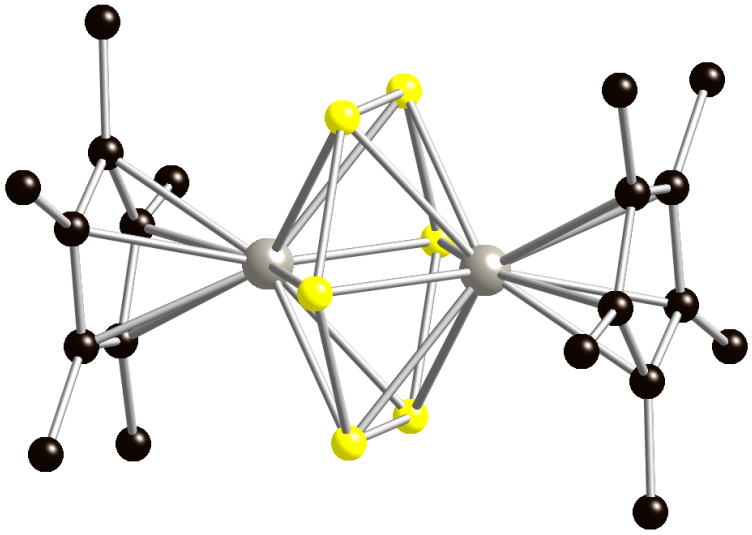

Figure 5.12: Ball and stick diagram of $[(WCp^*)_2(\mu_2{:}\eta^6,\eta^6\text{-}P_6)]$. W atoms are shown in grey, P atoms are shown in yellow and C atoms are shown in black. H atoms are omitted for clarity.

5.2 Objectives

Prior to the start of this project, there were no examples in the literature of transition metal mediated activation of E_7^{3-} (E = P, As, Sb) to form lower nuclearity E-containing moieties, although both P_4 and As_4 had been shown to undergo such activation reactions. Since the structure of E_7^{3-} is related to that of E_4, it seemed possible that E_7^{3-} would undergo similar reactions. In addition, there were no previously reported investigations of the reactivity of group 15 Zintl ions towards Co compounds.

This chapter will detail the reactivity of P_7^{3-} and As_7^{3-} towards $[Co(PEt_2Ph)_2(mes)_2]$. P_7^{3-} reacts with this compound to form $[Co(\eta^5\text{-}P_5)\{\eta^2\text{-}HP_2(mes)\}]^{2-}$, while the corresponding reaction with As_7^{3-} forms $[Co(\eta^3\text{-}As_3)\{\eta^4\text{-}As_4(mes)_2\}]^{2-}$.[63,64] These reactions represent the first examples of E_7^{3-} reacting with Co compounds and are similar to previously reported transition metal mediated activation reactions of P_4 and As_4.

5.3 Solution reactivity of P_7^{3-} towards $[Co(PEt_2Ph)_2(mes)_2]$

5.3.1 Synthesis of $[Co(\eta^5\text{-}P_5)\{\eta^2\text{-}HP_2(mes)\}]^{2-}$ (23)

Ethylenediamine solutions of K_3P_7 react with $[Co(PEt_2Ph)_2(mes)_2]$ in the presence of 2,2,2-crypt to form $[K(2,2,2\text{-crypt})]_2[Co(\eta^5\text{-}P_5)\{\eta^2\text{-}HP_2(mes)\}]$. This compound contains the novel anionic species $[Co(\eta^5\text{-}P_5)\{\eta^2\text{-}HP_2(mes)\}]^{2-}$ (**23**). Crystals of $[K(2,2,2\text{-crypt})]_2$[**23**] suitable for single crystal X-ray diffraction were obtained from an ethylenediamine solution layered with toluene.

5.3.2 Structure of $[Co(\eta^5\text{-}P_5)\{\eta^2\text{-}HP_2(mes)\}]^{2-}$ (23)

23 features an $\eta^5\text{-}P_5^-$ ring and an $\eta^2\text{-}HP_2(mes)$ group, which are both bonded to a central Co atom (Figure 5.13). The P_5^- ring is isoelectronic with Cp^-, and the $HP_2(mes)$ group can be considered to be a phosphorus analogue of an alkene. The position of the proton in the $HP_2(mes)$ fragment could not be determined crystallograpically, therefore it is unclear as to whether the *cis* or the *trans* isomer is present in the solid state. DFT calculations revealed a difference in energy between the *trans* and *cis* isomers of approximately 15 kJ mol^{-1}, with the *trans* isomer being slightly lower in energy. There are a few previously reported examples of transition metal compounds featuring an $\eta^5\text{-}P_5^-$ ring, including $[(\eta^5\text{-}P_5)M(\eta^5\text{-}C_5Me_4R)]$ (M = Fe, Ru; R = Me, Et).[54,55] However, **23** is the first example of an $\eta^5\text{-}P_5^-$ ligand bonded to a Co centre. Metal complexes featuring an $\eta^2\text{-}P_2R_2$ group have also been synthesised previously, although there is only one other reported example of an $\eta^2\text{-}P_2R_2$ group coordinated to a Co atom, namely $[(\eta^2\text{-}P_2Ph_2)Co(triphos)]$.[65] Symmetrically substituted $\eta^2\text{-}P_2R_2$ groups are much more common than asymmetrically substituted $\eta^2\text{-}P_2RR'$ systems. Examples of the latter include $[(\eta^2\text{-}^tBuP_2SiMe_3)Pt(PPh_3)_2]$.[66]

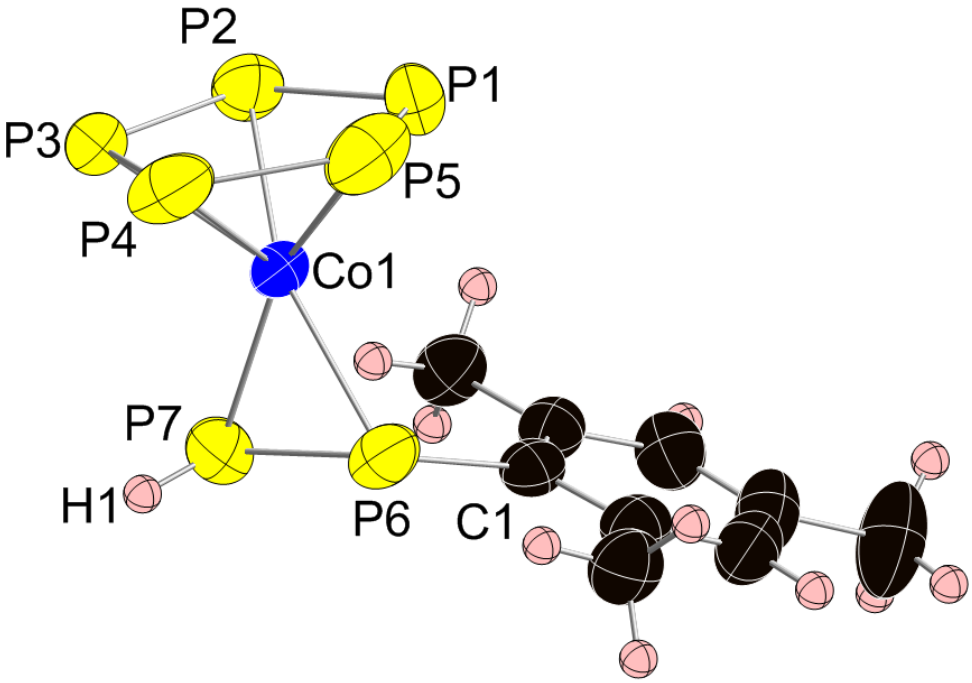

Figure 5.13: Thermal ellipsoid plot of the *trans* isomer of **23** with anisotropic displacement ellipsoids pictured at 50% probability. H atoms are shown as small spheres with arbitrary radii.

Anion **23** can be viewed as either a Co^{-I} complex of P_5^- and a neutral alkene-like diphosphene, HP=P(mes), or as a Co^{I} complex of P_5^- and a diphospanediide, $[HP–P(mes)]^{2-}$ (Figure 5.14). The P–P bond length in the η^2-HP_2(mes) group is in between typical values for P–P single and double bonds.[9,67] This can be explained by extensive π back-bonding from an electron-rich Co^{-I} centre into the π* orbital of a diphosphene, resulting in a lengthening of the P–P double bond. Alternatively, this can be rationalised as a contraction of the P–P single bond of a diphosphanediide due to a reduction in the electrostatic repulsion between the two P atoms on coordination to a Co^{I} centre. These two possibilities are analogous to the two limiting cases of the Dewar-Chatt-Duncanson model for the binding of alkenes to a transition metal centre.[68–70]

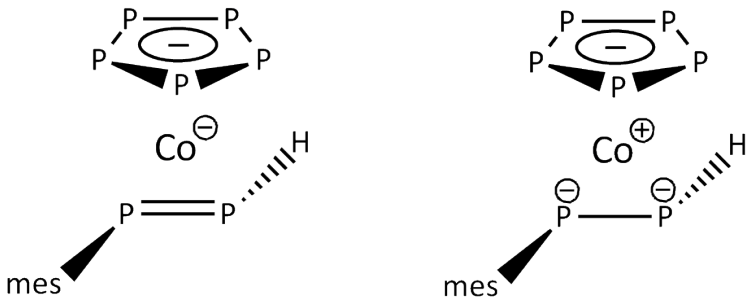

Figure 5.14: Diagram showing the two most likely charge assignments for **23**.

Figure 5.15 shows selected Kohn-Sham orbitals for the hypothetical diprotic analogue of **23**, *cis*-$[Co(\eta^5\text{-}P_5)(\eta^2\text{-}P_2H_2)]^{2-}$, and the hypothetical carbon analogue, *cis*-$[Co(\eta^5\text{-}C_5H_5)(\eta^2\text{-}C_2H_4)]^{2-}$. Several of the molecular orbitals calculated for $[Co(\eta^5\text{-}P_5)(\eta^2\text{-}P_2H_2)]^{2-}$ are similar in appearance to orbitals calculated for $[Co(\eta^5\text{-}C_5H_5)(\eta^2\text{-}C_2H_4)]^{2-}$, although the energy ordering of these orbitals is different in each case. Significant π back-bonding contributions are observed in the HOMO–2 and HOMO–4 of the P and C species, respectively. The frontier orbitals of both anions are largely metal *d* orbital in character.

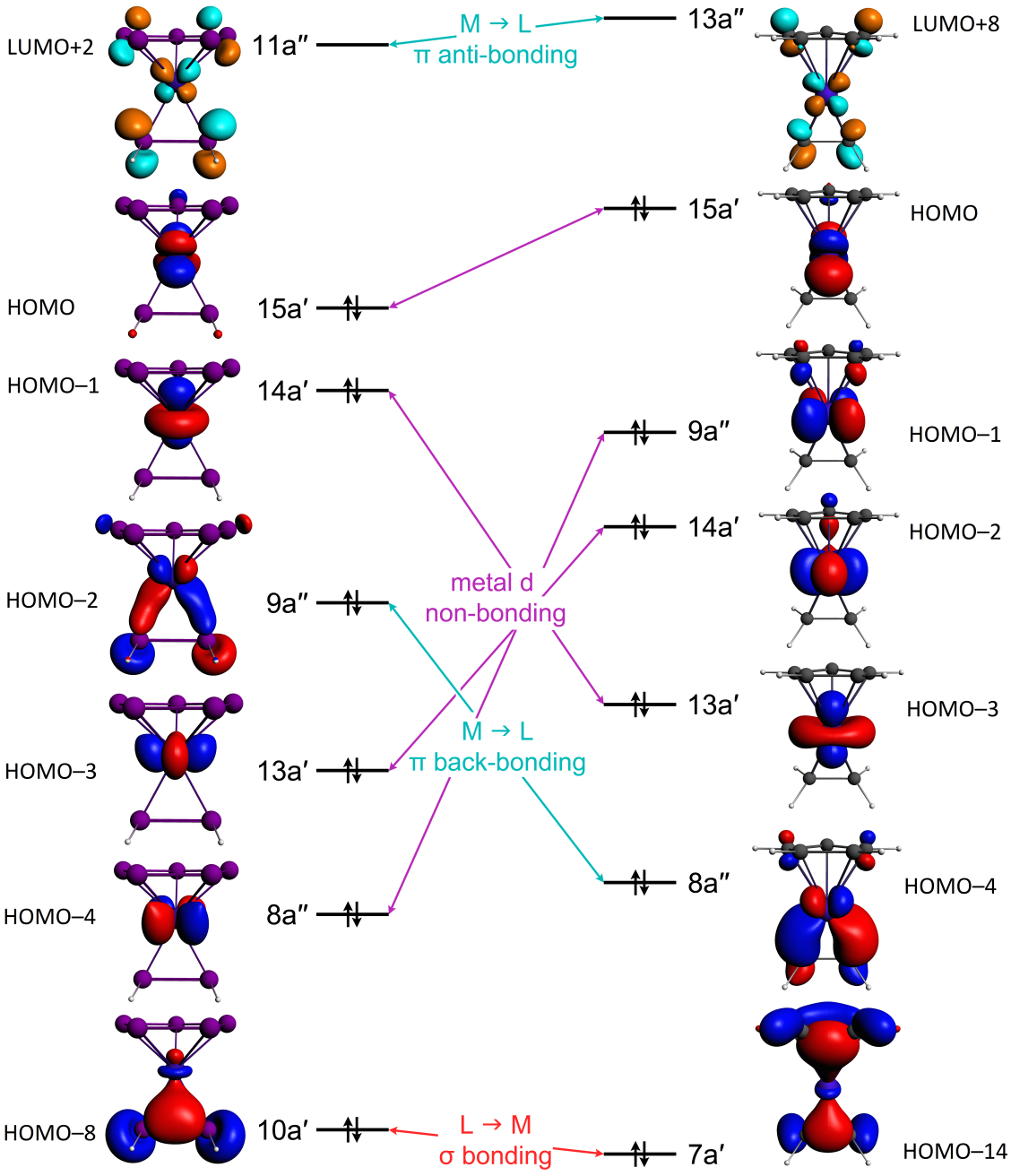

Figure 5.15: Selected Kohn-Sham orbitals for *cis*-$[Co(\eta^5\text{-}P_5)(\eta^2\text{-}P_2H_2)]^{2-}$ (left) and *cis*-$[Co(\eta^5\text{-}C_5H_5)(\eta^2\text{-}C_2H_4)]^{2-}$ (right).

Bader's Atoms in Molecules (AIM) methodology was used to analyse the calculated charge densities, $\rho(\mathbf{r})$, for **23** and its hypothetical carbon analogue.[71] The analysis was focussed on the Co–E6–E7 plane and revealed three bond critical points (BCP) and one ring critical point (RCP) in this plane for both anions (Figure 5.16). This is indicative of significant covalent character in both the P and the C species. The bond paths for **23** exhibit greater exocyclic character compared with those for the C analogue, which suggests that a greater level of π back-bonding is present in **23**.[72] The BCPs for Co1–P6, Co1–P7 and P6–P7 were found to have $\rho(\mathbf{r})$ values of 0.082, 0.083 and 0.114, respectively, while the corresponding values for the C compound were calculated to be 0.098, 0.108 and 0.253, respectively. There is much more variation in these values in the C species than in **23**, with the $\rho(\mathbf{r})$ value for the C6–C7 BCP being more than twice those calculated for the Co–C BCPs. In the case of **23**, the Co–P BCPs have similar $\rho(\mathbf{r})$ values to the P6–P7 BCP. This indicates that **23** possesses a higher degree of both metallacyclic and covalent character than its C analogue.

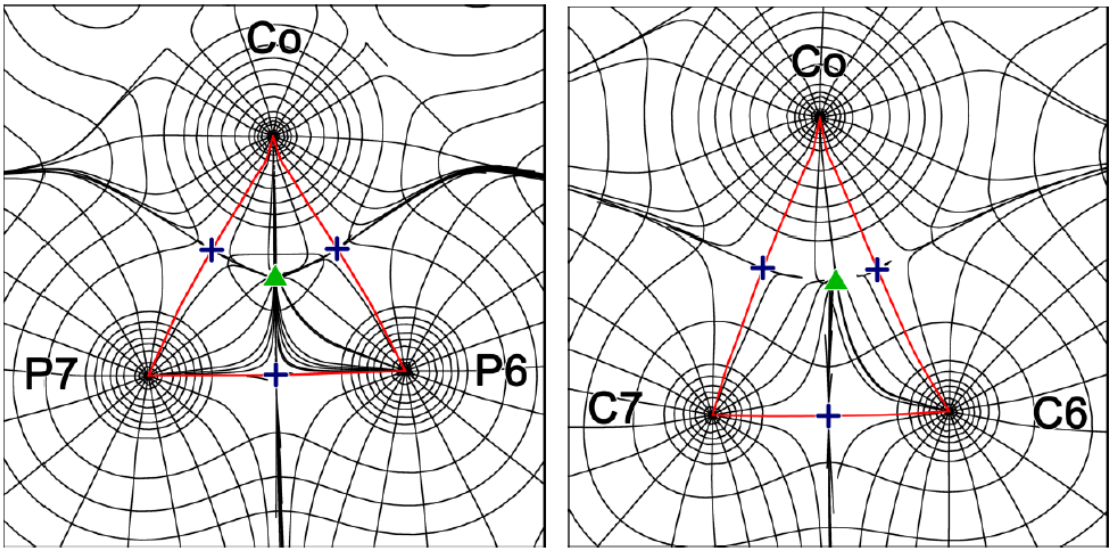

Figure 5.16: Contour maps of $\rho(\mathbf{r})$ in the Co–E6–E7 plane for **23** (left) and $[Co(\eta^5\text{-}C_5H_5)\{\eta^2\text{-}H_2C_2H(mes)\}]^{2-}$ (right). Bond critical points are shown as crosses and ring critical points are shown as triangles.

Selected bond lengths for **23** are provided in Table 5.1, along with selected bond distances for the optimised structures of both the *cis* and *trans* isomers. The P–P bond lengths within the $\eta^5\text{-}P_5^-$ ring range from 2.103(1) Å to 2.133(2) Å, while the P–P bond length in the $\eta^2\text{-}HP_2(mes)$ group is 2.141(1) Å. These bond lengths are all in between typical values for P–P single and double bonds (sum of covalent radii for P–P single bonds: 2.22 Å; for P–P double bonds: 2.04 Å).[9,67] A search of the CSD gave mean P–P bond lengths of 2.135(av) Å and 2.137(av) Å for

complexes featuring η^5-P_5^- and η^2-P_2R_2 ligands, respectively.[73] The Co–P bond lengths to the η^5-P_5^- ring are in the range 2.305(1) Å – 2.365(1) Å. The Co–P bonds to the η^2-HP_2(mes) unit are shorter than this, at 2.270(1) Å and 2.278(1) Å. The mean Co–P bond length obtained from a search of the CSD is 2.214(av) Å, while the sum of covalent radii for Co–P single bonds is 2.22 Å.[67,73]

Table 5.1: Selected bond lengths for the $[Co(\eta^5\text{-}P_5)\{\eta^2\text{-}HP_2(mes)\}]^{2-}$ species.

Bond	Experimental bond length in **23** (Å)	Calculated bond length for the *trans* isomer (Å)	Calculated bond length for the *cis* isomer (Å)
P1–P2	2.103(1)	2.142	2.148
P1–P5	2.129(2)	2.178	2.168
P2–P3	2.121(1)	2.172	2.161
P3–P4	2.133(2)	2.151	2.159
P4–P5	2.110(2)	2.151	2.150
P6–P7	2.141(1)	2.173	2.168
P6–C1	1.876(3)	1.887	1.895
Co1–P1	2.305(1)	2.317	2.342
Co1–P2	2.365(1)	2.378	2.347
Co1–P3	2.346(1)	2.316	2.377
Co1–P4	2.332(1)	2.369	2.326
Co1–P5	2.350(1)	2.343	2.365
Co1–P6	2.270(1)	2.273	2.274
Co1–P7	2.278(1)	2.277	2.270

5.3.3 NMR spectroscopic studies on $[Co(\eta^5\text{-}P_5)\{\eta^2\text{-}HP_2(mes)\}]^{2-}$ (23)

The ^{1}H NMR spectrum of **23** shows three singlets at 6.70, 2.06 and 2.02 ppm with relative intensities 2:6:3. These correspond to the two *meta*-protons, the two *ortho*-CH_3 groups and the single *para*-CH_3 group, respectively. The spectrum also shows a doublet of doublets of relative intensity one at 2.10 ppm, which can be assigned to the proton bonded to P7, H1. The one-bond ^{1}H–^{31}P coupling constant is equal to 119 Hz, and the two-bond ^{1}H–^{31}P coupling constant is equal to 22 Hz. This resonance appers as a singlet in the $^1H\{^{31}P\}$ spectrum (Figure 5.17). The H1 resonance overlaps with the methyl resonances of the mesityl group, as well as with resonances corresponding to ethylenediamine and toluene impurities. As a result, this resonance is difficult to discern, and so a 1D ^{1}H–^{31}P HMQC spectrum was recorded. This allowed the H1 resonance to be seen more clearly (Figure 5.18).

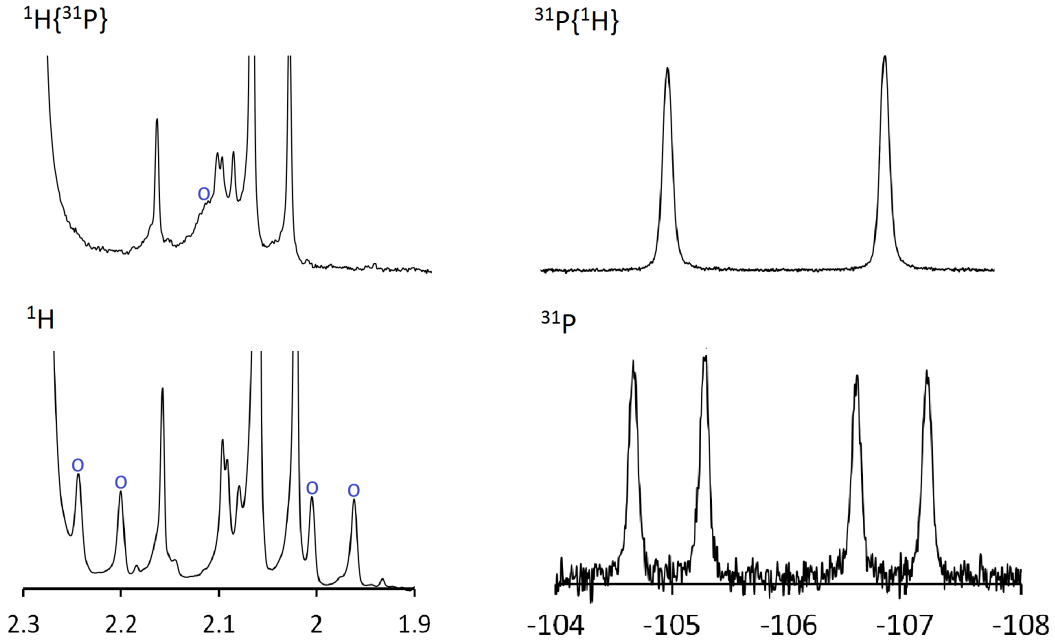

Figure 5.17: Close-ups of the H1 and P7 resonances in the $^{1}H\{^{31}P\}$, ^{1}H, $^{31}P\{^{1}H\}$ and ^{31}P NMR spectra of **23**. ^{1}H resonances of interest are labelled in purple.

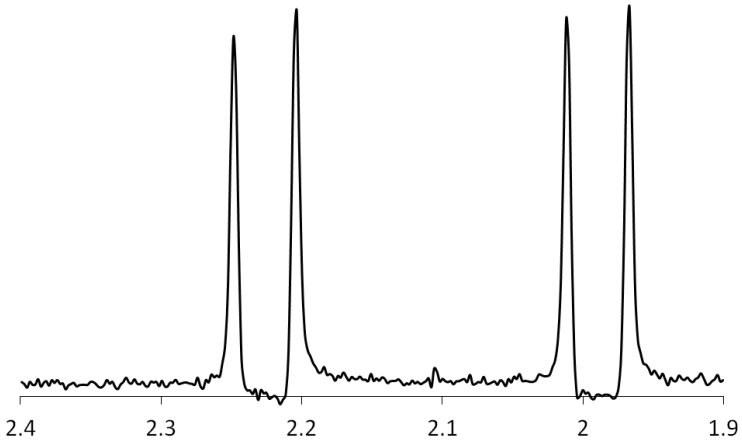

Figure 5.18: The H1 resonance as observed in the 1D ^{1}H–^{31}P HMQC spectrum of **23**.

The ^{31}P NMR spectrum of **23** shows a singlet of relative intensity five at 157.6 ppm and two doublets of doublets of relative intensity one at –12.6 and –105.9 ppm (Figure 5.19). These resonances correspond to P1, P2, P3, P4 and P5, P6, and P7, respectively. The P6 and P7 resonances appear as doublets in the $^{31}P\{^{1}H\}$ spectrum. The one-bond ^{31}P–^{31}P coupling constant is equal to –387 Hz.

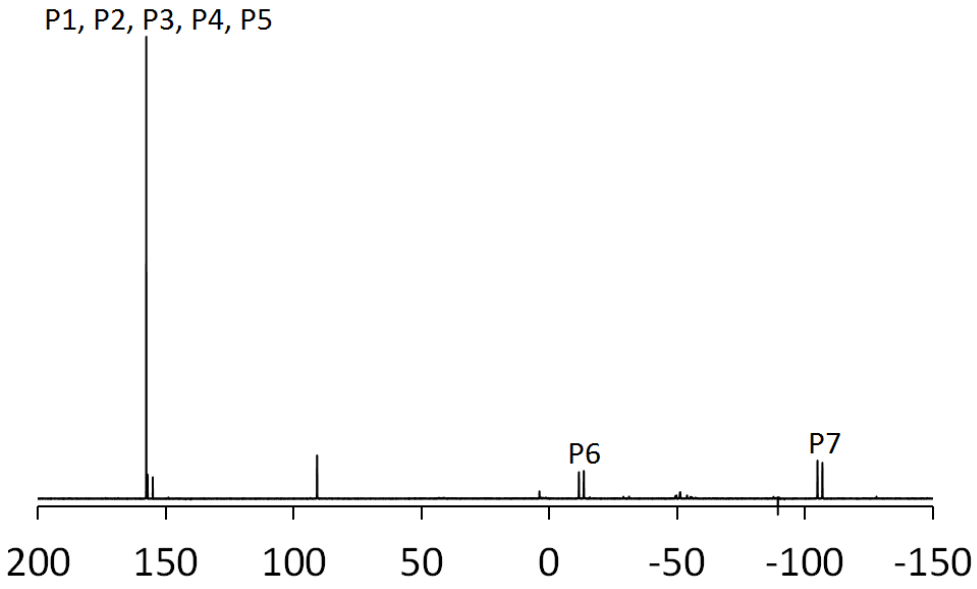

Figure 5.19: ^{31}P NMR spectrum of **23** recorded in d_5-pyridine.

The $^{13}C\{^1H\}$ NMR spectrum of **23** shows resonances at 143.2, 130.9, 129.8 and 128.7 ppm, corresponding to the four different aromatic environments, and at 28.2 and 21.5 ppm, corresponding to the *ortho*- and *para*-methyl groups, respectively.

5.3.4 Mass spectrometric studies

The postive and negative ion mode ESI mass spectra of **23** confirm that the product is $[Co(\eta^5\text{-}P_5)\{\eta^2\text{-}HP_2(mes)\}]^{2-}$. The major peak in the negative ion mode spectrum corresponds to the oxidised anion, $[Co(\eta^5\text{-}P_5)\{\eta^2\text{-}HP_2(mes)\}]^-$. The positive ion mode spectrum shows peaks due to the anion accompanied by two and three $[K(2,2,2\text{-crypt})]^+$ ions (Figure 5.20).

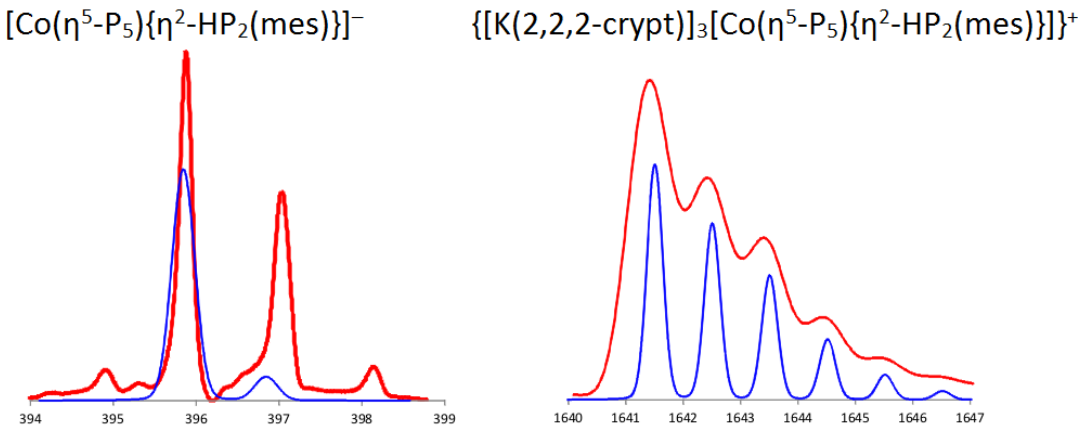

Figure 5.20: ESI-MS mass envelopes for $[Co(\eta^5\text{-}P_5)\{\eta^2\text{-}HP_2(mes)\}]^-$ and $\{[K(2,2,2\text{-crypt})]_3[Co(\eta^5\text{-}P_5)\{\eta^2\text{-}HP_2(mes)\}]\}^+$. Predicted isotopic distributions are shown in blue and observed mass spectrometric data are shown in red.

5.4 Solution reactivity of As_7^{3-} towards $[Co(PEt_2Ph)_2(mes)_2]$

5.4.1 Synthesis of $[Co(\eta^3\text{-}As_3)\{\eta^4\text{-}As_4(mes)_2\}]^{2-}$ (24)

K_3As_7 was found to react with $[Co(PEt_2Ph)_2(mes)_2]$ in ethylenediamine in the presence of 2,2,2-crypt to form $[K(2,2,2\text{-crypt})]_2[Co(\eta^3\text{-}As_3)\{\eta^4\text{-}As_4(mes)_2\}]$. This compound features the novel anionic species $[Co(\eta^3\text{-}As_3)\{\eta^4\text{-}As_4(mes)_2\}]^{2-}$ (**24**). Crystals of $[K(2,2,2\text{-crypt})]_2$[**24**]·py·0.5tol suitable for single crystal X-ray diffraction were obtained by slow diffusion of toluene into a solution of the compound in pyridine.

5.4.2 Structure of $[Co(\eta^3\text{-}As_3)\{\eta^4\text{-}As_4(mes)_2\}]^{2-}$ (24)

24 consists of an η^3-As_3 group and an η^4-$As_4(mes)_2$ group bonded to a central Co atom (Figure 5.21). A valence electron count of eighteen for the Co centre can be obtained using a radical electron counting protocol. A Co atom in the zero oxidation state has a d^9 electron configuration, and the η^3-As_3 unit and the η^4-$As_4(mes)_2$ ligand donate three and four electrons, respectively. An additional two electrons are obtained from the 2– charge. The η^3-As_3 unit has been observed in a number of previously reported transition metal compounds. These include $[(\eta^3\text{-}As_3)Co(CO)_3]$, $[(\eta^3\text{-}As_3)CrCp(CO)_2]$ and $[(\eta^3\text{-}As_3)MCp^*(CO)_2]$ (M = Cr, Mo, W).[31–34,74] **24** represents the first example of an η^4-As_4R_2 group coordinated to a metal centre, although a dianionic P analogue was isolated in $[Tl_2(\eta^4\text{-}P_4(Ar^{Dipp_2})_2)]$ (Ar^{Dipp_2} = C_6H_3-2,6-(C_6H_3-2,6-$^iPr_2$)$_2$).[52]

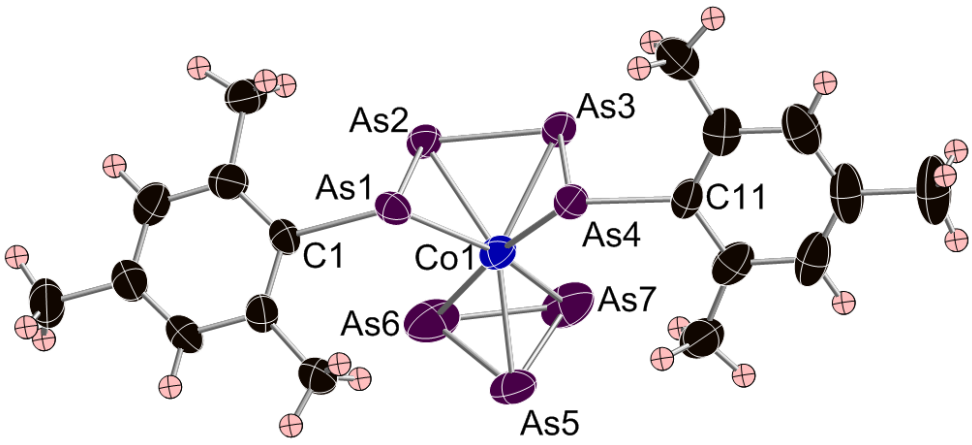

Figure 5.21: Thermal ellipsoid plot of **24** with anisotropic displacement ellipsoids pictured at 50% probability. H atoms are shown as small spheres of arbitrary radii.

There are three possible oxidation state assignments for **24**: a Co^{I} complex of a neutral 1,3-butadiene-like $As_4(mes)_2$ group and a six π electron As_3^{3-} ligand; a Co^{III} complex of a dianionic $[As_4(mes)_2]^{2-}$ group and an As_3^{3-} unit; or a Co^{-I} complex of an $[As_4(mes)_2]^{2-}$ ligand and a two π electron As_3^{+} group (Figure 5.22). The As–As bond lengths in both the η^4-$As_4(mes)_2$ unit and the η^3-As_3 group are in between typical values for As–As single and double bonds.[9,67] Notably, there is very little variation in the As–As bond lengths within the $As_4(mes)_2$ group, which implies that the bonding must be delocalised. This delocalisation suggests that the ligand is dianionic, although π back-bonding from the Co centre will also contribute to the bond lengths. Furthermore, there are examples of neutral butadiene species bonded to Co centres that do not exhibit the expected "short–long–short" alternation in bond lengths, instead featuring bond lengths that are approximately the same length. One such species is $[Co(\eta^4\text{-}C_4H_4{}^tBu_2)_2]^-$, which was synthesised by Cloke *et al.*[75] Power and co-workers observed that the P–P bond lengths in $[Tl_2(\eta^4\text{-}P_4(Ar^{Dipp_2})_2]$ are almost identical to each other and proposed that this compound consists of a $[P_4(Ar^{Dipp_2})_2]^{2-}$ ligand coordinated to two Tl^+ ions.[52]

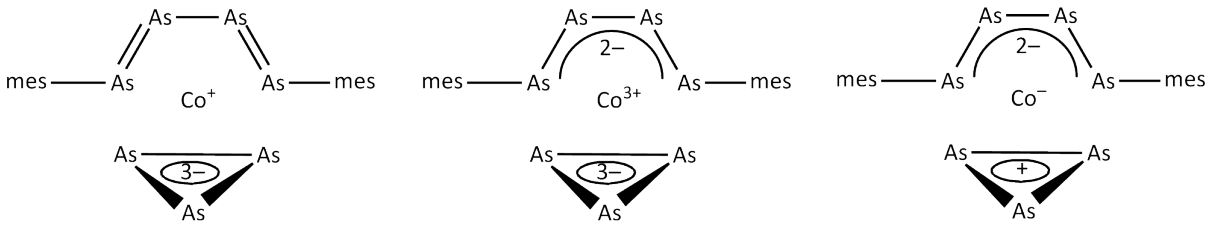

Figure 5.22: Diagram showing the three most plausible charge assignments for **24**.

Figure 5.23 shows selected Kohn-Sham orbitals for the hypothetical diprotic analogue of **24**, $[Co(\eta^3\text{-}As_3)(\eta^4\text{-}As_4H_2)]^{2-}$, and the hypothetical carbon analogue, $[Co(\eta^3\text{-}C_3H_3)(\eta^4\text{-}C_4H_6)]^{2-}$. Several of the molecular orbitals calculated for $[Co(\eta^3\text{-}As_3)(\eta^4\text{-}As_4H_2)]^{2-}$ are similar in appearance to orbitals calculated for $[Co(\eta^3\text{-}C_3H_3)(\eta^4\text{-}C_4H_6)]^{2-}$, although the energy ordering of these orbitals is different in each case. An interesting change occurs in the HOMO–4 on substituting C for As. This is a ligand to metal bonding orbital for both species, and in the case of $[Co(\eta^3\text{-}As_3)(\eta^4\text{-}As_4H_2)]^{2-}$, the electron density is distributed fairly evenly over the four As atoms of the As_4H_2 unit. In the C species, however, the electron density is predominantly centred on the central C2 and C3 atoms, which implies that ligand to metal bonding mainly occurs through the central C–C bond. Metal-to-ligand π back-bonding contributions are observed in the HOMO–6 and HOMO–5 of the As and C species, respectively. The frontier

orbitals of both anions exhibit mostly metal *d* orbital character and are largely non-bonding.

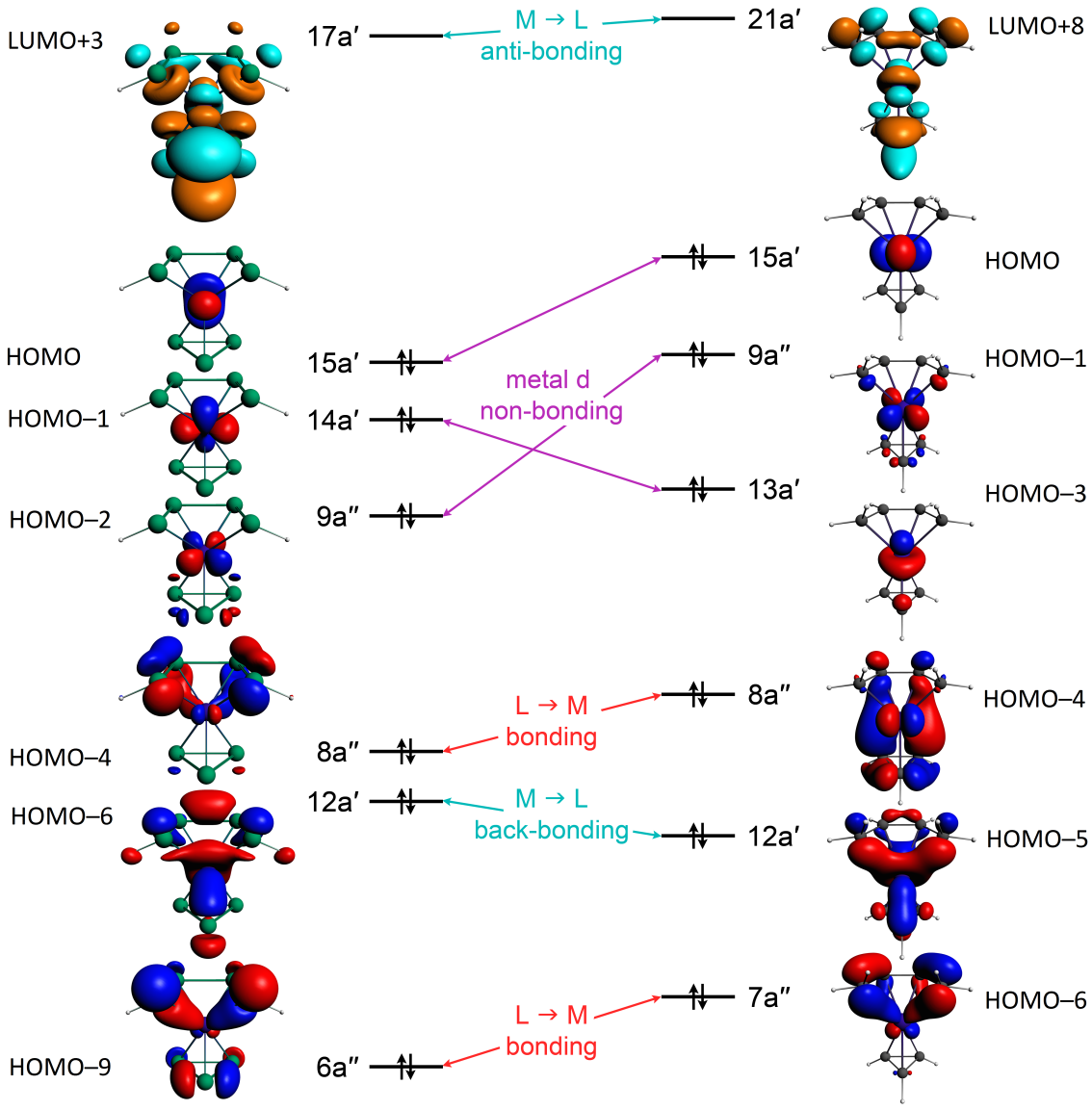

Figure 5.23: Selected Kohn-Sham orbitals for $[Co(\eta^3\text{-}As_3)(\eta^4\text{-}As_4H_2)]^{2-}$ (left) and $[Co(\eta^3\text{-}C_3H_3)(\eta^4\text{-}C_4H_6)]^{2-}$ (right).

Bader's AIM theory was used to analyse the calculated charge densities, $\rho(\mathbf{r})$, for **24** and its hypothetical carbon analogue. The analysis was focussed on the Co–E1–E2 and Co–E2–E3 planes. In the case of **24**, the analysis revealed three BCPs and one RCP in both planes, indicative of significant covalent character (Figure 5.24). The bond paths for both planes are comparable and exhibit a small amount of exocyclic character, which implies the presence of metal to ligand π back-bonding. The BCPs for Co1–As1, Co1–As2, As1–As2 and As2–As3 were found to have $\rho(\mathbf{r})$ values of 0.057, 0.066, 0.085 and 0.082, respectively. The $\rho(\mathbf{r})$ values for the As1–As2 and As2–As3 BCPs are almost identical, and this provides further evidence for the electron density being evenly distributed over the $As_4(mes)_2$ group. The Co–As BCPs

have similar $\rho(\mathbf{r})$ values to those of the As–As BCPs, which suggests that **24** possesses some metallacyclic character. In contrast, the bond paths for the Co–C2 and Co–C3 interactions in the C analogue are endocyclic, which implies that, in this case, the bonding is mostly ligand to metal donation (Figure 5.24). For the Co–C1–C2 plane, no BCP was observed between the Co centre and the terminal C1 atom, resulting in the absence of an RCP in this plane. This means that most of the ligand to metal bonding is likely to occur through the central C–C bond. The BCPs for Co1–C2, C1–C2 and C2–C3 were found to have $\rho(\mathbf{r})$ values of 0.102, 0.262 and 0.272, respectively. There is much more variation in these values in the C species than in **24**, which indicates that **24** possesses a higher degree of both metallacyclic and covalent character than its C analogue.

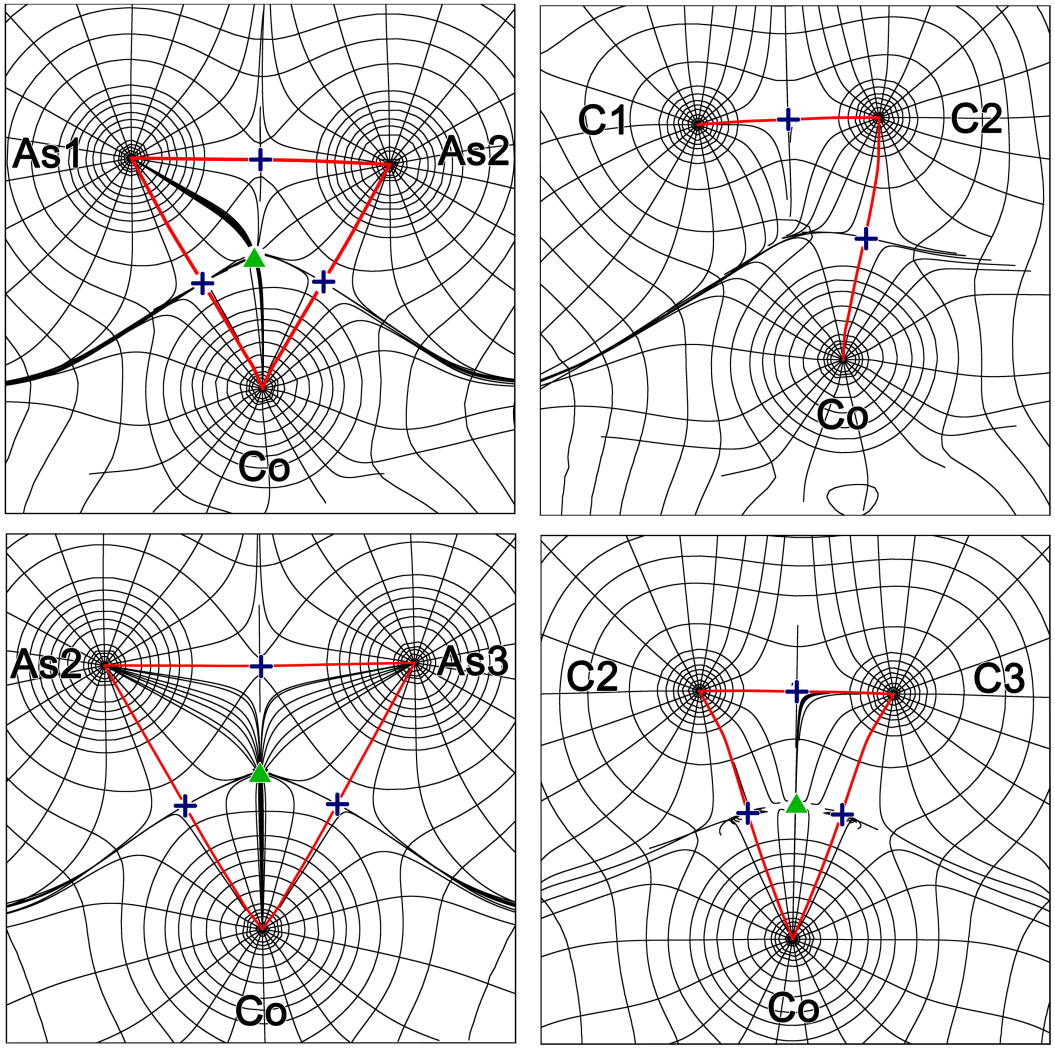

Figure 5.24: Contour maps of $\rho(\mathbf{r})$ in the Co–E1–E2 and Co–E2–E3 planes for **24** (left) and $[Co(\eta^3\text{-}C_3H_3)(\eta^4\text{-}C_4H_6)]^{2-}$ (right). Bond critical points are shown as crosses and ring critical points are shown as triangles.

Selected bond lengths for **24** are provided in Table 5.2, along with selected bond distances for

the optimised structure of **24**. The As–As bond lengths within the η^4-$As_4(mes)_2$ group range from 2.373(1) Å to 2.395(1) Å, while those within the η^3-As_3 ring are in the range 2.375(1) Å – 2.387(2) Å. These bond lengths are all in between typical values for As–As single and double bonds (sum of covalent radii for As–As single bonds: 2.42 Å; for As–As double bonds: 2.28 Å).[9,67] A search of the CSD gave a mean As–As bond length of 2.372(av) Å for complexes featuring an η^3-As_3 ring.[73] The Co–As bond lengths to the η^4-$As_4(mes)_2$ ligand are in the range 2.379(1) Å – 2.467(1) Å. The bonds to the outer As atoms, As1 and As4, are longer than those to the inner As atoms, As2 and As3, which suggests that the Co centre interacts more strongly with the inner As atoms than with the outer As atoms. The Co–As bond lengths to the η^3-As_3 group range from 2.364(1) Å to 2.415(1) Å and are slightly shorter than the Co–As bond lengths in the similar $[(\eta^3\text{-}As_3)Co(CO)_3]$ complex (2.439(5) Å).[74] The mean Co–As bond length obtained from a search of the CSD is 2.352(av) Å, while the sum of covalent radii for Co–As single bonds is 2.32 Å.[67,73]

Table 5.2: Selected bond lengths for the $[Co(\eta^3\text{-}As_3)\{\eta^4\text{-}As_4(mes)_2\}]^{2-}$ species.

Bond	Experimental bond length in **24** (Å)	Calculated bond length in $\mathbf{24_{DFT}}$ (Å)
As1–As2	2.373(1)	2.42
As1–C1	2.006(6)	2.02
As2–As3	2.395(1)	2.43
As3–As4	2.386(1)	2.42
As4–C11	2.019(6)	2.01
As5–As6	2.375(1)	2.43
As5–As7	2.381(1)	2.43
As6–As7	2.387(2)	2.42
Co1–As1	2.467(1)	2.49
Co1–As2	2.379(1)	2.41
Co1–As3	2.394(1)	2.41
Co1–As4	2.449(1)	2.49
Co1–As5	2.364(1)	2.40
Co1–As6	2.393(1)	2.44
Co1–As7	2.415(1)	2.44

5.4.3 ^{1}H NMR spectroscopic studies on $[Co(\eta^3\text{-}As_3)\{\eta^4\text{-}As_4(mes)_2\}]^{2-}$ (24)

The ^{1}H NMR spectrum of **24** shows three resonances at 6.77, 2.18 and 2.13 ppm with relative intensities 2:3:6 (Figure 5.25). These correspond to the *meta*-protons, the *para*-CH_3 groups

and the *ortho*-CH_3 groups, respectively. The spectrum also shows three intense resonances at 3.38, 3.32 and 2.31 ppm, which arise from the 2,2,2-crypt sequestering agent.

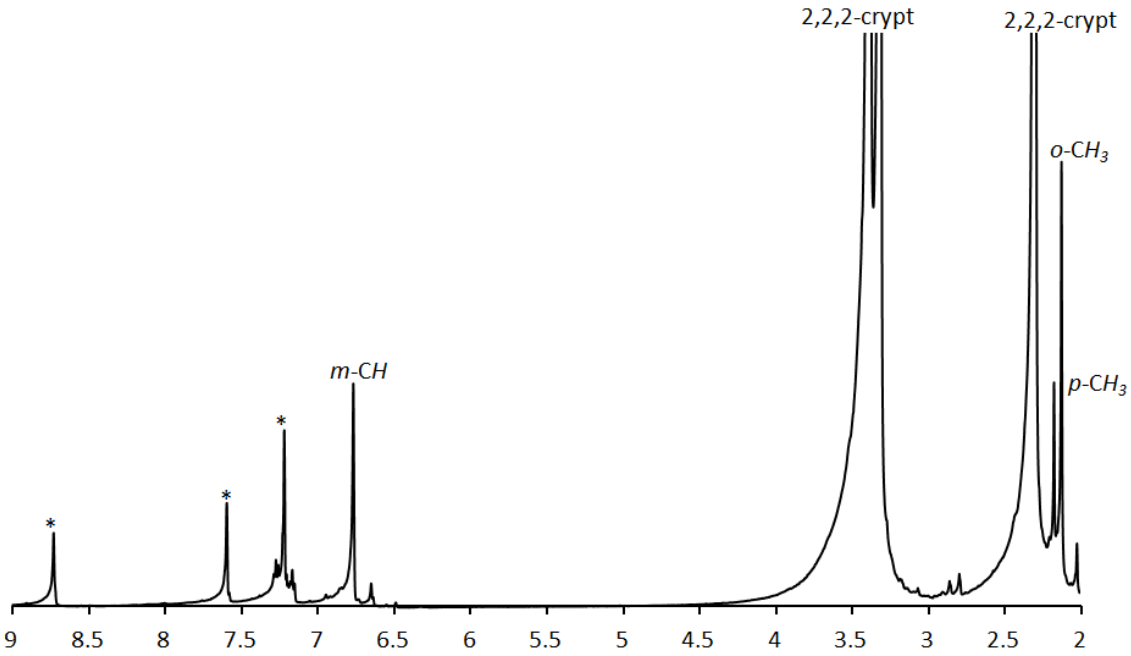

Figure 5.25: ^{1}H NMR spectrum of **24**. Resonances labelled * correspond to trace amounts of protic pyridine present in the d_5-pyridine solvent.

5.4.4 $^{13}C\{^{1}H\}$ NMR spectroscopic studies on $[Co(\eta^3\text{-}As_3)\{\eta^4\text{-}As_4(mes)_2\}]^{2-}$ (24)

The $^{13}C\{^{1}H\}$ NMR spectrum of **24** shows six resonances at 154.8, 142.8, 131.7 and 127.6 ppm, corresponding to the four different aromatic environments, and at 30.7 and 21.4 ppm, corresponding to the *ortho*- and *para*-methyl groups, respectively. The spectrum also shows three resonances at 70.9, 68.1 and 54.3 ppm, which arise from the 2,2,2-crypt sequestering agent, and five further resonances that can be assigned to toluene.[76]

5.4.5 Mass spectrometric studies

The positive and negative ion mode ESI mass spectra of **24** confirm that the product is $[Co(\eta^3\text{-}As_3)\{\eta^4\text{-}As_4(mes)_2\}]^{2-}$. The major peak in the negative ion mode spectrum corresponds to the oxidised anion, $[Co(\eta^3\text{-}As_3)\{\eta^4\text{-}As_4(mes)_2\}]^{-}$, while the positive ion mode spectrum shows peaks corresponding to the anion accompanied by two and three $[K(2,2,2\text{-crypt})]^{+}$ cations

(Figure 5.26).

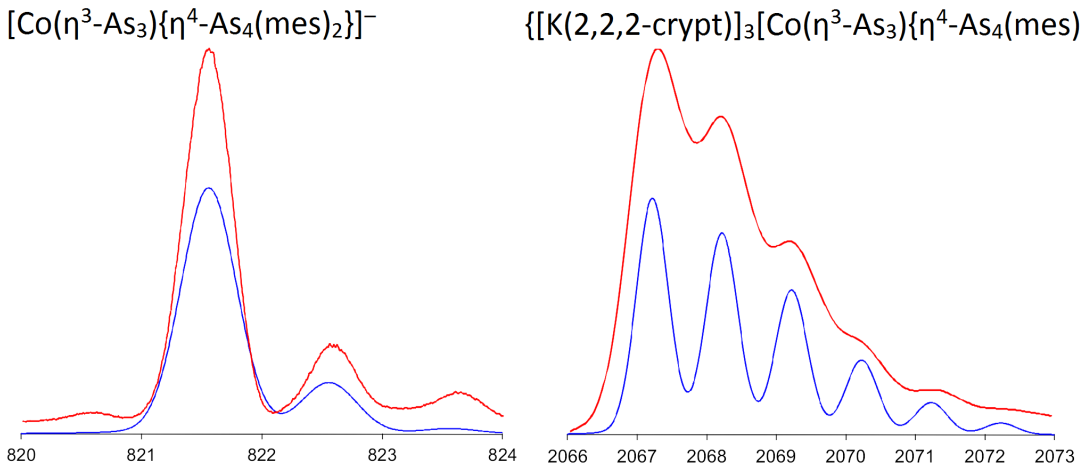

Figure 5.26: ESI-MS mass envelopes for $[Co(\eta^3\text{-}As_3)\{\eta^4\text{-}As_4(mes)_2\}]^-$ and $\{[K(2,2,2\text{-crypt})]_3[Co(\eta^3\text{-}As_3)\{\eta^4\text{-}As_4(mes)_2\}]\}^+$. Predicted isotopic distributions are shown in blue and observed mass spectrometric data are shown in red.

5.5 Conclusions

This chapter has described the reactions of P_7^{3-} and As_7^{3-} with $[Co(PEt_2Ph)_2(mes)_2]$ to form $[Co(\eta^5\text{-}P_5)\{\eta^2\text{-}HP_2(mes)\}]^{2-}$ (**23**) and $[Co(\eta^3\text{-}As_3)\{\eta^4\text{-}As_4(mes)_2\}]^{2-}$ (**24**), respectively. These reactions represent the first examples of E_7^{3-} reacting with Co compounds and are similar to previously reported transition metal mediated activation reactions of P_4 and As_4.[5–7] **23** and **24** have both been characterised by single crystal X-ray diffraction, multi-element NMR spectroscopy and mass spectrometry. The bonding within these two complexes has also been investigated computationally. Assignment of oxidation states and charges in **23** and **24** is non-trivial and may not be appropriate due to the high degree of delocalisation and covalency in these two species.

5.6 References

1. Kesanli, B.; Fettinger, J.; Scott, B.; Eichhorn, B. *Inorg. Chem.* **2004**, *43,* 3840–3846.
2. Eichhorn, B. W.; Mattamana, S. P.; Gardner, D. R.; Fettinger, J. C. *J. Am. Chem. Soc.* **1998**, *120,* 9708–9709.
3. Kesanli, B.; Fettinger, J.; Eichhorn, B. *J. Am. Chem. Soc.* **2003**, *125,* 7367–7376.
4. Moses, M. J.; Fettinger, J. C.; Eichhorn, B. W. *Inorg. Chem.* **2007**, *46,* 1036–1038.
5. Scherer, O. J. *Acc. Chem. Res.* **1999**, *32,* 751–762.

6. Cossairt, B. M.; Piro, N. A.; Cummins, C. C. *Chem. Rev.* **2010**, *110,* 4164–4177.
7. Caporali, M.; Gonsalvi, L.; Rossin, A.; Peruzzini, M. *Chem. Rev.* **2010**, *110,* 4178–4235.
8. Laplaza, C. E.; Davis, W. M.; Cummins, C. C. *Angew. Chem., Int. Ed. Engl.* **1995**, *34,* 2042–2044.
9. Pyykkö, P.; Atsumi, M. *Chem. Eur. J.* **2009**, *15,* 12770–12779.
10. Cherry, J. P. F.; Johnson, A. R.; Baraldo, L. M.; Tsai, Y. C.; Cummins, C. C.; Kryatov, S. V.; Rybak-Akimova, E. V.; Kapps, K. B.; Hoff, C. D.; Haar, C. M.; Nolan, S. P. *J. Am. Chem. Soc.* **2001**, *123,* 7271–7286.
11. Kuiper, D. S.; Wolczanski, P. T.; Lobkovsky, E. B.; Cundari, T. R. *J. Am. Chem. Soc.* **2008**, *130,* 12931–12943.
12. Curley, J. J.; Piro, N. A.; Cummins, C. C. *Inorg. Chem.* **2009**, *48,* 9599–9601.
13. Cherry, J. P. F.; Stephens, F. H.; Johnson, M. J. A.; Diaconescu, P. L.; Cummins, C. C. *Inorg. Chem.* **2001**, *40,* 6860–6862.
14. Scherer, O. J.; Sitzmann, H.; Wolmershäuser, G. *J. Organomet. Chem.* **1984**, *268,* C9–C12.
15. Simon, A.; Borrmann, H.; Craubner, H. *Phosphorus Sulfur* **1987**, *30,* 507–510.
16. Figueroa, J. S.; Cummins, C. C. *J. Am. Chem. Soc.* **2003**, *125,* 4020–4021.
17. Scherer, O. J.; Winter, R.; Wolmershäuser, G. *Z. Anorg. Allg. Chem.* **1993**, *619,* 827–835.
18. Scherer, O. J.; Ehses, M.; Wolmershäuser, G. *J. Organomet. Chem.* **1997**, *531,* 217–221.
19. Barr, M. E.; Dahl, L. F. *Organometallics* **1991**, *10,* 3991–3996.
20. Scherer, O. J.; Pfeiffer, K.; Heckmann, G.; Wolmershäuser, G. *J. Organomet. Chem.* **1992**, *425,* 141–149.
21. Hulley, E. B.; Wolczanski, P. T.; Lobkovsky, E. B. *Chem. Commun.* **2009**, 6412–6414.
22. Cannillo, E.; Coda, A.; Prout, K.; Daran, J. C. *Acta Crystallogr. B* **1977**, *33,* 2608–2611.
23. Etkin, N.; Benson, M. T.; Courtenay, S.; McGlinchey, M. J.; Bain, A. D.; Stephan, D. W. *Organometallics* **1997**, *16,* 3504–3510.
24. Di Vaira, M.; Ghilardi, C. A.; Midollini, S.; Sacconi, L. *J. Am. Chem. Soc.* **1978**, *100,* 2550–2551.
25. Bianchini, C.; Mealli, C.; Meli, A.; Sacconi, L. *Inorg. Chim. Acta* **1979**, *37,* L543–L544.
26. Di Vaira, M.; Sacconi, L.; Stoppioni, P. *J. Organomet. Chem.* **1983**, *250,* 183–195.
27. Dapporto, P.; Sacconi, L.; Stoppioni, P.; Zanobini, F. *Inorg. Chem.* **1981**, *20,* 3834–3839.
28. Goh, L. Y.; Chu, C. K.; Wong, R. C. S.; Hambley, T. W. *J. Chem. Soc., Dalton Trans.* **1989**, 1951–1956.
29. Scherer, O. J.; Sitzmann, H.; Wolmershäuser, G. *Acta Crystallogr. C* **1985**, *41,* 1761–1763.
30. Cossairt, B. M.; Diawara, M. C.; Cummins, C. C. *Science* **2009**, *323,* 602.
31. Chen, W.; Wong, R. C. S.; Goh, L. Y. *Acta Crystallogr. C* **1994**, *50,* 998–1000.
32. Scherer, O. J.; Wiedemann, W.; Wolmershäuser, G. *Chem. Ber.* **1990**, *123,* 3–6.

33. Bernal, I.; Brunner, H.; Meier, W.; Pfisterer, H.; Wachter, J.; Ziegler, M. L. *Angew. Chem., Int. Ed. Engl.* **1984**, *23,* 438–439.
34. Johnson, B. P.; Schiffer, M.; Scheer, M. *Organometallics* **2000**, *19,* 3404–3409.
35. Dapporto, P.; Midollini, S.; Sacconi, L. *Angew. Chem., Int. Ed. Engl.* **1979**, *18,* 469.
36. Peruzzini, M.; Marvelli, L.; Romerosa, A.; Rossi, R.; Vizza, F.; Zanobini, F. *Eur. J. Inorg. Chem.* **1999**, 931–933.
37. Gröer, T.; Baum, G.; Scheer, M. *Organometallics* **1998**, *17,* 5916–5919.
38. De Los Rios, I.; Hamon, J. R.; Hamon, P.; Lapinte, C.; Toupet, L.; Romerosa, A.; Peruzzini M. *Angew. Chem., Int. Ed.* **2001**, *40,* 3910–3912.
39. Caporali, M.; Di Vaira, M.; Peruzzini, M.; Seniori Costantini, S.; Stoppioni, P.; Zanobini, F. *Eur. J. Inorg. Chem.* **2010**, 152–158.
40. Schwarzmaier, C.; Timoshkin, A. Y.; Scheer, M. *Angew. Chem., Int. Ed.* **2013**, *52,* 7600–7603.
41. Lindsell, W. E.; McCullough, K. J.; Welch, A. J. *J. Am. Chem. Soc.* **1983**, *105,* 4487–4489.
42. Scherer, O. J.; Swarowsky, M.; Swarowsky, H.; Wolmershäuser, G. *Angew. Chem., Int. Ed. Engl.* **1988**, *27,* 694–695.
43. Scherer, O. J.; Swarowsky, M.; Wolmershäuser, G. *Organometallics* **1989**, *8,* 841–842.
44. Scherer, O. J.; Pfeiffer, K.; Wolmershäuser, G. *Chem. Ber.* **1992**, *125,* 2367–2372.
45. Santiso-Quiñones, G.; Reisinger, A; Slattery, J.; Krossing, I. *Chem. Commun.* **2007**, 5046–5048.
46. Krossing, I. *J. Am. Chem. Soc.* **2001**, *123,* 4603–4604.
47. Forfar, L. C.; Clark, T. J.; Green, M.; Mansell, S. M.; Russell, C. A.; Sanguramath, R. A.; Slattery, J. M. *Chem. Commun.* **2012**, *48,* 1970–1972.
48. Schwarzmaier, C.; Sierka, M.; Scheer, M. *Angew. Chem., Int. Ed.* **2013**, *52,* 858–861.
49. Scherer, O. J.; Vondung, J.; Wolmershäuser, G. *Angew. Chem., Int. Ed. Engl.* **1989**, *28,* 1355–1357.
50. Herberhold, M.; Frohmader, G.; Milius, W. *J. Organomet. Chem.* **1996**, *522,* 185–196.
51. Seidel, W. W.; Summerscales, O. T.; Patrick, B. O.; Fryzuk, M. D. *Angew. Chem., Int. Ed.* **2009**, *48,* 115–117.
52. Fox, A. R.; Wright, R. J.; Rivard, E.; Power, P. P. *Angew. Chem., Int. Ed.* **2005**, *44,* 7729–7733.
53. Scherer, O. J.; Schwalb, J.; Wolmershäuser, G.; Kaim, W.; Gross, R. *Angew. Chem., Int. Ed. Engl.* **1986**, *25,* 363–364.
54. Scherer, O. J.; Brück, T. *Angew. Chem., Int. Ed. Engl.* **1987**, *26,* 59.
55. Scherer, O. J.; Brück, T.; Wolmershäuser, G. *Chem. Ber.* **1988**, *121,* 935–938.
56. Scherer, O. J.; Wiedemann, W.; Wolmershäuser, G. *J. Organomet. Chem.* **1989**, *361,* C11–C14.
57. Scherer, O. J.; Blath, C.; Wolmershäuser, G. *J. Organomet. Chem.* **1990**, *387,* C21–C24.
58. Scherer, O. J.; Blath, C.; Heckmann, G.; Wolmershäuser, G. *J. Organomet. Chem.* **1991**, *409,* C15–C18.

59. Urnėžius, E.; Brennessel, W. W.; Cramer, C. J.; Ellis, J. E.; Von Ragué Schleyer, P. *Science* **2002**, *295,* 832–834.

60. Scherer, O. J.; Sitzmann, H.; Wolmershäuser, G. *Angew. Chem., Int. Ed. Engl.* **1985**, *24,* 351–353.

61. Scherer, O. J.; Sitzmann, H.; Wolmershäuser, G. *Angew. Chem., Int. Ed. Engl.* **1989**, *28,* 212–213.

62. Scherer, O. J.; Schwalb, J.; Swarowsky, H.; Wolmershäuser, G.; Kaim, W.; Gross, R. *Chem. Ber.* **1988**, *121,* 443–449.

63. Knapp, C. M.; Westcott, B. H.; Raybould, M. A. C.; McGrady, J. E.; Goicoechea, J. M. *Angew. Chem., Int. Ed.* **2012**, *51,* 9097–9100.

64. Knapp, C. M.; Westcott, B. H.; Raybould, M. A. C.; McGrady, J. E.; Goicoechea, J. M. *Chem. Commun.* **2012**, *48,* 12183–12185.

65. Winterhalter, U.; Zsolnai, L.; Kircher, P.; Heinze, K.; Huttner. G. *Eur. J. Inorg. Chem.* **2001**, 89–103.

66. Krautscheid, H.; Matern, E.; Olkowska-Oetzel, J.; Pikies, J.; Fritz, G. *Z. Anorg. Allg. Chem.* **2001**, *627,* 675–678.

67. Pyykkö, P.; Atsumi, M. *Chem. Eur. J.* **2009**, *15,* 186–197.

68. Dewar, M. *Bull. Soc. Chim. Fr.* **1951**, *18,* C79.

69. Chatt, J.; Duncanson, L. A. *J. Chem. Soc.* **1953**, 2939–2947.

70. Chatt, J.; Duncanson, L. A.; Venanzi, L. M. *J. Chem. Soc.* **1955**, 4456–4460.

71. Bader, F. W. *Atoms in Molecules: A Quantum Theory*; Clarendon Press: Oxford, 1990.

72. Scherer, W.; Eickerling, G.; Shorokhov, D.; Gullo, E.; McGrady, G. S.; Sirsch, P. *New J. Chem.* **2006**, *30,* 309–312.

73. Values taken from CSD version 5.33 (2012).

74. Foust, A. S.; Foster, M. S.; Dahl, L. F. *J. Am. Chem. Soc.* **1969**, *91,* 5631–5633.

75. Cloke, F. G. N.; Hitchcock, P. B.; McCamley, A. *J. Chem. Soc., Chem. Commun.* **1993**, 248–250.

76. Fulmer, G. R.; Miller, A. J. M.; Sherden, N. H.; Gottlieb, H. E.; Nudelman, A.; Stolz, B. M.; Bercaw, J. E.; Goldberg, K. I. *Organometallics* **2010**, *29,* 2176–2179.

Chapter 6 Conclusions

This thesis has described the synthesis and characterisation of twenty-four novel anionic species. Chapter 2 detailed the reactivity of E_7^{3-} (E = P, As) towards $[Cu_5(mes)_5]$, MPh_2 (M = Zn, Cd) and $InPh_3$. These reactions resulted in the formation of $[Cu_2(E_7)_2]^{4-}$ (E = P, As), $[M(E_7)_2]^{4-}$ (M = Zn: E = P, As; M = Cd: E = P) and $[E_7InPh_2]^{2-}$ (E = P, As), and are the first examples of E_7^{3-} reacting with compounds of group 11, group 12 and group 13 elements.

The reactions of E_7^{3-} (E = P, As) with a series of metal salts, namely $[M(nbe)_3][SbF_6]$ and MCl (M = Ag, Au), $InCl_3$, TlCl, and MI_2 (M = Sn, Pb), were discussed in Chapter 3. $[M_2(HP_7)_2]^{2-}$ (M = Ag, Au), $[In(E_7)_2]^{3-}$ (E = P, As), $[TlE_7]^{2-}$ (E = P, As) and $[ME_{15}]^{3-}$ (M = Sn, Pb; E = P, As) were isolated. These investigations showed that salt metathesis reactions are a versatile route to heteroatomic cluster anions.

Chapter 4 described the reactivity of P_7^{3-} towards a series of group 8 compounds. Reaction of P_7^{3-} with $FeCl_2$ and $[Ru(PPh_3)_3Cl_2]$ resulted in the formation of $[M(HP_7)_2]^{2-}$ and $[M(P_7)_2]^{4-}$ (M = Fe, Ru), which represent the first examples of P-containing metallocene analogues to be synthesised from P_7^{3-}. In addition, P_7^{3-} was found to react with $[Ru(COD)(\eta^3\text{-}CH_2C(CH_3)CH_2)_2]$ to form $[(C_4H_7)P_7Ru(COD)]^{2-}$.

The research discussed in Chapter 5 showed that E_7^{3-} ions (E = P, As) can undergo transition metal mediated activation reactions with $[Co(PEt_2Ph)_2(mes)_2]$ to form $[Co(\eta^5\text{-}P_5)\{\eta^2\text{-}HP_2(mes)\}]^{2-}$ and $[Co(\eta^3\text{-}As_3)\{\eta^4\text{-}As_4(mes)_2\}]^{2-}$. These reactions are the first examples of E_7^{3-} reacting with Co compounds, and of transition metal mediated activation of E_7^{3-} to form lower nuclearity P- and As-containing moieties. This research could potentially be extended to other transition metal compounds in the future.

Chapter 7 Experimental

7.1 General synthetic considerations

7.1.1 Manipulation of air- and moisture-sensitive compounds

Due to the highly air- and moisture-sensitive nature of many of the reagents and products described in this thesis, all manipulations were carried out under an inert atmosphere using standard Schlenk-line or glovebox techniques (MBraun UNIlab glovebox maintained at < 0.1 ppm O_2 and < 0.1 ppm H_2O).

7.1.2 Preparation and purification of reagents and solvents

The sources and purification procedures of the reagents and solvents used are provided in Table 7.1.

Table 7.1: Sources of chemicals.

Chemical	**Source**	**Purity**	**Purification Procedure**
K_3P_7	Synthesised[1]	Unknown	Used as obtained
K	Strem	99.95%	Used as received
P	Aldrich	99.99%	Used as received
K_3As_7	Synthesised[2]	Unknown	Used as obtained
As	Alfa Aesar	99%	Used as received
$[K(2,2,2\text{-crypt})]_2[HP_7]\cdot py$	Synthesised[3]	Unknown	Used as obtained
$[Cu_5(mes)_5]$	Synthesised[4]	Unknown	Used as obtained
Mg turnings	Fisher	General purpose grade	Used as received
2-Bromomesitylene	Alfa Aesar	99%	Used as received
CuCl	Strem	97+%	Used as received
1,4-Dioxane	Rathburn	HPLC grade	Distilled over Na metal/benzophenone
$ZnPh_2$	Strem	99%	Used as received
$CdPh_2$	Synthesised[5]	Unknown	Used as obtained
Phenylmagnesium chloride	Aldrich	2.0 M in THF	Used as received
$CdCl_2$	Strem	99+%	Used as received
$InPh_3$	Synthesised[6]	Unknown	Used as obtained
Phenyllithium	Aldrich	1.8 M in dibutyl ether	Used as received
$InCl_3$	Strem	99.999%	Used as received
$[Ag(nbe)_3][SbF_6]$	Synthesised[7]	Unknown	Used as obtained
Bicyclo[2.2.1]hept-2-ene	Aldrich	99%	Used as received
$Ag[SbF_6]$	Strem	98%	Used as received
$[Au(nbe)_3][SbF_6]$	Synthesised[8]	Unknown	Used as obtained
$[Au(SMe_2)Cl]$	Aldrich	Unknown	Used as received
AgCl	Strem	99.9%	Used as received
AuCl	Strem	97%	Used as received
TlCl	Strem	99.999%	Used as received
SnI_2	Strem	99%	Used as received
PbI_2	Strem	99.999%	Used as received
$FeCl_2$	Strem	98%	Used as received
$[Ru(PPh_3)_3Cl_2]$	Strem	99%	Used as received
$[Ru(COD)(\eta^3\text{-}CH_2C(CH_3)CH_2)_2]$	Synthesised[9]	Unknown	Used as obtained
3-Chloro-2-methylpropene	Alfa Aesar	98%	Used as received
1,5-Cyclooctadiene	Aldrich	99%	Used as received
$RuCl_3\cdot xH_2O$	Alfa Aesar	99%	Used as received
$[Co(PEt_2Ph)_2(mes)_2]$	Synthesised[10]	Unknown	Used as obtained
PEt_2Ph	Alfa Aesar	97%	Used as received
$CoBr_2$	Alfa Aesar	97%	Used as received

Chemical	Source	Purity	Purification Procedure
2,2,2-Crypt	Merck	99+%	Dried under vacuum
18-Crown-6	Alfa Aesar	99%	Dried under vacuum
$[NH_4][BPh_4]$	Aldrich	99%	Dried under vacuum
$K[N(SiMe_3)_2]$	Aldrich	95%	Dried under vacuum
KH	Alfa Aesar	30-35% w/w	Washed with hexane, then dried under vacuum
Ethylenediamine	Aldrich	99%	Distilled over Na metal
Pyridine	Rathburn	99.9%	Distilled over CaH_2
THF	Rathburn	99.9%	Distilled over Na metal/benzophenone
DMF	Rathburn	99.9%	Purified through an MBraun MB SPS-800 solvent system
Toluene	Rathburn	99.9%	Purified through an MBraun MB SPS-800 solvent system
Diethyl ether	Fisher	Pesticide residue grade	Purified through an MBraun MB SPS-800 solvent system
Hexane	Rathburn	99.9%	Purified through an MBraun MB SPS-800 solvent system
Dichloromethane	Fisher	HPLC grade	Purified through an MBraun MB SPS-800 solvent system
Benzene	Rathburn	99.9%	Purified through an MBraun MB SPS-800 solvent system
Ethanol	Aldrich	99.8+%	Used as received
d_5-pyridine	Cambridge Isotope Laboratories, Inc.	99.5%	Dried over CaH_2, then vacuum distilled
d_7-DMF	Cambridge Isotope Laboratories, Inc.	99.5%	Dried over CaH_2, then vacuum distilled

7.2 Characterisation techniques

7.2.1 Single crystal X-ray diffraction

Single crystal X-ray diffraction data for the $[K(2,2,2\text{-crypt})]^+$ or $[K(18\text{-crown-6})]^+$ salts of **2–6**, **8–10**, **12-16**, **18** and **23** were collected on an Enraf-Nonius Kappa CCD diffractometer. Crystals were mounted on a glass fibre using Paratone-N oil and cooled to 150 K using

an Oxford Cryosystems open flow N_2 cooling device.[11] Data were collected using graphite monochromated Mo K_α radiation (λ = 0.71073 Å), equivalent reflections were merged, and the images were processed using the DENZO and SCALEPACK programs.[12] Single crystal X-ray diffraction data for the $[K(2,2,2\text{-crypt})]^+$ salts of **22** and **24** were collected on an Oxford Diffraction Supernova dual-source diffractometer equipped with a 135 mm Atlas CCD area detector. Data were collected using mirror monochromated Cu K_α radiation (λ = 1.5418 Å) and processed using the CrysAlisPro package, including unit cell parameter refinement and interframe scaling (which was carried out using SCALE3 ABSPACK within CrysAlisPro).[13] Equivalent reflections were merged, and the images were processed using the CrysAlisPro suite. Corrections for Lorentz-polarisation effects were performed, and the structures were solved by direct methods and refined on F^2 using the SHELX 97-2 package.[14–16]

7.2.2 DFT calculations

Calculations on **8–10**, **12**, **13**, **15**, and **18–21** were performed by Dr Jose Goicoechea using the Amsterdam Density Functional package (ADF2010.02).[17–19] Calculations on **23** were performed by Melissa Raybould. A triple-ζ Slater-type basis set, extended with a single polarisation function, was used to describe all atoms, except in the case of **23**, where the basis set was extended with two polarisation functions. The local density approximation was employed for the optimisations, along with the local exchange-correlation potential of Vosko, Wilk and Nusair, and gradient corrections to exchange and correlation proposed by Becke and Perdew (BP86).[20–23] Relativistic effects were incorporated using the Zeroth Order Relativistic Approximation (ZORA).[24–26] The presence of cations in the crystal lattice was modelled by surrounding the anion with a continuum dielectric using COSMO.[27] The chosen dielectric constants ε = 16.9 and ε = 78.4 correspond to those of ammonia and water, respectively, although structural parameters are not strongly dependent on this choice. All structures were optimized using the gradient algorithm of Versluis and Ziegler.[28] Single point calculations were performed on the optimised structure of **23** using the Gaussian 03 program package in order to produce the relevant .wfn files for the Atoms In Molecules (AIM) calculations.[29] The BP86 functional was employed along with the 6-311G* basis set.[22,23,30,31] All calculations on **24** were carried out by Melissa Raybould using the Gaussian 03 program.[29]

Geometries were fully optimised using the BP86 functional in conjunction with a def-TZVP basis on Co and As and a def-SVP basis on C and H.[22,23,32–34] A polarisable continuum with ε = 78.4 was included in the model to mimic the confining effects of the crystal lattice. Topological properties of electron densities of **23** and **24** were characterised with the AIM2000 program package using the Atoms In Molecules theory of Bader.[35,36] The signs associated with the spin–spin coupling constants (*J*) for **3**, **5**, **6**, **10**, **14**, **16**, **19**, **21** and **22** were determined by computing Fermi contact values using the Gaussian 09 program package revision A02.[37] Initial atomic coordinates were taken from single-crystal X-ray diffraction experiments for **3**, **5**, **6**, **10**, **14**, **16** and **22**. The coordinates for **19** and **21** were taken from the optimised computed geometries of the anions.

7.2.3 NMR spectroscopy

^{1}H, ^{31}P and ^{13}C NMR spectra were recorded from d_5-pyridine or d_7-DMF solutions using a Varian Mercury-VX 300 spectrometer, a Varian Unity-Plus 500 spectrometer or a Bruker AVD500 spectrometer. 1D ^{1}H–^{31}P HMQC spectra were recorded on a Bruker DRX500 spectrometer. ^{1}H spectra were referenced to the most downfield residual protic solvent resonance (pyridine: δ = 8.74 ppm; DMF: δ = 8.03 ppm). ^{13}C spectra were referenced to d_5-pyridine (δ = 150.35 ppm). ^{31}P spectra were externally referenced to H_3PO_4 (δ = 0 ppm). ^{31}P NMR simulations were carried out using the gNMR software suite.[38]

7.2.4 Electrospray mass spectrometry

Positive and negative ion mode electrospray mass spectra were recorded from DMF solutions (10-20 μM) on a Waters LCT mass spectrometer with a Z-spray source (150 °C source temperature, 200 °C desolvation temperature, 3.2 kV capillary voltage and 25 V cone voltage). The samples were introduced directly using a 1 mL SGE syringe and a syringe pump at 10 μL per minute.

7.2.5 Elemental analyses

Elemental analyses were carried out by Stephen Boyer of the London Metropolitan University or by Elemental Microanalysis Ltd. Samples (approximately 5 mg) were submitted in sealed Pyrex ampoules.

7.3 Syntheses

7.3.1 Zintl phases

The K_3E_7 precursors (E = P, As) were synthesised from a stoichiometric mixture of the elements according to previously reported synthetic procedures.[1,2] The elements were heated (to 600 °C in the case of K_3P_7 and to 550 °C in the case of K_3As_7) for 72 hours in sealed niobium containers that were jacketed in evacuated, sealed silica ampoules.

7.3.2 $[K(2,2,2\text{-crypt})]_2[HP_7]\cdot py$

The synthesis of $[K(2,2,2\text{-crypt})]_2[HP_7]\cdot py$ was previously reported by the Goicoechea group.[3] A slurry of K_3P_7 (887 mg, 2.65 mmol) in approximately 50 mL pyridine was reacted with degassed and deionised H_2O (96 μL, 5.30 mmol), and the resulting mixture was stirred under argon for one hour. 2,2,2-Crypt (2.00 g, 5.30 mmol) was added, and the mixture was stirred for an additional five minutes and subsequently filtered. The bright yellow-orange filtrate was concentrated to the point of saturation under a dynamic vacuum, after which 500 mL toluene was added to precipitate the product as an orange microcrystalline solid. This solid was isolated by filtration and dried under vacuum, yielding 2.112 g (76% yield) $[K(2,2,2\text{-crypt})]_2[HP_7]\cdot py$.

7.3.3 Organometallic precursors

7.3.3.1 $[Cu_5(mes)_5]$

$[Cu_5(mes)_5]$ was synthesised using a method previously reported by Floriani and co-workers.[4] 2-Mesitylmagnesium bromide was prepared *in situ* by stirring magnesium turnings (1.823 g, 0.076 mol) and 2-bromomesitylene (7.65 mL, 0.050 mol) in approximately 60 mL THF at 0 °C overnight. This solution was then added dropwise to a suspension of CuCl (5 g, 0.051 mol) in approximately 90 mL THF at –20 °C. The grey-brown reaction mixture was stirred for 20 hours and allowed to warm to room temperature. Approximately 30 mL 1,4-dioxane was added dropwise, and the stirring was continued for a further 12 hours. The 1,4-dioxane fraction was filtered off, and the solid residue was dried under vacuum. The product was extracted into approximately 70 mL warm toluene and filtered. The toluene solution was then concentrated to approximately 30 mL and placed in a refrigerator overnight, after which yellow crystals of $[Cu_5(mes)_5]$ could be isolated in a yield of 5.2 g (56%).

7.3.3.2 $CdPh_2$

$CdPh_2$ was prepared using a similar method to that detailed by Tang and Richey.[5] 2.0 M phenylmagnesium chloride (40 mL, 0.080 mol) in THF was added dropwise to a solution of $CdCl_2$ (6.4 g, 0.035 mol) in approximately 40 mL THF at –78 °C. The reaction mixture was stirred overnight in a foil-covered Schlenk tube. The THF solvent was removed *in vacuo*, and then the product was extracted into approximately 100 mL warm toluene and filtered. The volume of the solution was reduced by half, after which the solution was cooled to –78 °C and filtered again. The toluene solvent was removed under a dynamic vacuum, yielding a white solid. This solid was dissolved in approximately 100 mL diethyl ether, and the resulting solution was filtered. The filtrate was dried under vacuum, yielding 1.207 g (13% yield) $CdPh_2$.

7.3.3.3 $InPh_3$

$InPh_3$ was synthesised according to a modified literature procedure.[6] 1.8 M phenyllithium (38.5 mL, 0.069 mol) in dibutyl ether was added dropwise to a solution of $InCl_3$ (4.99 g, 0.023 mol) in diethyl ether at –78 °C. The reaction mixture was stirred and allowed to warm to room temperature overnight. The resulting solution was subsequently filtered into a clean, dry Schlenk tube. The solvent was removed under a dynamic vacuum to yield an orange oil, which was dissolved in hexane to form an orange solution. This solution was filtered through Celite, and the filtrate was dried under vacuum to give $InPh_3$ as a white solid in a yield of 1.87 g (24%).

7.3.3.4 $[Ag(nbe)_3][SbF_6]$

$[Ag(nbe)_3][SbF_6]$ was synthesised using a literature reported method similar to that detailed by Fianchini *et al.*[7] A solution of bicyclo[2.2.1]hept-2-ene (norbornene) (1.5 g, 16.0 mmol) in approximately 90 mL dichloromethane was added to a Schlenk tube containing $Ag[SbF_6]$ (1.2 g, 3.49 mmol). The mixture was stirred for 16 hours at room temperature, and the solution obtained was concentrated to approximately 40 mL under a dynamic vacuum. Approximately 50 mL hexane was added, resulting in the production of a white precipitate, which was isolated by filtration. The white solid was redissolved in the minimum amount of dichloromethane, and the resulting solution was filtered into a clean, dry Schlenk tube and layered with hexane. After approximately one week, colourless cube-like crystals of $[Ag(nbe)_3][SbF_6]$ were obtained in a yield of 540 mg (25%).

7.3.3.5 $[Au(nbe)_3][SbF_6]$

$[Au(nbe)_3][SbF_6]$ was synthesised using a similar method to that detailed by Hooper *et al.*[8] A solution of norbornene (904 mg, 9.62 mmol) in approximately 40 mL dichloromethane was added to a Schlenk tube containing $[Au(SMe_2)Cl]$ (236 mg, 0.801 mmol) and $Ag[SbF_6]$ (276 mg, 0.803 mmol). The reaction mixture was stirred for 16 hours to give a grey-cream coloured solution. The solvent was removed *in vacuo*, and a further solution of norbornene

(452 mg, 4.81 mmol) in approximately 40 mL dichloromethane was added to the resulting grey solid. The mixture was stirred for two hours. The solution was subsequently filtered through Celite to remove the grey AgCl precipitate, and the residue was washed three times with dichloromethane. The resulting solution was concentrated to approximately 4 mL *in vacuo*, filtered into a clean, dry Schlenk tube and layered with diethyl ether. After approximately one week, large colourless cube-like crystals of $[Au(nbe)_3][SbF_6]$ were obtained in a yield of 280 mg (49%).

7.3.3.6 [Ru(COD)(η^3-$CH_2C(CH_3)CH_2)_2$]

$[Ru(COD)(\eta^3\text{-}CH_2C(CH_3)CH_2)_2]$ was synthesised from $[Ru(COD)Cl_2]_n$ and 2-methylpropenylmagnesium chloride according to a procedure reported by James and co-workers.[9] $[Ru(COD)Cl_2]_n$ was prepared according to a synthetic procedure previously reported by Gênet *et al.*[39] A mixture of $RuCl_3{\cdot}xH_2O$ (2.45 g) and 1,5-cyclooctadiene (9 mL, 0.074 mol) in approximately 100 mL ethanol was heated under reflux for three days under nitrogen. The resulting brown precipitate was separated by filtration, washed twice with ethanol and dried under vacuum. 2-methylpropenylmagnesium chloride was prepared *in situ* by stirring magnesium turnings (440 mg, 18.3 mmol) and 3-chloro-2-methylpropene (1.2 mL, 12.3 mmol) in 6 mL THF for half an hour in the presence of an iodine crystal. This solution was subsequently filtered before being added dropwise to a suspension of $[Ru(COD)Cl_2]_n$ (280 mg) in THF:diethyl ether (15 mL:10 mL). The mixture was stirred for 20 minutes, after which approximately 30 mL diethyl ether was added, resulting in the precipitation of a white solid. The colourless solution was filtered into a clean Schlenk tube and hydrolysed with approximately 50 mL deionised water. The aqueous layer was washed twice with diethyl ether, and then the organic layers were collected and dried over $MgSO_4$. The solution was filtered through Celite, and the solvent was removed *in vacuo*, yielding 242 mg (76% yield) $[Ru(COD)(\eta^3\text{-}CH_2C(CH_3)CH_2)_2]$.

7.3.3.7 $[Co(PEt_2Ph)_2(mes)_2]$

$[Co(PEt_2Ph)_2(mes)_2]$ was synthesised according to a previously reported synthetic procedure.[10] $[Co(PEt_2Ph)_2Br_2]$ was prepared by adding PEt_2Ph (4 mL, 0.023 mol) to a solution of $CoBr_2$ (2.5 g, 0.011 mol) in approximately 60 mL ethanol. The reaction mixture was stirred for half an hour, and then the ethanol solvent was removed under dynamic vacuum, yielding a green solid. 2-Mesitylmagnesium bromide was prepared *in situ* by stirring magnesium turnings (1.504 g, 0.062 mol) and 2-bromomesitylene (6.3 mL, 0.041 mol) in approximately 30 mL THF at 0 °C overnight. This solution was subsequently filtered and cooled to –30 °C. A solution of $[Co(PEt_2Ph)_2Br_2]$ in approximately 60 mL benzene was added dropwise, and the reaction mixture was allowed to slowly warm up to room temperature. The resulting brown solution was stirred under argon for 40 minutes, before being cooled to –30 °C and hydrolysed with dilute HCl. The mixture was warmed up to room temperature, and approximately 60 mL benzene was added. The organic layer was washed twice with deionised water, dried over $MgSO_4$ and filtered, and the solid residue was washed three times with benzene. The filtrate was subsequently dried under vacuum, yielding 5.241 g (73% yield) $[Co(PEt_2Ph)_2(mes)_2]$.

7.3.4 Novel anionic species

7.3.4.1 $[K(2,2,2\text{-crypt})]_4[Cu_2(P_7)_2]$ (1)

K_3P_7 (94 mg, 0.282 mmol), $[Cu_5(mes)_5]$ (69 mg, 0.075 mmol) and 2,2,2-crypt (339 mg, 0.902 mmol) were dissolved in approximately 5 mL ethylenediamine to form a brown solution, which was stirred under argon for approximately one hour. The resulting brown solution was filtered into an air-tight ampoule and layered with toluene. After several days, red plate-like crystals of $[K(2,2,2\text{-crypt})]_4[Cu_2(P_7)_2]$ were obtained in a yield of 113 mg (37%). These crystals proved unsuitable for X-ray diffraction due to their small size and extensive twinning. Anal. Calcd. for $C_{72}H_{144}K_4N_8O_{24}P_{14}Cu_2$: C 38.88, H 6.53, N 5.04. Found: C 38.72, H 6.42, N 5.00.

^{1}H NMR (499.93 MHz, d_7-DMF): δ (ppm) 3.60 (48H, s, 2,2,2-crypt), 3.56 (48H, t, 2,2,2-crypt, $^3J_{H–H}$ = 5 Hz), 2.55 (48H, t, 2,2,2-crypt).

$^{31}P\{^{1}H\}$ NMR (202.35 MHz, d_7-DMF, –50 °C): δ (ppm) –28.8 (4P, broad, P1, P7), –39.1 (2P, broad t, P4), –81.0 (8P, broad, P2, P3, P5, P6).

ESI-MS, negative ion mode (DMF): *m/z* 560.6 $[Cu_2(P_7)_2]^-$, 600.5 $[KCu_2(P_7)_2]^-$, 1016.8 {K[K(2,2,2-crypt)][$Cu_2(P_7)_2$]}$^-$, 1393.1 {[K(2,2,2-crypt)]$_2$[$Cu_2(P_7)_2$]}$^-$, 1807.3 {[K(2,2,2-crypt)]$_3$[$Cu_2(P_7)_2$]}$^-$. ESI-MS, positive ion mode (DMF): *m/z* 1809.2 {[K(2,2,2-crypt)]$_3$[$Cu_2(P_7)_2$]}$^+$, 2223.5 {[K(2,2,2-crypt)]$_4$[$Cu_2(P_7)_2$]}$^+$, 2637.6 {[K(2,2,2-crypt)]$_5$[$Cu_2(P_7)_2$]}$^+$.

7.3.4.2 $[K(2,2,2\text{-crypt})]_4[Cu_2(As_7)_2]\cdot 2en$ (2)

K_3As_7 (96 mg, 0.150 mmol), $[Cu_5(mes)_5]$ (27 mg, 0.030 mmol) and 2,2,2-crypt (187 mg, 0.497 mmol) were dissolved in approximately 5 mL ethylenediamine to form a brown solution, which was stirred under argon for approximately one hour. The resulting brown solution was filtered into an ampoule and layered with toluene. After several days, reddish-black block-like crystals of $[K(2,2,2\text{-crypt})]_4[Cu_2(As_7)_2]\cdot 2en$ suitable for X-ray diffraction were obtained in a yield of 134 mg (61%). Anal. Calcd. for $C_{76}H_{160}K_4N_{12}O_{24}As_{14}Cu_2$: C 30.84, H 5.45, N 5.68. Found: C 30.73, H 5.30, N 5.78.

ESI-MS, negative ion mode (DMF): *m/z* 1176.0 $[Cu_2(As_7)_2]^-$, 1216.0 $[KCu_2(As_7)_2]^-$, 1592.4 {[K(2,2,2-crypt)][$Cu_2(As_7)_2$]}$^-$, 2008.5 {[K(2,2,2-crypt)]$_2$[$Cu_2(As_7)_2$]}$^-$, 2422.4 {[K(2,2,2-crypt)]$_3$[$Cu_2(As_7)_2$]}$^-$. ESI-MS, positive ion mode (DMF): *m/z* 2839.0 {[(K(2,2,2-crypt)]$_4$[$Cu_2(As_7)_2$]}$^+$, 2877.0 {K[K(2,2,2-crypt)]$_4$[$Cu_2(As_7)_2$]}$^+$, 3253.3 {[K(2,2,2-crypt)]$_5$[$Cu_2(As_7)_2$]}$^+$.

7.3.4.3 $[K(2,2,2\text{-crypt})]_4[Zn(P_7)_2]\cdot 6py$ (3)

K_3P_7 (96 mg, 0.288 mmol), $ZnPh_2$ (64 mg, 0.293 mmol) and 2,2,2-crypt (338 mg, 0.898 mmol) were dissolved in approximately 5 mL ethylenediamine to form a yellow-brown solution, which was left to stir under argon for approximately one hour. The ethylenediamine solvent was subsequently removed under a dynamic vacuum, yielding a yellow-brown solid. The solid was redissolved in approximately 5 mL pyridine to form a reddish-brown solution, which was filtered into an ampoule and layered with toluene. After several days, red crystals of $[K(2,2,2\text{-crypt})]_4[Zn(P_7)_2]\cdot 6py$ suitable for X-ray diffraction were obtained in a yield of 138 mg

(36%). Anal. Calcd. for $C_{102}H_{174}K_4N_{14}O_{24}P_{14}Zn$: C 46.46, H 6.66, N 7.44. Found: C 46.29, H 6.55, N 7.32.

^{1}H NMR (299.86 MHz, d_5-pyridine): δ (ppm) 3.46 (48H, s, 2,2,2-crypt), 3.38 (48H, t, 2,2,2-crypt, $^3J_{H–H}$ = 5 Hz), 2.35 (48H, t, 2,2,2-crypt).

^{31}P{^{1}H} NMR (121.38 MHz, d_5-pyridine): δ (ppm) –14.9 (4P, m, P2, P3, $^1J_{P3–P6}$ = –428 Hz, $^1J_{P2–P5}$ = –411 Hz, $^1J_{P3–P1}$ = –260 Hz, $^1J_{P2–P1}$ = –253 Hz, $^2J_{P2–P3}$ = –29 Hz, $^2J_{P2–P4}$ = –12 Hz, $^2J_{P3–P4}$ = –12 Hz), –42.9 (2P, m, P1, $^1J_{P1–P4}$ = –336 Hz, $^2J_{P1–P7}$ = 41 Hz, $^2J_{P1–P6}$ = 31 Hz, $^2J_{P1–P5}$ = 23 Hz), –56.3 (2P, m, P4, $^1J_{P4–P7}$ = –418 Hz), –104.7 (2P, m, P7, $^1J_{P7–P5}$ = –206 Hz, $^1J_{P7–P6}$ = –202 Hz), –162.3 (4P, m, P5, P6, $^1J_{P5–P6}$ = –179 Hz).

ESI-MS, negative ion mode (DMF): *m/z* 498.5 $[Zn(P_7)_2]^-$, 536.3 $[KZn(P_7)_2]^-$, 911.1 {[K(2,2,2-crypt)][$Zn(P_7)_2$]}$^-$, 948.9 {K[K(2,2,2-crypt)][$Zn(P_7)_2$]}$^-$. ESI-MS, positive ion mode (DMF): *m/z* 1746.7 {[K(2,2,2-crypt)]$_3$[$Zn(P_7)_2$]}$^+$, 1784.7 {K[K(2,2,2-crypt)]$_3$[$Zn(P_7)_2$]}$^+$, 2160.8 {[K(2,2,2-crypt)]$_4$[$Zn(P_7)_2$]}$^+$.

7.3.4.4 [K(2,2,2-crypt)]$_4$[Zn(As$_7$)$_2$] (4)

K_3As_7 (96 mg, 0.149 mmol), $ZnPh_2$ (32 mg, 0.146 mmol) and 2,2,2-crypt (178 mg, 0.473 mmol) were dissolved in approximately 5 mL ethylenediamine to form a red solution, which was stirred under argon for approximately one hour. The resulting reddish-brown solution was filtered into an ampoule and layered with toluene. After several days, orange crystals of [K(2,2,2-crypt)]$_4$[$Zn(As_7)_2$] were obtained in a yield of 86 mg (40%). The crystal structure obtained exhibited extensive disorder of one of the [K(2,2,2-crypt)]$^+$ cations, and only a partial solution was possible. Anal. Calcd. for $C_{72}H_{144}K_4N_8O_{24}As_{14}Zn$: C 31.13, H 5.23, N 4.04. Found: C 30.02, H 5.18, N 4.06.

ESI-MS, negative ion mode (DMF): *m/z* 1114.3 $[Zn(As_7)_2]^-$, 1152.3 $[KZn(As_7)_2]^-$, 1570.6 {K[K(2,2,2-crypt)][$Zn(As_7)_2$]}$^-$, 1606.6 {K_2[K(2,2,2-crypt)][$Zn(As_7)_2$]}$^-$, 1983.0 {K[K(2,2,2-crypt)]$_2$[$Zn(As_7)_2$]}$^-$. ESI-MS, positive ion mode (DMF): *m/z* 2776.9 {[K(2,2,2-crypt)]$_4$[$Zn(As_7)_2$]}$^+$, 3191.0 {[K(2,2,2-crypt)]$_5$[$Zn(As_7)_2$]}$^+$.

7.3.4.5 $[K(2,2,2\text{-crypt})]_4[Cd(P_7)]_2]\cdot 6py$ (5)

K_3P_7 (95 mg, 0.284 mmol), $CdPh_2$ (38 mg, 0.141 mmol) and 2,2,2-crypt (222 mg, 0.590 mmol) were dissolved in approximately 5 mL ethylenediamine to form a brown solution, which was stirred under argon for approximately one hour. The ethylenediamine solvent was subsequently removed under a dynamic vacuum to leave a brown solid, which was redissolved in approximately 5 mL pyridine. The resulting brown solution was filtered into an ampoule and layered with toluene. After several days, red-orange plate-like crystals of $[K(2,2,2\text{-crypt})]_4[Cd(P_7)_2]\cdot 6py$ suitable for X-ray diffraction were obtained in a yield of 163 mg (43%). Anal. Calcd. for $C_{102}H_{174}K_4N_{14}O_{24}P_{14}Cd$: C 45.64, H 6.54, N 7.31. Found: C 45.57, H 6.47, N 7.25.

^{1}H NMR (299.86 MHz, d_5-pyridine): δ (ppm) 3.46 (48H, s, 2,2,2-crypt), 3.38 (48H, t, 2,2,2-crypt, $^3J_{H–H}$ = 5 Hz), 2.37 (48H, t, 2,2,2-crypt).

$^{31}P\{^1H\}$ NMR (121.37 MHz, d_5-pyridine): δ (ppm) –4.5 (4P, m, P2, P3, $^1J_{P3–P6}$ = –416 Hz, $^1J_{P2–P5}$ = –403 Hz, $^1J_{P3–P1}$ = –276 Hz, $^1J_{P2–P1}$ = –254 Hz), –36.0 (2P, m, P1, $^1J_{P1–P4}$ = –350 Hz), –82.1 (2P, m, P4, $^1J_{P4–P7}$ = –426 Hz), –134.7 (2P, m, P7, $^1J_{P7–P5}$ = –206 Hz, $^1J_{P7–P6}$ = –202 Hz), –161.0 (4P, m, P5, P6 $^1J_{P5–P6}$ = –210 Hz).

ESI-MS, negative ion mode (DMF): *m/z* 548.6 $[Cd(P_7)_2]^-$, 588.6 $[KCd(P_7)_2]^-$, 962.9 $\{[K(2,2,2\text{-crypt})][Cd(P_7)_2]\}^-$, 1379.1 $\{[K(2,2,2\text{-crypt})]_2[Cd(P_7)_2]\}^-$, 1793.4 $\{[K(2,2,2\text{-crypt})]_3[Cd(P_7)_2]\}^-$. ESI-MS, positive ion mode (DMF): *m/z* 2209.6 $\{[K(2,2,2\text{-crypt})]_4[Cd(P_7)_2]\}^+$, 2623.9 $\{[K(2,2,2\text{-crypt})]_5[Cd(P_7)_2]\}^+$.

7.3.4.6 $[K(2,2,2\text{-crypt})]_2[P_7InPh_2]$ (6)

K_3P_7 (96 mg, 0.288 mmol), $InPh_3$ (53 mg, 0.152 mmol) and 2,2,2-crypt (226 mg, 0.601 mmol) were dissolved in approximately 5 mL ethylenediamine to form an orange-brown solution, which was stirred under argon for approximately one hour. The ethylenediamine solvent was subsequently removed under a dynamic vacuum to leave a red solid, which was redissolved in approximately 5 mL pyridine to form a dark reddish-brown solution. The solution was filtered into an ampoule and layered with toluene. After several days, yellow crystals of [K(2,2,2-

crypt)]$_2$[P_7InPh_2] suitable for X-ray diffraction formed in a yield of 126 mg (63%). Anal. Calcd. for $K_2C_{48}H_{82}N_4O_{12}P_7In$: C 43.75, H 6.28, N 4.25. Found: C 43.79, H 6.28, N 4.29.

^{1}H NMR (300.27 MHz, d_5-pyridine): δ (ppm) 8.86 (2H, d, o_A-C*H*, $^3J_{ortho–meta}$ = 7 Hz), 8.21 (2H, d, o_B-C*H*, $^3J_{ortho–meta}$ = 7 Hz), 7.46 (2H, t, m_A-C*H*, $^3J_{meta–para}$ = 7 Hz), 7.29 (1H, t, p_A-C*H*), 7.18 (2H, t, m_B-C*H*, $^3J_{meta–para}$ = 7 Hz), 7.09 (1H, t, p_B-C*H*), 3.35 (24H, s, 2,2,2-crypt), 3.29 (24H, t, 2,2,2-crypt, $^3J_{H–H}$ = 5 Hz), 2.29 (24H, t, 2,2,2-crypt).

^{31}P{^{1}H} NMR (121.38 MHz, d_5-pyridine): δ (ppm) 3.6 (2P, m, P2, P3, $^1J_{P3–P6}$ = –410 Hz, $^1J_{P2–P5}$ = –366 Hz, $^1J_{P3–P1}$ = –257 Hz, $^1J_{P2–P1}$ = –208 Hz, $^2J_{P2–P3}$ = –30 Hz, $^2J_{P2–P4}$ = –20 Hz, $^2J_{P3–P4}$ = –20 Hz, $^2J_{P2–P7}$ = –10 Hz, $^2J_{P3–P7}$ = –10 Hz), –50.7 (1P, m, P1, $^1J_{P1–P4}$ = –341 Hz, $^2J_{P1–P7}$ = 60 Hz, $^2J_{P1–P5}$ = 27 Hz, $^2J_{P1–P6}$ = 25 Hz), –67.8 (1P, m, P4, $^1J_{P4–P7}$ = –402 Hz), –76.8 (1P, m, P7, $^1J_{P7–P5}$ = –221 Hz, $^1J_{P7–P6}$ = –205 Hz), –170.0 (2P, m, P5, P6, $^1J_{P5–P6}$ = –162 Hz).

^{13}C{^{1}H} NMR (75.41 MHz, d_5-pyridine): δ (ppm) 164.9 (*i*-C), 159.9 (*i*-C), 140.3 (*o*-C), 139.9 (*o*-C), 127.6 (*m*-C), 127.1 (*m*-C), 126.0 (*p*-C), 126.0 (*p*-C), 70.8 (2,2,2-crypt), 68.0 (2,2,2-crypt), 54.2 (2,2,2-crypt).

ESI-MS, negative ion mode (DMF): *m/z* 485.8 [P_7InPh_2]$^-$, 524.8 [KP_7InPh_2]$^-$, 900.9 {[K(2,2,2-crypt)][P_7InPh_2]}$^-$. ESI-MS, positive ion mode (DMF): *m/z* 1731.5 {[K(2,2,2-crypt)]$_3$[P_7InPh_2]}$^+$.

7.3.4.7 [K(2,2,2-crypt)]$_2$[As_7InPh_2] (7)

K_3As_7 (98 mg, 0.152 mmol), $InPh_3$ (37 mg, 0.107 mmol) and 2,2,2-crypt (115 mg, 0.306 mmol) were dissolved in approximately 5 mL ethylenediamine to form a deep red solution, which was stirred under argon for approximately one hour. The resulting red solution was filtered into an ampoule and layered with toluene. After several days, [K(2,2,2-crypt)]$_2$[As_7InPh_2] formed as a brown non-crystalline solid in a yield of 139 mg (56%). Anal. Calcd. for $C_{48}H_{82}K_2N_4O_{12}As_7In$: C 35.47, H 5.09, N 3.45. Found: C 35.35, H 4.96, N 3.38.

^{1}H NMR (300.17 MHz, d_5-pyridine): δ (ppm) 8.86 (2H, d, o_A-C*H*, $^3J_{ortho–meta}$ = 7 Hz), 8.24 (2H, d, o_B-C*H*, $^3J_{ortho–meta}$ = 7 Hz), 7.47 (2H, t, m_A-C*H*, $^3J_{meta–para}$ = 7 Hz), 7.29 (1H, t, p_A-C*H*), 7.20 (2H, t, m_B-C*H*, $^3J_{meta–para}$ = 7 Hz), 7.09 (1H, t, p_B-CH), 3.38 (24H, s, 2,2,2-crypt), 3.32 (24H, t, 2,2,2-crypt, $^3J_{H–H}$ = 5 Hz), 2.32 (24H, t, 2,2,2-crypt).

$^{13}C\{^{1}H\}$ NMR (75.41 MHz, d_5-pyridine): δ (ppm) 167.9 (*i*-C), 161.3 (*i*-C), 139.9 (*o*-C), 139.6 (*o*-C), 127.6 (*m*-C), 126.9 (*m*-C), 125.9 (*p*-C), 125.8 (*p*-C), 70.8 (2,2,2-crypt), 68.1 (2,2,2-crypt), 54.3 (2,2,2-crypt).

ESI-MS, negative ion mode (DMF): *m/z* 794.6 $[As_7InPh_2]^-$, 832.6 $[KAs_7InPh_2]^-$, 1208.9 $\{[K(2,2,2\text{-crypt})][As_7InPh_2]\}^-$. ESI-MS, positive ion mode: *m/z* 2039.4 $\{[K(2,2,2\text{-crypt})]_3[As_7InPh_2]\}^+$.

7.3.4.8 $[K(2,2,2\text{-crypt})]_2[Ag_2(HP_7)_2]$ (8)

7.3.4.8.1 Synthesis from $[Ag(nbe)_3][SbF_6]$

K_3P_7 (60 mg, 0.180 mmol), $[Ag(nbe)_3][SbF_6]$ (112 mg, 0.179 mmol) and 2,2,2-crypt (203 mg, 0.540 mmol) were dissolved in 5 mL ethylenediamine, and the resulting dark orange solution was left to stir for approximately two hours. The solution was filtered into a dry ampoule, and the ruby red filtrate was layered with toluene. After several days, thin yellow needle-like crystals of $[K(2,2,2\text{-crypt})]_2[Ag_2(HP_7)_2]$ suitable for X-ray diffraction formed in a yield of 15 mg (12%).

7.3.4.8.2 Synthesis from AgCl

K_3P_7 (97 mg, 0.290 mmol), AgCl (53 mg, 0.371 mmol), 2,2,2-crypt (225 mg, 0.598 mmol) and $[NH_4][BPh_4]$ (99 mg, 0.294 mmol) were dissolved in approximately 5 mL ethylenediamine to form a brown solution, which was stirred under argon for approximately three hours. The solvent was removed under a dynamic vacuum to leave a brown solid, which was washed twice with approximately 10 mL THF in an attempt to dissolve the chloride and tetraphenylborate salt by-products. The remaining solid residue was dried under vacuum, yielding 89.7 mg (42% yield) of $[K(2,2,2\text{-crypt})]_2$[**16**]. Anal. Calcd. for $C_{36}H_{74}Ag_2K_2N_4O_{12}P_{14}$: C 29.15, H 5.03, N 3.78. Found: C 28.70, H 4.65, N 3.92.

^{1}H NMR (499.93 MHz, d_7-DMF): δ (ppm) 3.59 (24H, s, 2,2,2-crypt), 3.56 (24H, t, 2,2,2-crypt, $^{3}J_{H–H}$ = 5 Hz), 2.54 (24H, t, 2,2,2-crypt).

^{31}P NMR (202.36 MHz, d_7-DMF): δ (ppm): 17.9 (1P, broad m), 8.0 (1P, m), –33.7 (1P, broad m), –41.5 (1P, m), –86.6 (1P, m), –197.0 (1P, broad m), –212.3 (1P, m).

ESI-MS, negative ion mode (DMF): *m/z* 652.5 $[Ag_2(HP_7)_2]^-$, 690.5 $[KAg_2(HP_7)_2]^-$, 1066.7 $\{[K(2,2,2\text{-crypt})][Ag_2(HP_7)_2]\}^-$. ESI-MS, positive ion mode (DMF): *m/z* 1897.0 $\{[K(2,2,2\text{-crypt})]_3[Ag_2(HP_7)_2]\}^+$.

7.3.4.9 $[K(2,2,2\text{-crypt})]_2[Au_2(HP_7)_2]$ (9)

7.3.4.9.1 Synthesis from $[Au(nbe)_3][SbF_6]$

K_3P_7 (45.7 mg, 0.137 mmol), $[Au(nbe)_3][SbF_6]$ (105 mg, 0.147 mmol) and 2,2,2-crypt (109 mg, 0.290 mmol) were dissolved in approximately 5 mL ethylenediamine, and the resulting dark brown solution was left to stir for approximately two hours. The solution was filtered into an ampoule, and the bright yellow filtrate was layered with toluene. After several days, pale yellow plate-like crystals of $[K(2,2,2\text{-crypt})]_2[Au_2(HP_7)_2]$ suitable for X-ray diffraction formed in a yield of 10 mg (15%).

7.3.4.9.2 Synthesis from AuCl

K_3P_7 (96 mg, 0.287 mmol), AuCl (69 mg, 0.297 mmol), 2,2,2-crypt (220 mg, 0.585 mmol) and $[NH_4][BPh_4]$ (96.7 mg, 0.287 mmol) were dissolved in approximately 5 mL ethylenediamine to form a brown solution, which was stirred under argon for approximately three hours. The solvent was removed under a dynamic vacuum to leave a brown solid, which was washed twice with approximately 10 mL THF in an attempt to dissolve the chloride and tetraphenylborate salt by-products. The remaining solid residue was dried under vacuum, yielding 146 mg (61% yield) of $[K(2,2,2\text{-crypt})]_2$[**17**]. Anal. Calcd. for $C_{36}H_{74}Au_2K_2N_4O_{12}P_{14}$: C 26.02, H 4.49, N 3.37. Found: C 25.83, H 4.37, N 3.22.

^{1}H NMR (499.93 MHz, d_7-DMF): δ (ppm) 3.53 (24H, s, 2,2,2-crypt), 3.50 (24H, t, 2,2,2-crypt, $^3J_{H–H}$ = 5 Hz), 2.48 (24H, t, 2,2,2-crypt).

^{31}P NMR (202.36 MHz, d_7-DMF): δ (ppm) 83.8 (1P, m), 50.5 (1P, m), –21.7 (1P, broad m), –92.0 (1P, m), –154.9 (1P, broad m), –213.1 (1P, m), –228.7 (1P, broad m).

ESI-MS, negative ion mode (DMF): *m/z* 830.4 $[Au_2(HP_7)_2]^-$, 868.3 $[KAu_2(HP_7)_2]^-$, 1244.4 $\{[K(2,2,2\text{-crypt})][Au_2(HP_7)_2]\}^-$. ESI-MS, positive ion mode (DMF): *m/z* 2074.5 $\{[K(2,2,2\text{-crypt})]_3[Au_2(HP_7)_2]\}^+$.

7.3.4.10 $[K(2,2,2\text{-crypt})]_3[In(P_7)_2]\cdot 3.5py$ (10)

K_3P_7 (93 mg, 0.278 mmol), $InCl_3$ (29 mg, 0.131 mmol) and 2,2,2-crypt (228 mg, 0.606 mmol) were dissolved in approximately 5 mL ethylenediamine, giving rise to an orange-brown solution, which was stirred under argon for approximately one hour. The ethylenediamine solvent was removed under a dynamic vacuum, yielding a yellow-brown solid, which was redissolved in approximately 5 mL pyridine to form a red solution. The solution was filtered into an ampoule and layered with toluene. After several days, orange rod-like crystals of $[K(2,2,2\text{-crypt})]_3[In(P_7)_2]\cdot 3.5py$ suitable for X-ray diffraction were obtained in a yield of 143 mg (50%). Anal. Calcd. for $C_{71.5}H_{125.5}InK_3N_{9.5}O_{18}P_{14}$: C 41.43, H 6.11, N 6.42. Found: C 41.37, H 6.13, N 6.36.

^{1}H NMR (299.86 MHz, d_5-pyridine): δ (ppm) 3.41 (36H, s, 2,2,2-crypt), 3.34 (36H, t, 2,2,2-crypt, $^3J_{H–H}$ = 5 Hz), 2.34 (36H, t, 2,2,2-crypt).

$^{31}P\{^1H\}$ NMR (121.38 MHz, d_5-pyridine): δ (ppm) 42.3 (4P, m, P12, P13, P22, P23, $^1J_{P13/P23–P16/P26}$ = –394 Hz, $^1J_{P12/P22–P15/P25}$ = –348 Hz, $^1J_{P13/P23–P11/P21}$ = –240 Hz, $^1J_{P12/P22–P11/P21}$ = –225 Hz, $^2J_{P12/P22–P13/P23}$ = –46 Hz, $^2J_{P12/P22–P17/P27}$ = –23 Hz, $^2J_{P13/P23–P17/P27}$ = –21 Hz, $^2J_{P13/P23–P14/P24}$ = –22 Hz, $^2J_{P12/P22–P14/P24}$ = –21 Hz, $^2J_{P13/P23–P15/P25}$ = –14 Hz, $^2J_{P12/P22–P16/P26}$ = –12 Hz), –51.3 (2P, m, P11, P21, $^1J_{P11/P21–P14/P24}$ = –339 Hz, $^2J_{P11/P21–P17/P27}$ = 65 Hz, $^2J_{P11/P21–P16/P26}$ = 31 Hz, $^2J_{P11/P21–P15/P25}$ = 26 Hz), –57.1 (2P, m, P14, P24, $^1J_{P14/P24–P17/P27}$ = –396 Hz), –104.2 (2P, m, P17, P27, $^1J_{P17/P27–P16/P26}$ = –217 Hz, $^1J_{P17/P27–P15/P25}$ = –201 Hz), –173.0 (4P, m, P15, P16, P25, P26, $^1J_{P15/P25–P16/P26}$ = –124 Hz).

ESI-MS, negative ion mode (DMF): *m/z* 550.6 $[In(P_7)_2]^-$, 588.6 $[KIn(P_7)_2]^-$, 964.9 $\{[K(2,2,2\text{-crypt})][In(P_7)_2]\}^-$, 1379.2 $\{[K(2,2,2\text{-crypt})]_2[In(P_7)_2]\}^-$. ESI-MS, positive ion mode (DMF): *m/z* 1795.7 $\{[K(2,2,2\text{-crypt})]_3[In(P_7)_2]\}^+$, 2210.1 $\{[K(2,2,2\text{-crypt})]_4[In(P_7)_2]\}^+$.

7.3.4.11 $[K(2,2,2\text{-crypt})]_3[In(As_7)_2]$ (11)

K_3As_7 (98 mg, 0.152 mmol), $InCl_3$ (23 mg, 0.104 mmol) and 2,2,2-crypt (115 mg, 0.306 mmol) were dissolved in approximately 5 mL ethylenediamine, yielding a brown solution, which was stirred under argon for approximately one hour. The resulting brown solution was filtered into

an ampoule and layered with toluene. After several days, $[K(2,2,2\text{-crypt})]_3[In(As_7)_2]$ formed as a red polycrystalline solid in a yield of 88 mg (48%). Anal. Calcd. for $C_{54}H_{108}As_{14}InK_3N_6O_{18}$: C 26.89, H 4.52, N 3.49. Found: C 26.84, H 4.49, N 3.48.

ESI-MS, negative ion mode (DMF): *m/z* 1164.9 $[In(As_7)_2]^-$, 1580.1 $\{[K(2,2,2\text{-crypt})][In(As_7)_2]\}^-$, 1994.4 $\{[K(2,2,2\text{-crypt})]_2[In(As_7)_2]\}^-$. ESI-MS, positive ion mode (DMF): *m/z* 2409.8 $\{[K(2,2,2\text{-crypt})]_3[In(As_7)_2]\}^+$, 2823.9 $\{[K(2,2,2\text{-crypt})]_4[In(As_7)_2]\}^+$.

7.3.4.12 $[K(2,2,2\text{-crypt})]_2[TlP_7]\cdot py$ (12)

K_3P_7 (94 mg, 0.281 mmol), TlCl (71 mg, 0.296 mmol) and 2,2,2-crypt (222 mg, 0.590 mmol) were dissolved in approximately 5 mL ethylenediamine to form a brown solution, which was stirred under argon for approximately one hour. The ethylenediamine solvent was removed under a dynamic vacuum, yielding a red solid. The solid was redissolved in approximately 5 mL pyridine to form a reddish-brown solution, which was filtered into an ampoule and layered with toluene. After several days, red block-like crystals of $[K(2,2,2\text{-crypt})]_2[TlP_7]\cdot py$ suitable for X-ray diffraction formed in a yield of 114 mg (31%). Anal. Calcd. for $C_{41}H_{77}K_2N_5O_{12}P_7Tl$: C 36.97, H 5.83, N 5.26. Found: C 36.45, H 5.52, N 5.04.

^{1}H NMR (499.93 MHz, d_7-DMF): δ (ppm) 3.59 (24H, s, 2,2,2-crypt), 3.55 (24H, t, 2,2,2-crypt, $^3J_{H-H}$ = 5 Hz), 2.54 (24H, t, 2,2,2-crypt).

$^{31}P\{^1H\}$ NMR (202.37 MHz, d_7-DMF, –50 °C): δ (ppm) 58.2 (1P, broad, P14), –99.0 (2P, broad, P11, P17), –147.2 (4P, broad, P12, P13, P15, P16).

ESI-MS, negative ion mode (DMF): *m/z* 422.8 $[TlP_7]^-$. ESI-MS, positive ion mode (DMF): *m/z* 1252.9 $\{[K(2,2,2\text{-crypt})]_2[TlP_7]\}^+$, 1667.1 $\{[K(2,2,2\text{-crypt})]_3[TlP_7]\}^+$.

7.3.4.13 $[K(18\text{-crown-}6)]_2[TlAs_7]$ (13)

K_3As_7 (105 mg, 0.163 mmol), TlCl (43 mg, 0.179 mmol) and 18-crown-6 (95 mg, 0.360 mmol) were dissolved in approximately 5 mL ethylenediamine, yielding a brown solution, which was stirred under argon for approximately one hour. The ethylenediamine solvent was removed under a dynamic vacuum to leave a brown solid, which was redissolved in approximately

5 mL pyridine. The resulting brown solution was filtered into an ampoule and layered with toluene. After several days, dark red plate-like crystals of $[K(18\text{-crown-6})]_2[TlAs_7]$ suitable for X-ray diffraction formed in a yield of 101 mg (46%). Anal. Calcd. for $C_{24}H_{48}As_7K_2O_{12}Tl$: C 21.57, H 3.62. Found: C 21.73, H 2.67.

ESI-MS, negative ion mode (DMF): *m/z* 731.0 $[TlAs_7]^-$, 769.1 $[KTlAs_7]^-$. ESI-MS, positive ion mode (DMF): *m/z* 1639.6 $\{[K(18\text{-crown-6})]_3[TlAs_7]\}^+$.

7.3.4.14 $[K(2,2,2\text{-crypt})]_3[SnP_{15}]\cdot$en (14)

K_3P_7 (50 mg, 0.150 mmol), SnI_2 (30 mg, 0.080 mmol) and 2,2,2-crypt (169 mg, 0.449 mmol) were dissolved in approximately 5 mL ethylenediamine to form a red solution, which was stirred under argon for approximately three hours. The resulting red solution was filtered into a clean Schlenk tube and reduced to dryness under a dynamic vacuum. Approximately 10 mL THF was added, and the mixture was sonicated for 20 minutes in an effort to dissolve the [K(2,2,2-crypt)]I by-product. The remaining red solid was redissolved in approximately 5 mL ethylenediamine to form a red solution, which was filtered into an ampoule and then carefully layered with diethyl ether. After several days, thin orange plate-like crystals of $[K(2,2,2\text{-crypt})]_3[SnP_{15}]\cdot$en suitable for X-ray diffraction were isolated alongside yellow block-like crystals of $[K(2,2,2\text{-crypt})]_2[HP_7]$ and trace amounts of colourless blocks of [K(2,2,2-crypt)]I.

^{1}H NMR (299.86 MHz, d_5-pyridine): δ (ppm) 3.45 (36H, s, 2,2,2-crypt), 3.39 (36H, t, 2,2,2-crypt, $^3J_{H-H}$ = 5 Hz), 2.38 (36H, t, 2,2,2-crypt).

$^{31}P\{^1H\}$ NMR (121.38 MHz, d_5-pyridine): δ (ppm) 50.6 (2P, m, P2, $^1J_{P2-P5}$ = –364 Hz, $^1J_{P2-P1}$ = –352 Hz, $^1J_{P2-P8}$ = –312 Hz), 22.8 (2P, m, P1, $^1J_{P1-P4}$ = –355 Hz, $^1J_{P1-P3}$ = –337 Hz, $^2J_{P1-P7}$ = 72 Hz, $^2J_{P1-P5}$ = 31 Hz), –31.7 (2P, m, P3, $^1J_{P3-P6}$ = –376 Hz), –54.0 (1P, m, P8, $^2J_{P8-P5}$ = 78 Hz), –61.5 (2P, m, P7, $^1J_{P7-P4}$ = –359 Hz, $^1J_{P7-P6}$ = –226 Hz, $^1J_{P7-P5}$ = –211 Hz), –115.8 (2P, m, P4), –152.1 (2P, m, P6, $^1J_{P6-P5}$ = –175 Hz), –176.3 (2P, m, P5).

ESI-MS, negative ion mode (DMF): *m/z* 586.7 $[SnP_{15}]^-$, 1001.0 $\{[K(2,2,2\text{-crypt})][SnP_{15}]\}^-$, 1415.3 $\{[K(2,2,2\text{-crypt})]_2[SnP_{15}]\}^-$. ESI-MS, positive ion mode (DMF): *m/z* 1830.8 $\{[K(2,2,2\text{-crypt})]_3[SnP_{15}]\}^+$, 2245.0 $\{[K(2,2,2\text{-crypt})]_4[SnP_{15}]\}^+$.

7.3.4.15 $[K(2,2,2\text{-crypt})]_3[SnAs_{15}]\cdot 2en$ (15)

K_3As_7 (50 mg, 0.078 mmol), SnI_2 (17 mg, 0.046 mmol) and 2,2,2-crypt (69 mg, 0.183 mmol) were dissolved in approximately 5 mL ethylenediamine to form a brown-black solution, which was left to stir under argon for approximately three hours. The resulting brown solution was filtered into a clean Schlenk tube and reduced to dryness under a dynamic vacuum. The remaining solid was washed with approximately 10 mL THF, and the mixture was sonicated for 20 minutes in an effort to dissolve the [K(2,2,2-crypt)]I by-product. The remaining black solid was redissolved in approximately 5 mL ethylenediamine to form a brown solution, which was filtered into an ampoule and carefully layered with diethyl ether. After several days, thin red plate-like crystals of $[K(2,2,2\text{-crypt})]_3[SnAs_{15}]\cdot 2en$ suitable for X-ray diffraction were obtained. Anal. Calcd. for $C_{58}H_{124}As_{15}K_3N_{10}O_{18}Sn$: C 26.68, H 4.79, N 5.37. Found: C 26.50, H 4.59, N 5.25.

ESI-MS, negative ion mode (DMF): *m/z* 1246.0 $[SnAs_{15}]^-$, 1660.3 $\{[K(2,2,2\text{-crypt})][SnAs_{15}]\}^-$, 2074.7 $\{[K(2,2,2\text{-crypt})]_2[SnAs_{15}]\}^-$. ESI-MS, positive ion mode (DMF): *m/z* 2490.1 $\{[K(2,2,2\text{-crypt})]_3[SnAs_{15}]\}^+$, 2904.3 $\{[K(2,2,2\text{-crypt})]_4[SnAs_{15}]\}^+$.

7.3.4.16 $[K(2,2,2\text{-crypt})]_3[PbP_{15}]\cdot en$ (16)

K_3P_7 (50 mg, 0.150 mmol), PbI_2 (37 mg, 0.080 mmol) and 2,2,2-crypt (135 mg, 0.359 mmol) were dissolved in approximately 5 mL ethylenediamine to form a dark red solution, which was left to stir under argon for approximately three hours. The resulting red solution was then filtered into a clean Schlenk tube and reduced to dryness *in vacuo*. Approximately 10 mL THF was added, and the mixture was sonicated for 20 minutes in an effort to dissolve the [K(2,2,2-crypt)]I by-product. The remaining brown solid was redissolved in approximately 5 mL ethylenediamine to form a red solution, which was filtered into an ampoule and carefully layered with diethyl ether. After several days, small orange plate-like crystals of $[K(2,2,2\text{-crypt})]_3[PbP_{15}]\cdot en$ suitable for X-ray diffraction were obtained in low yield, with evidence of [K(2,2,2-crypt)]I also present in the mixture.

^{1}H NMR (299.86 MHz, d_5-pyridine): δ (ppm) 3.31 (36H, s, 2,2,2-crypt), 3.25 (36H, t, 2,2,2-crypt, $^{3}J_{H–H}$ = 5 Hz), 2.23 (36H, t, 2,2,2-crypt).

^{31}P{^{1}H} NMR (121.39 MHz, d_5-pyridine): δ (ppm) 49.5 (2P, m, P2, $^{1}J_{P2–P5}$ = –367 Hz, $^{1}J_{P2–P1}$ = –359 Hz, $^{1}J_{P2–P8}$ = –310 Hz), 33.0 (2P, m, P1, $^{1}J_{P1–P4}$ = –351 Hz, $^{1}J_{P1–P3}$ = –322 Hz, $^{2}J_{P1–P7}$ = 72 Hz, $^{2}J_{P1–P5}$ = 31 Hz), –40.0 (2P, m, P3, $^{1}J_{P3–P6}$ = –381 Hz), –50.6 (1P, m, P8, $^{2}J_{P8–P5}$ = 87 Hz), –64.8 (2P, m, P7, $^{1}J_{P7–P4}$ = –368 Hz, $^{1}J_{P7–P6}$ = –223 Hz, $^{1}J_{P7–P5}$ = –202 Hz), –122.7 (2P, m, P4), –153.4 (2P, m, P6, $^{1}J_{P6–P5}$ = –176 Hz), –175.4 (2P, m, P5).

ESI-MS, negative ion mode (DMF): *m/z* 675.2 $[PbP_{15}]^{-}$, 1089.9 $\{[K(2,2,2\text{-crypt})][PbP_{15}]\}^{-}$, 1504.6 $\{[K(2,2,2\text{-crypt})]_2[PbP_{15}]\}^{-}$. ESI-MS, positive ion mode (DMF): *m/z* 1919.4 $\{[K(2,2,2\text{-crypt})]_3[PbP_{15}]\}^{+}$, 2333.9 $\{[K(2,2,2\text{-crypt})]_4[PbP_{15}]\}^{+}$.

7.3.4.17 $[K(2,2,2\text{-crypt})]_3[PbAs_{15}]$ (17)

K_3As_7 (50 mg, 0.078 mmol), PbI_2 (18 mg, 0.039 mmol) and 2,2,2-crypt (93 mg, 0.247 mmol) were dissolved in approximately 5 mL ethylenediamine to form a brown-black solution, which was left to stir under argon for approximately three hours. The resulting brown solution was filtered into a clean Schlenk tube and reduced to dryness under a dynamic vacuum. The remaining solid was washed with approximately 10 mL THF, and the mixture was sonicated for 20 minutes in an effort to dissolve the [K(2,2,2-crypt)]I by-product. The black solid residue was redissolved in approximately 5 mL ethylenediamine to form a brown solution, which was filtered into an ampoule and then carefully layered with diethyl ether. After several days, small red plate-like crystals of $[K(2,2,2\text{-crypt})]_3[PbAs_{15}]$ were isolated in very low yields alongside colourless blocks of [K(2,2,2-crypt)]I. These crystals proved unsuitable for single crystal X-ray diffraction.

ESI-MS, negative ion mode (DMF): *m/z* 1332.6 $[PbAs_{15}]^{-}$, 1749.2 $\{[K(2,2,2\text{-crypt})][PbAs_{15}]\}^{-}$, 2163.7 $\{[K(2,2,2\text{-crypt})]_2[PbAs_{15}]\}^{-}$. ESI-MS, positive ion mode: *m/z* 2579.1 $\{[K(2,2,2\text{-crypt})]_3[PbAs_{15}]\}^{+}$, 2993.4 $\{[K(2,2,2\text{-crypt})]_4[PbAs_{15}]\}^{+}$.

7.3.4.18 $[K(2,2,2\text{-crypt})]_2[Fe(HP_7)_2]$ (18)

K_3P_7 (123 mg, 0.368 mmol), $FeCl_2$ (30 mg, 0.236 mmol), $[NH_4][BPh_4]$ (95 mg, 0.282 mmol) and 2,2,2-crypt (228 mg, 0.606 mmol) were dissolved in approximately 5 mL ethylenediamine to form a red solution, which was left to stir under argon for approximately three hours. The resulting reddish-black solution was reduced to dryness under a dynamic vacuum, yielding a dark brown residue. This solid was washed twice with approximately 10 mL THF in an effort to dissolve the chloride and tetraphenylborate salt by-products. The remaining brown solid residue was dried under vacuum, yielding 184 mg (76% yield) of $[K(2,2,2\text{-crypt})]_2[Fe(HP_7)_2]$. Crystals of $[K(2,2,2\text{-crypt})]_2$[**18**] suitable for X-ray diffraction were obtained from a pyridine/toluene solvent mixture. Anal. Calcd. for $C_{36}H_{74}FeK_2N_4O_{12}P_{14}$: C 32.69, H 5.64, N 4.24. Found: C 32.39, H 5.47, N 4.18.

^{1}H NMR (499.93 MHz, d_5-pyridine): δ (ppm) 6.56 (2H, d, H1, H1A, $^1J_{H1/H1A–P1/P1A}$ = 169 Hz), 3.47 (24H, broad s, 2,2,2-crypt), 3.42 (24H, broad s, 2,2,2-crypt), 2.41 (24H, broad s, 2,2,2-crypt).

^{31}P NMR (202.38 MHz, d_5-pyridine): δ (ppm) 151.3 (2P, td, P1, P1A, $^1J_{P1/P1A–P2/P2A/P3/P3A}$ = –267 Hz, $^1J_{P1/P1A–H1/H1A}$ = 169 Hz), –0.5 (4P, m, P2, P2A, P3, P3A), –80.5 (4P, broad m, P4, P4A, P5, P5A or P6, P6A, P7, P7A), –121.6 (4P, broad m, P4, P4A, P5, P5A or P6, P6A, P7, P7A).

ESI-MS, negative ion mode (DMF): *m/z* 491.6 $[Fe(HP_7)_2]^-$, 907.0 $\{[K(2,2,2\text{-crypt})][Fe(HP_7)_2]\}^-$. ESI-MS, positive ion mode (DMF): *m/z* 1737.0 $\{[K(2,2,2\text{-crypt})]_3[Fe(HP_7)_2]\}^+$.

7.3.4.19 $[K(2,2,2\text{-crypt})]_4[Fe(P_7)_2]$ (19)

$[K(2,2,2\text{-crypt})]_2[Fe(HP_7)_2]$ (46.8 mg, 0.035 mmol), $K[N(SiMe_3)_2]$ (15.8 mg, 0.079 mmol) and 2,2,2-crypt (29.8 mg, 0.079 mmol) were dissolved in approximately 0.5 mL d_5-pyridine inside a Young's NMR tube. The mixture was sonicated for approximately half an hour, after which full conversion to $[K(2,2,2\text{-crypt})]_4[Fe(P_7)_2]$ according to ^{1}H and ^{31}P NMR spectroscopy was observed. Anal. Calcd. for $C_{72}H_{144}K_4N_8O_{24}P_{14}Fe$: C 40.17, H 6.75, N 5.21. Found: C 40.10, H 6.68, N 5.34.

^{1}H NMR (499.93 MHz, d_5-pyridine): δ (ppm): 3.31 (48H, broad s, 2,2,2-crypt), 3.23 (48H, broad s, 2,2,2-crypt), 2.20 (48H, broad s, 2,2,2-crypt).

$^{31}P\{^{1}H\}$ NMR (202.38 MHz, d_5-pyridine): δ (ppm): 234.4 (2P, t, P1, P1A, $^{1}J_{P1/P1A–P2/P2A}$ = –375 Hz, $^{1}J_{P1/P1A–P3/P3A}$ = –374 Hz), –0.5 (4P, m, P2, P2A, P3, P3A, $^{1}J_{P2/P2A–P6/P6A}$ = –233 Hz, $^{1}J_{P3/P3A–P5/P5A}$ = –233 Hz, $^{1}J_{P2/P2A–P4/P4A}$ = –230 Hz, $^{1}J_{P3/P3A–P7/P7A}$ = –225 Hz), –82.3 (8P, m, P4, P4A, P5, P5A, P6, P6A, P7, P7A, $^{1}J_{P4/P4A–P5/P5A}$ = –485 Hz, $^{1}J_{P6/P6A–P7/P7A}$ = –485 Hz).

ESI-MS, negative ion mode (DMF): *m/z* 489.6 $[Fe(P_7)_2]^-$, 906.1 $\{[K(2,2,2\text{-crypt})][Fe(P_7)_2]\}^-$, 1321.4 $\{[K(2,2,2\text{-crypt})]_2[Fe(P_7)_2]\}^-$, 1736.0 $\{[K(2,2,2\text{-crypt})]_3[Fe(P_7)_2]\}^-$. ESI-MS, positive ion mode (DMF): *m/z* 2154.6 $\{[K(2,2,2\text{-crypt})]_4[Fe(P_7)_2]\}^+$, 2570.8 $\{[K(2,2,2\text{-crypt})]_5[Fe(P_7)_2]\}^+$.

7.3.4.20 $[K(2,2,2\text{-crypt})]_2[Ru(HP_7)_2]$ (20)

K_3P_7 (50 mg, 0.150 mmol) and 2,2,2-crypt (113 mg, 0.301 mmol) were dissolved in approximately 5mL ethylenediamine to form a deep red solution, which was stirred under an argon atmosphere for approximately two hours. The ethylenediamine solution was subsequently transferred into a second Schlenk tube containing $[Ru(PPh_3)_3Cl_2]$ (101 mg, 0.105 mmol). The resulting red-brown solution was left to stir for approximately three hours and subsequently reduced to dryness under a dynamic vacuum. The remaining brown solid was washed twice with approximately 10 mL THF in an attempt to dissolve by-products including [K(2,2,2-crypt)]Cl. The remaining solid was dried under vacuum, yielding 114 mg of an orange-brown powder. ^{1}H and ^{31}P NMR spectroscopy showed that this solid contained an approximately 1:1 mixture of $[K(2,2,2\text{-crypt})]_2[Ru(HP_7)_2]$ (**20**) and $[K(2,2,2\text{-crypt})]_4[Ru(P_7)_2]$ (**21**).

^{1}H NMR (499.93 MHz, d_5-pyridine): δ (ppm) 6.44 (2H, d, H1, H1A, $^{1}J_{H1/H1A–P1/P1A}$ = 165 Hz), 3.36 (broad s, 2,2,2-crypt), 3.29 (t, 2,2,2-crypt, $^{3}J_{H–H}$ = 5 Hz), 2.24 (t, 2,2,2-crypt).

^{31}P NMR (202.39 MHz, d_5-pyridine): Assignable to **20**: δ (ppm) 125.0 (2P, td, P1, P1A, $^{1}J_{P1/P1A–P2/P2A/P3/P3A}$ = –266 Hz, $^{1}J_{P1/P1A–H1/H1A}$ = 165 Hz), 33.9 (4P, m, P2, P2A, P3, P3A), –84.0 (4P, broad m, P4, P4A, P5, P5A or P6, P6A, P7, P7A), –126.7 (4P, broad m, P4, P4A, P5, P5A or P6, P6A, P7, P7A). Assignable to **21**: δ (ppm) 217.3 (2P, t, P1, P1A, $^{1}J_{P1/P1A–P2/P2A/P3/P3A}$ = –362 Hz), 6.6 (4P, m, P2, P2A, P3, P3A), –72.7 (8P, m, P4, P4A, P5, P5A, P6, P6A, P7, P7A).

ESI-MS, negative ion mode (DMF): *m/z* 538.0 $[Ru(HP_7)_2]^-$, 951.9 $\{[K(2,2,2\text{-crypt})][Ru(HP_7)_2]\}^-$. ESI-MS, positive ion mode (DMF): *m/z* 1784.3 $\{[K(2,2,2\text{-crypt})]_3[Ru(HP_7)_2]^+$.

7.3.4.21 $[K(2,2,2\text{-crypt})]_4[Ru(P_7)_2]$ (21)

A mixture of $[K(2,2,2\text{-crypt})]_2[Ru(HP_7)_2]$ and $[K(2,2,2\text{-crypt})]_4[Ru(P_7)_2]$ (36.6 mg), $K[N(SiMe_3)_2]$ (11.6 mg, 0.058 mmol) and 2,2,2-crypt (27.9 mg, 0.074 mmol) were dissolved in approximately 0.5 mL d_5-pyridine inside a Young's NMR tube. The mixture was sonicated for approximately half an hour, after which full conversion to $[K(2,2,2\text{-crypt})]_4[Ru(P_7)_2]$ according to ^{1}H and ^{31}P NMR spectroscopy was observed.

^{1}H NMR (499.93 MHz, d_5-pyridine): δ (ppm) 3.40 (48H, broad s, 2,2,2-crypt), 3.32 (48H, broad s, 2,2,2-crypt), 2.30 (48H, broad s, 2,2,2-crypt).

$^{31}P\{^1H\}$ NMR (202.38 MHz, d_5-pyridine): δ (ppm) 212.4 (2P, t, P1, P1A, $^1J_{P1/P1A–P2/P2A}$ = –376 Hz, $^1J_{P1/P1A–P3/P3A}$ = –376 Hz), 13.6 (4P, m, P2, P2A, P3, P3A, $^1J_{P2/P2A–P4/P4A}$ = –251 Hz, $^1J_{P3/P3A–P5/P5A}$ = –243 Hz, $^1J_{P4/P4A–P6/P6A}$ = –241 Hz, $^1J_{P3/P3A–P7/P7A}$ = –237 Hz), –83.7 (8P, m, P4, P4A, P5, P5A, P6, P6A, P7, P7A, $^1J_{P4/P4A–P5/P5A}$ = –485 Hz, $^1J_{P6/P6A–P7/P7A}$ = –485 Hz).

ESI-MS, negative ion mode (DMF): *m/z* 536.8 $[Ru(P_7)_2]^-$, 951.1 $\{[K(2,2,2\text{-crypt})][Ru(P_7)_2]\}^-$, 1367.5 $\{[K(2,2,2\text{-crypt})]_2[Ru(P_7)_2]\}^-$, 1781.9 $\{[K(2,2,2\text{-crypt})]_3[Ru(P_7)_2]\}^-$. ESI-MS, positive ion mode (DMF): *m/z* 2200.8 $\{[K(2,2,2\text{-crypt})]_4[Ru(P_7)_2]\}^+$, 2615.9 $\{[K(2,2,2\text{-crypt})]_5[Ru(P_7)_2]\}^+$.

7.3.4.22 $[K(2,2,2\text{-crypt})]_2[(C_4H_7)P_7Ru(COD)]\cdot tol$ (22)

$[K(2,2,2\text{-crypt})]_2[HP_7]\cdot py$ (73.5 mg, 0.065 mmol), KH (4.2 mg, 0.105 mmol) and 2,2,2-crypt (45.2 mg, 0.120 mmol) were dissolved in approximately 5 mL ethylenediamine to form a red solution, which was stirred under argon for approximately one hour. The ethylenediamine solution was then transferred into a second Schlenk tube containing $[Ru(COD)(\eta^3\text{-}CH_2C(CH_3)CH_2)_2]$ (27.8 mg, 0.087 mmol), and the resulting orange-brown solution was stirred under argon for approximately two hours. The ethylenediamine solvent was subsequently removed *in vacuo* to leave a brown solid, which was washed with approximately 10 mL diethyl ether. The solid residue was redissolved in approximately 5 mL pyridine to form a brown solution, which was filtered into an ampoule and layered with toluene. After several days, orange plate-like crystals of $[K(2,2,2\text{-crypt})]_2[(C_4H_7)P_7Ru(COD)]\cdot tol$ suitable for X-ray diffraction were obtained in a yield

of 23 mg (25%).

^{1}H NMR (499.93 MHz, d_5-pyridine): δ (ppm) 5.11 (s), 5.01 (s), 4.67 (s), 4.63 (s), 3.44 (broad s, 2,2,2-crypt), 3.37 (broad s, 2,2,2-crypt), 2.35 (broad s, 2,2,2-crypt), 2.20 (s), 2.14 (s), 1.91 (s), 1.38 (s), 0.64 (s), 0.59 (s), 0.53 (s).

^{31}P{^{1}H} NMR (202.38 MHz, d_5-pyridine): δ (ppm) 127.1 (1P, t, P1, $^{1}J_{P1–P3}$ = –297 Hz, $^{1}J_{P1–P2}$ = –292 Hz), 83.8 (1P, m, P2, $^{1}J_{P2–P6}$ = –279 Hz, $^{1}J_{P2–P4}$ = –255 Hz), 76.9 (1P, m, P3, $^{1}J_{P3–P7}$ = –287 Hz, $^{1}J_{P3–P5}$ = –271 Hz), –127.7 (1P, m, P4, $^{1}J_{P4–P5}$ = –413 Hz), –133.1 (1P, m, P5), –139.4 (1P, m, P7, $^{1}J_{P7–P6}$ = –384 Hz), –144.5 (1P, m, P6).

^{13}C{^{1}H} NMR (125.71 MHz, d_5-pyridine): δ (ppm) 130.6, 70.9 (2,2,2-crypt), 68.1 (2,2,2-crypt), 66.1, 54.4 (2,2,2-crypt), 46.3, 29.7, 28.6, 26.6, 26.0, 15.9, 5.0.

ESI-MS, negative-ion mode (DMF): *m/z* 481.9 $[(C_4H_7)P_7Ru(COD)]^-$, 520.9 $[K(C_4H_7)P_7Ru(COD)]^-$, 897.2 $\{[K(2,2,2\text{-crypt})][(C_4H_7)P_7Ru(COD)]\}^-$. ESI-MS, positive-ion mode (DMF): *m/z* 1727.4 $\{[K(2,2,2\text{-crypt})]_3[(C_4H_7)P_7Ru(COD)]\}^+$.

7.3.4.23 $[K(2,2,2\text{-crypt})]_2[Co(\eta^5\text{-}P_5)\{\eta^2\text{-}HP_2(mes)\}]$ (23)

K_3P_7 (23.9 mg, 0.072 mmol), $[Co(PEt_2Ph)_2(mes)_2]$ (42.4 mg, 0.067 mmol) and 2,2,2-crypt (61.6 mg, 0.164 mmol) were dissolved in approximately 5 mL ethylenediamine to form a brown solution, which was stirred under argon for approximately two hours. The solution was then filtered into an ampoule and layered with toluene. After several days, dark red-brown block-like crystals of $[K(2,2,2\text{-crypt})]_2[Co(\eta^5\text{-}P_5)\{\eta^2\text{-}HP_2(mes)\}]$ suitable for X-ray diffraction were obtained in a yield of 26.2 mg (30%). Anal. Calcd. for $C_{45}H_{84}CoK_2N_4O_{12}P_7$: C 44.03, H 6.90, N, 4.57. Found: C 43.89, H 6.58, N 4.62.

^{1}H NMR (499.93 MHz, d_5-pyridine): δ (ppm) 6.70 (2H, s, *m*-C*H*), 3.36 (24H, s, 2,2,2-crypt), 3.30 (24H, t, 2,2,2-crypt, $^{3}J_{H–H}$ = 5 Hz), 2.29 (24H, t, 2,2,2-crypt), 2.10 (1H, dd, H1, $^{1}J_{H1–P7}$ =119 Hz, $^{2}J_{H1–P6}$ = 22 Hz), 2.06 (6H, s, *o*-CH_3), 2.02 (3H, s, *p*-CH_3).

^{31}P NMR (202.37 MHz, d_5-pyridine): δ (ppm) 157.6 (5P, s, P1, P2, P3, P4, P5), –12.6 (1P, dd, P6, $^{1}J_{P6–P7}$ = –387 Hz, $^{2}J_{P6–H1}$ = 22 Hz), –105.9 (1P, dd, P7, $^{1}J_{P7–H1}$ = 119 Hz).

$^{13}C\{^{1}H\}$ NMR (125.72 MHz, d_5-pyridine): δ (ppm) 143.2 (*i*-C), 130.9 (*o*-C), 129.8 (*p*-C), 128.7 (*m*-C), 70.8 (2,2,2-crypt), 68.0 (2,2,2-crypt), 54.3 (2,2,2-crypt), 28.2 (*o*-CH_3), 21.5 (*p*-CH_3).

ESI-MS, negative-ion mode (DMF): *m/z* 395.8 $[Co(\eta^5\text{-}P_5)\{\eta^2\text{-}HP_2(mes)\}]^-$. ESI-MS, positive-ion mode (DMF): *m/z* 1227.1 $\{[K(2,2,2\text{-crypt})]_2[Co(\eta^5\text{-}P_5)\{\eta^2\text{-}HP_2(mes)\}]\}^+$, 1641.4 $\{[K(2,2,2\text{-crypt})]_3[Co(\eta^5\text{-}P_5)\{\eta^2\text{-}HP_2(mes)\}]\}^+$.

7.3.4.24 $[K(2,2,2\text{-crypt})]_2[Co(\eta^3\text{-}As_3)\{\eta^4\text{-}As_4(mes)_2\}]\cdot py\cdot 0.5tol$ (24)

K_3As_7 (104 mg, 0.162 mmol), $[Co(PEt_2Ph)_2(mes)_2]$ (93.1 mg, 0.150 mmol) and 2,2,2-crypt (117 mg, 0.312 mmol) were dissolved in approximately 5 mL ethylenediamine to form a brown solution, which was stirred under argon for approximately two hours. The ethylenediamine solvent was subsequently removed under a dynamic vacuum to leave a brown solid, which was redissolved in approximately 5 mL pyridine. The resulting brown solution was filtered into an ampoule and layered with toluene. After several days, dark red block-like crystals of $[K(2,2,2\text{-crypt})]_2[Co(\eta^3\text{-}As_3)\{\eta^4\text{-}As_4(mes)_2\}]\cdot py\cdot 0.5tol$ suitable for X-ray diffraction formed in a yield of 94.5 mg (32%). Anal. Calcd. for $C_{54}H_{94}As_7CoK_2N_4O_{12}$: C 39.22, H 5.73, N 3.39. Found: C 38.93, H 5.55, N 3.18.

^{1}H NMR (499.93 MHz, d_5-pyridine): δ (ppm) 6.77 (4H, s, *m*-C*H*), 3.38 (24H, broad s, 2,2,2-crypt), 3.32 (24H, t, 2,2,2-crypt, $^{3}J_{H-H}$ = 5 Hz), 2.31 (24H, t, 2,2,2-crypt), 2.18 (6H, s, *p*-CH_3), 2.13 (12H, s, *o*-CH_3).

$^{13}C\{^{1}H\}$ NMR (125.72 MHz, d_5-pyridine): δ (ppm) 154.8 (*i*-C), 142.8 (*o*-C), 131.7 (*p*-C), 127.6 (*m*-C), 70.9 (2,2,2-crypt), 68.1 (2,2,2-crypt), 54.3 (2,2,2-crypt), 30.7 (*o*-CH_3), 21.4 (*p*-CH_3).

ESI-MS, negative ion mode (DMF): *m/z* 821.8 $[Co(\eta^3\text{-}As_3)\{\eta^4\text{-}As_4(mes)_2\}]^-$. ESI-MS, positive ion mode (DMF): *m/z* 1653.7 $\{[K(2,2,2\text{-crypt})]_2[Co(\eta^3\text{-}As_3)\{\eta^4\text{-}As_4(mes)_2\}]\}^+$, 2068.2 $\{[K(2,2,2\text{-crypt})]_3[Co(\eta^3\text{-}As_3)\{\eta^4\text{-}As_4(mes)_2\}]\}^+$.

7.4 References

1. Santandrea, R. P.; Mensing, C.; Von Schnering, H.G. *Thermochim. Acta* **1986**, *98,* 301–311.
2. Emmerling, F.; Röhr, C. *Z. Naturforsch. B* **2002**, *57,* 963–975.
3. Turbervill, R. S. P.; Goicoechea, J. M. *Organometallics* **2012**, *31,* 2452–2462.
4. Meyer, E. M.; Gambarotta, S.; Floriani, C.; Chiesivilla, A.; Guastini, C. *Organometallics* **1989**, *8,* 1067–1079.
5. Tang, H.; Richey, H. G. *Organometallics* **2001**, *20,* 1569–1574.
6. Barbero, M.; Cadamuro, S.; Dughera, S.; Giaveno, C. *Eur. J. Org. Chem.* **2006**, 4884–4890.
7. Fianchini, M.; Dai, H. X.; Dias, H. V. R. *Chem. Commun.* **2009**, 6373–6375.
8. Hooper, T. N.; Butts, C. P.; Green, M.; Haddow, M. F.; McGrady, J. E.; Russell, C. A. *Chem. Eur. J.* **2009**, *15,* 12196–12200.
9. MacFarlane, K. S.; Rettig, S. J.; Liu, Z. Q.; James, B. R. *J. Organomet. Chem.* **1998**, *557,* 213–219.
10. Chatt, J.; Shaw, B. L. *J. Chem. Soc.* **1961**, 285–290.
11. Cosier, J.; Glazer, A. M. *J. Appl. Crystallogr.* **1986**, *19,* 105–107.
12. Otwinowski, Z.; Minor, W. *Processing of X-ray Diffraction Data Collected in Oscillation Mode*; Academic Press: New York, 1997.
13. *CrysAlisPro* 1.171.35.8; Agilent Technologies, Yarnton, Oxfordshire, 2011.
14. Sheldrick, G. M. *Acta Crystallogr. A* **1990**, *46,* 467–473.
15. Sheldrick, G. M. *Acta Crystallogr. A* **2008**, *64,* 112–122.
16. Sheldrick, G. M. *SHELX97 - Programs for Crystal Structure Analysis* 7.2; University of Gottingen, Germany, 1998.
17. Te Velde, G.; Bickelhaupt, F. M.; Baerends, E. J.; Guerra, C. F.; Van Gisbergen, S. J. A.; Snijders, J. G.; Ziegler, T. *J. Comput. Chem.* **2001**, *22,* 931–967.
18. Guerra, C. F.; Snijders, J. G.; Te Velde G.; Baerends, E. J. *Theor. Chem. Acc.* **1998**, *99,* 391–403.
19. *ADF* 2010.02; SCM, Theoretical Chemistry, Vrije Universiteit, Amsterdam, The Netherlands, 2010.
20. Parr R. G.; Yang, W. *Density Functional Theory of Atoms and Molecules*; Oxford University Press: Oxford, 1989.
21. Vosko, S. H.; Wilk, L.; Nusair, M. *Can. J. Phys.* **1980**, *58,* 1200–1211.
22. Becke, A. D. *Phys. Rev. A* **1988**, *38,* 3098–3100.
23. Perdew, J. P. *Phys. Rev. B* **1986**, *33,* 8822–8824.
24. Van Lenthe, E.; Baerends, E. J.; Snijders, J. G. *J. Chem. Phys.* **1993**, *99,* 4597–4610.
25. Van Lenthe, E.; Baerends E. J.; Snijders, J. G. *J. Chem. Phys.* **1994**, *101,* 9783–9792.
26. Van Lenthe, E.; Ehlers, A.; Baerends, E. J. *J. Chem. Phys.* **1999**, *110,* 8943–8953.

27. Klamt, A. *J. Phys. Chem.* **1995**, *99,* 2224–2235.

28. Versluis L.; Ziegler, T. *J. Chem. Phys.* **1988**, *88,* 322–328.

29. *Gaussian 03* (Revision A.1); Gaussian, Inc., Pittsburgh, PA, 2003.

30. Krishnan, R.; Binkley, J. S.; Seeger, R.; Pople, J. A. *J. Chem. Phys.* **1980**, *72,* 650–654.

31. Blaudeau, J. P.; McGrath, M. P.; Curtiss, L. A.; Radom, L. *J. Chem. Phys.* **1997**, *107,* 5016–5021.

32. Weigend, F.; Häser, M.; Patzelt, H.; Ahlrichs, R. *Chem. Phys. Lett.* **1998**, *294,* 143–152.

33. Weigend, F.; Ahlrichs, R. *Phys. Chem. Chem. Phys.* **2005**, *7,* 3297–3305.

34. Schäfer, A.; Horn, H.; Ahlrichs, R. *J. Chem. Phys.* **1992**, *97,* 2571–2577.

35. Bader, F. W. *Atoms in Molecules: A Quantum Theory*; Clarendon Press: Oxford, 1990.

36. Biegler-König, F.; Schönbohm, J. *AIM2000* version 2.0; Büro für Innovative Software, 2002.

37. Frisch, M. J. *Gaussian 09* (Revision A.02); Gaussian, Inc., Wallingford, CT, 2009.

38. Budzelaar, P. H. M. *gNMR* 5.0; IvorySoft, 2006.

39. Gênet, J. P.; Pinel, C.; Ratovelomanana-Vidal, V.; Mallart, S.; Pfister, X.; Caño De Andrade, M. C.; Laffitte, J. A. *Tetrahedron: Asymmetry* **1994**, *5,* 665–674.

Appendix 1 Selected data collection and refinement parameters

Compound	[K(2,2,2-crypt)]$_4$[**2**]·2en	[K(2,2,2-crypt)]$_4$[**3**]·6py
Chemical formula	$C_{76}H_{160}As_{14}Cu_2K_4N_{12}O_{24}$	$C_{102}H_{174}K_4N_{14}O_{24}P_{14}Zn$
FW (g mol^{-1})	2958.52	2635.90
Crystal system	Triclinic	Orthorhombic
Space group	$P\bar{1}$	*Fdd*2
Z	1	8
a (Å)	15.1540(2)	23.6766(2)
b (Å)	15.1810(2)	74.2498(6)
c (Å)	15.7640(2)	15.1492(2)
α (°)	111.460(1)	90.00
β (°)	90.070(1)	90.00
γ (°)	118.900(1)	90.00
V (Å^3)	2883.41(7)	26632.0(5)
ρ_{calcd} (g cm^{-3})	1.704	1.315
Radiation, λ (Å)	Mo K$_\alpha$, 0.71073	Mo K$_\alpha$, 0.71073
T (K)	150(2)	150(2)
μ (mm^{-1})	4.565	0.545
No. refined parameters	595	718
Reflections collected	19140	14850
Unique reflections	10050	14850
R_{int}	0.0350	0.0840
R_1/wR_2,[a] $I \geq 2\sigma_I$ (%)	4.81/13.18	4.77/10.60
R_1/wR_2,[a] all data (%)	5.83/13.72	6.87/11.73
GOF	1.066	1.013

[a] $R_1 = [\Sigma||F_o| - |F_c||]/\Sigma|F_o|$; w$R_2 = \{[\Sigma w[(F_o)^2 - (F_c)^2]^2]/[\Sigma w(F_o{}^2)^2]\}^{1/2}$; $w = [\sigma^2(F_o)^2 + (AP)^2 + BP]^{-1}$, where $P = [(F_o)^2 + 2(F_c)^2]/3$ and the A and B values are 0.0703 and 13.1803 for [K(2,2,2-crypt)]$_4$[**2**]·2en, and 0.0558 and 49.7941 for [K(2,2,2-crypt)]$_4$[**3**]·6py.

Compound	[K(2,2,2-crypt)]$_4$[**5**]·6py	[K(2,2,2-crypt)]$_2$[**6**]
Chemical formula	$C_{102}H_{174}CdK_4N_{14}O_{24}P_{14}$	$C_{48}H_{82}InK_2N_4O_{12}P_7$
FW (g mol^{-1})	2682.93	1316.99
Crystal system	Orthorhombic	Monoclinic
Space group	*Fdd*2	$P2_1/c$
Z	8	4
a (Å)	23.5977(2)	11.4911(1)
b (Å)	75.1887(8)	24.2435(2)
c (Å)	15.1082(1)	22.4105(2)
α (°)	90.00	90.00
β (°)	90.00	92.211(1)
γ (°)	90.00	90.00
V (Å^3)	26806.2(4)	6238.57(9)
ρ_{calcd} (g cm^{-3})	1.330	1.402
Radiation, λ (Å)	Mo K$_\alpha$, 0.71073	Mo K$_\alpha$, 0.71073
T (K)	150(2)	150(2)
μ (mm^{-1})	0.521	0.748
No. refined parameters	726	667
Reflections collected	10425	21140
Unique reflections	10425	10893
R_{int}	0.0460	0.0620
R_1/wR_2,[a] $I \geq 2\sigma_I$ (%)	5.41/10.86	5.90/18.35
R_1/wR_2,[a] all data (%)	7.69/11.61	7.16/19.06
GOF	1.027	1.037

[a] $R_1 = [\Sigma||F_o| - |F_c||]/\Sigma|F_o|$; w$R_2 = \{[\Sigma w[(F_o)^2 - (F_c)^2]^2]/[\Sigma w(F_o{}^2)^2]\}^{1/2}$; $w = [\sigma^2(F_o)^2 + (AP)^2 + BP]^{-1}$, where $P = [(F_o)^2 + 2(F_c)^2]/3$ and the A and B values are 0.0435 and 162.0573 for [K(2,2,2-crypt)]$_4$[**5**]·6py, and 0.1071 and 28.3581 for [K(2,2,2-crypt)]$_2$[**6**].

Compound	$[K(2,2,2\text{-crypt})]_2$[**8**]	$[K(2,2,2\text{-crypt})]_2$[**9**]
Chemical formula	$C_{36}H_{74}Ag_2K_2N_4O_{12}P_{14}$	$C_{36}H_{74}Au_2K_2N_4O_{12}P_{14}$
FW (g mol^{-1})	1482.56	1660.76
Crystal system	Monoclinic	Monoclinic
Space group	$P2_1/c$	$P2_1/n$
Z	4	4
a (Å)	10.7536(1)	14.4130(2)
b (Å)	27.0054(2)	10.8462(2)
c (Å)	10.6651(1)	19.9351(4)
α (°)	90.00	90.00
β (°)	92.3363(5)	102.8771(8)
γ (°)	90.00	90.00
V (Å^3)	3094.63(5)	3038.00(9)
ρ_{calcd} (g cm^{-3})	1.591	1.815
Radiation, λ (Å)	Mo K_α, 0.71073	Mo K_α, 0.71073
T (K)	150(2)	150(2)
μ (mm^{-1})	1.182	5.383
No. refined parameters	320	321
Reflections collected	57032	66526
Unique reflections	7032	6906
R_{int}	0.029	0.113
R_1/wR_2,[a] $I \geq 2\sigma_I$ (%)	3.13/6.00	4.88/12.89
R_1/wR_2,[a] all data (%)	5.82/7.83	8.19/14.17
GOF	0.9505	0.9335

[a] $R_1 = [\Sigma||F_o| - |F_c||]/\Sigma|F_o|$; $wR_2 = \{[\Sigma w[(F_o)^2 - (F_c)^2]^2]/[\Sigma w(F_o{}^2)^2]\}^{1/2}$. For $[K(2,2,2\text{-crypt})]_2$[**8**], w = [weight][1 − [(|F_o| − |F_c|)/6σ|F_o|]^2]^2, where [weight] is obtained from the Chebychev polynomial: [weight] = $[A_0T_0(|F_c|/|F_o|) + A_1T_1(|F_c|/|F_o|) + ... + A_{n-1}T_{n-1}(|F_c|/|F_o|)]^{-1}$. The values of the Chebychev coefficients, A_i, are 7.76, 11.2, 6.42, 2.69 and 0.570. For $[K(2,2,2\text{-crypt})]_2$[**9**], w = $[\sigma^2(F_o)^2 + (AP)^2 + BP]^{-1}$, where P = $[(F_o)^2 + 2(F_c)^2]/3$ and the A and B values are 0.10 and 0.00.

Compound	[K(2,2,2-crypt)]$_3$[**10**]·3.5py	[K(2,2,2-crypt)]$_2$[**12**]·py
Chemical formula	$C_{71.5}H_{125.5}InK_3N_{9.5}O_{18}P_{14}$	$C_{41}H_{77}K_2N_5O_{12}P_7Tl$
FW (g mol^{-1})	2072.02	1331.44
Crystal system	Triclinic	Triclinic
Space group	$P\bar{1}$	$P\bar{1}$
Z	2	4
a (Å)	15.9776(1)	12.1833(1)
b (Å)	25.1208(1)	20.5010(2)
c (Å)	27.1871(2)	25.6093(3)
α (°)	113.8600(10)	66.9990(10)
β (°)	94.3940(10)	79.2500(10)
γ (°)	94.2590(10)	87.8950(10)
V (Å^3)	9883.65(10)	5779.95(10)
ρ_{calcd} (g cm^{-3})	1.392	1.530
Radiation, λ (Å)	Mo K_α, 0.71073	Mo K_α, 0.71073
T (K)	150(2)	150(2)
μ (mm^{-1})	0.655	3.189
No. refined parameters	2096	1189
Reflections collected	82170	33025
Unique reflections	44881	20159
R_{int}	0.0491	0.0477
R_1/wR_2,[a] $I \geq 2\sigma_I$ (%)	4.62/9.05	6.72/18.10
R_1/wR_2,[a] all data (%)	10.57/10.64	12.52/19.99
GOF	1.012	1.040

[a] $R_1 = [\Sigma||F_o| - |F_c||]/\Sigma|F_o|$; w$R_2 = \{[\Sigma w[(F_o)^2 - (F_c)^2]^2]/[\Sigma w(F_o{}^2)^2]\}^{1/2}$; $w = [\sigma^2(F_o)^2 + (AP)^2 + BP]^{-1}$, where $P = [(F_o)^2 + 2(F_c)^2]/3$ and the A and B values are 0.0417 and 1.9222 for [K(2,2,2-crypt)]$_3$[**10**]·3.5py, and 0.1087 and 0.0000 for [K(2,2,2-crypt)]$_2$[**12**]·py.

Compound	[K(18-crown-6)]$_2$[**13**]	[K(2,2,2-crypt)]$_3$[**14**]·en
Chemical formula	$C_{24}H_{48}As_7K_2O_{12}Tl$	$C_{56}H_{116}K_3N_8O_{18}P_{15}Sn$
FW (g mol^{-1})	1335.63	1890.11
Crystal system	Monoclinic	Orthorhombic
Space group	$P2_1/c$	*Ibca*
Z	4	8
a (Å)	18.8701(3)	23.8480(3)
b (Å)	11.4835(3)	24.4219(4)
c (Å)	20.8037(3)	30.8233(4)
α (°)	90.00	90.00
β (°)	107.8300(10)	90.00
γ (°)	90.00	90.00
V (Å^3)	4291.53(15)	17951.9(4)
ρ_{calcd} (g cm^{-3})	2.067	1.399
Radiation, λ (Å)	Mo K_α, 0.71073	Mo K_α, 0.71073
T (K)	150(2)	150(2)
μ (mm^{-1})	9.361	0.752
No. refined parameters	554	456
Reflections collected	14444	13132
Unique reflections	7489	6818
R_{int}	0.0349	0.0219
R_1/wR_2,[a] $I \geq 2\sigma_I$ (%)	7.04/18.69	6.38/14.20
R_1/wR_2,[a] all data (%)	8.06/19.10	9.02/16.03
GOF	1.125	1.026

[a] $R_1 = [\Sigma||F_o| - |F_c||]/\Sigma|F_o|$; w$R_2 = \{[\Sigma w[(F_o)^2 - (F_c)^2]^2]/[\Sigma w(F_o{}^2)^2]\}^{1/2}$; $w = [\sigma^2(F_o)^2 + (AP)^2 + BP]^{-1}$, where $P = [(F_o)^2 + 2(F_c)^2]/3$ and the A and B values are 0.0661 and 107.0257 for [K(18-crown-6)]$_2$[**13**], and 0.0510 and 131.5054 for [K(2,2,2-crypt)]$_3$[**14**]·en.

Compound	[K(2,2,2-crypt)]$_3$[**15**]·2en	[K(2,2,2-crypt)]$_3$[**16**]·en
Chemical formula	$C_{58}H_{124}As_{15}K_3N_{10}O_{18}Sn$	$C_{56}H_{116}K_3N_8O_{18}P_{15}Pb$
FW (g mol^{-1})	2609.46	1978.61
Crystal system	Monoclinic	Orthorhombic
Space group	$P2_1/c$	*Ibca*
Z	4	8
a (Å)	17.0409(1)	23.8547(2)
b (Å)	18.3450(2)	24.2093(2)
c (Å)	30.3204(3)	30.8457(3)
α (°)	90.00	90.00
β (°)	93.7830(10)	90.00
γ (°)	90.00	90.00
V (Å^3)	9457.97(15)	17813.6(3)
ρ_{calcd} (g cm^{-3})	1.833	1.476
Radiation, λ (Å)	Mo K$_\alpha$, 0.71073	Mo K$_\alpha$, 0.71073
T (K)	150(2)	150(2)
μ (mm^{-1})	5.671	2.365
No. refined parameters	946	447
Reflections collected	32094	15030
Unique reflections	16456	7792
R_{int}	0.0580	0.0157
R_1/wR_2,[a] $I \geq 2\sigma_I$ (%)	5.51/14.08	8.47/17.48
R_1/wR_2,[a] all data (%)	7.51/15.02	9.47/17.79
GOF	1.039	1.172

[a] $R_1 = [\Sigma||F_o| - |F_c||]/\Sigma|F_o|$; w$R_2 = \{[\Sigma w[(F_o)^2 - (F_c)^2]^2]/[\Sigma w(F_o{}^2)^2]\}^{1/2}$; $w = [\sigma^2(F_o)^2 + (AP)^2 + BP]^{-1}$, where $P = [(F_o)^2 + 2(F_c)^2]/3$ and the A and B values are 0.0893 and 7.2783 for [K(2,2,2-crypt)]$_3$[**15**]·2en, and 0.0000 and 356.9491 for [K(2,2,2-crypt)]$_3$[**16**]·en.

Compound	$[K(2,2,2\text{-crypt})]_2$[**18**]	$[K(2,2,2\text{-crypt})]_2$[**22**]·tol
Chemical formula	$C_{36}H_{74}FeK_2N_4O_{12}P_{14}$	$C_{55}H_{99}K_2N_4O_{12}P_7Ru$
FW (g mol^{-1})	1322.62	1404.44
Crystal system	Triclinic	Triclinic
Space group	$P\bar{1}$	$P\bar{1}$
Z	1	2
a (Å)	10.9876(3)	11.1933(2)
b (Å)	12.1241(4)	14.1372(2)
c (Å)	12.7331(6)	23.7501(3)
α (°)	66.7100(10)	104.3320(10)
β (°)	84.9550(10)	91.7800(10)
γ (°)	73.754(2)	107.5140(10)
V (Å^3)	1495.31(10)	3449.76(9)
ρ_{calcd} (g cm^{-3})	1.469	1.352
Radiation, λ (Å)	Mo K_α, 0.71073	Cu K_α, 1.54178
T (K)	150(2)	150(2)
μ (mm^{-1})	0.820	4.917
No. refined parameters	385	767
Reflections collected	8683	72098
Unique reflections	5154	14341
R_{int}	0.0427	0.0455
R_1/wR_2,[a] $I \geq 2\sigma_I$ (%)	4.27/8.63	4.26/10.96
R_1/wR_2,[a] all data (%)	7.57/10.00	4.38/11.05
GOF	0.979	1.119

[a] $R_1 = [\Sigma||F_o| - |F_c||]/\Sigma|F_o|$; w$R_2 = \{[\Sigma w[(F_o)^2 - (F_c)^2]^2]/[\Sigma w(F_o{}^2)^2]\}^{1/2}$; $w = [\sigma^2(F_o)^2 + (AP)^2 + BP]^{-1}$, where $P = [(F_o)^2 + 2(F_c)^2]/3$ and the A and B values are 0.0227 and 1.1239 for $[K(2,2,2\text{-crypt})]_2$[**18**], and 0.0443 and 4.5023 for $[K(2,2,2\text{-crypt})]_2$[**22**]·tol.

Compound	$[K(2,2,2\text{-crypt})]_2$[**23**]	$[K(2,2,2\text{-crypt})]_2$[**24**]·py·0.5tol
Chemical formula	$C_{45}H_{84}CoK_2N_4O_{12}P_7$	$C_{62.5}H_{103}As_7CoK_2N_5O_{12}$
FW (g mol^{-1})	1227.08	1778.07
Crystal system	Triclinic	Triclinic
Space group	$P\bar{1}$	$P\bar{1}$
Z	2	2
a (Å)	11.1630(1)	13.1075(4)
b (Å)	12.2130(2)	13.6595(4)
c (Å)	22.7373(2)	24.3451(8)
α (°)	92.7580(10)	78.450(3)
β (°)	103.6300(10)	84.386(3)
γ (°)	94.3790(10)	62.288(3)
V (Å^3)	2996.77(6)	3780.6(2)
ρ_{calcd} (g cm^{-3})	1.360	1.562
Radiation, λ (Å)	Mo K_α, 0.71073	Cu K_α, 1.54178
T (K)	150(2)	150(2)
μ (mm^{-1})	0.669	6.635
No. refined parameters	1113	800
Reflections collected	19484	56712
Unique reflections	10441	13342
R_{int}	0.0268	0.1252
R_1/wR_2,[a] $I \geq 2\sigma_I$ (%)	5.03/13.98	6.44/17.36
R_1/wR_2,[a] all data (%)	6.53/14.85	8.20/18.45
GOF	1.050	0.995

[a] $R_1 = [\Sigma||F_o| - |F_c||]/\Sigma|F_o|$; w$R_2 = \{[\Sigma w[(F_o)^2 - (F_c)^2]^2]/[\Sigma w(F_o{}^2)^2]\}^{1/2}$; $w = [\sigma^2(F_o)^2 + (AP)^2 + BP]^{-1}$, where $P = [(F_o)^2 + 2(F_c)^2]/3$ and the A and B values are 0.0813 and 1.5975 for $[K(2,2,2\text{-crypt})]_2$[**23**], and 0.1022 and 3.6220 for $[K(2,2,2\text{-crypt})]_2$[**24**]·py·0.5tol.

Appendix 2 List of publications

1. “Reactivity studies of group 15 Zintl ions towards homoleptic post-transition metal organometallics: a ‘bottom-up’ approach to bimetallic molecular clusters”. **Knapp, C.**; Zhou, B.; Denning, M. S.; Rees, N. H.; Goicoechea, J. M. *Dalton Trans.* **2010**, *39*, 426–436.

2. “A versatile salt-metathesis route to heteroatomic clusters derived from phosphorus and arsenic Zintl anions”. **Knapp, C. M.**; Large, J. S.; Rees, N. H.; Goicoechea, J. M. *Dalton Trans.* **2011**, *40*, 735–745.

3. “The bis(hydrogenheptaphosphide)iron(II) dianion: a Zintl ion analogue of ferrocene?”. **Knapp, C. M.**; Large, J. S.; Rees, N. H.; Goicoechea, J. M. *Chem. Commun.* **2011**, *47*, 4111–4113.

4. “Heteroatomic Molecular Clusters Derived from Group 15 Zintl Ion Cages: Synthesis and Isolation of $[M_2(HP_7)_2]^{2-}$ (M = Ag, Au), Two Novel Cluster Anions Exhibiting Metallophilic Interactions”. **Knapp, C. M.**; Jackson, C. S.; Large, J. S.; Thompson, A. L.; Goicoechea, J. M. *Inorg. Chem.* **2011**, *50*, 4021–4028.

5. “$[Co(\eta^5\text{-}P_5)\{\eta^2\text{-}P_2H(mes)\}]^{2-}$: A Phospha-Organometallic Complex Obtained by the Transition-Metal-Mediated Activation of the Heptaphosphide Trianion”. **Knapp, C. M.**; Westcott, B. H.; Raybould, M. A. C.; McGrady, J. E.; Goicoechea, J. M. *Angew. Chem., Int. Ed.* **2012**, *51*, 9097–9100.

6. “Transition-metal-mediated activation of the heptaarsenide trianion: isolation of a diaryltetraarsenabutadienediide”. **Knapp, C. M.**; Westcott, B. H.; Raybould, M. A. C.; McGrady, J. E.; Goicoechea, J. M. *Chem. Commun.* **2012**, *48*, 12183–12185.